ISMRM | DACH CHAPTER

MAX PLANCK INSTITUTE FOR BIOLOGICAL CYBERNETICS

26th Annual Meeting of the
German-speaking section of ISMRM

DACH-ISMRM 2024

Program & Proceedings

September 4 - 5, 2024

Tübingen




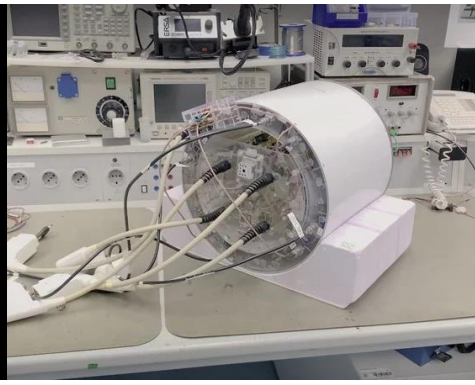

Sponsors

Many thanks to the sponsors for their valuable support of the DACH-ISMRM 2024 in Tübingen!

The German Chapter (and thus indirectly the Annual Meeting) was financially supported by the following sponsors in 2024: Bruker BioSpin (500€), Mr Shim GmbH (500€), Neoscan Solutions GmbH (1,000€), NVision Imaging Technologies (500€), Pure Devices GmbH (500€), Siemens Healthineers (2,500€), Skope Magnetic Resonance Technologies (1,000€).

Organizing Committee

DACH-ISMRM Board

Sebastian Schmitter
Susanne Schnell

On-site Committee

Dana Ramadan
Dario Bosch
Sebastian Müller
Felix Glang

Reviewers

A big thank you to all the volunteer abstract reviewers for their expertise, time, and dedication! Your efforts behind the scenes are what make this conference possible.

Aaron von Raven (Tübingen)
Ali Aghaeifar (Tübingen)
Andre Martins (Tübingen)
Andreas Korzowski (Heidelberg)
Armin Nagel (Erlangen)
Chris Wiggins (Jülich)
Christoph Aigner (Berlin)
Dana Ramadan (Tübingen)
Dario Bosch (Tübingen)
Felix Glang (Tübingen)
Florian Birk (Tübingen)
Frederik Laun (Erlangen)
Fritz Schick (Tübingen)
Gisela Hagberg (Tübingen)
Henri de Maissin (Freiburg)
Jonas Bause (Tübingen)
Julius Steiglechner (Tübingen)
Kai Buckenmaier (Tübingen)
Max Zimmermann (Tübingen)
Kengo Takahashi (Amsterdam)
Klaus Scheffler (Tübingen)
Martin Korzeczek (Ulm)
Maxim Terekhov (Würzburg)
Naman Jain (Tübingen)
Nicolas Kempf (Tübingen)
Patrick Schuenke (Berlin)
Praveen Valsala (Tübingen)
Qi Wang (Tübingen)
Rahel Heule (Zürich)
Rolf Pohmann (Tübingen)
Rüdiger Stirnberg (Bonn)
Ruth Tuura (Zürich)
Sebastian Müller (Tübingen)
Stephan Orzada (Heidelberg)

Program

Day 1: Wednesday, September 04

07:45	**Registration & Coffee**		
08:30	**Welcome**	**Prof. Dr. Klaus Scheffler,** Max Planck Institute for Biological Cybernetics	
08:45	**Plenary Talk**	**Prof. Laura M. Schreiber, PhD, MBA** *„Excellence and Objectivity and the Human Factor in Research"*	
09:30	**Scientific Session 1**	**Hyperpolarization and Metabolic Imaging**	**Chairs:** Maria Anikeeva, Jan-Bernd Hövener
09:30	Anaïs Choffart	***101***	*Non-invasive Mapping of Acidosis and Extracellular Lactosis for Assessing Tumor Invasion In Vivo*
09:42	Josh Peters	***102***	*T1 alterations in nitrogen-15 hyperpolarized molecules*
09:54	Jakob Gaubatz	***103***	*Phase-based 3D pH imaging in vivo using hyperpolarized [1,5-13C2]Z-OMPD*
10:06	Friedemann Bullinger	***104***	*Magnetic resonance in the zero and ultralow field regime – a transition from one-dimensional oscillation to precession*
10:18	Nicolas Kempf	***105***	*13C imaging of pyruvate with SABRE at Ultra-Low field*
10:30	**Coffee Break**		
11:00	**Scientific Session 2**	**MRI System Hardware and Technical Innovations**	**Chairs**: Georgiy Solomakha, Pavel Povolni
11:00	Yenal Gökpek	***201***	*A parahydrogen polarizer for >30 bars hydrogenation and automated purification*
11:12	Jonathan Stelter	***202***	*B_0 self-navigation achieves contrast-independent respiratory motion estimation in radial stack-of-stars imaging*
11:24	Teresa Reichl	***203***	*From 4D Flow MRI to MPI: A study of the flow dynamics in an aneurysm phantom*
11:36	Christoph Aigner	***204***	*Towards UHF Spinal Cord MRI: Overcoming B_0 & B_1^+ Challenges*
11:48	Tim Haigis	***205***	*Quantitative Comparison of pTx Coils at 9.4T*
12:00	**Lunch Break**		
13:15	**Gorter Session I**		**Chairs:** Susanne Schnell, Dario Bosch
13:30	Jonathan Endres	***G1***	*Phase distribution graphs for fast, differentiable, and spatially encoded Bloch simulations of arbitrary MRI sequences*
14:00	Vanessa Franke	***G2***	*In vivo determination of pH and magnesium ion concentration by means of 31P MRSI: A multi-parametric look-up approach*
14:30	Martin Grashei	***G3***	*Simultaneous magnetic resonance imaging of pH, perfusion and renal filtration using hyperpolarized 13C-labelled Z-OMPD*
15:00	**Coffee Break**		
15:30	**Gorter Session II**		**Chairs:** Susanne Schnell, Dario Bosch
15:30	Tor Rasmus Memhave	***G4***	*Establishing an MR-based profile of lithium treatment*
16:00	Niklas Wallstein	***G5***	*Anisotropic Longitudinal Water Proton Relaxation in White Matter Investigated Ex Vivo in Porcine Spinal Cord with Sample Rotation*
16:30	**Poster Session**		
17:45	**Plenary Talk**	**Dr. Lars G. Hanson** *"Mapping current-induced fields in the brain using MRI"*	
18:30	**Get Together**	**Saints & Scholars** Wilhelmstraße 44 72074 Tübingen	

Day 2: Thursday, September 05

08:30	**Plenary Talk**	**Natalia Petridou, D.Sc.** *"From blood to neuron - how close can we get with BOLD fMRI in humans?"*		
09:15	**Scientific Session 3.1**	**MRI Sequence Development and Optimization I**	**Chairs:**	Klaus Scheffler, Praveen Valsala
09:15	Andreas Holl	***301*** *Open SPEN and Non-linear Gradient Implementation using Pulseq*		
09:27	Simon Weinmüller	***302*** *MR-zero meets FLASH – Controlling the transient signal decay in gradient- and rf-spoiled gradient echo sequences using Phase Distribution Graphs*		
09:39	Martin Freudensprung	***303*** *Reproducible pTx sequence development using Pulseq*		
09:51	Ariel Hannum	***304*** *PNS-Constrained Arbitrary Gradient Waveform Design for DWI on Ultra-High-Performance MRI Systems*		
10:05	**Coffee Break**			
10:40	**Scientific Session 3.2**	**MRI Sequence Development and Optimization II**	**Chairs:**	Klaus Scheffler, Praveen Valsala
10:40	Fabian Gutjahr	***305*** *Addressing the Ejection Fraction Dependence of FAIR-ASL Perfusion*		
10:52	Jacopo Frignani	***306*** *3D Filter-Exchange Imaging Using Slab-Selective Excitation*		
11:04	Niklas Himburg	***307*** *Errors in Actual Flip Angle Imaging (AFI) of polyvinylpyrrolidone (PVP) solutions at 3T and 7T*		
11:16	Yannik Ott	***308*** *Training deep learning reconstruction models for radial real-time cardiac cine MRI using synthetic golden-angle data*		
11:30	**Career Opportunities**		**Chairs:**	Emily Hoffmann, Dana Ramadan
12:30	**Lunch Break**			
13:45	**Scientific Session 4**	**Clinical and Biological Applications**	**Chairs:**	Gisela Hagberg, Benjamin Bender
13:45	Dennis C. Thomas	***401*** *Mapping of cerebral metabolite concentrations in brain tumors using 1H-MRSI and quantitative MRI*		
13:57	Enrica Wilken	***402*** *bSSFP acquisition in time-lapse MRI: three-dimensional single-cell tracking with high temporal resolution*		
14:09	Robert Alexander Vornhusen	***403*** *Light-switchable giant unilamellar vesicles: A model for cell size and transmembrane water exchange*		
14:21	Vinod Kumar	***404*** *Mesoscopic functional mapping of the globus pallidus nuclei at 9.4T*		
14:33	Rolf Otto Reiter	***405*** *Intervertebral disc degeneration assessed by in vivo multifrequency MR elastography*		
14:45	Maik Rothe	***406*** *Multi-parametric characterization and clustering of fast relaxing knee tissues using 3D UTE*		
14:57	Elizabeth Huaroc Moquillaza	***407*** *Free-breathing full pancreas water T1 mapping*		
15:09	Christoph Birkl	***408*** *Performance of Quantitative Susceptibility Mapping in brain tissue with extreme iron content*		
15:25	**Voting for Poster Prizes**			
15:40	**Coffee Break**			
16:00	**DACH-ISMRM Business Meeting**			
17:00	**Plenary Talk**	**Prof. Dr. Dr. h.c. Jürgen Hennig** *"Innovation in MRI: Back to the Future?"*		
17:45	**Awards & Farewell**			

Venue

Lecture Hall of the MPI for Intelligent Systems
Max Planck Ring 4
72076 Tübingen

Lunch Catering

Salam Box
Mühlstraße 14
72074 Tübingen

Poster Session Wednesday, September 04, 16:30 - 17:45

Hyperpolarization and Metabolic Imaging

P101	Martin Sandbrink	*Implementation of SLIC-SABRE hyperpolarization of 1-13C pyruvate*
P102	Maria Anikeeva	*Implementing a Xenon polarizer for in vitro and in vivo imaging*
P103	Aaron Diercks	*Metabolic imaging with deuterated Glucose (and HP pyruvate) in a colitis model*

MRI System Hardware and Technical Innovations

P201	Pavel Povolni	*A Low-Cost Magnetic Measurement System for Low-Field MRI Magnets based on a Motion Tracked Flexible-Joint Robot with 5 Degrees of Freedom*
P202	Harriet Wulff	*Automated Gas Delivery System for Parahydrogen-Induced Polarisation at up to 10 bar*
P203	Judith Samlow	*Easy Rebuildable Cubic 3-Axis Positioning Robot Based on Open-Source Hardware: Validated via Camera-Based Motion Tracking and Initial Application in Magnetic Low Field Mapping*
P204	Moritz Sander	*Inductively coupled coils for 1.5 T, 3 T and 7 T MRI*
P205	Sergej Maltsev	*SQUID based Method of Evaluating Noise Characteristics of High Temperature Superconductors used in Novel Low Field MRI Scanner Designs*

MRI Sequence Development and Optimization

P301	Chris Lippe	*CEST MRI multi-pool quantification through simplified model-based analysis*
P302	Jonathan Endres	*Direct Encoded Signal Control with Phase Distribution Graphs for readout-tailored multipulse pTx optimization*
P303	Franziska Lohrengel	*Implementing whole brain spectroscopy on a vendor agnostic pulse programming platform*
P304	Caroline Scheufler	*Optimization of multi-VENC compressed sensing 4D flow MRI for high-resolution neurovascular applications*
P305	Clemens Mey	*SNR requirements for quantitative frequency-modulated bSSFP*
P306	Clemens Mey	*T2 mapping based on frequency-modulated bSSFP*
P307	Fabian Müller	*The impact of fat-navigator resolution on motion parameter estimation accuracy*
P308	Jakob Schattenfroh	*Ultra-Low Frequency MR Elastography*

Clinical and Biological Applications

P401	Fiona Mankertz	*Association Between Arterial Hypertension and Spinal Degeneration: An MRI-Based Cross-Sectional Study*
P402	Sascha Santaniello	*Automatic evaluation of the properties of the glymphatic system using diffusion MRI data*
P403	Simon Mayr	*Cardiac CINE imaging at 0.55T – a comparison to 1.5T*
P404	Gisela Hagberg	*How similar is quantitative MRI in the human brain measured ex vivo and in vivo?*
P405	Ali Ajouz	*Impact of image registration and fibre orientation on the DTI-ALPS-index*
P406	Wolfgang Weber-Fahr	*Neurobiochemical correlates of long-term neuropsychiatric consequences of COVID-19 disease*
P407	Yan Ma	*Optogenetic fPET/fMRI Reveals Distinct Roles of the Substania Nigra in Motor and Cognitive Processes*
P408	Aayush Nepal	*Semi-Automated Segmentation Pipeline for Dynamic MRI Analysis of Knee Joint Kinematics*
P409	Aref Kalantari	*Tract masks for refined analysis of diffusion properties in motor tracts related to functional recovery after stroke in mice*
P410	Fatima Anum	*Unravelling yeast metabolism with real-time deuterium magnetic resonance spectroscopy*

Gorter Prize Finalists

G1	Jonathan Endres	*Phase distribution graphs for fast, differentiable, and spatially encoded Bloch simulations of arbitrary MRI sequences*
G2	Vanessa Franke	*In vivo determination of pH and magnesium ion concentration by means of 31P MRSI: A multi-parametric look-up approach*
G3	Martin Grashei	*Simultaneous magnetic resonance imaging of pH, perfusion and renal filtration using hyperpolarized 13C-labelled Z-OMPD*
G4	Tor Rasmus Memhave	*Establishing an MR-based profile of lithium treatment*
G5	Niklas Wallstein	*Anisotropic Longitudinal Water Proton Relaxation in White Matter Investigated Ex Vivo in Porcine Spinal Cord with Sample Rotation*

Phase distribution graphs for fast, differentiable, and spatially encoded Bloch simulations of arbitrary MRI sequences

Jonathan Endres,[1*] Simon Weinmüller[1] and Moritz Zaiss[1,2]

[1] Institute of Neuroradiology, University Hospital Erlangen, FAU, Erlangen, Germany.
[2] Artificial Intelligence in Biomedical Engineering, FAU, Erlangen, Germany.

Synopsis:

We introduce an analytical approach to Bloch simulations for MRI sequences that enables time efficient calculations of signals free of Monte-Carlo noise. It provides full flexibility and differentiability in RF flip angles, RF phases, magnetic field gradients and time, as well as insights into image formation.

The new approach can fully replace isochromat based simulations by improving upon the Extended Phase Graph concept and including the contribution of dephased states, spatial encoding, T_2' effects and arbitrary timing. It outperforms existing solutions in terms of simulation time and produces signals that are quantitatively comparable to in vivo measurements.

Introduction

Bloch simulations are an indispensable tool for testing, analyzing and optimizing MR sequences. Common solutions use isochromats[1] to calculate the signal response of an MRI sequence dependent on the properties of the simulated phantom.

An alternative for using isochromats is given by the extended phase graph (EPG) formalism.[2-4] EPG is an analytical description of the Bloch equations in the Fourier domain and handles spatial frequencies exactly. When using EPG to simulate MR sequences, typically a tensor of states is used,[5-7] which in the following we label state-tensor-EPG (ST-EPG) to better distinguish between EPG in general and how it is typically used to compute the magnetization produced by MR sequences.

Because ST-EPGs sample k-space on an equidistant grid and don't support arbitrary dephasing for a single simulation step, they are only used to simulate periodic sequences with an identical amount of dephasing between any pair of subsequent RF pulses, usually sampling the echo tops of the signal.[7] With this limitation, ST-EPG is not suitable as a full replacement for isochromat-based Bloch simulations.

Inspired by this concept, we present a novel algorithm labeled phase distribution graphs (PDG), which lifts the limitations of ST-EPG. PDGs describe the magnetization by splitting it into a variable number of states, each representing a part of the magnetization with arbitrary gradient and time dephasing (Fig 1). PDGs contain the exact dephasing and thus encoding of all parts of the magnetization, describing complete echo shapes, while being fully differentiable in time, gradients and RF pulse flip angle and phase, allowing for efficient sequence optimization.

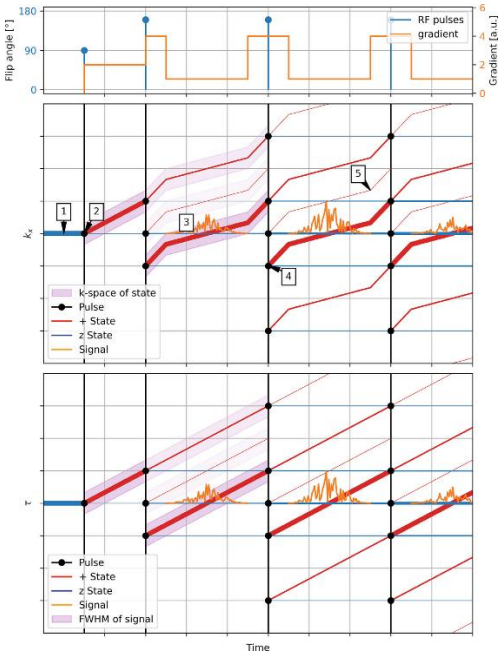

Fig. 1: Views of the PDG of a TSE sequence, plotted as τ and k_x state dephasing over time. Both are views of the same graph. Pulses split up states, which then dephase with time or gradient fields. The dephasing of states is not limited in any way and purely depends on the sequence, all transversal states can contribute to the measured signal.

To achieve efficient simulation of sequences with arbitrary timing and gradients, novel techniques were implemented to control the number of states involved in the simulation, limiting them to the states that actually impact the measured signal. That way, an "explosion" of the state count is avoided, while keeping the error of the calculated signal low. We show that PDG yields identical results to isochromat-based simulation while outperforming them by at least one order of magnitude, without introducing any of the Monte-Carlo noise found in isochromat-based approaches. We demonstrate that PDG allows full simulation and end-to-end optimization of MRI sequences, and provides insights into the MRI signal contributions.

Theory

Following the principles of the Extended Phase Graphs (EPG) framework[3], magnetization is decomposed into configuration states. For this, a complex coordinate system is used, which simplifies the description of transverse magnetization, assuming that the main magnetic field B_0 is aligned with the z axis. Description of $T_{1/2}$ relaxation, as well as diffusion, is identical between EPG and PDG.

When decomposing the magnetization into states, the $\hat{e} \in \{+, -, z\}$ components of the complex coordinate system are treated separately.[6] The application of an RF pulse to a single state splits it into three new ones, which is also known as partition method.[8] Simulating relaxation and dephasing works identical to EPG, with the difference that dephasing is differentiated between gradient and time-based ($\Delta\omega_0$ and T_2') dephasing, and can be any value $(k, \tau) \in \mathbb{R}^4$.

In contrast to the Fourier decomposition of EPG, PDG states include spatial and frequency distributions $V(r)$ and $W(\omega, r)$, as seen in eq. 1:

$$M^{\hat{e}}(r, \omega) = F^{\hat{e}}_{k,\tau} \cdot e^{ikr} \cdot e^{i\tau\omega} \cdot W(\omega, r) \cdot V(r) \quad (1)$$

Where $F^{\hat{e}}_{k,\tau} \in \mathbb{C}$ is the amplitude of the state with $\hat{e} \in \{+, -, z\}$, k is the modulation from B_0 field gradients, and τ describes the width of the phase distribution as a result of off-resonance. A new distribution of off-resonance frequencies $W(\omega, r)$ is introduced, enabling the description of spatially varying T_2' dephasing and B_0 inhomogeneities. Additionally, a spatial modulation $V(r)$ is included, representing the proton density distribution. The ST-EPG algorithm is a special case of our formalism, as eq. 1 is equal to a plane wave if $W(\omega) = \delta(\omega)$, meaning no off-resonance and infinite T_2', and $V(r) = 1$, meaning infinite, homogeneous magnetization as assumed in ST-EPG.[2,9] Typically, a Cauchy distribution[8] centered around $\Delta\omega_0$ is used for $W(\omega)$, leading to an exponential T_2' decay, as well as sinc-shaped voxels $V(r)$, which limits the signal to the first k-space and is consistent with the assumptions made by the Fourier Transformation.

Where a Fourier Decomposition of the magnetizations encountered in MRI would need an infinite number of discrete states, as those distributions and their Fourier Transformation are continuous, PDG only needs a finite number of states, as these distributions are embedded in the model. By integrating over space and frequencies, as well as summing over all voxels, and transversal states, the measured signal is obtained. Eq. 2 shows the signal equation resulting from sinc and Cauchy distributions:

$$\begin{aligned} S^+ = \sum_v \sum_{k,\tau} \int_V \int_\Omega & F^+_{k,\tau} \cdot e^{ikr} \cdot e^{i\tau\omega} \\ & \cdot \frac{1}{\pi} \frac{1/T_2'}{(1/T_2')^2 + (\omega - \Delta\omega_0)} \\ & \cdot \operatorname{sinc} \frac{r - r_v}{l_v} \cdot d\omega \, dr \\ = \sum_v \sum_{k,\tau} & F^+_{k,\tau} \cdot \left(e^{i\Delta\omega_0\tau} \cdot e^{-|\tau|/T_2'}\right) \cdot \left(e^{ikr_v} \cdot \Theta(k - k_v)\right) \quad (2) \end{aligned}$$

As each RF pulse splits every state into three, their number grows exponentially. This makes simulation only feasible, if states can be merged. This is possible by summing their factors if they have identical dephasing values, as those states describe the same distribution of isochromats.

The best-case state count of $\mathcal{O}(N)$ states after N pulses is achieved, if the sequence is periodic and symmetric with regard to the gradient moment,[9] so that states end up on an equidistant grid. With the introduction of T_2' dephasing the same is true for timing, meaning that the duration between any pair of pulses has to be constant. Sequences where this does not apply are in the following called "incoherent". Incoherent sequences lead to exponential growth of the number of states, as each RF pulse splits every state into three, resulting in computational overwhelming $\mathcal{O}(3^N)$ states after N RF pulses. We use 4 principle ideas to efficiently reduce the number of states:

- Multiple $F^{\hat{e}}_{k,\tau}$ states with identical $(\vec{k}, \tau)$ can be merged by adding the coefficients. This leads to the best-case state count of $\mathcal{O}(N)$.
- States that only contain a vanishing amount of magnetization can be removed, as the contribution to the measured signal is proportional to the magnetization. This follows the fact that relaxation or diffusion limit the number of necessary states, as demonstrated for EPGs.[10]

- Only include states above an “emitted” signal threshold in the signal equation. States with high $(\vec{k}, \tau)$ values can have a vanishing contribution to the signal.
- Simulate only states above a “latent” signal threshold. By determining the contribution of a state to all future magnetization pathways, some states can be omitted completely.

In order to apply the third and fourth idea, a two-pass simulation approach is used to estimate the “emitted” and “latent” signal of all states. A first pre-pass of the simulation uses a fast, single voxel approximation of the magnetization. The number of states is reduced by the first two techniques and a PDG is emitted, containing states augmented by the two signal metrics. Afterward, the main-pass repeats the simulation on the created PDG but uses the last two techniques in order to reduce the states further, this time calculating the exact signal for the full phantom.

Materials and Methods

The simulation runs in two steps, the pre-pass and the main-pass. The pre-pass uses a single voxel approximation to estimate the signal of all states. It generates the full graph for any given sequence, and augments it with this estimated “emitted signal”. While simulating, the graph is built and states with identical dephasing are merged while states with low magnetization are removed, as a first measure to reduce the overall state count. Afterwards, the graph is traversed a second time for the “latent signal”. The PDG augmented in this way can then be used in the main-pass, which now simulates the sequence again, this time with a fully spatially resolved phantom. While doing so, only states with their metrices above user given thresholds are included in the calculation. This ensures that an explosion of state counts is avoided, while keeping the error low. Figure 2 shows a schematic of the simulation pipeline.

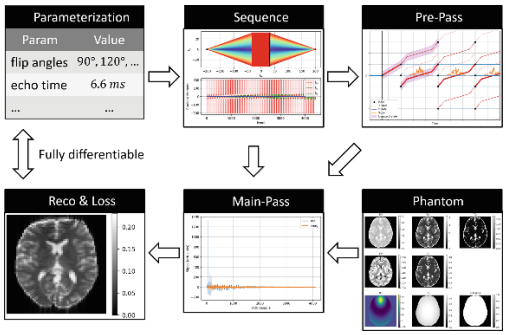

Fig. 2: Simulation and optimization pipeline. The pre-pass computes the optimized graph based on the sequence, which is built based on given sequence parameters. Sequence, graph, and phantom are used by the main-pass to compute a signal, which can be reconstructed into an image. The reconstruction is differentiable with respect to all inputs like the sequence parameters.

The latent signal metric is used to remove unimportant states from the simulation. Simply skipping the simulation of all states that don’t contribute to the signal would lead to artifacts, as their magnetization could be measured in later repetitions. This is especially evident for z states that themselves are never measured, but can be fundamental to a sequence. The overall influence of a state to the measured signal is represented by the latent signal metric, which is the maximum value of all possible ways of a state to contribute to the emitted signal, either directly or by providing magnetization to subsequent states. By using backpropagation, this metric can be calculated in $\mathcal{O}(N)$ time, where N is the total number of states.

Research questions and used sequences

To evaluate the correctness and efficiency of the simulation, a series of comparisons was performed:

I. Comparison of PDG and signal equation
II. Comparison of PDG and isochromat simulation convergence
III. PDG based MR sequence analysis
IV. Simulation of an incoherent sequence

Results

I. Comparison of PDG and signal equation

Figure 3 depicts a close match between simulation and the signal equation for a bSSFP sequence. The difference in contrast varies between different tissues, but stays everywhere below 0.1 %.

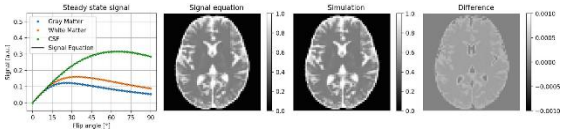

Fig. 3: Comparison of simulation and signal equation[11] of a bSSFP. The flip angle dependency predicted by steady state formulas could be replicated within numerical precision by simulating a sufficiently long sequence.

II. Comparison of PDG and isochromat convergence

Figure 5 shows a 90° FLASH sequence, as a best case for PDG, where the simulation produces no noise while still running much quicker than isochromats. Using a TR of 100ms, the T_2 relaxation of spoilt magnetization helps the isochromat simulation by reducing the undersampled high frequency part of the magnetization. At a TR of 30ms, 100 spins per voxel are not sufficient to simulate the sequence. PDG performs identically for both variants of the sequence while still producing

results close to the measurement. Please, note that this sequence uses 90° pulses, leading to high amount of dephased transverse magnetization, which is especially challenging for random-sampled isochromat solutions as used here. Both sequences were compared to in-vivo measurements to confirm a close match in contrast.

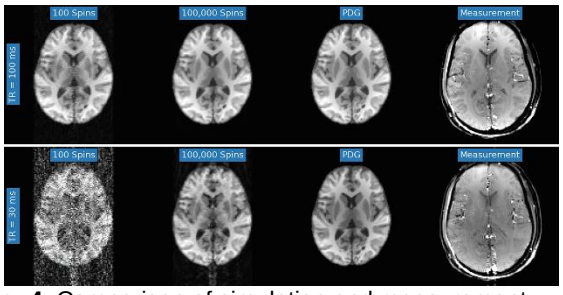

Fig. 4: Comparison of simulation and measurement of the FLASH sequence. With a short TR, isochromats struggle to capture the gradient spoiling, while PDG efficiently produces a contrast close to the measurement. Simulating 100.000 spins per voxel took roughly 11 hours and still contains artifacts, while PDG manages to calculate the signal within 2.6 seconds.

III. PDG based MR sequence analysis

In contrast to ST-EPG, PDG can provide the contributions of different echo paths as images. We use this to reevaluate the answer to the 20 years old question of Scheffler and Hennig[12] "Is TrueFISP [bSSFP] a Spin Echo or a Gradient Echo sequence" by simulating the 70° bSSFP sequence. Figure 5 shows that a centered bSSFP sequence in steady-state (i) is an equal mix of GRE and SE, (ii) has mostly zero phase not due to a pure SE character, but due to cancelation of the opposite phases of the contributions, and (iii) has a frontal banding artifact that occurs when the GRE-to-SE phase difference is 180°.

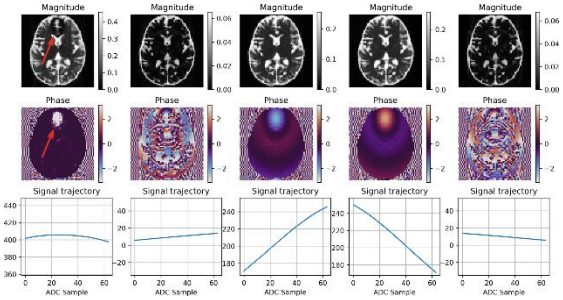

Fig. 5: Individual states of a bSSFP simulation. The left column shows magnitude and phase of the full reconstruction, with a banding artifact produced by B0 inhomogeneities (arrow). The remaining columns show states with τ dephasings of -2, -1, 0 and 1 times TR.

IV. Simulation of an incoherent sequence

As can be seen in Figure 6, PDG is capable of simulating incoherent sequences. The reconstructed images closely match those produced by isochromats, even for $TR \ll T_1$. Because more states contribute to the signal, the amount of simulated states and thus simulation time grows with decreasing TR, but slower than exponentially. This indicates that even for incoherent sequences, only a part of all states is sufficient to describe the resulting images and occurring artifacts.

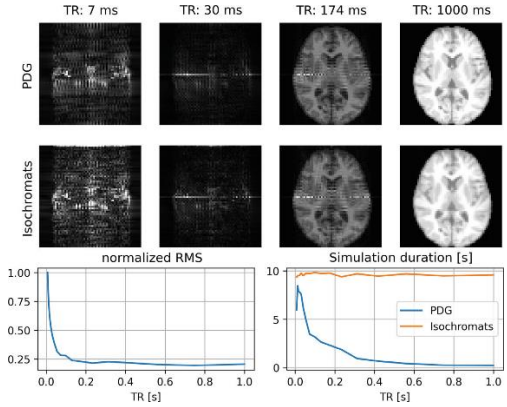

Fig. 6: Comparing PDG (first row) and isochromats (second row) for a SSFP without rewinder gradient. When $TR \gg T_2$, the relaxation will suppress artifacts. This also means less PDG states need to be simulated, as their magnetization vanishes. Still, the simulation duration of PDG does not explode for short TRs while it still stays visually indistinguishable from the isochromat simulation except for the lowest TR.

Discussion

In this work, we present an implementation of the phase graph formalism based on the concept of EPGs[2-5] and ST-EPGs, called PDG. The new simulation describes the echo shape by implicitly introducing three distributions: (i) an arbitrary frequency distribution enabling the description of T_2' relaxation, (ii) an arbitrary spatial intra-voxel distribution, and (iii) an arbitrary spatial distribution of voxels. (i-iii) allows the prediction of the total signal evolution over time, not just echo amplitudes where spins are in phase, but the complete echo shape. Both (ii+iii) are enabling free gradient encoding of 3D magnetization and thus MR sequence simulation and MR image generation. In the literature context PDGs can be seen as an efficient implementation of Kaiser's approach,[8] with extension for spatial encoding. Furthermore, while ST-EPG implementations are usually limited to periodic and symmetric sequences with regard to the gradient moments within TR, PDGs allow to simulate a time resolved signal for any k-space readout, spoiling and flip angle patterns while still preserving the advantages of EPG, like fast computation times, noise free analytical outputs and information about magnetization pathways. For this, PDG modifies the representation of magnetization while controlling the potentially "astronomical"[4] number of states carefully using a pre-pass selection algorithm to remove signal-

irrelevant states before the main simulation. PDGs describe the magnetization at any point during the sequence by splitting it into a variable number of states, each representing a part of the magnetization with arbitrary gradient and time dephasing. Furthermore, PDGs contain the exact dephasing and thus encoding of all parts of the magnetization, while being fully differentiable in all parameters allowing for efficient sequence optimization. It outperforms isochromat simulations especially in cases of sequences which require parts of the magnetization encoded or spoiled to high frequencies to be described correctly.

Related Bloch simulations

As PDG aims to compete with isochromat-based numerical simulations like MRIlab,[13] JEMRIS[1] or KOMA,[14] it was compared to isochromat simulations regarding speed and quality of the generated signal. PDG outperforms state-of-the-art isochromat Bloch simulations with regard to simulation time. It also does not suffer from aliasing artifacts produced by high frequencies, where in isochromat simulations one must typically choose between a sufficiently resolved regular grid sampling or random sampling, which can introduce noise.

Limitations

PDG currently only handles instantaneous on-resonant pulses, so off-resonance, either to simulate fat, slice selection, or dynamic parallel transmission (pTx) pulses are not yet possible to be simulated. Subdivision into multiple instantaneous pulses is possible, but the resulting performance and precision is yet to be analyzed. Nonetheless, PDG can already be extended to handle static pTx pulses. Chemical Excange Saturation Transfer (CEST) and Magnetization Transfer (MT) effects can can in principle be included as shown before for EPG.[15]

Conclusion

In this work, we derived and implemented a fully differentiable Bloch simulation based on the principles of EPG. Contrary to state tensor (ST-) EPG, it is capable of simulating the actual MRI signal of arbitrary sequences, while exhibiting the same advantages like efficient computation and no simulation noise. This makes it possible to simulate and optimize sequences that otherwise would need a vast number of isochromats to be described correctly, making it a suitable replacement for these applications. Furthermore, additional analysis of magnetization and signal is possible that is not available otherwise.

References

1. Stöcker T, Vahedipour K, Pflugfelder D, Shah NJ. High-performance computing MRI simulations. Magn Reson Med. 2010;64:186-193
2. Weigel M. Extended phase graphs: dephasing, RF pulses, and echoes—pure and simple. J Magn Reson Imaging. 2015;41:266-295
3. Hennig J. Echoes - how to generate, recognize, use or avoid them. Part II. Concepts in Magnetic Resonance. Wiley Online Library. 1991
4. Hennig J. Echoes - how to generate, recognize, use or avoid. Part I. Concepts Magn Res. 1991;3:125-143
5. Weigel M, Schwenk S, Kiselev VG, Scheffler K, Hennig J. Extended phase graphs with anisotropic diffusion. J Magn Reson. 2010;205:276-285
6. Weigel M. Extended phase graphs: dephasing, RF pulses, and echoes—pure and simple. J Magn Reson Imaging. 2015;41:266-295
7. Malik SJ, Padormo F, Price AN, Hajnal JV. Spatially resolved extended phase graphs: modeling and design of multipulse sequences with parallel transmission. Magn Reson Med. 2012;68:1481-1494
8. Kaiser R, Bartholdi E, Ernst RR. Diffusion and field-gradient effects in NMR Fourier spectroscopy. J Chem Phys. 2003;60:2966-2979
9. Hennig J. Multiecho imaging sequences with low refocusing flip angles. J Magn Reson. 1969;78:397-407
10. Malik SJ, Sbrizzi A, Hoogduin H, Hajnal JV. Equivalence of EPG and Isochromat-Based Simulation of MR Signals In Proceedings of the 24th Annual Meeting of ISMRM, Singapore, 2002 p. 5111
11. Hänicke W, Vogel HU. An analytical solution for the SSFP signal in MRI. Magn Reson Med. 2003;49:771-775
12. Scheffler K, Hennig J. Is TrueFISP a gradient-echo or a spin-echo sequence? Magn Reson Med. 2003;49:395-397
13. Liu F, Velikina JV, Block WF, Kijowski R, Samsonov AA. Fast realistic MRI simulations based on generalized multi-Pool exchange tissue model. IEEE Trans Med Imaging. 2017;36:527-537
14. Castillo-Passi C, Irarrazaval P. doi:10.5281/zenodo.6627503
15. Malik SJ, Teixeira RPAG, Hajnal JV. EPG formalism for systems with magnetization transfer and exchange. Magn Reson Med. 2018;80:767-779

In vivo determination of pH and magnesium ion concentration by means of ^{31}P MRSI: A multi-parametric look-up approach

Vanessa L. Franke[1]

[1]Division of Medical Physics in Radiology, German Cancer Research Center (DKFZ), Heidelberg

Synopsis: In this work, a novel approach for the in vivo imaging of pH and magnesium ion concentration [Mg^{2+}] by means of ^{31}P MRSI was developed, which is applicable for various chemical conditions. To this end, I developed a multi-parametric look-up algorithm, which uses multiple ^{31}P spectral properties for the assessment of the underlying biochemical conditions. Application of the developed approach to in vivo ^{31}P MRSI data acquired at 7T resulted in volumetric maps of plausible pH and [Mg^{2+}] values in healthy and tumorous tissues.

Introduction

With the development towards personalized approaches in precision medicine, the importance of imaging biomarkers is constantly increasing. Particularly in cancer research, the search for valuable imaging biomarkers plays an important role, not only for diagnostics and for classification of tumors, but also for the non-invasive investigation of treatment response of newly developed targeted therapies in vivo. Among the vast number of potentially valuable imaging biomarkers, the pH value and the magnesium ion concentration [Mg^{2+}] are of high interest for cancer research. Both pH and [Mg^{2+}] play key roles in numerous metabolic and enzymatic processes and can be altered under pathophysiological conditions. The pH gradient is known to be reversed in cancer[1], and also the role of magnesium in the tumor progression is currently investigated, e.g. in breast cancer[2]. Therefore, the in vivo assessment of pH and [Mg^{2+}] is of great value as they can potentially be used as imaging biomarkers.

A method to non-invasively determine pH and [Mg^{2+}] in vivo is phosphorus (^{31}P) magnetic resonance spectroscopy (MRS). The use of MRS imaging (MRSI) methods even allows for two- or three-dimensional imaging of pH and [Mg^{2+}] in the entire investigated volume which is of great value for the comparison of healthy and diseased tissue from a single scan. The determination of pH and [Mg^{2+}] via ^{31}P MRS(I) is possible due to the strong sensitivity of the resonance frequencies (i.e. chemical shifts) of specific ^{31}P metabolites to changes of the chemical environment, and therewith also to changes in pH and [Mg^{2+}]. Conventionally, the quantified chemical shifts of inorganic phosphate (P_i) and adenosine triphosphate (ATP) are translated to pH and [Mg^{2+}] via suitable calibration equations, like the modified Henderson-Hasselbalch equation in case of pH[3]. However, the required constants in these calibration equations, e.g. the pK_a value or the dissociation constants, are known only for normal physiological conditions. This poses a particular challenge for the application of these calibration equations to pathologic conditions, like tumors, where the biochemical environment can be altered substantially. Although the pitfalls and weaknesses of these calibration equations for the application to different tissue types was extensively discussed in the past[4-6], so far, the existing ^{31}P MRS(I) methods for pH and [Mg^{2+}] determination do not properly account for varying chemical conditions.

In my dissertation, I developed a multi-parametric look-up algorithm by means of ^{31}P MRS(I) aiming at the condition-independent determination of pH and [Mg^{2+}] in vivo. To this end, I created a look-up table based on the measured ATP chemical shifts of 114 model solutions with varying chemical compositions. I increased the number of look-up entries by inter- and extrapolation of the chemical shifts in dependence on pH, [Mg^{2+}] and the ionic strength by using a herein developed model function. The implemented look-up algorithm was applied to in vivo ^{31}P MRSI datasets from healthy volunteers and patients with glioblastoma which were acquired at B_0 = 7T.

Materials and Methods

Basic concept

The basic idea of the developed approach is to make use of not only one, but multiple spectral properties of a ^{31}P spectrum to determine the underlying biochemical parameters in the form of a look-up algorithm. As first proof-of-concept, I implemented a look-up algorithm that determines pH and [Mg^{2+}] for different ionic

conditions by using the chemical shifts of the three resonances of ATP, namely (δ_γ, δ_α, δ_β) (in order as they appear in the spectrum; cf. Fig. 1). To this end, I created a look-up table composed of the quantified ATP chemical shifts measured from suitable model solutions prepared with different pH, Mg^{2+} and ionic compositions. Based on the created look-up table, the implemented search algorithm assigns possible solution triples (pH, Mg, Ion) to the measured input chemical shift triple (δ_γ, δ_α, δ_β). Hereby, the parameter Ion is a measure for ionic changes in general.

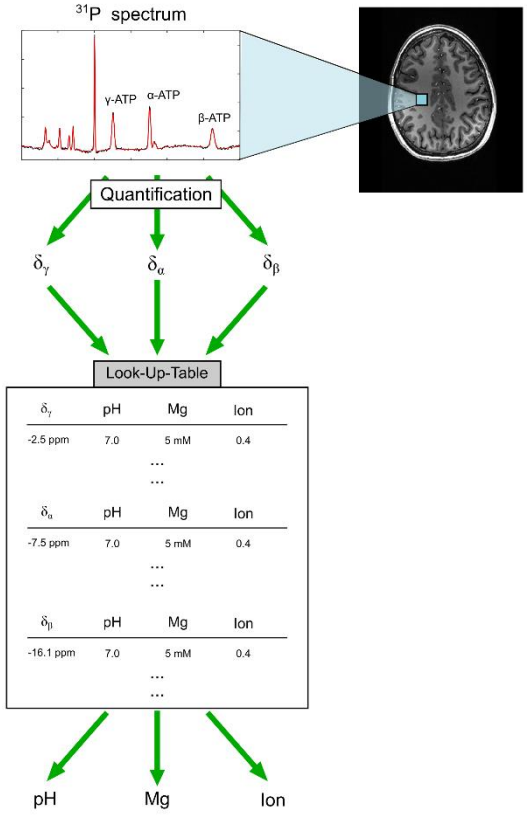

Figure 1: Schematic representation of the basic concept of the developed look-up approach: multiple parameters of a quantified ^{31}P spectrum are used for the determination of the underlying biochemical parameters. As proof-of-concept, a look-up algorithm was implemented using the chemical shifts of the three ATP resonances (δ_γ, δ_α, δ_β) to determine pH, the magnesium ion concentration and the parameter Ion as a measure for the ionic strength in general.

Acquisition of look-up table elements

In total, 114 model solutions with different chemical compositions were prepared and measured on the same day or one day after the preparation, at a 9.4-T Bruker small animal scanner using a double-resonant ^{31}P–^{1}H volume resonator with an inner diameter of 35 mm. ^{31}P spectra were acquired in a temperature-controlled manner (T = (37.1 ± 0.3) °C) with a ^{31}P FID-sequence. The concentration of ^{31}P metabolites was 5 mM. Due to the use of sodium-based salts, all solutions had a sodium concentration of 29 mM. The variation of the parameter Ion was realized by adding different amounts of potassium chloride (KCl) (an Ion value of 1 corresponds to [KCl] = 200 mM). The magnesium ion content was increased by adding $MgCl_2$. The prepared and measured 114 different model solution covered the following value ranges: pH = [6.8 – 7.4], [$MgCl_2$] = [0 – 10] mM, [KCl] = [0 - 200] mM.

Implementation of the look-up algorithm

The limited number of acquired entries for the look-up table, i.e. the quantified chemical shifts from the 114 model solutions, was extended by inter- and extrapolating the measured chemical shifts (δ_γ, δ_α, δ_β) in dependence on (pH, Mg Ion) using a model function I developed based on the Hill equation[7] (the full description of the model development δ_{model}(pH,Mg,Ion) can be found in chapter 5.3 of [8]). The extrapolation of [Mg^{2+}] values to up to 25 mM is assumed to be justified, because the δ(Mg) dependence starts to plateau at around [Mg^{2+}] = 10 mM[8]. For inter- and extrapolation of the multi-dimensional value space, the following sampling grids were chosen: pH = [6.7:0.01:7.5]; [Mg^{2+}] = [0:0.1:25] mM, Ion = [0:0.025:1], yielding 833,571 entries in the interpolated look-up table.

In principle, the assignment of a measured chemical shift δ_i^{meas}, i ϵ (γ, α, β) to possible combinations of the underlying parameters (pH, Mg, Ion) is given by the model functions δ_i^{model}(pH, Mg, Ion). However, the non-linearity of the model functions makes their inversion challenging. Therefore, I implemented a search algorithm, which finds possible solution triples (pH, Mg, Ion) for a given measured chemical shift δ_i^{meas} in a numerical manner (cf. Fig. 2). The assignment of a measured chemical shift to possible solution triples (pH_k, Mg_k, Ion_k) is done separately for γ-, α- and β-ATP based on the corresponding model function, yielding the solution sets $(pH_k, Mg_k, Ion_k)_\gamma$, $(pH_k, Mg_k, Ion_k)_\alpha$ and $(pH_k, Mg_k, Ion_k)_\beta$. Because the measured chemical shifts δ_γ, δ_α and δ_β result from the same ^{31}P spectrum, and therefore correspond to the same chemical environment (thus the same values for (pH, Mg, Ion)), only the solution triple for which the condition

$$(pH_k, Mg_k, Ion_k)_\gamma = (pH_k, Mg_k, Ion_k)_\alpha = (pH_k, Mg_k, Ion_k)_\beta \quad (1)$$

holds is assumed to be the correct solution triple. However, under realistic conditions, the constraint in Eq. 1 cannot be found exactly due uncertainties on the quantified chemical shift, as well as uncertainties of the developed model functions. Therefore, the assignment as described above was extended by incorporating

a realistic error margin on the obtained chemical shifts. Hence, the assignment of possible solution triples (pH_k, Mg_k, Ion_k) is done not only for δ^{meas}, but for each point in the range $\delta = (\delta^{meas} \pm \Delta\delta^{meas})$. The error margin $\Delta\delta^{meas}$ is determined by a pre-defined chemical shift range, which is weighted according to a Gaussian distribution with a width of σ (cf. Fig. 2A). In this study, σ is defined based on the approximated frequency precision of the quantification model.

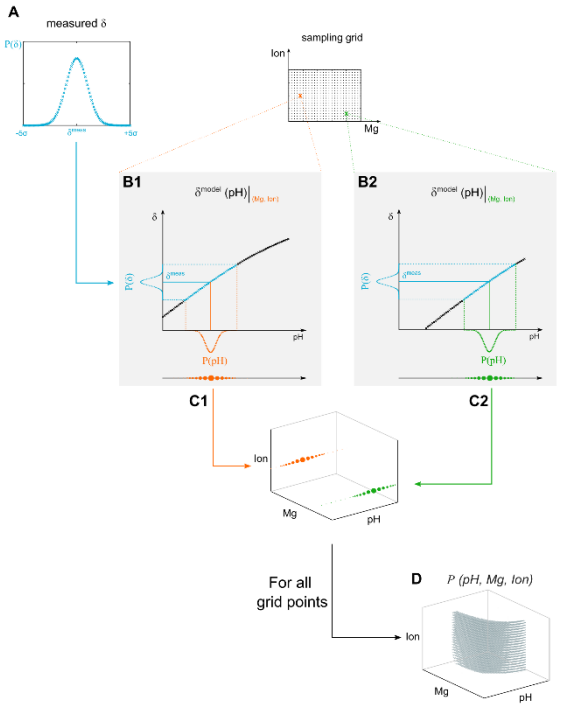

Figure 2: Schematic workflow for the calculation of the multi-dimensional probability distributions *P*(pH,Mg,Ion). (A) The error margin of the measured chemical shift δ_{meas} is determined by a pre-defined range $\Delta\delta_{meas}$ weighted by a Gaussian distribution with a specific width σ, approximated from the frequency precision of the used quantification model. (B1,B2) For each point in the sampling grid defined by the subspace (Mg–Ion), the probability distribution $P(\delta_{meas}\pm5\sigma)$ is projected onto the pH axis, which is defined by the model function $\delta_{model}(pH)|_{(Mgk,Ionk)}$. (C1,C2) The probability distribution *P*(pH) is interpolated and assigned to the corresponding point in the sampling grid. In the illustration, the dot size corresponds to the value for *P*(pH). (D) The assignment is done for all grid points (Mg_k,Ion_k), yielding a multi-dimensional probability distribution *P*(pH, Mg, Ion), which assigns each point in the grid a specific probability.

The probability distributions *P* (cf. Fig. 2D) are determined separately for δ_γ, δ_α and δ_β, yielding $P(pH,Mg,Ion)_\gamma$, $P(pH,Mg,Ion)_\alpha$, and $P(pH, Mg, Ion)_\beta$. Condition (1) yielding the "correct" solution triple is realized by calculating the joint probability distribution P_{joint} by multiplying $P(pH, Mg, Ion)_i$, i ϵ (γ, α, β). The final output values of the look-up algorithm (pH_{out}, Mg_{out}, Ion_{out}) are determined as the weighted mean values of all possible solutions.

Application to in vivo ^{31}P MRSI data

The implemented look-up algorithm was applied to various in vivo ^{31}P MRSI datasets acquired at B_0 = 7T, i.e. three datasets from the human lower leg muscle of healthy volunteers, and three datasets acquired in the human brain of patients with glioblastoma. The acquisition parameters and processing steps of these datasets can be found in [9,10]. The quantified chemical shifts (δ_γ, δ_α, δ_β) from the in vivo datasets were fed voxelwise into the algorithm, yielding 3D maps for pH, Mg, and Ion. For the error margin, a Gaussian distribution with a width of σ = 0.02 ppm was assumed. The magnesium ion content is displayed as the ratio $R = [Mg_{total}] / [ATP_{total}]$ as this ratio is driving the chemical shift differences of the ATP resonances. The resulting maps were compared with maps for pH and the free magnesium ion concentration $[Mg^{2+}]_{free}$ as calculated conventionally following [3,11].

Results

The ^{31}P spectra acquired from the model solutions were of high quality enabling a robust quantification of all metabolites contained in the solutions (cf. Fig. 3), thus enabling the extraction of 114 triples of measured ATP chemical shifts. The extension of the look-up table elements beyond the measured entries via inter- and extrapolation using the developed model functions δ_i^{model} (pH,Mg,Ion), i ϵ (γ, α, β) was possible (Adjusted $R^2 > 0.99$).

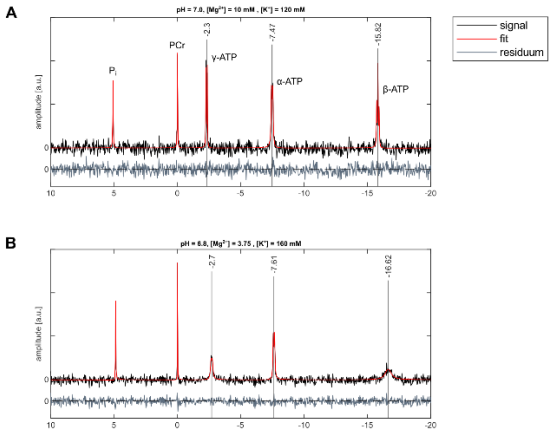

Figure 3: Representative ^{31}P spectra acquired in model solutions with a ^{31}P FID sequence at B_0 = 9.4T.

After passing a basic plausibility test by applying the implemented look-up algorithm to the measured ATP chemical shifts of the 114 model solutions for verification, the algorithm was applied to in vivo ^{31}P MRSI datasets from healthy volunteers and from patients with glioblastoma. The application of the look-up

algorithm to these in vivo datasets yielded a determination of solution triples (pH_{Out}, Mg_{Out}, Ion_{Out}) in only a small number of voxels. The failed assignment of solution triples was found to be resulting from mismatches of the chemical shifts of α-ATP, which will be discussed later. Therefore, the look-up algorithm was reduced to only the chemical shifts of γ- and β-ATP, and then applied to the in vivo data. With this reduced version of the algorithm, in 99% (muscle data) and 94% (brain data) of all tissue voxels plausible output values for (pH, Mg, Ion) could be determined (cf. Figs. 4 and 5).

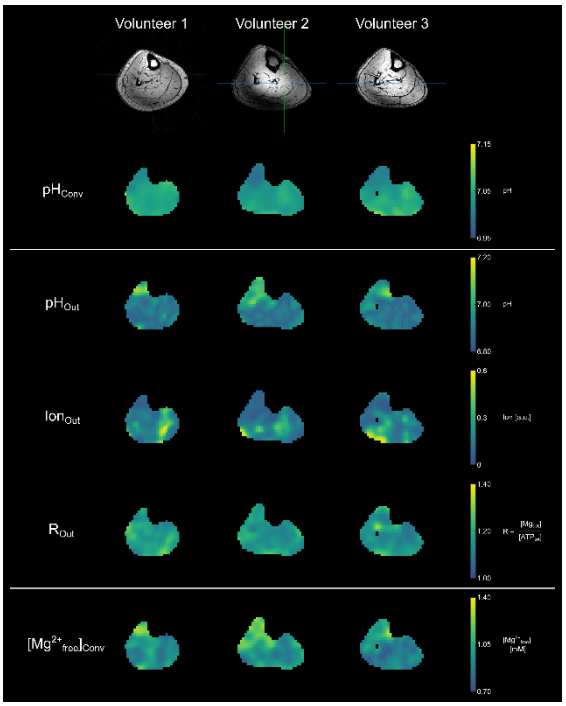

Figure 4: 3D maps (transversal view) for pH_{Out}, Ion_{Out}, and R_{Out} resulting from the application of the implemented look-up algorithm to ^{31}P MRSI datasets acquired in the lower leg muscles of healthy volunteers. The magnesium ion content is given as R = $[Mg_{total}]/[ATP_{total}]$ assuming $[ATP_{total}]$ = 5 mM for human muscle tissue[12]. In rows 1 and 5, the conventionally calculated maps for pH and the free magnesium ion concentration, i.e. pH_{Conv} and $[Mg^{2+}_{free}]_{Conv}$, are shown. Note the different value ranges.

The application of the reduced version of the implemented look-up algorithm to the lower leg muscle data sets resulted in plausible values for pH between 6.8 and 7.3, and for the magnesium ion content R of 1-1.5 (corresponding to a total magnesium ion concentration of (5.0-7.5) mM). Local differences of the determined values (pH_{Out}, Ion_{Out}, R_{out}) are apparent in the maps, which show the same trends for all three volunteers, e.g. slightly higher pH values in the *tibialis anterior* muscle, higher Ion values in the *soleus* muscle (Fig. 4, rows 2-4). The observed patterns in the output maps partly differ from the patterns in the conventionally calculated maps for pH and the free magnesium ion concentration (cf. Fig. 4, rows 1 and 5), e.g. in the pH_{Conv} maps, lower pH values are observed in the *tibialis anterior* muscle. Interestingly, the look-up-based pH_{Out} map seems to have a similar pattern as the $[Mg^{2+}_{free}]_{Conv}$ map, whereas the pH_{Conv} map seems to be resembled in the Ion_{Out} map.

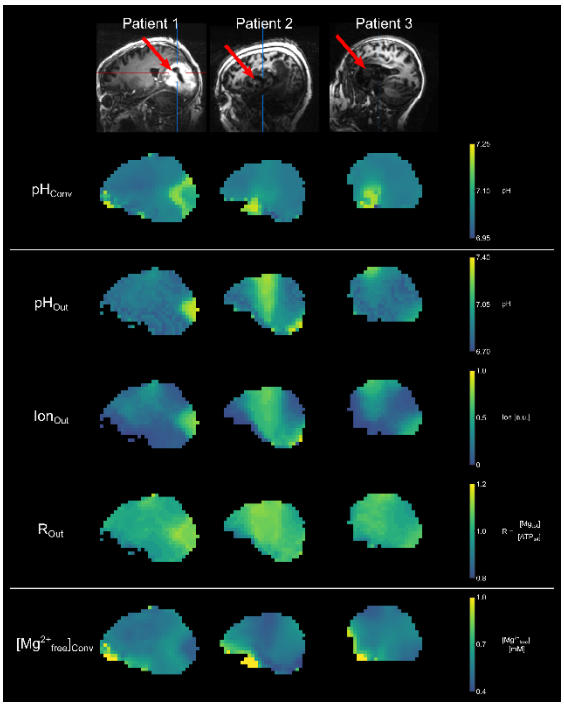

Figure 5: 3D maps (sagittal view) for pH_{Out}, Ion_{Out}, and R_{Out} resulting from the application of the implemented look-up algorithm to ^{31}P MRSI datasets acquired in the brains of patients with glioblastoma. The locations of the tumors are indicated with red arrows in the first row. Mg is given as R = $[Mg_{total}]/[ATP_{total}]$ assuming $[ATP_{total}]$ = 3 mM for the human brain[13]. In rows 1 and 5, the conventionally calculated maps for pH and the free magnesium ion concentration, i.e. pH_{Conv} and $[Mg^{2+}_{free}]_{Conv}$, are also shown. Note the different value ranges.

The application of the reduced look-up algorithm to the datasets of patients with glioblastoma resulted in a larger range of pH values than for the muscle datasets, i.e. (6.7 - 7.4). The value ranges for R_{Out} and Ion_{Out} are slightly different from the ranges in the muscle data, i.e. higher Ion and lower R values. For patient 1, pH values of up to 7.4 were found in the tumor compared to ~6.9 in healthy tissue (cf. Fig. 5, row 2). The pH_{Out} map shows a stronger contrast than the pH_{Conv} map, where values of only up to 7.25 in the tumor were determined (cf. Fig. 5, row 1). The Ion_{Out} and R_{Out} maps of patient 1 show increased values in the depicted slice of the map (Fig. 5, rows 3 and 4). Also here, the patterns of the look-up-based output maps differ from the patterns of the conventionally calculated maps pH_{Conv} and $[Mg^{2+}_{free}]_{Conv}$. Compared to the datasets of the lower leg muscle, a larger inter-subject variation is observed.

Discussion

In my thesis, I developed an alternative to the conventional calibration equations for the determination of pH and [Mg^{2+}] by means of ^{31}P MRS(I) aiming for a method accounting for varying ionic conditions. The focus of my work lied on two main aspects: (i) the introduction of the concept of mapping multiple dependencies of ^{31}P spectral properties to biochemical parameters, and (ii) the implementation of a suitable look-up algorithm directly incorporating measurement uncertainties making the determination of output values more robust.

A decisive strength of the developed method is its expandability by inclusion of other quantifiable parameters in a ^{31}P spectrum, like additional chemical shifts or the linewidths and J-coupling constants, which also show clear dependencies on the chemical environment (cf. chapter 5.1 in [8]). Moreover, the developed method reduces the complexity of the pH and [Mg^{2+}] assignment by focusing solely on conditions being relevant in vivo. Moreover, a reduction in measurement time, particularly important for the application in vivo, is possible due to the use of only the signals from ATP compared to the use of P_i having a lower signal to noise ratio in vivo.

However, the application of the developed look-up algorithm using all three ATP chemical shifts to the in vivo data was possible only in small number of the voxels. Analyses revealed that the failing assignment of joint solution triples is due to the solution triples determined by the chemical shift of α-ATP. Either the input value, i.e. the measured chemical shift in vivo δ_α^{meas}, was not represented in the entries of the look-up table, or the possible solution triples based on δ_α i.e. $(pH, Mg, Ion)_\alpha$, differed from the possible solution triples based on δ_γ and δ_β, i.e. $(pH, Mg, Ion)_\gamma$ and $(pH, Mg, Ion)_\beta$. Because the α-ATP shift could not be employed for the in vivo data, the results demonstrated in Figures 4 and 5 are subject to ambiguities, i.e. three parameters (pH, Mg, Ion) are determined by the use of only two input parameters (δ_γ, δ_β).

Nevertheless, based on the work herein presented and published in [14], further advances of the original look-up algorithm have been performed in the meanwhile, which overcome the under-determination. An updated version of the look-up algorithm incorporates the dependency of the chemical shift $\delta_{Pi-\alpha}$ and uses the relative ATP chemical shifts $\delta_{\gamma\alpha}$ and $\delta_{\alpha\beta}$. The application of this advanced version to in vivo data of healthy volunteers resulted in a clear improvement regarding robustness and reliability of the determined values[15]. This improvement demonstrates the strength of developed approach as it allows the straight-forward inclusion of additional parameters. Furthermore, the application of this advanced version to a pilot cohort of patients with glioma identified a possible benefit in stratifying glioma subtypes non-invasively[16].

Conclusion

In my dissertation, I have developed a multi-parametric look-up algorithm aiming at the condition-independent estimation of the pH value and the magnesium ion content by means of ^{31}P MRS(I). As proof of concept, I applied a look-up algorithm employing only the chemical shifts of γ- and β-ATP to in vivo ^{31}P MRSI data acquired at B_0 = 7T resulting in volumetric maps visualizing pH and magnesium ion content. In order to overcome the challenges of the originally implemented algorithm, improvements were already achieved by including additional spectral properties allowing for a more reliable determination of pH and [Mg^{2+}] in vivo[15].

References

1. White KA et al. *J Cell Sci.* 2017; 130(4):663-669.
2. Mendes, PMV, et al. *Biol Trace Elem Res.* 2018;184:334–339.
3. De Graaf RA. In Vivo NMR Spectroscopy. *John Wiley & Sons*; 2007.
4. Petroff OA, et al. *Neurology.* 1985;35(6):781-788.
5. Pettegrew JW, et al. *Magn Reson Imaging.* 1988;6(2):135-142.
6. Roberts JKM, et al. *Biochemistry.* 1981;20(19):5389-5394.
7. Markley JL, et al. *Acc Chem Res.* 1975;8(2):70-80.
8. Franke VL. Dissertation Heidelberg University 2023. https://archiv.ub.uni-heidelberg.de/volltextserver/32909
9. Korzowski A et al. *Front Neurol*. 2021;12:735071
10. Franke VL et al. *Magn Reson Med.* 2022;88(2):511-523.
11. Barker PB et al. *Magn Reson Med.* 1999;41(2):400-406.
12. Schmidt RF. *Springer-Lehrbuch.* Physiologie des Menschen: Mit Pathophysiologie. 2010.
13. Ren J, et al. *NMR Biomed.* 2015;28(11):1455-1462.
14. Franke VL et al. *NMR in Biomed.* 2024; e5113.
15. Seng B et al. *Proc ISMRM 2024*. #3038.
16. Franke VL et al. *Proc ISMRM 2024*. #5082.

Simultaneous magnetic resonance imaging of pH, perfusion and renal filtration using hyperpolarized ^{13}C-labelled Z-OMPD

Martin Grashei[1,8], Pascal Wodtke[1,8], Jason G. Skinner[1], Sandra Sühnel[1], Nadine Setzer[1], Thomas Metzler[2], Sebastian Gulde[3], Mihyun Park[4], Daniela Witt[4], Hermine Mohr[3], Christian Hundshammer[1], Nicole Strittmatter[4], Natalia S. Pellegata[3,5], Katja Steiger[2], Franz Schilling[1,6,7]

1 Department of Nuclear Medicine, TUM School of Medicine and Health, Klinikum rechts der Isar, Technical University of Munich, Munich, Germany.
2 Comparative Experimental Pathology (CEP), Institute of Pathology, School of Medicine, Technical University of Munich, Munich, Germany.
3 Institute for Diabetes and Cancer, Helmholtz Zentrum München, Neuherberg, Germany.
4 Department of Biosciences, TUM School of Natural Sciences, Technical University of Munich, Garching, Germany.
5 Department of Biology and Biotechnology, University of Pavia, Pavia, Italy.
6 Munich Institute of Biomedical Engineering, Technical University of Munich, Garching, Germany
7 German Cancer Consortium (DKTK), Partner Site Munich and German Cancer Research Center (DKFZ), Heidelberg, Germany.

Synopsis: We introduce [1,5-$^{13}C_2$]Z-OMPD as a new hyperpolarized MRI sensor for extracellular pH and perfusion sensor which allows to generate a multiparametric fingerprint of renal disease status and to detect local tumor acidification. Exceptional long T_1, high pH sensitivity and suitability of using the C_1-label as internal frequency reference enables multi-compartment pH imaging in healthy rat kidneys. Spectrally selective ^{13}C-label targeting enables simultaneous 3D imaging of perfusion and filtration and 2D imaging of pH within one minute to quantify renal blood flow, glomerular filtration rates and renal pH in hydronephrotic kidneys with superior sensitivity compared to clinical routine methods.

Introduction

Onco-nephrology is an emerging medical field in the interdisciplinary care of patients to identify and prevent kidney damage or failure related to cancer treatments as well as to assess risk for cancer due to kidney disease. While treatment outcome can be significantly affected by prevailing pH conditions in the tumor, pH-regulating adjuvant therapies might be crucial to enhance patient outcome, as long and ineffective therapies often pose a severe kidney burden. Therefore, for many therapies it might be essential to assess the tumor pH, as well as the renal function before, during and following cancer treatment. In clinical routine, kidney function is probed by CT or scintigraphy which involve ionizing radiation and or even bear the risk of nephropathies. Simultaneously, there is a strong clinical need for safe and fast imaging of extracellular pH to assess tumor acidification for patient stratification, efficacy of adjuvant therapies or early response to therapy. pH imaging by hyperpolarized magnetic resonance using [^{13}C]bicarbonate (1) and [1,5-$^{13}C_2$]zymonic acid (2) has been introduced but not clinically translated yet. In this work, we introduce hyperpolarized, ^{13}C-labelled [1,5-$^{13}C_2$]Z-4-methyl-2-oxopent-3-enedioic acid (Z-OMPD), which has been shown to naturally occur in tulips (3) and is assumed to occur in interstellar meteorites (4), as a probe for simultaneous 3D imaging of renal perfusion and filtration and 2D imaging of pH *in vivo* within a single injection. This technique shows superior sensitivity for pathological kidney alterations compared to safe clinical routine methods.

Materials and Methods

Synthesis of [1,5-$^{13}C_2$]Z-OMPD

A synthesis protocol for ^{13}C-labelled [1,5-$^{13}C_2$]Z-OMPD using [1-^{13}C]ethyl pyruvate as precursor was developed based on a previous reports (5).

Characterization of [1,5-$^{13}C_2$]Z-OMPD

pH sensitivity of [1,5-$^{13}C_2$]Z-OMPD was determined by titration of aqueous solutions containing 25mM Z-OMPD and 25mM [^{13}C]urea as a reference at 37 °C and acquisition of ^{13}C NMR spectra on a Bruker 7T preclinical MRI scanner.

Hyperpolarization and agent preparation

DMSO with 7.1M [1,5-$^{13}C_2$]Z-OMPD and 25mM OX063 trityl and glycerol containing 10M [^{13}C]urea and 30mM OX063 was co-polarized using a HyperSense dDNP polarizer. Dissolution used TRIS-buffered D_2O to yield an injection concentration of 84 mM.

pH imaging protocols

Experiments were performed on a Bruker 7T preclinical MRI scanner. For pH imaging of

kidneys in 7-11 weeks old Wistar healthy rats, CSI parameters were FA = 10°, resolution 3 × 3 x 5mm³, BW = 3.2kHz, spectral points = 256. For pH imaging in subcutaneous EL4 following 7-10 days after implantation in healthy 6 weeks old C57Bl/6 mice, CSI used FA = 15°, resolution 1.4 × 1.4 × 3mm³, BW= 3.2kHz, 256 spectral points.

Imaging protocol for simultaneous imaging of perfusion and pH

To image perfusion, the C_1-label of Z-OMPD, exhibiting only a weak pH sensitive change in chemical shift, was excited using a slightly off-resonant narrow bandwidth excitation, to avoid excitation of the C_5-resonance and co-injected [^{13}C]urea. Excitation and signal readout were performed using a 3D bSSFP sequence starting with start of injection. Combined perfusion and pH imaging in hydronephrotic kidneys of 8-9 months *MENX* rats (6) used bSSFP parameters FA = 12°, excitation bandwidth = 240Hz, resolution 4mm³ isotropic, number of frames = 10, total scan time 32.2s and CSI parameters FA = 10°, resolution 4mm³ isotropic, BW = 3.2kHz, 256 spectral points, total scan time 18.6s.

pH retrieval and pH map reconstruction

For pH measurements relative to [^{13}C]urea as external reference, the difference between each compartmental C_5-resonance position and the urea peak position was taken. For pH map reconstruction using the Z-OMPD C_1-resonance as internal reference, the difference of each compartmental C_5-resonance relative to the C_1-resonance was taken. The chemical shifts of the ^{13}C-labelled positions can be modelled as a function of pH by a scaled logistic function:

$$OMPD_{1/5}(pH) = OMPD_{1/5,min} + \frac{\delta_i}{1+10^{(pKa-10)}}$$

Calculation of glomerular filtration rates and renal blood flow

A two-compartment model with unidirectional flow according to Baumann and Rudin (7) was used for modelling filtration according to:

$$\frac{dC_{Medulla+Pelvis}(t)}{dt} = k_{cl}C_{Cortex}(t)$$

where $C_{\text{Medulla+Pelvis}}(t)$ and $C_{\text{Cortex}}(t)$ are the signal time curves for the cortex and the combined medulla and pelvis region and k_{cl} is the clearance rate. To quantify perfusion, a central blood- and the renal cortex time curves were used to calculate the renal blood flow according to:

$$\frac{\sum AUC_{Cortex}}{\Delta t \cdot \sum AIF}$$

With AUC_{Cortex} being the summed cortex signal, *AIF* being the blood vessel time curve and Δt the delay between two image frames.

Results

Characterization of Z-OMPD as pH sensor

Recently emerging synthesis routes and structures of pyruvic acid-derived molecules were analyzed for molecules with favourable hyperpolarization properties and T_1 relaxation times (5). We identified Z-OMPD (Fig. 1a) as the pyruvic acid dimer with the most favourable pH-sensing properties having the lowest energy level of OMPD isomers and high biocompatibility. A titration series (Fig. 1b) of thermal ^{13}C-NMR spectra in the *in vivo* relevant pH range (~pH 7) reveals either strong or weak changes of the chemical shift of the C_5- and C_1-labels respectively with pH in opposite field directions relative to [^{13}C]urea. T_1 relaxation time constants measurements for both ^{13}C-labels in D_2O and blood and *in vivo* and at 1T and 7T yield T_1 values of up to two minutes for both ^{13}C-labels *in vitro* at 1T and half a minute *in vivo* at 7T (Fig. 1c).

In vivo pH imaging in healthy kidneys

Validation of *in vivo* pH imaging was done in healthy rat kidneys, which possess physiological tissue acidification due to the renal filtration process. The resulting and overlaid compartment maps (Fig. 1d) reveal a global physiologic compartment, while acidification due to the first and the second acidic compartment are only present in the kidneys and the kidney center respectively. Based on spatial distribution and pH, compartments can be assigned to the anatomical renal regions of the cortex, the medulla, and the pelvis. The pH maps calculated with an internal reference (Fig. 1e) are virtually identical to [^{13}C]urea-referenced maps, where all major image features are preserved. Quantitative comparison of pH compartments determined either by external or internal reference (Fig. 1f) demonstrates no relevant deviations between referencing.

Imaging of tumor acidification in subcutaneous EL4 lymphoma in mice

pH imaging in EL4 lymphoma reveals acidification of the tumor mean pH (Fig. 2a). This mean pH is composed of one physiologic compartment, which is globally present in healthy tissue and most of the tumor (Fig. 2b) and a second, acidic compartment which is only detectable in tumor subregions (Fig. 2c). Presence of one or two compartments can be distinguished by either one (Fig. 2d) or two C_5-peaks (Fig. 2e) of varying relative intensity in CSI spectra. pH imaging in multiple mice indicates a physiologic pH for healthy spine muscle and most of the time in central blood vessels (Fig. 2f). A few subjects show blood acidification, potentially due to anaesthesia-induced respiratory acidosis. The first pH compartment corresponds to tumor vessels and

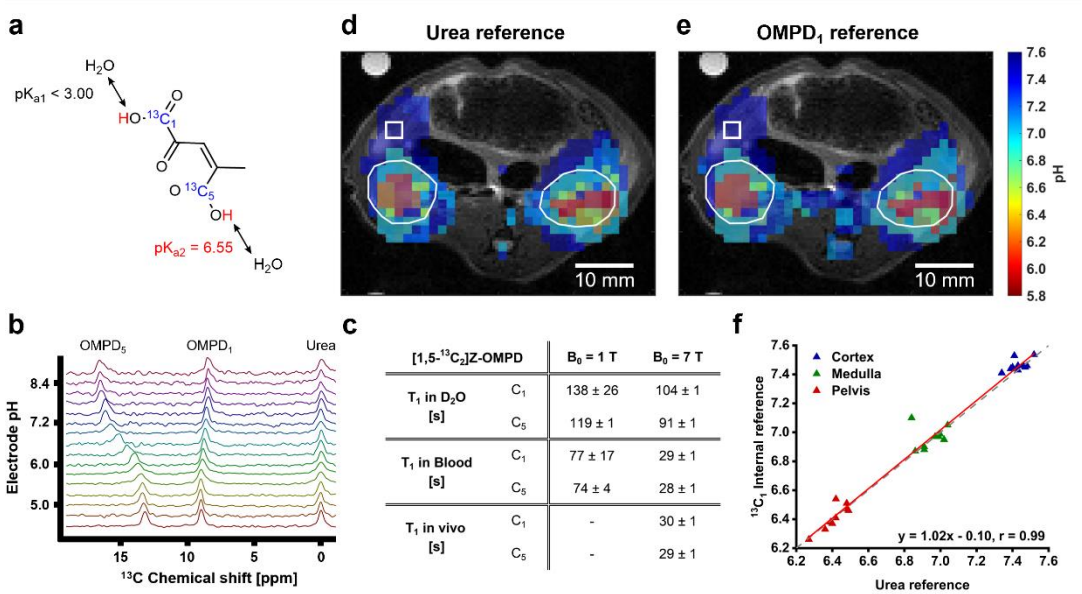

Fig. 1: Characterization and *in vivo* pH imaging in healthy rat kidneys using [1,5-$^{13}C_2$]Z-OMPD. a The pH sensitivity of the ^{13}C resonances in the physiological pH range originates from the C_5-group. **b** ^{13}C spectra from a titration series of Z-OMPD show strong and weak pH sensitivity for the C_5- and C_1-resonance, respectively. White squares: Native CSI resolution. **d, e** *In vivo* pH maps up to three pH compartments of healthy rat kidneys (white ROIs) overlaid on each other and a T_2-weighted anatomical image using either urea or the C_1-resonance of Z-OMPD as chemical shift reference can be generated. **f** A quantitative comparison of the two chemical shift reference shows good agreement between the two methods.

shows no acidification while there is also a second, acidic compartment, representing extracellular space. The latter causes overall tumor acidification and is the dominant compartment in the most acidified regions.

Simultaneous imaging of pH and perfusion in healthy and diseased rat kidneys

Beyond sole pH imaging, Z-OMPD can be used for combined imaging of pH and perfusion. For pH imaging with Z-OMPD, pH is mainly retrieved from the C_5-resonance. Hence, most of the C_1-magnetization can be used to image the distribution of Z-OMPD in kidneys within the first 30 seconds after start of injection without

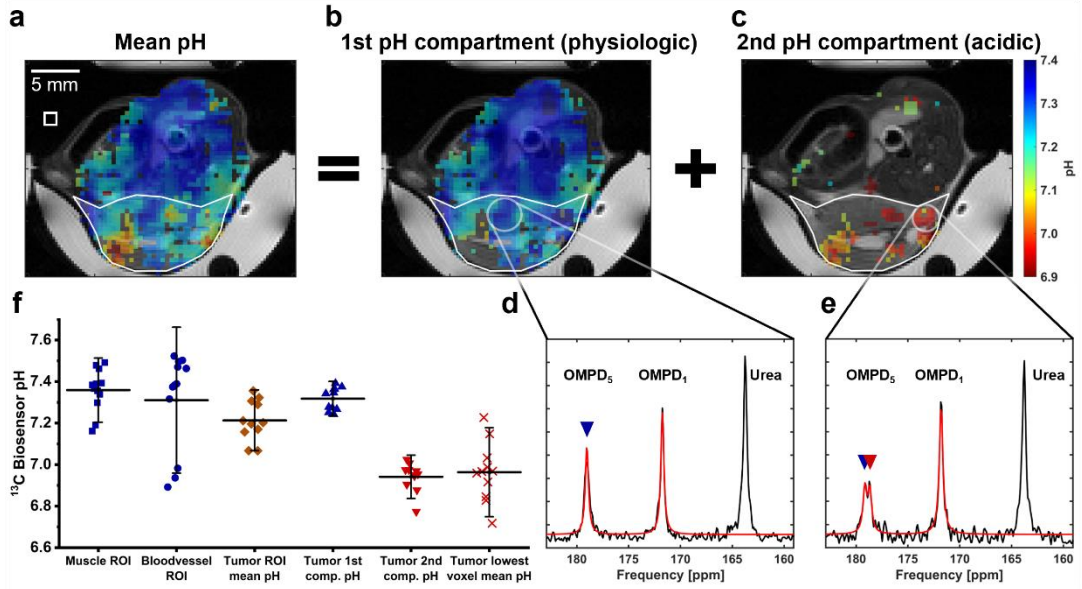

Fig. 2: *In vivo* pH imaging in subcutaneous EL4 lymphoma allows assessment of tumor pH heterogeneity. a pH imaging in subcutaneously implanted EL4 lymphoma (white ROI) reveals heterogeneous tumor acidification. White square: Native CSI resolution. **b** The majority of the tumor exhibits a pH compartment being close to physiological pH conditions, indicated by one OMPD-C_5-peak (**d**, blue triangle). **c** One or multiple subregions exhibit a second, acidic pH compartment, which is detectable as a second peak for the OMPD-C_5-resonance (red triangle) in the spectrum (**e**). Tumors generally show acidification of the mean pH (orange diamonds) compared to healthy muscle (blue squares) or blood pH (blue circles) (**f**). While its physiological compartment (blue triangle) is comparable to muscle pH, the acidic pH compartment (red triangle) and the lowest single voxel mean pH (red crosses) are acidified by up to 0.6 pH units.

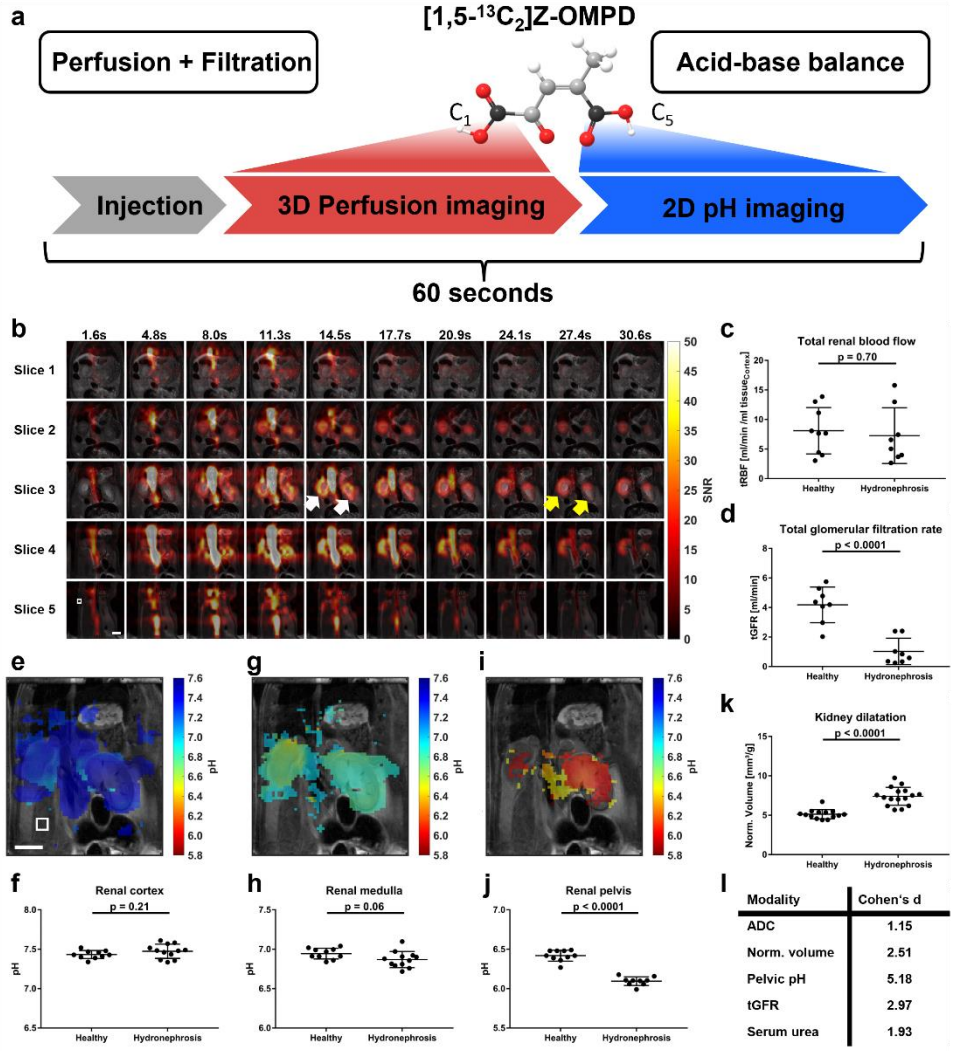

Fig. 3: Simultaneous *in vivo* imaging of renal perfusion, filtration, and acid-base balance in hydronephrotic and healthy kidneys. **a** Scheme for simultaneous combined imaging of renal perfusion and filtration in 3D and renal pH in 2D within one minute where functional information is selectively obtained from each ^{13}C label. **b** Dynamic 3D imaging of hydronephrotic kidneys shows poor filtration of Z-OMPD towards the renal pelvis (yellow arrows) despite strong cortical perfusion (white arrows), being reflected by normal tRBF (**c**) but strongly reduced tGFR (**d**). pH compartments for the cortex (**e**, **f**) and the medulla (**g**, **h**) appear physiological while the pelvis exhibits strong, pathologic acidification (**i**, **j**). Anatomical MRI shows a volume increase (**k**) of hydronephrotic kidneys. (**l**) Comparison of significant parameters using Cohen's d indicates pelvic pH and tGFR measured by imaging of Z-OMPD to be most sensitive to this kidney disease. White square: Native resolution, scale bars: 10 mm.

affecting its use as an internal frequency reference for later pH measurements. For perfusion imaging, a narrow-bandwidth frequency-selective 3D balanced steady-state free precession (bSSFP) scan leaves the C_5-resonance unaffected, allowing subsequent pH imaging of the remaining C_1-magnetization and the full C_5-magnetization by a 2D CSI during the following 30 seconds (Fig. 3a). To demonstrate the value of measuring up to five parameters (RBF, GFR, pH_{Cortex}, $pH_{Medulla}$, pH_{Pelvis}) within one minute and a single injection, the technique was used to probe the kidney function state in MENX rats. bSSFP imaging (Fig. 3b) shows strong perfusion of the renal cortex, reflected by physiological RBF values (Fig. 3c), but no transport of Z-OMPD towards the renal pelvis, indicating reduced glomerular filtration rates (Fig. 3d). pH mapping of the cortex- (Fig. 3e), medulla- (Fig. 3g) and pelvis-associated (Fig. 3i) compartments show no alteration for cortex (Fig. 3f) and medulla (Fig. 3h) but strong, pathological acidification of the renal pelvis (Fig. 3j). Together, this suggests that the renal medulla and pelvis are most severely affected by the hydronephrotic kidney state. T_{2w}-MRI reveals kidney dilatation (Fig. 3k), supporting the finding from ^{13}C MRI. Further, all parameters, which were found to be significantly indicative of kidney damage are compared using Cohen's d (Fig. 3l). Here, ^{13}C-MRI-derived parameters, namely pH_{Pelvis} and tGFR show higher sensitivity compared to

standard blood counts, anatomical or diffusion-weighted ^{1}H-MRI.

Discussion

Here, we introduced a hyperpolarized extracellular pH sensor molecule, namely [1,5-$^{13}C_2$]Z-OMPD. DNP demonstrated excellent hyperpolarization properties, particularly long T_1 relaxation times at various field strengths and *in vivo* that are among the highest ever reported for ^{13}C-labelled hyperpolarized agents (8). Following successful pH imaging validation in healthy kidneys, the C_1-resonance was shown to be suitable as internal reference. For pH imaging in tumors, extracellular acidification was traced back to acidified second pH compartments, which could be unravelled spectroscopically. The extension of the imaging protocol to dynamically acquire 3D images prior to pH mapping for perfusion and renal filtration assessment was demonstrated and renders the presented protocol to our knowledge the fastest technique to simultaneously assess renal perfusion, filtration, and acid-base balance non-invasively. One limitation is the low temporal resolution, resulting effectively in only 4–8 frames to capture flow and filtration dynamics which might result in some quantification error. The technique was applied to a clinically relevant hydronephrosis model. Here, up to five parameters being indicative of renal function status were measured within a single injection within one minute. Investigation of other kidney disease models will be crucial to determine whether different kidney diseases provide an unambiguous pattern of these parameters. Also, model is limited in studying the sensitivity to less severe forms of kidney diseases.

Conclusion

In summary, [1,5-$^{13}C_2$]Z-OMPD presents a promising new hyperpolarized extracellular pH sensor, which offers advantages compared to existing agents, namely longer T_1 and an internal frequency reference. These molecular properties, together with tailored MR pulse sequences enabled the simultaneous readout of multiple imaging biomarkers within a single imaging session after one injection of Z-OMPD within one minute, which is a unique feature of Z-OMPD as a molecular imaging agent for use in tumors and kidneys. In addition, the combined set of five Z-OMPD-derived parameters, of which two are pathologically altered and three within physiological ranges, provides a comprehensive picture of the renal function and disease state for the investigated hydronephrosis model, in good agreement with Standard diagnosis. This versatile, multi-parametric hyperpolarized imaging protocol shows great potential for nephrology and oncology, making it a promising candidate for clinical translation.

References

1. Gallagher FA, Kettunen MI, Day SE, Hu DE, Ardenkjaer-Larsen JH, Zandt R, Jensen PR, Karlsson M, Golman K, Lerche MH, Brindle KM. Magnetic resonance imaging of pH *in vivo* using hyperpolarized ^{13}C-labelled bicarbonate. Nature 2008;453(7197):940-943.
2. Düwel S, Hundshammer C, Gersch M, Feuerecker B, Steiger K, Buck A, Walch A, Haase A, Glaser SJ, Schwaiger M, Schilling F. Imaging of pH *in vivo* using hyperpolarized ^{13}C-labelled zymonic acid. Nat Commun 2017;8.
3. Ohyama T, Hoshino T, Ikarashi T. Isolation and structure of a new organic acid accumulated in tulip plant (Tulipa gesneriand). Soil Science and Plant Nutrition 1988;34(1):75-86.
4. Cooper G, Reed C, Nguyen D, Carter M, Wang Y. Detection and formation scenario of citric acid, pyruvic acid, and other possible metabolism precursors in carbonaceous meteorites. Proc Natl Acad Sci U S A 2011;108(34):14015-14020.
5. Rios AC, Bera PP, Moreno JA, Cooper G. The Pyruvate Aldol Condensation Product. A Metabolite that Escaped Synthetic Preparation for Over A Century. ACS Omega 2020;5(25):15063-15068.
6. Wiedemann T, Peitzsch M, Qin N, Neff F, Ehrhart-Bornstein M, Eisenhofer G, Pellegata NS. Morphology, Biochemistry, and Pathophysiology of MENX-Related Pheochromocytoma Recapitulate the Clinical Features. Endocrinology 2016;157(8):3157-3166.
7. Baumann D, Rudin M. Quantitative assessment of rat kidney function by measuring the clearance of the contrast agent by Gd(DOTA) using dynamic MRI. Magnetic Resonance Imaging 2000;18(5):587-595.
8. Keshari KR, Wilson DM. Chemistry and biochemistry of ^{13}C hyperpolarized magnetic resonance using dynamic nuclear polarization. Chem Soc Rev 2014;43(5):1627-1659.

Establishing an MR-based profile of lithium treatment

Tor Rasmus Memhave[1,2,3], Susann Boretius[1,2,3]

[1] Functional Imaging Laboratory, German Primate Center, Göttingen, Germany
[2] Georg-August University of Göttingen, Göttingen, Germany
[3] International Max Planck Research School for Neurosciences, Göttingen, Germany

Synopsis: An MR-based profile of lithium treatment must first detect it in the brain. We developed *in vivo* ^{7}Li MRI in mice using a SPIRAL sequence. We found higher lithium concentrations in central brain regions. Using a multi-nuclear approach, we established an MR-based profile of mice on a lithium-enriched diet – indicating increased glial activity. To test if astrocytes drove this response, we developed an MR-compatible bioreactor that allowed us to study astrocytes in cell cultures directly. Here, we found increased astrocyte metabolism at therapeutic lithium concentrations. Taken together, the MR-based profile of lithium treatment provides evidence for potentially neuroprotective astrocyte activation.

Introduction

Lithium was originally intended as a treatment of "psychotic excitement"[1]. Today, we refer to this illness as bipolar disorder, a psychiatric illness with a lifetime prevalence of up to 3%[2]. Approved in 1970, lithium is the frontline and recommended treatment of bipolar disorder[2].

Bipolar disorder is an affective illness characterized by periods of mania and depression[2]. In manic episodes, patients have elevated mood alongside psychotic symptoms (e.g. delusion)[3]. In depressive episodes, bipolar patients are often difficult to distinguish from patients with unipolar or major depression[3]. Onset in early adulthood and 12-fold elevated risk of suicide makes bipolar disorder a leading cause of disability in young adults[4].

Despite the success of lithium treatment in patients with bipolar disorder, only about 30% of patients respond optimally[5]. This is of concern as lithium treatment may cause severe renal damage[6].

Lithium's mode of action is not fully understood and there are no clear biomarkers indicating the success of treatment. Monitoring treatment response in patients is further complicated by clinical symptoms first subsiding after weeks or even months of treatment. During this phase of treatment blood serum concentrations are checked frequently to ensure that the lithium concentration is within the recommended range (0.4-1.2 mM)[7].

In this work, we tackle the main problem associated with lithium treatment – the absence of detectable biomarkers – starting at the level of developing *in vivo* ^{7}Li MRI and MRS in the mouse brain. While ^{7}Li MRI had been performed in humans and rats, it was not until our recent work that it was possible in mice[8]. Having established ^{7}Li MRI (part 1), we focused on creating a multi-nuclear MR-based profile of lithium treatment in the healthy mouse brain (part 2). Based on our finding of increased glial activity, we developed an MR-compatible bioreactor for measuring the effect of lithium on 3D astrocyte cell cultures (part 3).

MR hardware

The experiments were performed on a preclinical 9.4T MRI system with a 12-cm gradient system insert (BioSpec 94/30; ParaVision 6.0.1, Bruker Biospin). ^{1}H data were acquired with an 86-mm resonator and 4-channel mouse brain RF coil (Bruker Biospin). Dual-resonance, single-loop RF coils were used for ^{7}Li and ^{31}P (Rapid Biomedical).

Part 1: *In vivo* ^{7}Li MRI in mice

Establishing *in vivo* ^{7}Li MRI in mice on a lithium-enriched diet presents significant challenges due to the low expected signal-to-

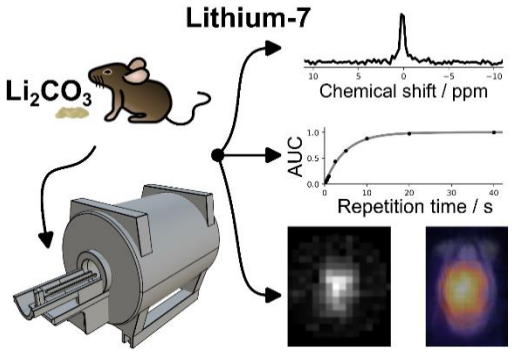

Figure 1: *In vivo* ^{7}Li MRI and MRS were acquired from mice on a lithium-enriched diet. Weekly ^{7}Li MRS was performed to monitor the uptake of lithium and to estimate the T1 relaxation time. 4-hour SPIRAL ^{7}Li MRI was at a resolution of 2×2×3 mm^3. [Reproduced from Memhave et al.[16]]

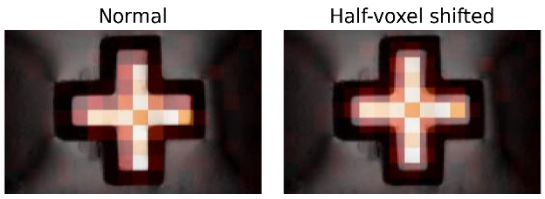

Figure 2: ^{7}Li MRI (false color) was acquired at a resolution of 1×1×5 mm^3 with a FLASH sequence. When corrected the voxel position by 0.5 mm towards the top-left, it overlaps the ^{1}H image (greyscale).

noise ratio (SNR) and the small brain size. ^{7}Li is a spin-3/2 nucleus with a relative receptivity of 0.29 compared to 1 of protons and has a long T1 time *in vivo* of 4.6s (fig. 1)[8] – characteristics that confer only semi-favorable MR properties.

Prior to this work, no *in vivo* ^{7}Li MRI studies on mice had been reported. Our goal was to surpass the previously highest reported resolution of ^{7}Li MRI in rodents (2×2×4 mm^3) while reducing the scan time from 36 hours to no more than 4 hours to make *in vivo* imaging feasible[9].

For *in vivo* imaging to be feasible, we first needed to find (and optimize) an MRI sequence for *in vivo* ^{7}Li MRI in mice that would provide sufficient SNR in a 4-hour measurement to allow for meaningful investigation of the distribution of lithium in the brain. We therefore tested four different MR sequences on lithium-containing **phantoms**: fast low-angle shot (FLASH), rapid acquisition with relaxation enhancement (RARE), balanced steady-state free precession (bSSFP), and SPIRAL. The non-cartesian SPIRAL sequence uses sinusoidal gradient switching, allowing a whole k-space acquisition in a single shot.

Phantom experiments unveiled two important results, first that the SPIRAL sequence yielded the highest SNR. ^{7}Li images acquired with a SPIRAL sequence had higher SNR (8.2) than ^{7}Li images acquired with a bSSFP (SNR = 6.8), FLASH (SNR = 3.2), and RARE sequence (SNR = 1.8). Second, we observed a distinct half-voxel shift when low resolution Bruker data was resampled to a higher resolution. The half-voxel shift, fig. 2, occurs due to the origin of the reconstructed image being in the upper left corner, rather than the center of the image. This shift was corrected during the analysis.

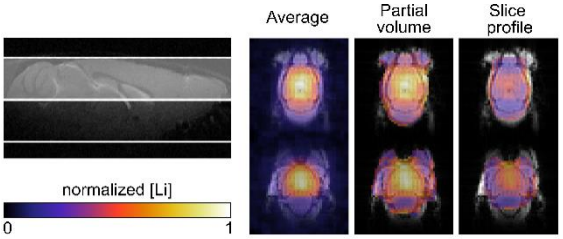

Figure 3: *In vivo* ^{7}Li MRI of mice. The average ^{7}Li image was corrected for partial volume and coil profile. The highest lithium signal in the cerebrum and less in the olfactory bulb and cerebellum. [Adapted from Memhave et al.[16]]

In analogy to the treatment commonly used in humans, all **mice** received a lithium-enriched diet containing 0.3% Li_2CO_3 (w/w). SPIRAL ^{7}Li MRI was acquired with the parameters: TR|TE=2500|1.58 ms, 36.1° flip angle, 16×16 matrix size, 7500 Hz acquisition bandwidth, 2 coronal-oriented slices, 2×2×3 mm^3 voxel size, 5760 averages, and 4-hour acquisition time.

^{7}Li images were averaged and corrected for partial volume and coil profile, fig. 3. Images corrected in this way showed an increased signal of lithium in the central brain. Notably, lithium was only found in low amounts in the olfactory bulb and cerebellum.

We demonstrated that *in vivo* ^{7}Li MRI of mice is feasible with a 4-hour SPIRAL sequence at a resolution of $2 \times 2 \times 3$ mm^3. We found indications that lithium is non-homogenously distributed *in vivo*. SPIRAL ^{7}Li MRI may be used to study lithium treatment and response in mice with the promise of linking regional lithium concentrations to structural or metabolic changes.

Part 2: Multi-nuclear MR-based profile of lithium treatment in mice

To establish an MR-based profile of lithium treatment in clinically healthy mice, we acquired multi-nuclear MR imaging (^{1}H, ^{7}Li MRI) and MR spectroscopy (^{1}H, ^{7}Li, ^{31}P MRS). ^{1}H and ^{31}P were acquired at baseline and after three weeks on a lithium-enriched/placebo diet. In week 4, ^{7}Li MRI/S was acquired. The modalities used are shown schematically in Figure 4.

Twenty mice were enrolled in the study and placed on either a high lithium (0.3% Li_2CO_3 [w/w], n=8), low lithium (0.2% Li_2CO_3 [w/w], n=4), or a placebo diet (n=8) for 3-4 weeks.

Anatomical ^{1}H MRI was acquired using a magnetization transfer sequence with 100 µm isotropic voxels and an acquisition time of 18.6 min. Volumetric analysis was performed in Python with a custom-built mouse atlas.

Diffusion ^{1}H MRI was acquired using echo planar imaging with the following imaging parameters: 4 segments, two b-values (1000 and 2000 s/mm^2), 30 directions, 5 b=0 s/mm^2 images, TR|TE=2000|21.5 ms, 100×100 µm^2 in-plane resolution, 500 µm slice thickness, 18 slices, 1 average, and 8.7 min acquisition time. Diffusion data analysis included diffusion tensor imaging (DTI) with the Python package DIPY and neurite orientation dispersion and density imaging (NODDI)[10,11] with the Python package DMIPY.

^{1}H MRS was acquired using a STEAM sequence from three brain regions: cortex, corpus callosum, and hippocampus, fig. 4. ^{1}H MRS was acquired with the following

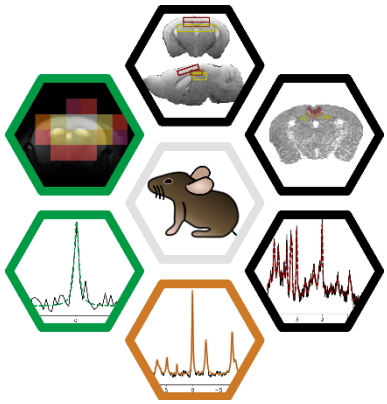

Figure 4: Schematic representation of multi-nuclear MRI in mice. Clockwise from the top: ^{1}H anatomical and diffusion MRI as well as MRS for (micro)structural changes and metabolism (in black); ^{31}P MRS (in orange) for energy metabolism; and ^{7}Li MRS and MRI for lithium uptake and distribution (green)

parameters: TR|TE|TM=6000|10|10 ms, 128 averages, and 12.8 min acquisition time. The spectra were analyzed with LCModel[12].

^{31}P and ^{7}Li MRS were acquired using an ISIS sequence with a voxel size of 6×5×8 mm^3 (whole brain) and acquisition time of 40 min and 10.7 min, respectively. ^{7}Li and ^{31}P spectra were analyzed with scripts developed in-house for preprocessing and curve fitting (MATLAB and Python).

^{7}Li MRI was acquired using a 2D SPIRAL sequence with similar parameters to the previous section, except the slice orientation was switched from coronal to axial. This was done to better utilize the elongated shape of a mouse brain.

^{7}Li MRS of mice on a lithium-enriched diet showed brain lithium concentrations within the therapeutic window (high lithium: 0.9±0.1 mM; low lithium: 0.4±0.1 mM).

^{31}P MRS hinted at increased phosphocreatine in the brain of mice on a high lithium diet which was confirmed by ^{1}H MRS obtained from cortex, corpus callosum, and hippocampus ($p = 0.01$).

^{1}H MRS showed an increase in glial markers and decrease in neuronal markers in mice on a high lithium diet. Myo-inositol, a biomarker associated with glial cells, was increased by 39% in cortex ($p=0.02$). The neuronal marker total N-acetylaspartate was decreased by 11% in corpus callosum ($p=0.009$) and 10% in hippocampus ($p=0.01$). The glutamate-to-glutamine ratio, glutamate being a neurotransmitter and glutamine synthesized in astrocytes, was decreased by 16% in hippocampus ($p=0.05$). The total creatine concentration was unchanged, confirming that no systematic concentration shift was present.

Diffusion MRI showed decreased apparent diffusion coefficient (ADC from DTI) and increased neurite density index (NDI from NODDI) across cortex, corpus callosum, and hippocampus in mice on a high lithium diet. The ADC was decreased by 4% in cortex ($p=0.005$), 5% in corpus callosum ($p=0.004$), and 4% in hippocampus ($p=0.01$). We did not observe changes in FA in response to a lithium-enriched diet. Using the NODDI model, we observed increased NDI across the three brain regions for high lithium mice. The NDI was increased by 6% in cortex ($p=0.01$), 7% in corpus callosum ($p=0.007$), and 6% in hippocampus ($p=0.02$). We did not observe changes in beta fraction or orientation dispersion.

We observed no change in the total brain volume ($p=0.84$) and cerebrospinal fluid volume ($p=0.44$) in mice on a high lithium diet.

The acute phase of lithium treatment may easily be mistaken for illness. The data presented here shows similarities to neurodegenerative phenotypes observed in established mouse models – decreased N-acetyl aspartate, increased osmolytes and glutamine. However, we would like to offer an alternative hypothesis: increased glial activity. Specifically, an increased neurite density index and myo-inositol – a non-specific glial marker – both of which may suggest increased glial contribution. These changes were observed across three distinct brain regions in both grey and white matter. Given that the animals remained clinically healthy during treatment, our findings hint at increased astrocyte activity and density. This lends support to the hypothesis that astrocytes are a target of lithium treatment and that they may facilitate the neuroprotective effects of lithium[13].

Part 3: MR-based profile of astrocyte response to lithium

To investigate our hypothesis that astrocytes drive the MR-based profile of lithium treatment, we examined the direct impact of lithium on 3D astrocyte cell cultures. We used MRS to assess the effect of lithium at two concentrations (0.8 and 4.4 mM) on astrocyte metabolism. To our knowledge, this is the first MRI and MRS study to evaluate the feasibility of measuring 3D cell cultures in a preclinical MRI system.

Preclinical cell culture MRI necessitates a solution to the problem of inaccessibility during measurements, meaning that repositioning or checking on the cells cannot be done during a measurement. As such, the cell culture equipment is separated from the bioreactor by roughly five meters, fig. 5, so changing the conditions in the setup is a slow process.

The bioreactor and incubator, fig. 5, were designed to provide flexibility in the setup and monitoring of the conditions. The bioreactor was specifically designed to fit on a standard mouse head coil. The valves on the bioreactor allowed

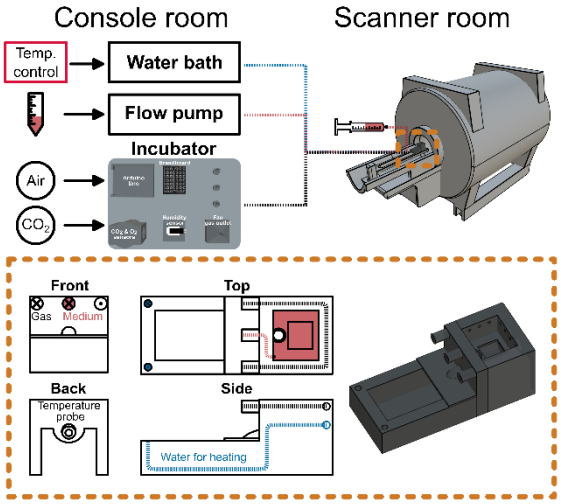

Figure 5: **Bioreactor setup in a preclinical MR system.** The bioreactor (inside the orange box) is separated by 5 meters from the console room during measurements.

gas and medium perfusion. The gas in the incubator was monitored to ensure desired CO_2 concentration, humidity, and gas temperature.

Experiments were performed on immortalized human astrocytes (P10251-IM, Innoprot, Spain) that were seeded in a collagen hydrogel. The astrocytes were measured in four types of cell culture medium (normal medium: DMEM, low glucose, 10% FBS, 1% antibiotics) with varying concentrations of lithium and magnesium added: normal (no Li, no Mg), magnesium (no Li, 10 mM Mg), low lithium (0.8 mM Li, 10 mM Mg), and high lithium (4.4 mM Li, 10 mM Mg). Low lithium medium corresponds to therapeutic concentrations and the high lithium medium is toxic *in vivo*.

Structural ^{1}H MRI was acquired to aid MRS voxel positioning, using a 2D RARE sequence in two orientations (axial and coronal).

MRS was acquired with a STEAM sequence with the following parameters: TR|TE|TM=6000|10|10 ms, 1 average, 600 repetitions, 5×1.5×5 mm^3 voxel size, and 1 hr total scan time. The spectra were preprocessed by digital filter removal, zero-filling, and phase correction in Python using the package nmrglue. The spectra were then binned into 10-min spectra. The preprocessed spectra were analyzed with LCModel[12]. All LCModel soft constraints were removed and, due to the low creatine signal, the chemical shift was referenced to water.

Statistical analysis of the MRS data was performed in Python. A one-way ANOVA (medium type) was performed on the average metabolite concentration of each 1-hour time series. Post-hoc testing was performed using Tukey's honestly significant difference test.

The astrocytes in the four different medium types gave visually similar spectra with a quality assurance threshold for the coefficient of determination of 0.70 (defined based on Otsu's method). The relatively high coefficient of determination showed that LCModel can reliably quantify the spectra with adequate accuracy.

Metabolite changes for all medium types compared to the standard medium are summarized in Table 1. Astrocytes in low lithium medium showed decreased myo-inositol (-48%, p=0.03), phosphocreatine (-41%, p=0.006), total glutamate and glutamine (-30%, p=0.01). Glucose showed a mild decreased (-4%, n.s.). Glycine levels were increased in astrocytes across all three magnesium-containing media.

We observed a dose-dependent effect of lithium on metabolism, particularly noting that myo-inositol, phosphocreatine, total glutamate and glutamine, and glucose (n.s.) were reduced in astrocytes in the low lithium medium. The decreased total glutamate and glutamine and glucose level in astrocytes under low lithium conditions is particularly intriguing, suggesting elevated astrocytic activity at therapeutic lithium concentrations.

When comparing our findings directly to the *in vivo* mouse experiments (part 2), it is apparent that 3D astrocyte cell cultures respond differently to lithium than the whole mouse brain. Lithium-fed mice showed increased phosphocreatine and myo-inositol, contrary to astrocyte cell cultures. This discrepancy can be partly understood through the inositol depletion hypothesis. According to this, lithium inhibits key enzymes in the inositol cycle[14].

However, inositol depletion has not been unanimously observed in human studies[15] and was also not present in the high lithium medium. Comparable to our results from astrocytes in low lithium medium, it is believed that following the start of lithium administration the myo-inositol decrease is accompanied by a glycine increase[16]. This interplay is significant because myo-inositol and glycine have overlapping spectra in the chemical shift range (4.2-0.2 ppm), complicating accurate distinction and quantification.

Table 1: **The impact of medium type on astrocyte metabolism**. The arrows indicate change relative to astrocytes in standard medium. Legend: myo-inositol (Ins), glycine (Gly) phosphocreatine (PCr), total glutamate and glutamine (Glu+Gln), and glucose (Glc). Parenthesis indicate changes >30% that are not statistically significant.

Metabolite	Magnesium	Low lithium	High lithium
Ins	-	↓	-
Gly	(↑)	(↑)	↑
PCr	-	↓	-
Glu+Gln	↓	↓	-
Glc	-	-	(↑)

To make our cell culture findings transferable to *in vivo* studies, co-culture and/or organoids should be explored in 3D matrices. Here, we provide a proof-of-concept study with a 3D monoculture illustrating that measuring relevant differences is possible.

Towards a unified hypothesis of lithium's mode of action

A unified hypothesis of lithium's mode of action necessarily starts and ends with its uptake and distribution in the brain. We observed a non-homogenous distribution of lithium, with high lithium in the central cerebrum and low lithium in the olfactory bulb and cerebellum. Furthermore, the uptake of lithium in the brain was dose-dependent. However, the extent to which lithium concentration in the brain correlates with its distribution remains unclear.

In vivo multi-nuclear MRI and MRS of lithium-fed mice showed increased glial contribution, with changes in grey and white matter but no adverse clinical effects. These findings support the astrocyte hypothesis of lithium treatment, suggesting that lithium leads to neuroprotective astrocyte activation.

In vitro MRS of 3D astrocyte cell cultures showed increased metabolic activity at therapeutic concentrations of lithium. However, direct comparisons of metabolic changes between *in vivo* and *in vitro* experiments proved difficult. Therefore, a better translational system is needed to provide a more accurate model for lithium treatment and response.

We propose the usage of brain organoids to create a better model for lithium treatment and response. Future experiments will investigate the effect of lithium on organoid metabolism and development, aiming to establish an optimal translational tool for predicting lithium treatment efficacy and response at the individual patient level.

Conclusion

In these studies, we have developed *in vivo* ^{7}Li MRI in mice for the first time (part 1), established an MR-based profile of lithium treatment in mice (part 2), and verified using MRS that therapeutic lithium concentrations lead to increased astrocyte activity at the cellular level (part 3).

Acknowledgements

The authors thank K. Bhat, R. Willumeit-Römer, L. Hanke, and E. Quandt for collaborating on the astrocyte cell culture project. TRM was a doctoral student of the Ph.D. program "Neurosciences" – International Max Planck Research School and the Göttingen Graduate School for Neurosciences, Biophysics, and Molecular Biosciences (GGNB) (DFG grant GSC 226) at the Georg August University Göttingen.

References

1. Cade JFJ. Lithium salts in the treatment of psychotic excitement. *The Medical journal of Australia*. 1949;2(10):349-352. doi:10.1080/j.1440-1614.1999.06241.x
2. Sköld M, Rolstad S, Joas E, et al. Regional lithium prescription rates and recurrence in bipolar disorder. *Int J Bipolar Disord*. 2021;9(1):18. doi:10.1186/s40345-021-00223-7
3. Grande I, Berk M, Birmaher B, Vieta E. Bipolar disorder. *The Lancet*. 2016;387(10027):1561-1572. doi:10.1016/S0140-6736(15)00241-X
4. Grunze H. Bipolar Disorder. In: *Neurobiology of Brain Disorders*. ; 2015:655-673. doi:10.1016/b978-0-12-398270-4.00040-9
5. Alda M. Who are excellent lithium responders and why do they matter? *World Psychiatry*. 2017;16(3):319-320. doi:10.1002/wps.20462
6. Alsady M, Baumgarten R, Deen PMT, de Groot T. Lithium in the Kidney: Friend and Foe? *Journal of the American Society of Nephrology*. 2016;27(6):1587-1595. doi:10.1681/ASN.2015080907
7. Nolen WA, Licht RW, Young AH, et al. What is the optimal serum level for lithium in the maintenance treatment of bipolar disorder? A systematic review and recommendations from the ISBD/IGSLI Task Force on treatment with lithium. *Bipolar Disorders*. 2019;21(5):394-409. doi:10.1111/bdi.12805
8. Memhave TR, Moussavi A, Boretius S. SPIRAL MRI for in vivo lithium-7 imaging: a feasibility study in mice after oral lithium treatment. *Sci Rep*. 2024;14(1):681. doi:10.1038/s41598-023-50841-7
9. Stout J, Hanak AS, Chevillard L, et al. Investigation of lithium distribution in the rat brain ex vivo using lithium-7 magnetic resonance spectroscopy and imaging at 17.2 T. *NMR in Biomedicine*. 2017;30(11). doi:10.1002/nbm.3770
10. Tariq M, Schneider T, Alexander DC, Gandini Wheeler-Kingshott CA, Zhang H. Bingham–NODDI: Mapping anisotropic orientation dispersion of neurites using diffusion MRI. *NeuroImage*. 2016;133:207-223. doi:10.1016/j.neuroimage.2016.01.046
11. Zhang H, Schneider T, Wheeler-Kingshott CA, Alexander DC. NODDI: Practical in vivo neurite orientation dispersion and density imaging of the human brain. *NeuroImage*. 2012;61(4):1000-1016. doi:10.1016/j.neuroimage.2012.03.072
12. Provencher SW. Estimation of metabolite concentrations from localized in vivo proton NMR spectra. *Magnetic Resonance in Medicine*. 1993;30(6):672-679. doi:10.1002/mrm.1910300604
13. Rivera AD, Butt AM. Astrocytes are direct cellular targets of lithium treatment: novel roles for lysyl oxidase and peroxisome-proliferator activated receptor-γ as astroglial targets of lithium. *Translational Psychiatry*. 2019;9(1):211. doi:10.1038/s41398-019-0542-2
14. Atack JR. Inositol monophosphatase, the putative therapeutic target for lithium. *Brain Research Reviews*. 1996.
15. Silverstone PH, McGrath BM. Lithium and valproate and their possible effects on the myo-inositol second messenger system in healthy volunteers and bipolar patients. *International Review of Psychiatry*. 2009;21(4):414-423. doi:10.1080/09540260902962214
16. Hirvonen MR, Savolainen K. Lithium-induced decrease of brain inositol and increase of brain inositol-1-phosphate is transient. *Neurochem Res*. 1991;16(8):905-911. doi:10.1007/BF00965540

Anisotropic Longitudinal Water Proton Relaxation in White Matter Investigated Ex Vivo in Porcine Spinal Cord with Sample Rotation

Niklas Wallstein[1], André Pampel[1], Carsten Jäger[2,3], Roland Müller[1], and Harald E. Möller[1,4]

[1] NMR Methods & Development Group, Max Planck Institute for Human Cognitive and Brain Sciences, Leipzig, Germany

[2] Department of Neurophysics, Max Planck Institute for Human Cognitive and Brain Sciences, Leipzig, Germany

[3] Paul Flechsig Institute – Center of Neuropathology and Brain Research, Medical Faculty, Leipzig University, Germany

[4] Felix Bloch Institute for Solid State Physics, Leipzig University, Germany

Synopsis: So far, variations in T_1 relaxation time in brain regions that differ in their main fiber direction have been reported with inconsistent results. The aim of this study is to resolve such inconsistencies, and in addition, to understand the origin of the potential T_1 orientation dependence. This is done by directly rotating a fixed spinal cord white matter sample and comparing the T_1 measurements obtained from different methods (e.g., inversion-recovery and MP2RAGE) at 22°C and 36°C. More pronounced anisotropy was consistently obtained with techniques more sensitive to MT effects. A comprehensive analysis based on the binary spin-bath model for MT revealed an interplay of several orientation-dependent parameters.

Introduction

A recent aim of MRI is to use relaxation parameters such as water protons T_1 for quantitative analysis and interpretation in terms of microstructure and myelination patterns. The remarkable reported variation in white matter (WM) T_1 values for different anatomical regions and measurement techniques has hampered improvements in the understanding of the underlying physical mechanism. Longitudinal relaxation in WM is often analyzed under the oversimplified assumption of a mono-exponential recovery. On the other hand, an important contribution to water proton relaxation is due to cross-relaxation with the 'semi-solid' membrane components and macromolecules. For comprehensive modeling, consideration of multiple pools and magnetization transfer between them is therefore mandatory (1).

Recent work (2-4) has further drawn attention to anisotropic longitudinal relaxation characteristics in WM in vivo *(2,3)* and ex vivo *(2,4)* tissue samples. These studies have reported conflicting observations, including a maximum around fiber-to-field angles $\theta_{FB}\approx50°$ with an orientation-dependent variation of about 7% resulting from an MP2RAGE protocol (2), or monotonically increasing longitudinal relaxation rate R_1 by approximately 3% upon increasing θ_{FB} from 0° to 90° in human WM using a two-point measurement (3).

Although the accuracy of the aforementioned studies is not questioned, there are limitations, for example, related to scanner hardware and imaging protocols. In particular, T_1 anisotropy was assessed by comparing regions with different θ_{FB} in in-vivo human studies. Inversion times (TIs) were restricted to a narrow range due to tolerable scan time *in vivo* and the need to integrate the imaging readout. Moreover, only soft inversion pulses were used, which do not achieve well-defined initial conditions for the semi-solid proton pool. Finally, gradient-recalled-echo sequences employ a considerable number of readout pulses leading to MT effects.

An initial goal of the current study was, therefore, to establish carefully controlled experimental conditions for precise and reproducible investigations of orientation-dependent T_1 in WM. This included experiments at different temperatures to address one aspect of limited comparability between ex vivo MRI in fixed tissue (at room temperature), and in vivo MRI (at physiological temperature). Our main hypothesis was that T_1 anisotropy results from an interplay of orientation-dependent longitudinal relaxation of non-aqueous protons and MT with water protons. We further hypothesized that different strategies for T_1 measurements may show distinct differences in their sensitivity to orientation effects. To investigate these hypotheses, we compared different T_1 measurement techniques, including

the classical inversion recovery (IR) as well as GRE approaches with variable flip angles (VFA) and MP2RAGE, which are frequently employed in brain MRI studies. Differences between these methods include: different dynamic ranges for measuring the recovery of longitudinal magnetization, different initial magnetization states, especially for non-aqueous protons, and different sensitivities to MT processes between aqueous and non-aqueous proton pools. Another aim was to isolate 'true' orientation effects by directly reorienting ex vivo WM samples using a tiltable coil to exclude confounding factors such as differences in myelination or in distribution of fibers within a voxel when comparing different brain regions.

A small segment of well-oriented porcine spinal cord WM was used. This allowed one-dimensional (1D) acquisitions along the main fiber orientation in order to consistently investigate a large number of experimental conditions in a reasonable scan time, including measurements at very short TIs.

Materials and Methods

Sample Preparation: Pieces of porcine spine were obtained from a local slaughterhouse within 2–3 hours of death, immediately fixated in 4% paraformaldehyde (PFA) in phosphate buffered saline (PBS) at pH 7.4, and stored at 4 °C. After 6 weeks of fixation the samples were transferred into PBS with 0.1% sodium azide. From the lumbar segment (L5-6) the spinal cord was extracted and stored in PBS/NaN3. A small, largely homogeneous section of WM of the posterior funiculus (length 17 mm, diameter ≤4 mm) was excised from the center of the vertebra (Fig. 1), and washed in PBS for several hours. Subsequently, it was placed in a 5mm NMR glass tube (Wilmad®) and embedded in Fomblin® (Solvay).

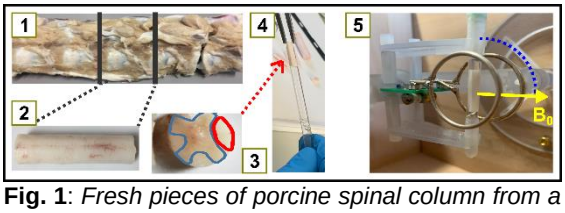

Fig. 1: *Fresh pieces of porcine spinal column from a local slaughterhouse were fixated in 4% PFA/PBS solution (1). A piece of spinal cord from segment L5/6 (lumbar vertebrae) was carefully dissected (2) and a part of the WM region (highlighted in red) (3) was placed in an NMR tube embedded in Fomblin (4). Finally, the tube was placed in the central region of a Helmholtz coil (5).*

Hardware Setup: The NMR tube was placed in the center region of a custom-made TxRx Helmholtz coil (5). This coil was mounted inside a cuboid wooden box to enable measurements above room temperature. Elevated temperature was achieved by a stream of heated air from a heat exchanger located outside the magnet room. The airflow was transferred through of flexible tubing (thermally insulated with polyurethane foam). Details of the temperature control unit are described elsewhere (6).

The design of the coil allowed precise sample reorientation without removing the box from the scanner's isocenter. In particular, a 3D-printed universal joint, combined with a worm gear, was mounted on the outside of the wooden box to transfer the rotation of a wooden crank.

MR-Investigations: Experiments were performed on a MAGNETOM Skyra Fit 3T scanner (Siemens Healthineers, Erlangen, Germany). For all measurements, customized pulse sequences were utilized with an identical 1D readout (0.965 mm nominal resolution) along the sample axis. During the experiments (10–12 hours for each temperature), the temperature inside the box was maintained at 35.7–36.2 °C or at 21.6–22.9 °C to minimize confounds due to temperature fluctuations or drifts. The low reference transmitter amplitude for a 1ms-long 180° rectangular pulse was carefully calibrated (17.3 V) with a pulse-width array experiment and enables short (inversion) pulses.

The sample orientation was varied between angles of 0° (parallel alignment with the external field $\mathbf{B_0}$) and 90° (perpendicular alignment with the external field $\mathbf{B_0}$) in a pseudorandomized order (11 rotation angles; starting and ending with a 90° orientation, to verify stable conditions (e.g., no tissue degradation). θ_{FB} was validated by diffusion tensor imaging (DTI; echo time, TE=80 ms; repetition time, TR=4 s; b=1500 s/mm^2) with 60 gradient directions interleaved with 7 measurements at b=0, as the angle between diffusion tensor eigenvector corresponding to the largest eigenvalue and the direction of $\mathbf{B_0}$.

The methods for measuring T_1 included IR, MP2RAGE, and VFA, which all employed 1D projections (i.e., without slice selection and phase encoding). IR experiments were performed with both hard, rectangular (τ_p=40 µs) and soft, adiabatic inversion pulses (BIR-4, τ_p=5 ms) to create different initial conditions, in particular of proton magnetization associated with motion-restricted macromolecules or lipid membrane structures. Datasets consisting of 23 logarithmically spaced inversion times (770 µs ≤ TI ≤ 10 s, TR=13 s) were acquired for both cases.

An alternative gradient spoiling strategy was implemented for 1D MP2RAGE imaging and thirteen pairs of inversion times were acquired in separate scans (7). Some of the TI-values were adopted from Kauppinen et al. (2).

VFA experiments consisted of 11 acquisitions with α ranging from 4° to 60° using an identical spoiling strategy as for MP2RAGE. Additional two-point calculations of T_1 were also performed using parameters from a multi-parameter mapping (MPM) protocol (α=4°; α=25°) (8).

For comparison reasons, MT measurements were performed with a train of 250 Gaussian RF pulses (τ_p=2 ms, amplitude $\gamma B_{1,RMS}/(2\pi)$ = 500 Hz or 705 Hz, offset frequency 10 kHz; $B_{1,RMS}$ is the root-mean-squared amplitude of the pulse) followed by a GRE readout (same as used for VFA experiments). Dual-sided saturation was achieved by alternating the offset frequency of subsequent RF events and by cosine modulation of the RF pulse shapes (inter-pulse delay of 250 µs) in separate experiments.

Data Analysis: The raw data obtained from the scanner were pre-processed using routines developed in-house in MATLAB (R2020b). Fitting was performed with real signals for IR experiments and with magnitude signals for all other measurements. Non-linear regression used the function “nlinfit”. The uncertainties of the determined T_1 values were specified as 95% confidence intervals using the “nlparci” algorithms.

Two general approaches were used to analyze the data: (I) fitting was performed according to analytical expressions for the specific measurement protocols, (II) more sophisticated approaches were used to try to explain differences in estimated T_1 times and degrees of anisotropy obtained for distinct subsets of the IR curves covering different ranges of TIs. These further analyses included simulations and parameter estimations based on an established matrix-algebra approach and the binary spin-bath (BSB) model with a free (liquid) water pool A and a macromolecular (semisolid) pool B. This explicitly considered relaxation during RF pulse application (relevant for the semisolid pool) and MT between the pools. Briefly, the entire pulse sequences were simulated by sequentially multiplying the magnetization vector by a chain of propagators (9), assuming perfect spoiling of transverse magnetization, neglecting transverse magnetization of the pool B, and splitting the sequence into *n* episodes with constant parameters.

To obtain a first estimate of the spin-system parameters, both IR datasets from all orientations were simultaneously adjusted without consideration of anisotropy. The obtained parameters were then used as starting values for more complex analyses considering orientation dependence. As an exception, the macromolecular proton fraction (MPF) was fixed to the initial (isotropic) result because the pool sizes should not depend on θ_{FB}. Fixing MPF also achieved reductions of parameter correlations in the fits. We further assumed that k and T_1^A are invariant upon reorientation. For all other parameters, different contributions from anisotropy were successively included in the fitting routine. In model [1], only the influence of RF pulses on the semi-solid pool B was adapted independently for each orientation, that is, M_z^B (0^+) varies with θ_{FB}. Model [2] additionally assumed orientation-dependence of the transverse relaxation time T_2^A. Finally, model [3] also assumed orientation dependence of the longitudinal relaxation time T_1^B in addition to model [2].

Results

The fractional anisotropy (FA) obtained with DTI indicated a high anisotropy in the WM sample, which does not change significantly when repeating the measurements after 24 hours at room temperature. Two ROIs (4 voxels each, FA>0.65) were selected for further analyses. In all orientation-dependent experiments, the results from the first and last acquisition at 90° rotation agreed within the experimental accuracy.

(I) Analyses Assuming a Uniform T_1

Inversion-Recovery Experiments: The IR data showed systematic deviations from a monoexponential recovery, which was particularly noticeable at short TI (TI<100 ms). Analyzing the experiments under the simplifying assumption of monoexponential recovery resulted in apparent T_1 values ranging from 710 to 800 at 36 °C for the hard-pulse inversion (Fig. 2, results of adiabatic inversion similar but not shown). At 36 °C, and somewhat less evident at 22 °C, a T_1 maximum appeared at θ_{FB} between 30° and 40°, when all data points were included in the fits. In contrast, the dependence of the apparent T_1 on θ_{FB} changed towards a monotonically decaying function when only longer TIs were considered (TI>100 ms or TI>450 ms), and became more similar across temperatures. Overall, the T_1 differences between θ_{FB}=0° and 90° were small (on the order of 3–5%).

MP2RAGE Experiments: The T_1 values measured with MP2RAGE also exhibited a maximum around θ_{FB} between 30° and 40° at 36 °C and a trend of a T_1 decay with increasing θ_{FB} at 22 °C, similar to the IR results obtained with longer TIs (data not shown).

VFA and MPM Experiments: Both VFA and MPM determine T_1 without inverting the magnetization. Remarkably, the obtained T_1 values showed the highest anisotropy (Fig. 3), with variations of about 10% and 8% for VFA (T_1 = 710–790 ms, Fig. 3a) and MPM (T_1 = 680–

740 ms, Fig. 3b), respectively. Both methods yielded similar trends with maxima at θ_{FB} between 30° and 40°, albeit with reduced T_1 values for MPM. Compared to the results obtained at 36°C, the orientation dependence was slightly lower at 22 °C.

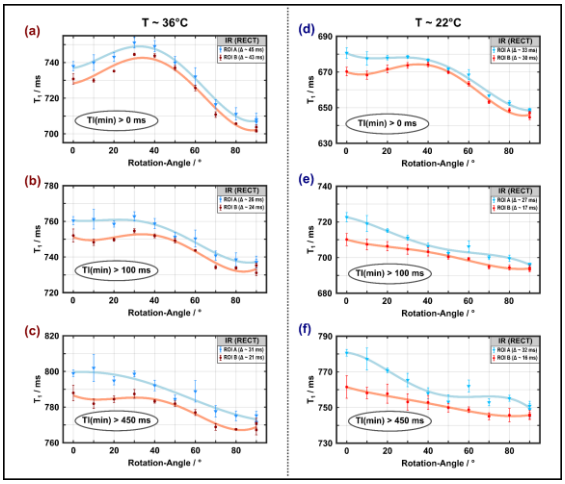

Fig. 2: *Apparent spin-lattice relaxation times obtained from monoexponential fitting of IR curves measured with hard-pulse inversion (τ_p=40 µs) at 36 °C (a–c) and 22 °C (d–f) as a function of the rotation angle.*

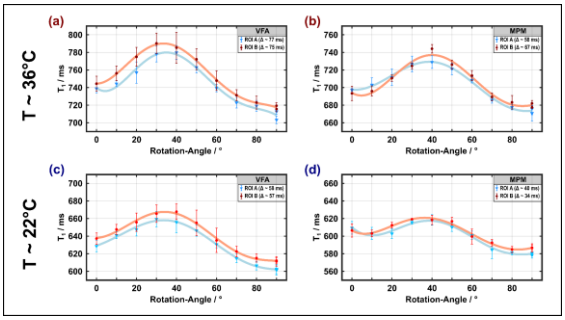

Fig. 3: *Apparent T_1 times obtained with VFA and MPM at 36 °C (a,b) and 22 °C (c,d) as a function of the rotation angle.*

MT Experiments: θ_{FB}-dependent changes in the signal attenuation induced by MT were visible in all MT experiments (data not shown). Regardless of the amplitude of the off-resonant MT pulse or the strategy to achieve dual-sided saturation, a maximum of MT-saturation (MTsat) was obtained between 30° and 40°. Alternating the offset frequency produced a slightly larger range of MTsat variation compared to cosine modulation.

(II) Analysis of the IR Experiments within the BSB Model

Results from ROI A obtained at 36 °C from BSB model analyses with different considerations of orientation dependence are shown in Figures 4 and 5. Since MTsat changed significantly with θ_{FB}, M_z^B (0^+) was assumed to be orientation dependent in model [1] due to a variable efficiency of the inversion pulse. Taking into account the differences in M_z^B (0^+), as shown in Figure 5 (orange box), the associated effect of the build-up of a maximum signal difference could be reproduced qualitatively (Fig. 4, model [1]). However, if orientation effects would impact only M_z^B (0^+), both pools would relax in synchrony once the populations are equilibrated. Therefore, model [1] fails to explain the observed crossings of transients that were obtained for different θ_{FB} (Fig. 4, left column). This is further evident in Figure 5 (orange box): Model [1] yielded orientation dependence of T_1 if all TIs were included in the monoexponential fitting but failed to explain the experimental result for analyses including only TI>100 ms. Model [2] achieved some refinement of the fits suggesting an orientation-dependent variation of T_2^A between 34 and 42 ms (Fig. 5). Like model [1], however, it did not explain the dynamic behavior of transients as a function of TI (Fig. 4). Finally, spin-lattice relaxation in the semi-solid pool was assumed to be anisotropic in model [3]. This therefore considered MPF fixed (=0.17), k and T_1^A as free isotropic BSB parameters, T_2^A (θ_{FB}) and T_1^B (θ_{FB}) as free orientation-dependent parameters, as well as $M_{Z,Rect}^B$ (0^+,θ_{FB}) and $M_{Z,BIR\text{-}4}^B$ (0^+,θ_{FB}) as free orientation-dependent parameters that were allowed to differ for the different types of inversion pulses (rectangular and BIR-4, respectively). Figure 5 shows that all trends in the anisotropy of T_1 estimates were reproduced with this model, including a subtle peak at θ_{FB}=30–40° for experiments with a hard-pulse and a monotonic T_1 decay upon increasing θ_{FB} from 0° to 90°.

Discussion

A reproducible orientation dependence of the apparent T_1 in fixed porcine spinal cord WM was demonstrated. We avoided potential confounds due to differences in myelination, present in previous work comparing different WM regions, by direct sample reorientation. Furthermore, by combining different techniques to measure T_1, the hypothesis that inconsistencies in the observed orientation dependence of T_1 might be related to the acquisition method could be directly addressed and confirmed. Remarkably, the decay of T_1^B with increasing θ_{FB} (Fig. 5) obtained with the BSB analysis and model [3] is in excellent agreement with recent theoretical predictions from a lateral diffusion model for bound protons in axon bundles (11).

Conclusion

Longitudinal proton relaxation in WM depends on orientation, which is attributed to microstructural anisotropy due to the presence of bundles of approximately cylindrical nerve fibers (myelinated axons).

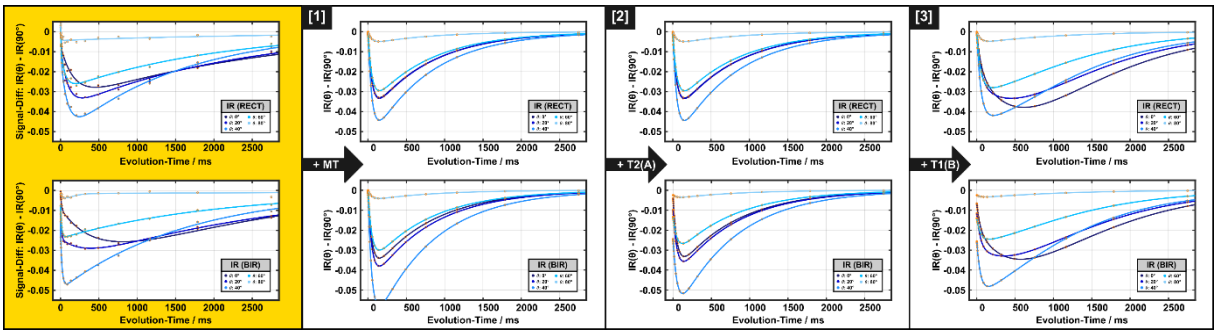

Fig. 4: *IR datasets recorded at different orientation angles (indicated by different symbols) shown as the difference from the result for θ_{FB}=90° for both inversion pulses (top row: rectangular hard pulse, bottom row: BIR-4 adiabatic pulse). The solid lines are guides to the eye. Experimental data (left, golden background) is presented as mean over ROI A. For comparison, BSB model forward simulations with different levels of combinations of anisotropic parameters are shown. Note that crossings of transients of different rotation angles observed experimentally are only observed with model [3].*

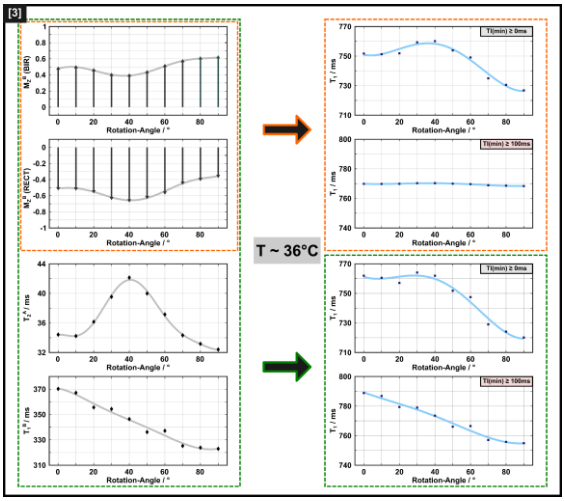

Fig. 5: *Overview of anisotropic BSB model parameters as a function of θ_{FB} (left column), obtained from the analyses illustrated in Figure 4 and resulting orientation-dependent T_1 (right column) from fits to the simulated IR data.*

The arrangement of associated membrane components is sensed by mobile water protons through dipolar cross-relaxation and/or chemical exchange. The extent of observed orientation-dependent T_1 variation depends on the exact experimental conditions and, thus, on the relaxometry pulse sequence, in particular, on the type, amplitude and number of applied RF pulses. A sufficient description of the observed effects is already obtained with the BSB model for MT, which considers only two microanatomical compartments. The results suggest that T_2^B, which characterizes the dipolar lineshape, and also T_1^B of the semi-solid pool are anisotropic. This corroborates previous interpretations of MT anisotropy (10). Remarkably, the results also suggest anisotropy of T_2^A of the mobile pool. In summary, our findings clarify apparent inconsistencies in the literature and demonstrate that orientation-dependent T_1 provides a valuable link to microstructure beyond simple correlation analyses.

References

1. Manning, A. P. et al. Understanding aqueous and non-aqueous proton T1 relaxation in brain. J. Magn. Reson. 2021; 323
2. Kauppinen, R. A. et al. Axon fiber orientation as the source of T1 relaxation anisotropy in white matter: A study on corpus callosum in vivo and ex vivo. Magn. Reson. Med. 2023; 90:708-721
3. Hänninen, N. E. et al. Relaxation anisotropy of quantitative MRI parameters in biological tissues. Sci. Rep. 2022: 12, 12155
4. Schyboll, F. et al. The impact of fibre orientation on T1-relaxation and apparent tissue water content in white matter. Magn. Reson. Mater. Phy. 2018; 31, 501-510
5. Wallstein, N. et al. Radiation damping at clinical field strength: Characterization and compensation in quantitative measurements. Magn. Reson. Med. 2023; 91, 1239-1253
6. Wallstein, N. et al. A low-cost setup for orientation-dependent post-mortem MRI under temperature control. In: Proceedings of the 32nd Annual Meeting of ISMRM, Singapore, 2024; p. 1594.
7. Wallstein, N. et al. Anisotropic longitudinal water proton relaxation in white matter investigated ex vivo in porcine spinal cord with sample rotation. Sci Rep 2024; 14, 12961
8. Weiskopf, N. et al. Quantitative multi-parameter mapping of R1, PD*, MT, and R2* at 3T: A multi-center validation. Fron. Neurosc. 2013; 7, 95.
9. Müller, D. et al. Matrix-algebra-based calculations of the time evolution of the binary spin-bath model for magnetization transfer. J. Magn. Reson. 2013; 230, 88-97
10. Sukstanskii, A. L. and Yablonskiy, D. A. Microscopic theory of spin-spin and spin-lattice relaxation of bound protons in cellular and myelin membranes-a lateral diffusion model (LDM). Magn. Reson. Med. 2023; 89, 370-383
11. Pampel, A. et al. Orientation dependence of magnetization transfer parameters in human white matter. Neuroimage. 2015; 114, 136-146

Scientific Session 1

Hyperpolarization and Metabolic Imaging

Oral presentations

101	Anaïs Choffart	*Non-invasive Mapping of Acidosis and Extracellular Lactosis for Assessing Tumor Invasion In Vivo*
102	Josh Peters	*T1 alterations in nitrogen-15 hyperpolarized molecules*
103	Jakob Gaubatz	*Phase-based 3D pH imaging in vivo using hyperpolarized [1,5-13C2]Z-OMPD*
104	Friedemann Bullinger	*Magnetic resonance in the zero and ultralow field regime – a transition from one-dimensional oscillation to precession*
105	Nicolas Kempf	*13C imaging of pyruvate with SABRE at Ultra-Low field*

Posters

P101	Martin Sandbrink	*Implementation of SLIC-SABRE hyperpolarization of 1-13C pyruvate*
P102	Maria Anikeeva	*Implementing a Xenon polarizer for in vitro and in vivo imaging*
P103	Aaron Diercks	*Metabolic imaging with deuterated Glucose (and HP pyruvate) in a colitis model*

Non-invasive Mapping of Acidosis and Extracellular Lactosis for Assessing Tumor Invasion In Vivo.

Anaïs Choffart,[1,2*] Remy Chiaffarelli,[1,2] Max Zimmermann,[1,2] Laura Kuebler[1,2,3], André F. Martins[1,2,3]

[1]University Hospital of Tuebingen, Werner Siemens Imaging Center, Department of Preclinical Imaging, Tuebingen, Germany,
[2]University of Tuebingen, Cluster of Excellence iFIT (EXC 2180), Tuebingen, Germany,
[3]German Cancer Consortium (DKTK), partner site Tübingen, German Cancer Research Center (DKFZ), Heidelberg, Germany

*anais.choffart@uni-tuebingen.de

Synopsis: We demonstrate for the first time that combining shiftCEST and acidoCEST allows for non-invasive mapping of extracellular lactate and pH simultaneously, enabling accurate discrimination of tumor aggressiveness in vivo.

Introduction

Tumor cells typically display a hyperglycolytic metabolic phenotype characterized by increased lactate production, known as the Warburg effect. This shift in oxidative metabolism frequently leads to a more acidic microenvironment [1]. This adverse micro-environment represents a metabolic hallmark in invasive cancer cells. However, to date, no effective methods are available to evaluate cancer progression and metastatic potential in vivo. To bridge this gap, we have developed a molecular imaging technique (CEST-MRI) that can track extracellular pH (pHe; acidoCEST) and extracellular lactate levels (shiftCEST) simultaneously to discern different cancer phenotypes.

Methods

Two PyMT-derived murine breast cancer cell lines, a parental and a G6 metastatic, were selected for their distinct phenotypic aggressiveness and organ tropism. Cells were injected orthotopically in the 4th mammary fat pad of C57BL/6N mice. Hybrid shift/acidoCEST spectra were acquired on cells supernatant or tumor-bearing mice on a 7T preclinical MR scanner (Brucker Biospec 70/30) following the injection of the iopamidol+Shift Reagent (SR) solution. CEST acquisitions were performed using 3 or 14 µT and 6- or 5- second continuous saturation pulses for acidoCEST [2] or shiftCEST [3], respectively. The uptake of [^{13}C]lactate was assessed following the incubation of the cell lines with medium containing 3 mM of [1-^{13}C]lactate. Metabolites were extracted from the supernatant and analyzed using NMR.

Results

The *in vitro* characterization of the PyMT-derived cells demonstrated a pronounced invasion phenotype for the metastatic cell line that correlated with enhanced metabolic activity (Fig. 1A, B). We investigated whether this metabolic drift resulted in an increased extracellular lactate secretion or acidity. Simultaneous shift/acidoCEST performed on supernatants revealed an increased acidification with the metastatic cell line, despite a lower lactate secretion (Fig. 1C).

The same tendency was observed in the tumor-bearing mice, where metastatic tumors exhibited a negative correlation between tumor volume and pHe (Fig. 1D). In contrast, no correlation was observed for the parental non-metastatic tumors. Moreover, metastatic tumors exhibited reduced lactate levels compared to parental tumors.

Discussion

The reduced lactate level observed in the metastatic tumors despite a higher acidity are indicator of a potential altered metabolic adaptation. Metabolomics suggested a new capability of metastasis to uptake lactate from the tumor microenvironment, matching our preclinical results.

Conclusion

In conclusion, our study underlines the efficacy of shift/acidoCEST as a reliable method for non-invasive detection of extracellular acidity and lactate production in tandem by MRI. Our research highlights the adaptability of tumor metabolism, demonstrating its ability to repurpose waste products such as lactate to thrive in hostile environments and potentially facilitating invasion of surrounding tissues.

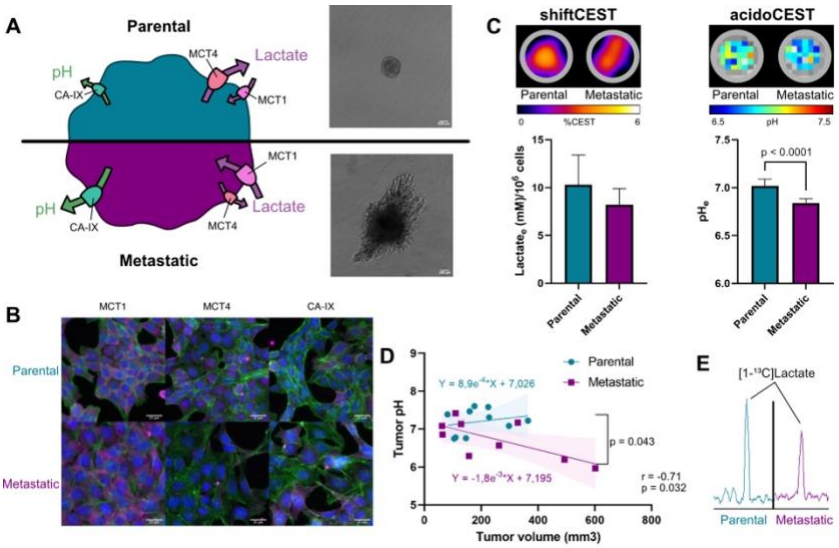

Figure 1: Hybrid CEST imaging for extracellular metabolic detection of tumor aggressiveness.
A) Left: Schematic representation of the altered metabolism in the two murine cell lines. Right: Microscopy images of the spheroid invasion assay on Day 5. B) Microscopy images of protein expression assessed by immunofluorescence. C) Left: CEST image at 47 ppm (top) and shiftCEST MRI quantification (bottom) of lactate produced by the cells over 48h. Right: Voxel representation (top) and acidoCEST MRI quantification (bottom) of the corresponding pH. D) Correlation plot comparing Tumor pHe and tumor volume. E) [13C] NMR spectra of cells' supernatant after 48h of incubation with [1-13C]lactate.

References

[1] Corbet C, Feron O. Tumour acidosis: from the passenger to the driver's seat. Nat Rev Cancer 2017;17:577–93. https://doi.org/10.1038/nrc.2017.77.

[2] Moon BF, Jones KM, Chen LQ, Liu P, Randtke EA, Howison CM, et al. A comparison of iopromide and iopamidol, two acidoCEST MRI contrast media that measure tumor extracellular pH. Contrast Media Mol Imaging 2015;10:446–55. https://doi.org/10.1002/cmmi.1647.

[3] Zhang L, Martins AF, Mai Y, Zhao P, Funk AM, Clavijo Jordan MV, et al. Imaging Extracellular Lactate In Vitro and In Vivo Using CEST MRI and a Paramagnetic Shift Reagent. Chemistry 2017;23:1752–6. https://doi.org/10.1002/chem.201604558.

T_1 alterations in nitrogen-15 hyperpolarized molecules

Josh P. Peters[1,*], Charbel D. Assaf[1], Arne Brahms[2], Kolja Them[1], Rainer Herges[2], Jan-Bernd Hövener[1], Andrey N. Pravdivtsev[1]

[1] University Medical Center Schleswig-Holstein, Kiel University, Department of Radiology and Neuroradiology, Section Biomedical Imaging, Molecular Imaging North Competence Center (MOIN CC), Am Botanischen Garten 14, 24118 Kiel

[2] Otto Diels Institute of Organic Chemistry, Otto-Hahn-Platz 4, 24098 Kiel, Germany

*josh.peters@rad.uni-kiel.de

Synopsis: This work aims to cumulate experimental data about the relaxation behavior of several ^{15}N tracers that have the potential to become novel hyperpolarization-enhanced molecular MRI tracers. We explored approaches to extend the hyperpolarization lifetime. This is especially relevant for molecules like nicotinamide that have relaxation times in the range of 1 s to over 60 s, depending on conditions. Suppose an effective way to reduce the effects of exchange and impurities of the hyperpolarization lifetime is found. This is expected to significantly enhance the retained signal at the measuring site, which is necessary for successful in vivo applications.

Introduction

The hyperpolarization of nuclear spins boosts the MR signal of selected molecules and has enabled real-time metabolic imaging in vivo (Ref. 1). Still, hyperpolarized MR has not become a gold standard for metabolomics so far - partially because of the method's complexity and the lack of a diversified portfolio of disease-specific tracers which can be efficiently polarized. Hyperpolarized nicotinamide (NAM) derivatives are promising imaging targets as they play a critical role in glycolysis and metabolism of fatty acids. NAM can, therefore, be used to assess the activity of several enzymes. We present our studies of ^{15}N hyperpolarization of tracers: NAM, pyridine, 1-methyl NAM, pyrimidine, metronidazole, and urea by dynamic nuclear polarization (dDNP).

It is known that inflammatory bowel diseases (IBD, a terrible threat to modern society) are associated with the deficit of tryptophan and other metabolites. We set out to use ^{15}N-nicotinamide, a metabolic product of tryptophan, as a hyperpolarized diagnostic marker of IBD. Therefore, it is essential to find an efficient method to hyperpolarize nicotinamide for in vivo imaging of the foreseen.

Methods

^{15}N signals were acquired in the polarizer or after dissolution using a 1 T benchtop NMR, a 9.4 T WB NMR, and a 7 T MRI. dDNP was performed using a cryogen-free dDNP system (SpinAligner, POLARIZE) operating at ~1.4 K and 6.7T. A microwave (MW) frequency between 187.07 and 187.19 GHz with 10 to 45 mW power was used for polarization.

About 50 mg samples with different compositions of the tracer with trityl radical (AH111501) in deionized water and trehalose. As a substrate, we used in-house synthesized 1-^{15}N-NAM according to (Ref. 2), ^{15}N-pyridine (48183, Sigma-Aldrich), metronidazole (MTZ, M1547, Sigma-Aldrich), $^{15}N_2$-urea (316830, Sigma-Aldrich), pyrimidine (131695, Sigma-Aldrich).

Results

To our surprise, although we were successfully polarizing nicotinamide in solid state using DNP, there was no remaining polarization at the time of the administration 16 seconds after dissolution at neutral pH. However, at basic pH a substantial part of the signal was retained (**Figure 1**). The reason for the polarization loss is rapid proton exchange with the pyridine nitrogen (Ref. 3) that accelerates relaxation at low fields. By changing pH we measured T_1 at high fields, which is also greatly pH dependent, changing from 6 to 45 s (**Figure 2**). At the region between 4 and 6, no signals were observed; an estimated T_1 is below 2.5 s at fields below 1 T. The only way to preserve it was to move to a basic pH incompatible with in vivo imaging (**Figure 1**).

Then we studied the behavior of other ^{15}N hyperpolarized substrates: urea, pyridine, metronidazole, and pyrimidine. The observed polarization of pyridine, and the N3 nitrogen of metronidazole is greatly affected by pH as their polarization is reduced or completely vanishes after sample transfer at neutral pH. The highest polarization values were reached using dissolution media with basic pH. Urea, NO_2-MTZ, and pyrimidine do not have such effects. One of the solutions to this issue is dissolution with basic pH and rapid pH neutralization at a high magnetic field above 1 T.

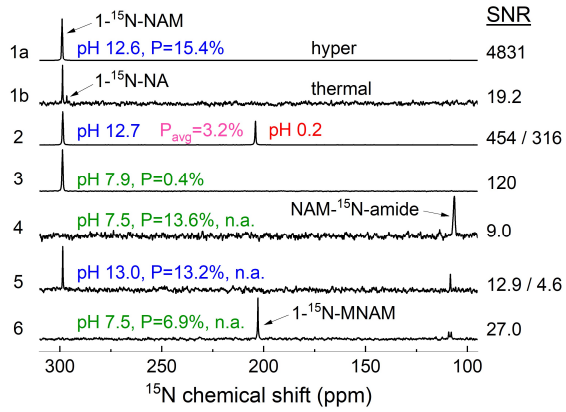

***Fig. 1**: pH dependent behavior of 1-^{15}N-nicotinamide, -nicotinic acid, and -methyl nicotinamide. One can see that when neutralizing pH after the transfer (3) only little signal is retained compared to basic pH (1). If D_2O instead of H_2O is used, a common method to prolong T_1 of hyperpolarization, no signal of the 1-^{15}N is retained. If naturally abundant methyl nicotidine is used, where the CH_3-group protects the 1-^{15}N, polarization is retained and the T_1 is over 200 s long.*

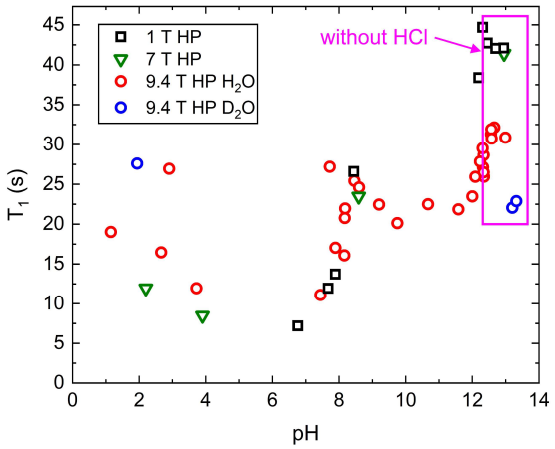

***Fig. 2**: This figure demonstrates the volatility of hyperpolarized 1-^{15}N-NAM T_1 values depending on pH. Basic pH (without HCl added) was used for imaging.*

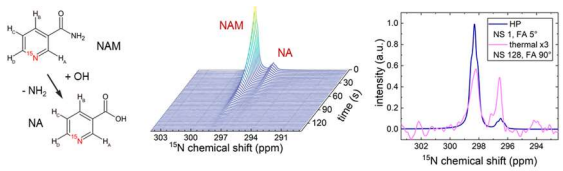

***Fig. 3**: Depending on pH unwanted effects may occur, such as spontaneous conversion of NAM to nicotinic acid, which might impair analysis or even harm the organism during an in vivo experiment.*

Discussion

The data presented in here and in Ref. 3 suggest that indeed relaxation and impurities are the main causes of the rapid relaxation of NAM and its derivates. However, measured relaxation of hyperpolarized 1-^{15}N- methyl nicotinamide (MNAM) of about 200 s is rather pH independent due to the protected 1-^{15}N. This suggests the theoretical maximum for the T_1 of NAM and derivates.

When the pH value is close to the pKa of the protonated pyridine nitrogen, chemical exchange is rapid and can destroy magnetization at low fields most efficiently. This effect on relaxation can be also used to study rapid proton interactions, which are not visible by conventional NMR.

Conclusion

Overall, the relaxation behavior of ^{15}N labeled dDNP tracers remains an issue, preventing many potential tracers from being used. Understanding the behavior aids the development of counterfeits and the future employment of such tracers in vitro and in vivo. Our data strongly suggests the interplay of exchange at the nitrogen site and impurities in the DNP juice that led to a drastic variation in observed polarization.

Acknowledgments

We acknowledge funding from the German Federal Ministry of Education and Research (BMBF) within the framework of the e:Med research, funding concept (01ZX1915C), DFG (PR 1868/3-1, PR 1868/5-1, HO-4602/2-2, HO-4602/3, EXC2167, FOR5042, TRR287), and support by the hyperquant consortium, 03WIR6208A, BlueHealthTech, BMBF. MOIN CC was founded by a grant from the European Regional Development Fund (ERDF) and the Zukunftsprogramm Wirtschaft of Schleswig-Holstein (Project no. 122-09-053).

References

1. Nelson SJ, Kurhanewicz J, Vigneron DB, et al. Metabolic Imaging of Patients with Prostate Cancer Using Hyperpolarized [1-13C]Pyruvate. Sci Transl Med. 2013;5(198):198ra108.
2. Shchepin RV, Barskiy DA, Mikhaylov DM, Chekmenev EY. Efficient Synthesis of Nicotinamide-1-15N for Ultrafast NMR Hyperpolarization Using Parahydrogen. Bioconjugate Chem. 2016;27(4):878-882.
3. Peters JP, Brahms A, Janicaud V, et al. Nitrogen-15 dynamic nuclear polarization of nicotinamide derivatives in biocompatible solutions. Science Advances. 2023;9(34):eadd3643.

Phase-based 3D pH imaging in vivo using hyperpolarized [1,5-$^{13}C_2$]Z-OMPD

Andre Wendlinger[1], Jakob Gaubatz [1*], Martin Grashei[1], Ann-Marie Wintergerst[1] and Franz Schilling[1]

[1] Department of Nuclear Medicine, Klinikum rechts der Isar, Technical University of Munich, Germany.

* jakob.gaubatz@tum.de

Synopsis: A novel approach to measure pH using hyperpolarized ^{13}C MRI with [1,5-$^{13}C_2$]Z-OMPD and phase-based imaging has been tested on healthy rat kidneys. 3D pH maps were acquired in under 7 s at different time points of the renal filtration process, showing the physiological acidification through filtration. A potential improvement of the method was discovered in simulations that suggest non-linear modeling of the acquired signal phase to resolve the pH compartments of the kidneys.

Introduction

The non-invasive measurement of extracellular pH in vivo enables new diagnostic capabilities in oncology and nephrology. Deviations from the normal pH range can serve as an indicator of kidney disease or the acidic environment of a tumor. Current limitations of MRI-based methods for pH measurement in vivo are long imaging times (1) or the restriction to 2D imaging (2). A novel approach using hyperpolarized ^{13}C MRI of [1,5-$^{13}C_2$]Z-OMPD (2) and phase-based imaging has been demonstrated by our group (3), providing fast and accurate 3D pH imaging in vitro. In this work, the capability of this method to measure pH in vivo was tested on healthy rat kidneys.

Methods

3D pH imaging was performed on a total of eight Wistar rats that were anesthetized with isoflurane and continuously monitored. For each measurement, 31 mg of Z-OMPD was polarized using a HyperSense DNP Polarizer and dissolved in 2.5 ml D_2O containing 80 mmol/L TRIS. The injections were made via a tail vein catheter. All measurements were conducted on a 7 T preclinical scanner (Agilent MR901 with Bruker Avance III electronics) using a 72 mm dual-tuned ^{1}H / ^{13}C volume resonator for signal transmission and a 30 mm single channel flexible surface coil (Rapid Biomedical). A multi-gradient echo sequence with varying echo spacings was used to allow unwrapping of phase images at high magnetic field strength according to the UMPIRE algorithm (4). To suppress the weakly pH-sensitive C1-peak, high flip-angle, narrow bandwidth excitation followed by gradient spoiling was applied twice before each excitation. The sequence parameters were: spatial resolution = 3.0 x 3.0 x 3.0 mm^3 (except for two scans with 1.5 x 1.5 x 3.0 mm^3), FA = 8°, excitation BW of 10 kHz, acquisition BW of 100 kHz, δT_E = 0.5 ms, ΔT_E = 0.928 ms, 9 monopolar echoes, T_R = 29 ms and a total acquisition time of 6.96 s. The delay between the end of injection and start of imaging was varied between 3, 9, and 15 s to observe different Z-OMPD distributions within the renal compartments. In post-processing, the signal phase in each voxel was unwrapped using the UMPIRE phase-unwrapping algorithm, and a voxel-wise linear regression was applied to determine the signal frequency. The calculated, pH-dependent, frequency offset was corrected for B_0-field inhomogeneities, subtracted by an empirical global offset of 50 Hz, and converted to pH using a prerecorded calibration curve for Z-OMPD. Voxels below an SNR threshold of 10 were masked.

Results

All scans exhibited sufficient renal perfusion of Z-OMPD. Exemplary scans can be seen in Fig. 1A-C with varying delays between the end of injection and sequence start. Homogeneous pH values were measured covering the majority of the kidney region. A trend towards more acidic pH values at later time points is observed, as well as a shift in signal intensity towards the kidney center (Fig. 1C) and a disappearance of the signal in the main blood vessel (Fig. 1B, C). The observation that the majority of Z-OMPD is in the main blood vessel at very early time points (3 s) is consistent with the findings of (2), who showed that a peak in renal perfusion occurs at approximately 11 s post-injection. A linear regression analysis of the mean pH values of all kidney slices plotted against the sequence delay times (Fig. 1D) supports the observation of a trend towards acidic values over time, although a moderate correlation and statistical insignificance ($r=-0.52$, $p=0.23$) must be acknowledged, due to the limited number of early and late time points and two outliers at 9s.

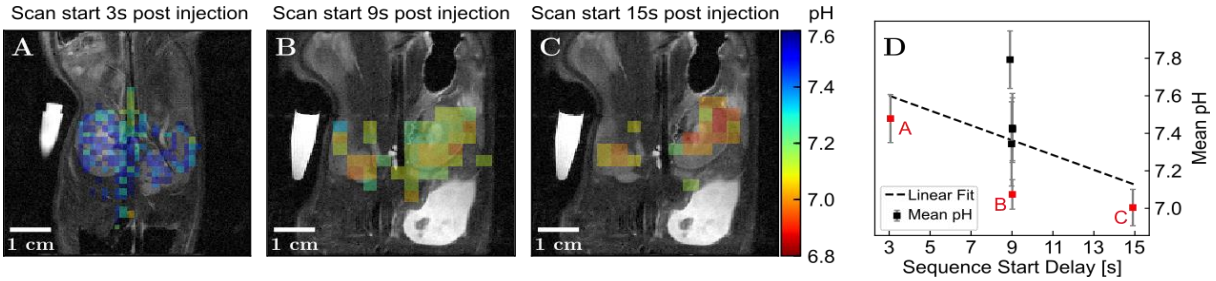

Fig. 1: (A-C) Exemplary pH maps of three different scans started 3 s (A), 9 s (B), and 15 s (C) post-injection, overlaid over corresponding anatomical proton images. (D) Mean pH values of the entire rat kidneys, measured at different time points post-injection. The error bars represent the standard error.

Discussion

Although the measured pH values lie in the physiological range of the kidneys (6.4 - 7.4) and the trend towards more acidic values for later time points can be explained by the renal filtration process, the presented findings do not match the expectations based on earlier works (1,2). Grashei et al. (2) spectroscopically observed a pH compartmentalization within the kidneys, corresponding to the physiological pH of the kidney cortex, medulla, and calyx. Assuming the acquisition of a compartment-weighted pH image, a gradient towards the renal center should be observable. Instead, relatively homogeneous pH values and no spatial pH gradient were measured.

A possible explanation for this contradiction lies in the kidney anatomy. The structures involved in the filtration process are not strictly located in specific areas of the kidney but span over multiple areas. The expected pH gradient results from a larger fraction of acidic structures towards the kidney center. With the employed voxel sizes of 1.5 or 3.0 mm^3 more than one pH compartment is likely present in one voxel, leading to a non-linear phase evolution of the signal and an erroneous frequency offset estimation, caused by an incorrect linear fit. Simulated measurements with two pH-dependent signal peaks, considering different pH-compartments, reveal an increased non-linearity of the combined signal phase for an increased pH-dependent shift of one peak, which leads to false predictions of the mean pH using the here applied method (Fig. 2).

Conclusion

The proposed method allowed rapid 3D pH imaging in under 7 s. Although previous observations of a pH gradient towards the kidney center were not measurable, a potential solution was discovered in follow-up simulations. Due to the complex multi-pH-compartment physiology of the kidneys, a linear signal phase evolution cannot be assumed. Therefore, a non-linear modeling of the signal phase will be employed in the future, to build on the promising results of the in vitro study.

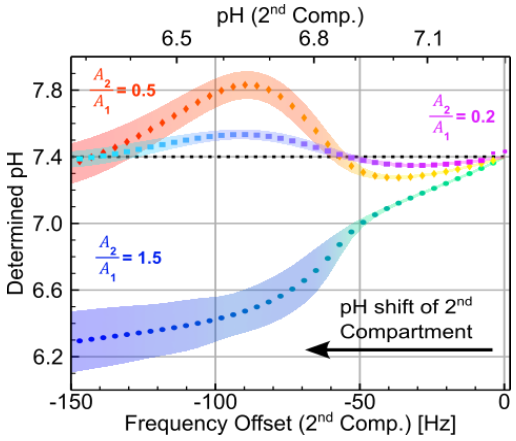

Fig. 2: pH values calculated in a simulated voxel with one steady (at 0 Hz/pH = 7.4) and one shifting pH compartment. Three different amplitude ratios A_2/A_1 of the two signal peaks were used (colors). The envelopes show the uncertainty of the linear fits of the signal phase.

References

1. Villano D, Romdhane F, Irrera P, Consolino L, Anemone A, Zaiss M, Dastrù W, Longo DL. A fast multislice sequence for 3D MRI-CEST pH imaging. Magn Reson Med. 2021;85(3):1335-1349.

2. Grashei M, Wodtke P, Skinner JG, Sühnel S, Setzer N, Metzler T, Gulde S, Park M, Witt D, Mohr H, Hundshammer C, Strittmatter N, Pellegata NS, Steiger K, Schilling F. Simultaneous magnetic resonance imaging of pH, perfusion and renal filtration using hyperpolarized (13)C-labelled Z-OMPD. Nat Commun 2023;14(1):5060.

3. Wendlinger A, Grashei M, Wintergerst AM, Schilling F. Fast 3D pH imaging in vitro using hyperpolarized [1,5-$_{13}$C^2]Z-OMPD. MoBi 2023: 6th GyMIC Molecular Imaging Symposium Tübingen;

4. Robinson S, Schödl H, Trattnig S. A method for unwrapping highly wrapped multi-echo phase images at very high field: UMPIRE. Magn Reson Med. 2014;72(1):80-92.

Magnetic resonance in the zero and ultralow field regime – a transition from one-dimensional oscillation to precession

F. Bullinger[1], N. Kempf[1], P. Povolni[1], R. Neumann[1], J. Engelmann[1], J. Romanowski[1], A. Pravdivtsev[2], R. Körber[3], M. Plaumann[4], K. Scheffler[1,5] and K. Buckenmaier[1*]

[1] High-Field Magnetic Resonance Center, Max Planck Institute for Biological Cybernetics, Max-Planck-Ring 11, 72076 Tübingen, Germany

[2] Section Biomedical Imaging, Molecular Imaging North Competence Center (MOIN CC), Department of Radiology and Neuroradiology, University Medical Center Schleswig-Holstein and Kiel University, Am Botanischen Garten 14, 24118 Kiel, Germany

[3] Physikalisch-Technische Bundesanstalt (PTB), Abbestraße 2–12, 10587 Berlin, Germany

[4] Institute for Molecular Biology and Medicinal Chemistry, Medical Faculty, Otto-von-Guericke University Magdeburg, Leipziger Str. 44, 39120 Magdeburg, Germany

[5] Department of Biomedical Magnetic Resonance, Eberhard-Karls University, Hoppe-Seyler-Straße 3, 72076 Tübingen, Germany

* Contact communicating author

Synopsis: The transition between zero and low field spectra was theoretically predicted and measured. One-dimensional spin oscillations are observed in the zero field, while Larmor precession occurs in the presence of a magnetic field. The detector direction is essential for signal maximization in the zero field.

Introduction

Ultralow field (ULF) nuclear magnetic resonance spectroscopy (MRS) and magnetic resonance imaging (MRI) are promising spectroscopy and imaging methods[1], e.g., for simultaneous detection of multiple nuclei or imaging in the vicinity of metals. To overcome the inherently low signal-to-noise ratio that usually hinders a wider application, we present an alternative approach to prepolarized ULF MRS using hyperpolarization techniques such as signal amplification by reversible exchange (SABRE)[2]. SABRE allows continuous hyperpolarization of ^{1}H and other MR-active nuclei. For the implementation, a superconducting quantum interference device (SQUID)-based ULF MRS/MRI detection scheme was constructed (Fig. 1)[3]. The broadband characteristic of SQUIDs allows the simultaneous acquisition of the MR signals of different nuclei such as ^{1}H, ^{13}C or ^{15}N. Since SQUIDs directly detect the MR signal, they are an ideal tool for the quantitative investigation of hyperpolarization techniques such as SABRE[4].

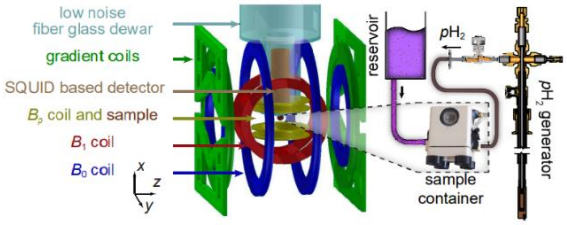

Fig. 1: Schematic diagram of the ULF MR system. Freshly produced parahydrogen (pH_2) is supplied to the sample container inside a magnetic shield.

Methods

Parahydrogen based hyperpolarization techniques can easily reach polarization levels above 1 % using field cycling methods. The magnetic field pattern for the SABRE sequence is shown in Fig. 2. The magnetic fields B_{hyp} and B_{low} need to be in the 100 nT range for maximum spin order transfer.

[1] Inglis et al., "MRI of the Human Brain at 130 Microtesla."

[2] Schmidt et al., "Catalyst-Free Aqueous Hyperpolarized [1- ^{13} C] Pyruvate Obtained by Re-Dissolution Signal Amplification by Reversible Exchange."

[3] Buckenmaier et al., "Mutual Benefit Achieved by Combining Ultralow-Field Magnetic Resonance and Hyperpolarizing Techniques."

[4] Buckenmaier et al., "SQUID-Based Detection of Ultra-Low-Field Multinuclear NMR of Substances Hyperpolarized Using Signal Amplification by Reversible Exchange."

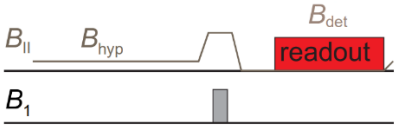

Fig. 2: Field cycling hyperpolarization sequence

Results

The home-built SQUID system allowed us to measure ^{1}H and ^{13}C hyperpolarized signals of [1-^{13}C] pyruvate in magnetic fields from 0 to 100 µT, covering frequencies from DC to about 5 kHz. For this range, the sensitivity was sufficient to track the spin system with an exclusive spectral resolution below 100 mHz. We demonstrated the significance of the orientation of the detector with respect to the directions of the residual magnetic field and the magnetization (Fig. 3-5). At zero field, there is no spin precession but there is still spin evolution (if the system is polarized). If the sensor is aligned along the polarization axis (in our case the x-axis), one can observe magnetization oscillations with the J-coupling frequency. Due to spin precession at high fields, the detector orientation is of less importance, provided the sensor is positioned orthogonal to the external magnetic field B_0 (in our case the z-axis).

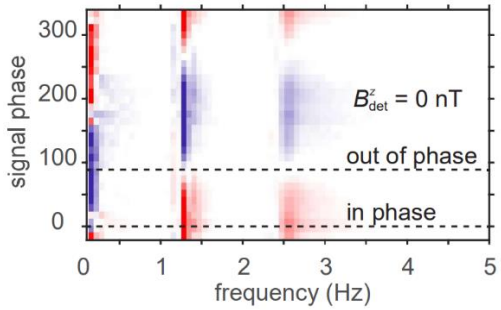

Fig. 3: Measured zero field spectra as a function of signal phase.

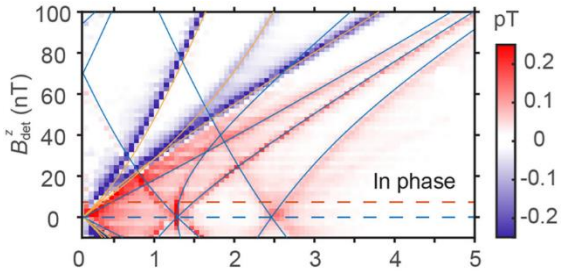

Fig. 4: Measured in phase spectra as a function of the detection field B_{det}. The solid lines indicate the simulated position of resonances. Dashed lines indicate the position of the spectra in Fig. 6.

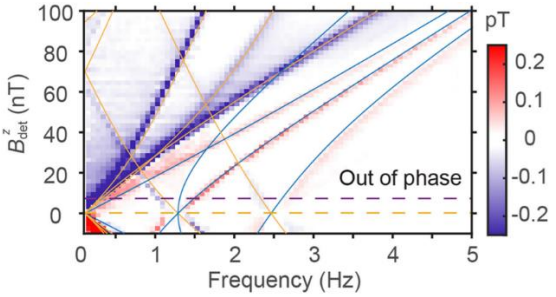

Fig. 5: Measured out of phase spectra as a function of the detection field B_{det}.

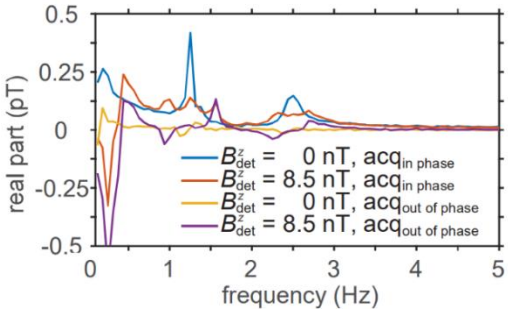

Fig. 6: Measured selected in phase and out of phase spectra.

Summary and Discussion

The NMR spectra for [1-^{13}C] pyruvate in the transition from the magnetic zero field to the high field could be predicted. It could be described theoretically and shown experimentally that spin transitions oscillate in only one direction in zero magnetic field. The transition from one-dimensional oscillation to precession of the spins in the high field was observed.

The results can be used in zero-field spectroscopy. It is of great importance to excite the transitions parallel to the detector direction in order to maximize the recorded signal.

For future studies, it is possible to infer the time evolution of spins in zero magnetic field, although the data acquisition takes place in non-zero magnetic fields. One example of this would be a COSY (correlation spectroscopy) sequence in which the magnetic field is reduced between the two RF pulses (ZF COSY, Zero Field COSY). This avoids the problem that the data acquisition in the zero field must be aligned parallel to the direction of oscillation.

^{13}C imaging of pyruvate with SABRE at Ultra-Low field

Nicolas Kempf[1*], Rainer Körber[2], Markus Plaumann[3], Andrey N. Pravdivtsev[4], Jörn Engelmann[1], Johannes Boldt[1], Klaus Scheffler[1,5], Thomas Theis[1,6] and Kai Buckenmaier[1]

[1]High-Field Magnetic Resonance Center, Max Planck Institute for Biological Cybernetics, 72076 Tübingen, Germany.
[2]Physikalisch-Technische Bundesanstalt, 10587 Berlin, Germany.
[3]Institute for Molecular Biology and Medicinal Chemistry, Medical Faculty, Otto-von-Guericke University, 39120 Magdeburg, Germany.
[4]Section Biomedical Imaging, Molecular Imaging North Competence Center (MOIN CC), Department of Radiology and Neuroradiology, University Medical Center, Kiel University, 24118 Kiel, Germany.
[5]Departement of Biomedical Magnetic Resonance, Eberhard-Karls University, 72076 Tübingen, Germany.
[6]Departement of Chemistry and Physics, NC State University, Raleigh 27695, USA.

* nicolas.kempf@tuebingen.mpg.de

Synopsis: The ultra-low magnetic field regime opens up new opportunities for magnetic resonance through parahydrogen-based hyperpolarization. Our *in situ* combination of Signal Amplification by Reversible Exchange (SABRE) with a Superconducting Quantum Interference Device (SQUID) embodies a highly versatile MRI system. Recent results demonstrate 3-dimensional ^{13}C imaging of [1-^{13}C] pyruvate in a phantom at twice the Earth's magnetic field with sub-millimeter resolution. The results pave the way for *in vivo* ULF imaging with SABRE.

Introduction

In recent years, ultralow-field magnetic resonance imaging (ULF MRI) has come close to clinical applications, due to improvements in computer-aided data processing, enhancing image quality(1), and novel, task-specific systems using e.g. superconducting quantum interference devices (SQUIDs) as magnetic field detectors. ULF MRI offers the possibility of low-cost, lightweight imaging, in addition to providing differing tissue contrast than high-field MRI.(2) The ULF regime applies up to ~10 mT, which is the optimal field regime for various hyperpolarization techniques, such as Overhauser dynamic nuclear polarization (ODNP) and signal amplification by reversible exchange (SABRE).

Methods

In this work, we aimed to enhance the image quality of ULF MRI with the parahydrogen and non-hydrogenative based SABRE technique(3), which repeatably transfers the spin order of parahydrogen to a substrate via an e.g. iridium-based catalyst. To this aim, we have optimized the spin order transfer from parahydrogen to the substrate via field cycling methods and different RF pulse sequences for the hyperpolarization of a bolus. In particular, we have focused on the polarization of [1-^{13}C]pyruvate in methanol.

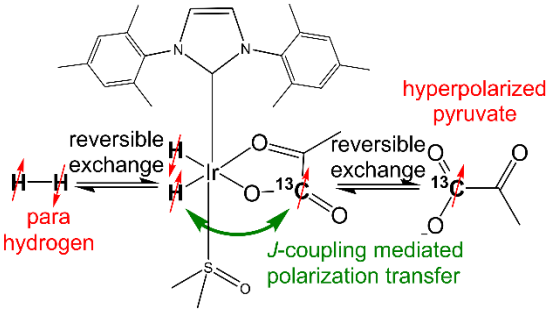

Fig. 1: Schematic of the SABRE process that yields hyperpolarization of the [1-^{13}C]pyruvate via *J*-coupling interactions in appropriate alternating (AC) or constant (DC) magnetic fields.

Results

Comparable ^{13}C polarization to SABRE in shield enables alignment transfer to heteronuclei (SABRE-SHEATH) with magnetic field cycling has been achieved with low-irradiation generation of high tesla (LIGHT)-SABRE in a constant magnetic field.(4) LIGHT-SABRE uses a continuous-wave spin-locking pulse with amplitudes as low as 1 µT at a frequency of 1270 Hz, during the hyperpolarization period. As aforementioned, this scheme does not require any magnetic field cycling. This spin-locking pulse mimics the SABRE-SHEATH condition, enabling a strong coupling between the hydrogen and the ^{13}C nuclei, within the Iridium complex.

With these hyperpolarization techniques, we have been able to obtain enough signal to perform the first hyperpolarized ^{13}C ULF MRI

experiments, using SABRE-hyperpolarized [1-^{13}C]pyruvate at 120 µT with millimolar concentrations and sub-millimeter voxel size.(5)

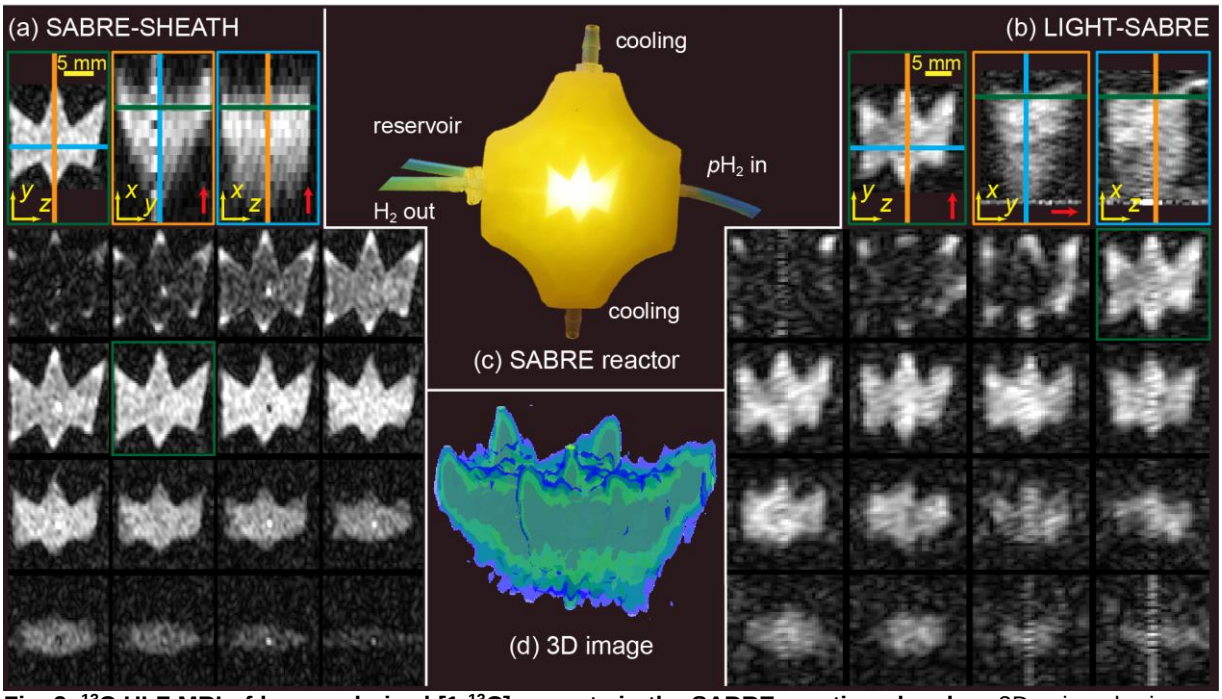

Fig. 2: **^{13}C ULF MRI of hyperpolarized [1-^{13}C]pyruvate in the SABRE reaction chamber.** 3D spin-echo image of [1-^{13}C]pyruvate polarized with SABRE-SHEATH (a) or LIGHT-SABRE (b) HP sequence. Red arrows indicate the frequency encoding direction. Photograph of 3D printed SABRE reaction chamber, illuminated from underneath (c). 3D multi-isosurfaces image acquired with SABRE-SHEATH (d).

Conclusion

In summary, SABRE offers a cost-effective, highly scalable alternative to other hyperpolarization methods, that significantly benefits ULF MRI with trillion-fold time savings compared to using thermal polarization at these low fields. SABRE hyperpolarized ULF MRI may provide a viable alternative to high-field MRI, opening up a new magnetic field regime, with far fewer implant limitations.

Remaining challenges, such as bolus biocompatibility and short acquisition time, are currently being addressed in the community. We are working on multiple spin echo sequences, like Turbo Spin Echo (TSE) or balanced Steady State Free Precession (bSSFP) sequences, to reduce the overall acquisition time from currently ≈ 4 hours by an order of magnitude. This will enable fast, steady-state *in vivo* imaging sequences that may open the possibility of real-time tracking of a hyperpolarized bolus at ULF.

References

1. Inglis B, Buckenmaier K, SanGiorgio P, Pedersen AF, Nichols MA, Clarke J. MRI of the human brain at 130 microtesla. Proceedings of the National Academy of Sciences 2013;110:19194–19201 doi: 10.1073/pnas.1319334110.

2. Busch S, Hatridge M, Mößle M, et al. Measurements of T1-relaxation in ex vivo prostate tissue at 132 µT. Magnetic Resonance in Medicine 2012;67:1138–1145 doi: 10.1002/mrm.24177.

3. Buckenmaier K, Rudolph M, Fehling P, et al. Mutual benefit achieved by combining ultralow-field magnetic resonance and hyperpolarizing techniques. Review of Scientific Instruments 2018;89:125103 doi: 10.1063/1.5043369.

4. Pravdivtsev AN, Buckenmaier K, Kempf N, et al. LIGHT-SABRE Hyperpolarizes 1-13C-Pyruvate Continuously without Magnetic Field Cycling. J. Phys. Chem. C 2023;127:6744–6753 doi: 10.1021/acs.jpcc.3c01128.

5. Kempf N, Körber R, Plaumann M, et al. 13C MRI of hyperpolarized pyruvate at 120 µT. Sci Rep 2024;14:4468 doi: 10.1038/s41598-024-54770-x.

Implementation of SLIC-SABRE hyperpolarization of 1-13C pyruvate

Martin Sandbrink[1], Philip Saul[1], Casper Sax[1], Josh Peters[1], Charbel Assaf[1], Jule Kuhn[1], Ella Dieball[1], Yenal Gökpek[1], Harriet Wulff[1,2], Andreas B. Schmidt[3], Stefan Petersen[3], Andrey N. Pravdivtsev[1], Jan-Bernd Hövener[1]

[1] University Medical Center Schleswig-Holstein, Kiel University, Department of Radiology and Neuroradiology, Section Biomedical Imaging, Molecular Imaging North Competence Center (MOIN CC), Am Botanischen Garten 14, 24118 Kiel.
[2] Department of Physics, University College Cork, T12 CY82 Cork, Ireland.
[3]Department of Radiology, Medical Physics, Medical Center—University of Freiburg, Faculty of Medicine, University of Freiburg, Breisacherstrasse 60a, Freiburg 79106, Germany

* martin.sandbrink@rad.uni-kiel.de

Synopsis: We present an approach to a hardware design for hyperpolarization using SLIC-SABRE. We varied several parameter: the main magnetic field B_0, amplitude of the radio frequency magnetic field B_1. and temperature to find optimal conditions. We obtained 2.5% ^{13}C polarization of [1-^{13}C]pyruvate.

Introduction

Although widely used in medical diagnostics, magnetic resonance imaging (MRI) struggles to image metabolism with great sensitivity. Here, the hyperpolarization (HP) of nuclear spins in selected contrast agents boosting the signal by several orders of magnitude. Hyperpolarized MRI (HMI) allows for the observation of metabolism in real time e.g., for the early detection of cancer or monitoring therapy response.

All clinical studies, to date, were performed with dynamic nuclear polarization, a quite versatile, but complex and expensive technology. Only recently, [1-^{13}C]pyruvate-d_3 was polarized to over 20 % by using a signal amplification by reversible exchange (SABRE, Fig. 1) and and spin-lock induced level anti crossings (SLIC) spin order transfer.[1] Following this work, we present our approach to implementing this technique.

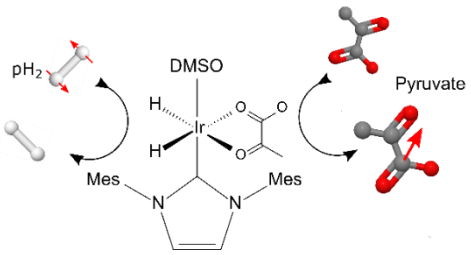

Fig. 1: Illustration of SABRE polarization of pyruvate, where parahydrogen (pH$_2$) and pyruvate reversibly bind to an Iridium center to allow for transfer of polarization.

Methods

The SLIC-SABRE experiments were implemented using a polarizer consisting of a process control unit (PCU), a fluid control unit (FCU) and an NMR unit (NU, Fig 2). The PCU was used to control the timing of the experiments and to generate the spin order transfer sequence (2 min 29 mV SLIC pulse + 2 s 58 mV adiabatic pulse) using a custom software and commercial hardware (Matlab, National Instruments). The FCU allowed to supply 8 bar pH_2 to a custom-made reaction chamber based on a 5 mm high-pressure NMR tube cooled to a set temperature of 7 °C. The NU consisted of a 4-layer µ-metal shield (Twinleaf, MS-2), a two-layer solenoid B_0 coil (360 mm length, 120 mm diameter), a power supply (Twinleaf, CSBA-30), a six-layer saddle shape B_1 coil (100 mm diameter), and an RF amplifier (onkyo, TX8555). Ca. 90 % pH_2 was generated using a custom-made generator.

After cooling the sample to the desired temperature, pH_2 was supplied at the set pressure and flow while the SOT was applied. After the adiabatic pulse, the pressure was released and the tube was transferred to a benchtop NMR system, where a ^{13}C spectrum was acquired (Spinsolve 60, Magritek).

All experiments were conducted using 500 µL of a methanol-d_3 sample solution containing sodium pyruvate-1-^{13}C (50.39 mM), [Ir(COD)(IMes)Cl] (5.84 mM), dimethylsulfoxide (DMSO) (39.74 mM) and Na_2-EDTA (1.10 mM).

Results

The setup was successfully assembled and yielded strongly enhanced ^{13}C signal. We observed high ^{13}C polarization of up to 2.5 % in

a 50 mM solution (Fig. 3). An average polarization of (2.3 ± 0.01) % was observed in three experiments on day 1, and (2.0 ± 0.3) % in 8 experiments on day 2 (Fig. 4).

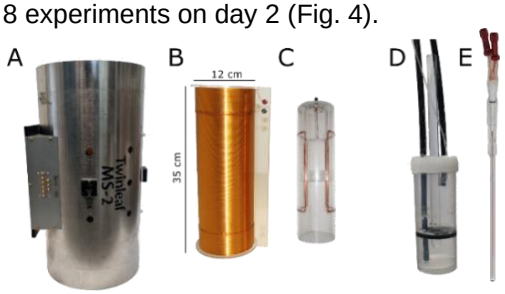

Fig. 2: Setup used for the experiment: (A) µ-metal shield (Twinleaf MS-2), (B) In-house built B_0-coil, (C) In-house built B_1-coil, (D) water bath for temperature control, (E) high-pressure NMR-tube with capillaries for bubbling parahydrogen.

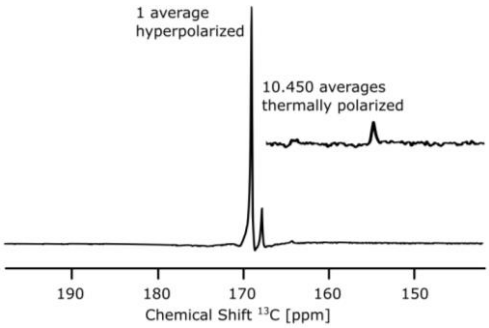

Fig. 3: ^{13}C-NMR spectra of 50 mM hyperpolarized pyruvate and 100 mM thermally polarized pyruvate (10.450 averages). By comparing the signals, the polarization was quantified to 2.5 %.

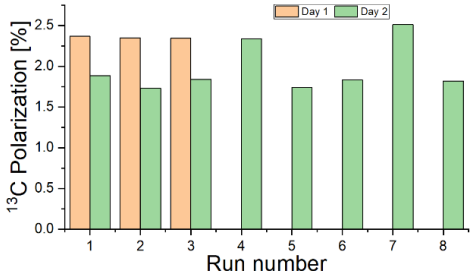

Fig. 4: ^{13}C polarization of [1-^{13}C]pyruvate acquired on two different days with identical experimental settings. The average was (2.3 ± 0.01) % on day one, and (2.0 ± 0.3) % on day 2.

We conducted the experiment with different settings for the static magnetic field and observed a bell-like distribution of the polarization, which is in good agreement with the theory (Fig. 5)[2].

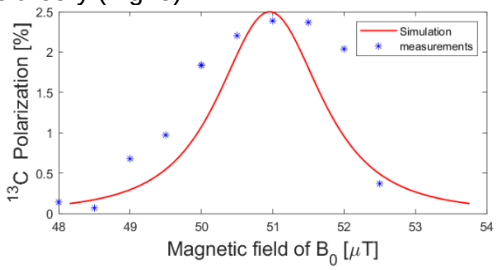

Fig. 5: Polarization of [1-^{13}C]pyruvate as a function of B_0 magnetic field applied during the polarization.

Variation of the B_1 field yielded a more constant polarization, which was not expected (Fig. 6).

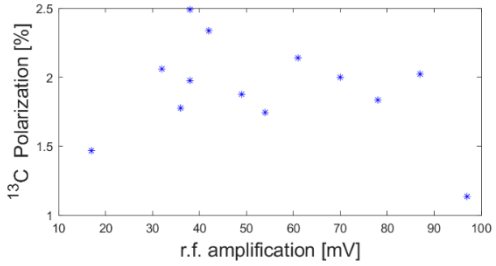

Fig. 6: Polarization of [1-^{13}C]pyruvate as function of voltage of the SLIC pulse.

Discussion

The setup enables fast and reproducible polarization of 50 mM [1-^{13}C]pyruvate, although about 4 times lower as reported in literature (8 % for protio-pyuvate).[1] The polarization may be increased by lowering the concentration of pyruvate and improving SLIC and adiabatic pulses, or using deuterated pyruvate.

Variation of B_0 yielded the expected results, indicating the observation of a SLIC effect. The variation of B_1 showed to be more constant than expected, which is not yet fully understood, possibly indicating poor field homogeneity or magnetic field stability.

In the future, an automated sample transfer to the spectrometer would not only make the experiment more reproduceable but also allow for a better understanding of the underlying mechanisms of HP as well as the effect of the respective fields. Furthermore, for applicability in actual medical imaging there's a need for a purification step to eliminate the solvent and residual catalyst.

Conclusion

The semi-automated setup for the hyperpolarization of 50 mM [1-^{13}C]pyruvate provided robustly about 2 % polarization in 5 min – less than reported in literature, but a good starting point for further optimization.

References

1. de Maissin H et al. *Angew Chem*. 2023. 10.1002/ange.202306654

2. Pravdivtsev AN et al. *J Phys Chem C*. 2023. 10.1021/acs.jpcc.3c01128

Implementing a Xenon polarizer for in vitro and in vivo imaging

M. Anikeeva M.,[1*] F. Anum,[1] B. Kavitha-Rajendran[1], A. N. Pravdivtsev[1]and Hövener J-B[1]

[1] Section Biomedical Imaging, Molecular Imaging North Competence Center, Department. Radiology and Neuroradiology, University Hospital Schleswig-Holstein (UKSH), Campus Kiel, Kiel University, Kiel, Germany
* maria.anikeeva@rad.uni-kiel.de

Synopsis: Magnetic resonance imaging (MRI) with hyperpolarized Xenon is a versatile tool for many applications. Establishing imaging protocols with Xenon is complex, requiring components such as a xenon polarizer, gas mixture, quality control measures, MRI xenon options, specialized coils, specific sequences, and regulatory approval. Here, we discuss our current progress in implementation of these steps, and challenges, e.g. in reproducibility and system maintenance. Our future work will address these challenges, focusing on Xenon quantification, sequence optimization, and regulatory compliance.

Introduction

Magnetic resonance imaging (MRI) with hyperpolarized xenon is a quite versatile tool with applications ranging from material science for investigating nanostructures[1] and analysing gas flow to the imaging of lungs in both animals and humans[2]. Setting up a xenon imaging program, however, is a complex procedure, as a “complete package” is not readily available or quite expensive. We identified the following essential steps: (1) xenon polarizer, (2) Xenon gas (mixture), (3) quality control of Xenon gas (polarization, purity, gas sterility e.g.), (4) Xenon option on the MRI, (5) Xenon coils, (6) Xenon sequences, (7) regulatory approval for human use. In this contribution, we describe the essential steps of this procedure, how we addressed them and which challenges we encountered.

Methods

We analyzed the literature and discussed the matter with several companies and researchers active in the field.

Results and Discussion.

1. Xenon polarizer: several commercial options or own developments exist (e.g. Xeus, Polarean, Polaris, 10^5 - 10^6 €). We decided for a polarizer equipped with a 3.5 l cell and a 180 W, 794.77 nm array diode laser which was successfully setup in 2021 (Polaris, Sheffield, UK). With respect to maintenance, we expect that we will have to replace the laser as well as the cell in given time.
Precautions have to be taken to operate a powerful laser, trained personnel and safety is required. The heat produced by the system (oven comprising the SEOP cell needs to be heated up to 125°C) proved to be an issue for the room, whose temperature rose quickly beyond 30 °C. Here, discharging the heated air to the exhaust of the room and a smarter heating scheme may improve the matter.

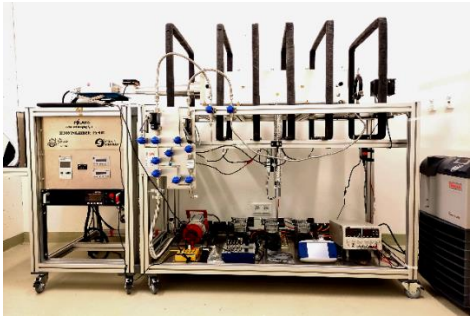

Fig. 1: Xenon SEOP polarizer installed in the University Clinic Schleswig-Holstein.

2. Xenon gas: The NMR active isotope is Xe-129, which has a natural abundance of 26 %; enrichment up to 86 % is commercially available (e.g. Linde, Air Liquide, Merck). For polarization, a mix of varying amounts of Xe, N_2 and He is used, which is available commercially or has to be produced using a dedicated mixing setup, which will be described elsewhere.

3. Quality control: the polarization, the purity and sterility of the gas have to be assessed. **The polarization** is monitored during the built-up process at 3 mT using a small detection coil placed on top of the SEOP cell. Absolute quantification, however, is difficult, as no thermally polarized reference is available. Here, we aim at using our low-field NMR unit to detect 1H signal of the liquid sample, which can be placed in the detection coil and withstand high temperatures, and that can be used for in situ polarization quantification. The polarization

after the gas extraction can be quantified in an MR system. Here, we tested transfer to a 9.4 T NMR at 3 km distance, a 1.5 T benchtop NMR 100 m distance and a 3 T MRI 50 m distant. Using a holding field (Fig. 2 (a)) improved the polarization significantly, but no reproducible results were achieved yet. Because of the elevated temperature, the benchtop NMR could not yet be setup inside the polarizer room. **Impurities:** We plan to have the gas analysed by a commercial service especially for residues of Rubidium. **Sterility** will be access using the common clinical tests.

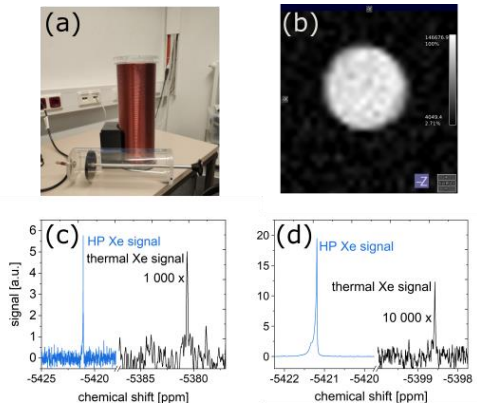

Fig. 2: Delivery setup for HP xenon: (a) Solenoid coil (a) used for the delivery of the syringe (front) or of the Tedlar bag. (b) FLASH MR imaging of the Xe gas inside the 35-mL glass container acquired 23 min after the polarization delivered with the delivery coil using a hand-made saddle Xe coil. Hyperpolarized (blue) and thermal (black) signals of 129Xe measured for the samples delivered without (c) and with the coil (d) at 9.4 T NMR.

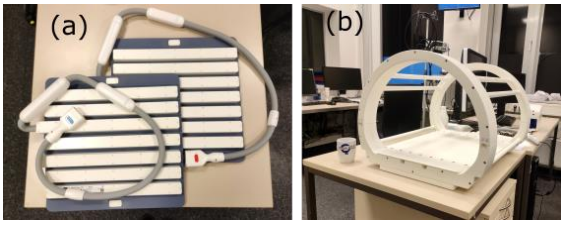

Fig. 3: Receive (a) and Transmit Receive coils (b) available for Xenon MR imaging at 3T.

4. Multi-nuclei options are commercially available by the major vendors at a few 100 k€.

5. Xenon coils are available as a medical product from different sources (10^3 – 10^5 €). Here, we chose a relatively large, four legged ^{129}Xe transmit-receive coil suitable for a human torso or large in vitro setups which can be combined with a ^{1}H ^{129}Xe dual tune multi-channel receive array (Rapid Biomedical). We acquired first signals with the coil, but cannot comment on the efficiency yet. The large volume and the limited r.f. power of the broad band amplifier may pose a problem, as 180° pulses were reported to be as long as 4 ms (limiting the excitation bandwith). For the pre-clinical imaging, apart from the commercial 70-mm rat volume coil (Rapid) we have assembled two saddle coils of 45 mm and 55-mm diameter that were also successfully tested for imaging (Fig 2 (b)).

6. Sequences: For our preclinical MRI (Bruker Biospec, Avance neo), the nucleus can be freely choses e.g. to be ^{1}H or ^{129}Xe, so that all standard sequences can be applied for Xenon, too. This option is only available for our clinical MRI when the manufacturer grants access to a special mode (Cimax, Siemens). Of course, specialized sequence for xenon MRI will have to be implemented e.g. using the manufacturers sequence development platform or a vendor diagnostic option such as pulseq or gammaStar.

7. Regulatory matters: Xenon, as a substance used for diagnostics, is likely to fall under the Arzeimittelgesetz (AMG) in Germany, although the inert gas does not interact with the body and may cause only short-term anaesthetic effect. The use of HP Xe MRI was approved by the FDA in 2022 as an alternative to SPECT lung imaging, and several studies are registered on clinicaltrials.gov and CETIS. Self-experiments, individual healing attempts, clinical studies and routine application to patients may be considered. At the same time, ethic approval for the pre-clinical imaging was easily obtained, as Xe gas is considered to harmless for the animals. Of course, all these matters do not apply for in vitro applications.

Conclusion

We successfully setup a Xenon MRI suite, consisting of a SEOP polarizer, an MNO MRI, Xenon coils and some Xenon sequences. Future work will focus on obtaining high reproducible polarization, quality control of the gas, sequences and regulatory matters.

Acknowledgement

This project is supported by Sonderforschungsbereich/Transregio 287 BULK-REACTION (Projekt-ID 422037413) (DFG), BMBF with framework of e:Med research funding concept (01ZX1915C), BMBF hyperquant consortium (BlueHealthTeach, 03WIR6208A9).

References

1. Comotti A et al., *J Am Chem Soc*. 2008;130(41):13664-13672. doi:10.1021/ja802589u
2. Marshall H et al, *Progress in Nuclear Magnetic Resonance Spectroscopy*. 2021;122:42-62. doi:10.1016/j.pnmrs.2020.11.002

Metabolic imaging with deuterated Glucose (and HP pyruvate) in a colitis model

Aaron Diercks[1*], Fatima Anum[1], Elton Montrazi[2], Josh Peters[1], Charbel Assaf[1], Olga Will[1], Farhad Haj-Mohamad[1], Andrey Pravdivtsev[1], Lucio Frydman[2], Jan-Bernd Hövener[1*]

[1] University Medical Center Schleswig-Holstein, Kiel University, Department of Radiology and Neuroradiology, Section Biomedical Imaging, Am Botanischen Garten 14, 24118 Kiel
[2] Department of Chemical and Biological Physics, Weizmann Institute of Science, Rehovot, Israel

* aaron.diercks@rad.uni-kiel.de, jan.hoevener@rad.uni-kiel.de

Synopsis: This study explores the use of deuterated glucose and hyperpolarized pyruvate for metabolic imaging in a colitis model. Using magnetic resonance imaging (MRI), including chemical shift imaging (CSI), the research investigates the metabolic fate of these labels in vivo. The findings demonstrate significant signals from deuterium-labeled glucose and hyperpolarized pyruvate, suggesting potential for non-invasive monitoring of metabolic changes associated with gut inflammation. This work aims to enhance early disease detection and personalized treatment through improved imaging modalities.

Introduction

Changes in metabolism are among the first indicators of disease and treatment response. These alterations occur earlier than macroscopic changes in tissue and anatomy, enabling early interventions, individually tailored treatment and improved welfare. As such, much research is focused on developing methods to measure or image metabolism. Undoubtedly, imaging the accumulation of 18F-labelled desoxyglucose with position emission tomography has revolutionized cancer diagnostics and has become the standard of care since the 1990s. While radioisotopes provide information on the location of the label with superb sensitivity, however, there is no information on the labeled molecule itself. The magnetic resonance signal, in contrast, allows to identify the emitting molecule, but with much less sensitivity.

As a result, MR spectroscopy (MRS) has become a standard for analytical chemistry and is used in specialized cases in humans. It has not become, however, a widespread diagnostic standard. The reason for this is that the temporal, spatial and chemical resolution is usually limited to minutes, cubic centimeters, and millimolar concentrations. There are only few applications where MRS is needed to make clinical decision that cannot be reached otherwise.

Two new developments, promise to boost the biomedical significance of MRS: metabolic imaging with hyperpolarized molecules or deuterium-labelled molecules. Both methods allow to access and image the metabolism in living organisms non-invasively and in vivo by introducing a labelled nucleus into metabolic chains. In deuterium MRI (DMI), the low signal is partially compensated by averaging the signal (made possible by a short T1). In hyperpolarized MRI (HMI), the signal of the label is boosted for a limited time increasing the polarization of nuclear spins using quantum physical tricks.

Both methods allow imaging the fate of the labels in metabolism, DMI over minutes to hours, and HMI within seconds to one or two minutes.

Because the physical properties of the DMI and HMI signal are different to that of conventional, thermally polarized proton MRI (TMI), specialized imaging methods are required to make optimal use of the signals.

In DMI, the challenge lies in obtaining the optimal SNR with ca. 1 ppm chemical shift resolution of a fast relaxing and recovering species (HDO at 4.8 ppm to lactate at 1.33 ppm, T1 = 100-500ms, T2 = 10-300ms). Various sequences were used, including FID- or spin-echo based chemical shift imaging and balanced steady state free precession sequences with either a multi-echo[1] or (gradient-free) FID readout[2]. In HMI, ca. 10 ppm are needed and the relaxation is slow but does not recover (e.g. pyruvate at 170 ppm, lactate at 183 ppm, T1 = 20-60s, T2 = 0.5-2s). Different approaches to address these challenges were reported.

Here, we report on our experiences in imaging the metabolism of thermally polarized, 6,6'-Glucose-d_2 (Glu-d_2) and hyperpolarized 1-^{13}C-pyruvate in a model of colitis, an inflammation of the gut.

Methods

A 7 T MRT with volume transmit-receive coil was used (Bruker Biospec 7/30, Avance Neo) to acquire non-localized FID, slice selective FID,

product CSI and bSSFP-CSI[2]. A *colitis ulcerosa* mouse model was induced by adding dextran sulphate sodium (DSS) to the drinking water in compliance with regulatory approval (TVA number: V242-52836/2019(92-8/19)). The animals status was monitored by the Disease Activity Index (DAI) score[3]. During MRI, anaesthesia was used. 6-6'glucose-d2 was injected (100µl, 1-4mol) though a tail vein catheter.

^{13}C pyruvate was hyperpolarized by dissolution dynamic nuclear polarization (dDNP) to about 40% as described before[4].

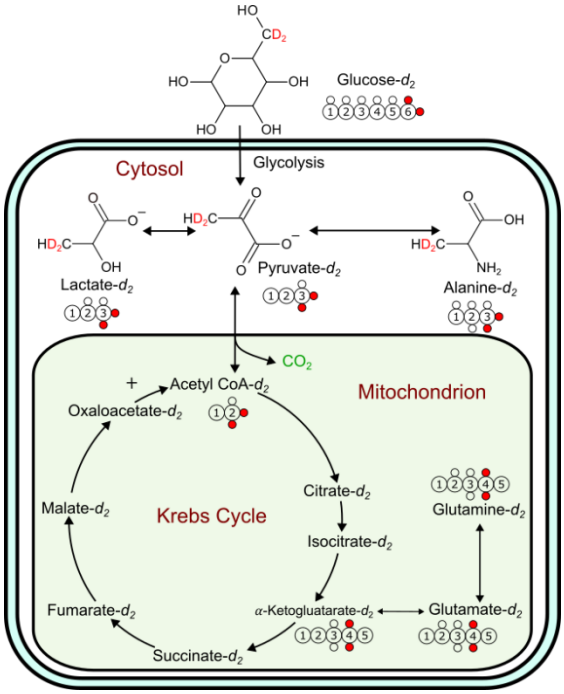

Fig. 1: Illustration the metabolic chains probed by imaging deuterated glucose.

Results & Discussion

The Water Peak is about 10 times higher than the Noise. Imaging the fate of the deuterium label was achieved with FID, FID-CSI, and bSSFP-CSI (Fig. 3). Here, a clear signal for HDO and glucose were observed. After the injection of HP pyruvate, lactate, alanine, and pyhdrate signals were observed clearly (Fig. 2).

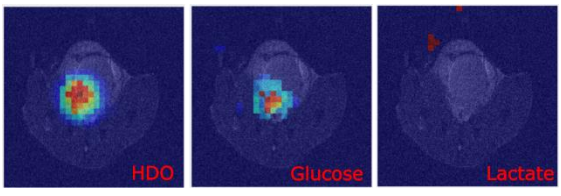

Fig 2: ^{2}H image of HDO, Glucose and lactate in a colitis model at day 8, acquired with FID-CSI. Averages=20, TR=250 ms.

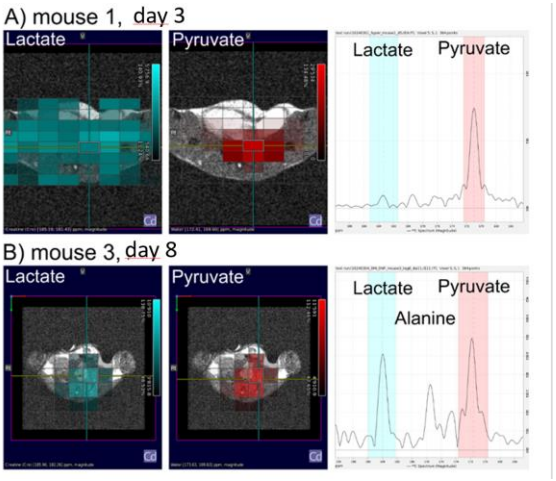

Fig. 3: In vivo ^{13}C-MR spectrum and image of HP pyruvate and lactate in a DSS model at day 3 and 8. Note the increase in lactate signal with progressing inflammation and the limited resolution of the FID-CSI data.

Conclusion

Both HMI and DMI allow metabolic imaging non-invasively and in vivo. The time scales probed are quite different. Despite of the huge signal enhancement or many repetitions, the SNR remains a challenge. In addition to the special physical properties of the HMI and DMI signal, specialized sequences are required to make good use of the signal. In future experiments, the second approach with hyperpolarized ^{13}C pyruvate will also be investigated in detail. Furthermore, the sequence should be adapted to short TR.

References

1. Markovic S, Roussel T, et al. Deuterium MRSI characterizations of glucose metabolism in orthotopic pancreatic cancer mouse models. *NMR in Biomedicine*. 2021;34(9):e4569.doi:10.1002/nbm.4569

2. Montrazi ET, Sasson K, Agemy L, et al. High-sensitivity deuterium metabolic MRI differentiates acute pancreatitis from pancreatic cancers in murine models. *Sci Rep*. 2023;13(1):19998. doi:10.1038/s41598-023-47301-7

3. Siegmund B, Lehr HA, Fantuzzi G, Dinarello CA. IL-1β-converting enzyme (caspase-1) in intestinal inflammation. *Proc Natl Acad Sci USA*. 2001;98(23):13249-13254. doi:10.1073/pnas.231473998

4. Ferrari A, Peters J, Anikeeva M, et al. Performance and reproducibility of 13C and 15N hyperpolarization using a cryogen-free DNP polarizer. *Sci Rep*. 2022;12(1):11694. doi:10.1038/s41598-022-15380-7

Scientific Session 2

MRI System Hardware and Technical Innovations

Oral presentations

201	Yenal Gökpek	*A parahydrogen polarizer for >30 bars hydrogenation and automated purification*
202	Jonathan Stelter	*B_0 self-navigation achieves contrast-independent respiratory motion estimation in radial stack-of-stars imaging*
203	Teresa Reichl	*From 4D Flow MRI to MPI: A study of the flow dynamics in an aneurysm phantom*
204	Christoph Aigner	*Towards UHF Spinal Cord MRI: Overcoming B_0 & B_1^+ Challenges*
205	Tim Haigis	*Quantitative Comparison of pTx Coils at 9.4T*

Posters

P201	Pavel Povolni	*A Low-Cost Magnetic Measurement System for Low-Field MRI Magnets based on a Motion Tracked Flexible-Joint Robot with 5 Degrees of Freedom*
P202	Harriet Wulff	*Automated Gas Delivery System for Parahydrogen-Induced Polarisation at up to 10 bar*
P203	Judith Samlow	*Easy Rebuildable Cubic 3-Axis Positioning Robot Based on Open-Source Hardware: Validated via Camera-Based Motion Tracking and Initial Application in Magnetic Low Field Mapping*
P204	Moritz Sander	*Inductively coupled coils for 1.5 T, 3 T and 7 T MRI*
P205	Sergej Maltsev	*SQUID based Method of Evaluating Noise Characteristics of High Temperature Superconductors used in Novel Low Field MRI Scanner Designs*

A parahydrogen polarizer for >30 bars hydrogenation and automated purification

Yenal Gökpek[1], Ella Dieball[1], Martin Sandbrink[1], Charbel Assaf[1], Frowin Ellermann[1], Jan-Bernd Hövener[1], Andrey N. Pravdivtsev[1,*]

[1] University Medical Center Schleswig-Holstein, Kiel University, Department of Radiology and Neuroradiology, Section Biomedical Imaging, Molecular Imaging North Competence Center (MOIN CC), Am Botanischen Garten 14, 24118 Kiel

* andrey.pravdivtsev@rad.uni-kiel.de

Synopsis: This project aims to integrate an automated purification module into our existing 0.5 T PHIP-SAH system, designed for rapid and cost-effective hyperpolarization of pyruvate. Pressure caps and NMR tubes were designed using PEEK, PSU, and PEI materials for high-pressure operations (up to 34 bars). The customized caps let us automate injections of liquids, gases and rapid vacuuming of the organic solvent. Future work will focus on fine-tuning hyperpolarization and purification stages for biochemical and in-vivo applications.

Introduction

Magnetic resonance (MR) is a highly versatile diagnostic tool commonly used in both medicine and chemical analysis. Enhancing nuclear spin polarization boosts the sensitivity of MRI, facilitating real-time metabolic imaging within living organisms.[1]

Dissolution dynamic nuclear polarization (dDNP) is the leading technology for clinical hyperpolarization research, but it is costly and relatively slow. Parahydrogen-induced polarization (PHIP), particularly PHIP with side arm hydrogenation (PHIP-SAH)[2], provides a much faster and more economical alternative to dDNP for hyperpolarizing pyruvate, the most frequently used tracer in hyperpolarized MRI.

A previous study from our research group demonstrated an automated PHIP-SAH system (Fig. 1)[3]. The system is based on a permanent 0.5 T magnet and allows for rapid hyperpolarization with a duty cycle of 1 minute.

One of the problems of in vivo applications of the PHIP-SAH is the high acetone concentration and the heavy metal content of the catalyst[4]. The designed purification system also aims to overcome these problems by automating the process with high accuracy and repeatability, which is needed for pre-clinical and in-vivo applications.

Methods

The main polarizer was based on a design described before[3]. We designed and investigated five reactors, each based on a custom-made cap and either one of 5 mm, 10 mm NMR tubes (no pressure rating), a 16 mm flanged glass tube (41 bar), or a custom-made PEEK tube. The mechanical stress of caps and tubes was simulated with the finite elemental method (FEM) for polyetheretherketone (PEEK) polysulfone (PSU) and polyetherimide (PEI, Fig. 2). In addition, we designed and constructed a fluid control unit made of stepper motors, servos, and syringes, controlled by customized software (Fig. 3). All valves and tubes that are used in the design and construction were HPLC grade equipment with a pressure rating of at least 34 bars. For the high-volume reactor, we tested 16 mm tube (10 mL Pressure Vessels, CEM GmbH) with specified pressures below up to 41 bar.

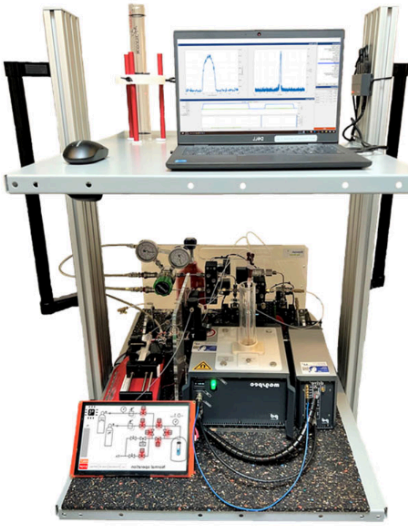

Fig. 1: Automated system for PHIP-SAH.

Results

The FEM indicated that all pressure caps and tubes from PEEK and PEI were suitable for up to 200 bars, while the PSU versions fail the mechanical stress limit of around 180 bars.

The standard 5 mm and 10 mm glass NMR tubes, lacking pressure specifications, successfully passed the experimental test at 10 bars.

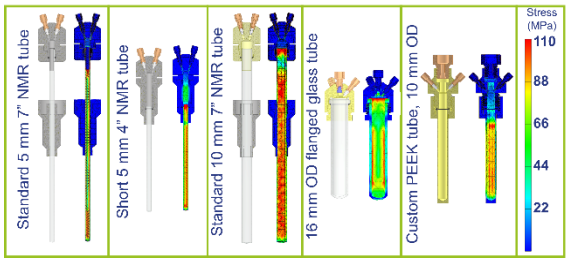

Fig. 2: Drawing and simulated mechanical stress of reactors 1 – 5 with a pressure of 200 bars applied on the inner surface.

Three steps are essential for implementing the purification method: a) the addition of Na_2CO_3, for cleaving the sidearm, b) evaporating the organic solvent by applying a vacuum, and c) redissolving the pyruvate in an isotonic buffer. We designed an automated, high-pressure system (up to 34 bars, Fig. 3) to conduct these steps precisely.

The syringe pump manifold was designed to precisely control the injection of three chemicals into the PHIP reactor at the required doses with an estimated accuracy of 2.5 µl and a 200 ml/min injection speed. It allows the injection of the desired chemical into the reactor at the desired time, controls the vacuum tank, and flushes the reactor after the experiment.

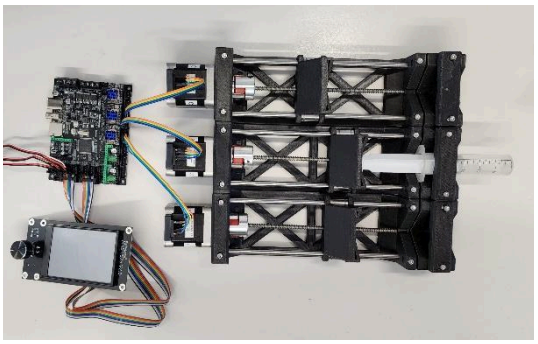

Fig. 3: Syringe setup with controlling parts.

Discussion

As all caps were simulated to be pressure resistant to 200 bar, the limiting factor with respect to pressure was the other parts of the system: 10 bars when standard 5 mm NMR tubes are used or, 34 bars when the custom tubes or 16 mm flanged tubes are used (the limit is the safety rating for the shut-off valves, P-782 - IDEX). With a safety coefficient of 2, experiments up to 100 bars appear feasible using caps and tubes designed here. Note that the chemical degradation of the polymers is not considered.

The syringe pump was designed to have the most precise accuracy with the micro-stepping function. This trade-off corresponded to having a maximum injection speed of 200 mL/min. The small design of the manifold allows it to be placed as desired, reducing the footprint of the polarizer.

Conclusion

The newly designed pressure caps made from PEEK and PEI materials are promising for conducting PHIP-hyperpolarization experiments up to 100 bars, ensuring robust performance under PHIP-SAH conditions. With high accuracy, the syringe pump can control the required chemicals in desired doses to be injected into the reactor automatically. The automated system, equipped with stepper motors, servos, and customized software, precisely controls chemical injections, enabling reliable and consistent hyperpolarization processes. Future work will focus on purifying the hyperpolarized agent without signal loss, for use in biochemical applications and in-vivo experiments.

Acknowledgments

We acknowledge our funding from the German Federal Ministry of Education and Research (BMBF) within the framework of the e:Med research funding concept (01ZX1915C), DFG (PR 1868/3-1, PR 1868/5-1, HO-4602/3, EXC2167, FOR5042, TRR2879) and support by the hyperquant consortium, 03WIR6208A, BlueHealthTech, BMBF. MOINCC was founded by the grant from the European Regional Development Fund (ERDF) and the Zukunftsprogramm Wirtschaft of Schleswig-Holstein (Project no. 122-09-053)

References

1. Schmidt AB, Bowers CR, Buckenmaier K, et al. Instrumentation for Hydrogenative Parahydrogen-Based Hyperpolarization Techniques. *Anal Chem*. 2022;94(1):479-502. doi:10.1021/acs.analchem.1c04863
2. Reineri F, Boi T, Aime S. ParaHydrogen Induced Polarization of 13C carboxylate resonance in acetate and pyruvate. *Nat Commun*. 2015;6(1):5858. doi:10.1038/ncomms6858
3. Ellermann F, Sirbu A, Brahms A, et al. Spying on parahydrogen-induced polarization transfer using a half-tesla benchtop MRI and hyperpolarized imaging enabled by automation. *Nat Commun*. 2023;14(1):4774. doi:10.1038/s41467-023-40539-9
4. Mamone S, Jagtap AP, Korchak S, Ding Y, Sternkopf S, Glöggler S. A Field-Independent Method for the Rapid Generation of Hyperpolarized [1- ^{13} C]Pyruvate in Clean Water Solutions for Biomedical Applications. *Angew Chem Int Ed*. 2022;61(34):e202206298. doi:10.1002/anie.202206298

B0 self-navigation achieves contrast-independent respiratory motion estimation in radial stack-of-stars imaging

Jonathan Stelter,[1*] Kilian Weiss,[2] Patrick T. Haft[1], and Dimitrios C. Karampinos[1]

[1] Institute of Diagnostic and Interventional Radiology, School of Medicine and Health, Technical University of Munich, Munich, Germany.
[2] Philips GmbH Market DACH, Hamburg, Germany.
* jonathan.stelter@tum.de

Synopsis: The radial stack-of-stars trajectory enables free-breathing quantitative liver imaging which may not be feasible in a breath-hold. However, motion navigation can be challenging in acquisitions with rapid contrast variations like T1 mapping based on a Look-Locker scheme. A B0 self-navigation approach is proposed to correct temporal B0 variations and enable motion navigation independent of magnitude variations.

Introduction

Free-breathing acquisitions enable volumetric imaging at high resolution or quantitative imaging which may not be feasible in a breath-hold or in patients that cannot hold their breath. Radial stack-of-stars (SoS) trajectories are particularly popular for motion-robust acquisitions as they oversample the center of k-space and have an inherent self-navigation capability. However, estimating a reliable motion signal may be difficult in acquisitions with varying contrast during the scan.

The Look-Locker acquisition is an example of such an acquisition where the contrast changes for different inversion times (TI) and which has been previously combined with a SoS trajectory to perform water-specific T1 (wT1) mapping[1,2]. On the other hand, a Dixon-based B0 self-navigation approach has been proposed for SoS imaging, which is independent of magnitude variations and allows for correction of B0 drift and temporal B0 fluctuations[3], but has not yet been applied in moving anatomies such as the liver.

The purpose of this work is to apply the B0 self-navigator for whole-liver wT1 mapping to evaluate the feasibility of contrast-independent respiratory motion estimation.

Methods

Free-breathing SoS Look-Locker sequence: A Look-Locker data acquisition was combined with a bipolar gradient echo SoS readout. After an inversion prepulse, different TI contrasts (TI_i with $i = 1,..,7$) were acquired followed by a delay with free relaxation ($T_{meas} = 3$s). In each

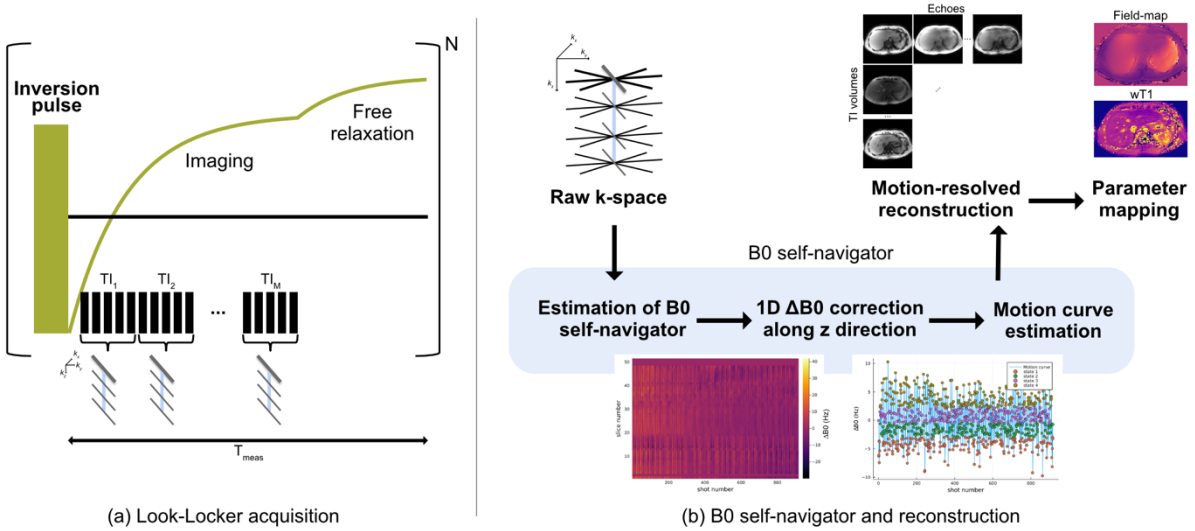

(a) Look-Locker acquisition (b) B0 self-navigator and reconstruction

Fig. 1: Schematic overview of the proposed Look-Locker acquisition (a) and the B0 self-navigator and reconstruction pipeline (b). The B0 self-navigator is estimated based on the oversampled k-space center and allows the correction of B0 drift and temporal fluctuations. A motion-resolved reconstruction is performed based on the motion states estimated by the self-navigator.

shot per TI contrast (duration = 297ms), profiles along the k_z direction are read out at a fixed angle of the radial spokes.

B0 self-navigator: The oversampled k-space center was extracted and a graph cut-based water-fat separation was performed coil-wise on the feet-head profiles enforcing smoothness in the slice and time dimension. The median field map per coil, contrast, and slice was used to compute the field map difference ΔB0. The ΔB0 estimates per coil were combined based on a smoothness criterion. The resulting B0 self-navigator was employed to correct a constant phase for each radial spoke due to B0 drift and to estimate three motion states using k-medoids clustering.

Experiments: Measurements were performed at 3T (Ingenia Elition X, Philips Healthcare) on two volunteers (N_{TE} = 4, $TE_1/\Delta TE$ = 1.08/1.07 ms, FA = 3°, FOV = 350x350x200 mm^3, voxel size = 3x3x5 mm^3). The respiratory signal estimated by the B0 self-navigator was compared to a respiratory motion-tracking camera provided by the vendor. Reconstruction was performed offline using an iterative reconstruction with spatial TV regularization. Temporal TV regularization along the motion states was applied additionally for the motion-resolved reconstruction. Water-fat separation was performed using a multi-resolution graph-cut algorithm[4] followed by T1 fitting, taking into account incomplete T1 recovery[5].

Results

Fig. 2 compares the B0 self-navigator with a respiratory motion-tracking camera showing a good correlation with a possible short delay. The contrast variations in the magnitude signal have a similar period to the pseudo-periodic respiratory motion, but their pattern is different. The reconstructed wT1 maps are shown in Fig. 3 for one volunteer, comparing the motion-resolved with the motion-averaged reconstruction.

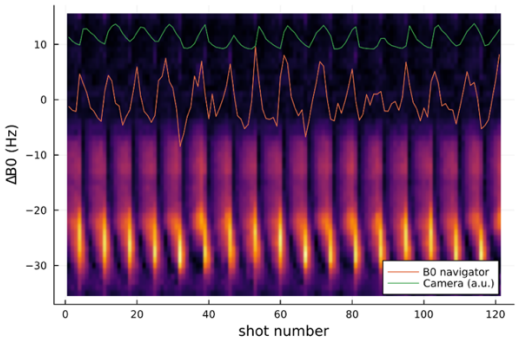

Fig. 2: Comparison of the B0 self-navigator with a respiratory motion-tracking camera. The motion estimates are plotted on top of the magnitude of the first echo and central FH profiles which periodically depict the contrast variations due to the Look-Locker scheme.

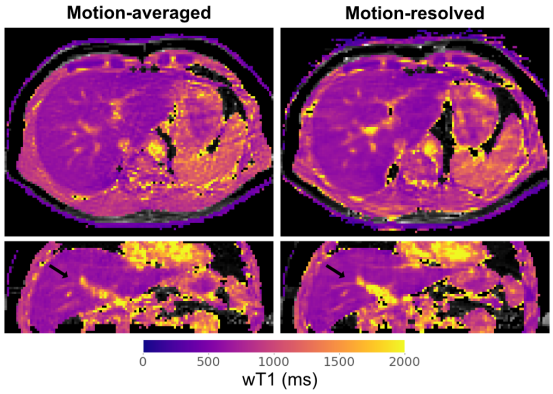

Fig. 3: The B0 self-navigated motion-resolved reconstruction improves the depiction of vessels compared to the motion-averaged reconstruction (arrows on coronal reformats).

Discussion

Results indicate that the B0 self-navigator can be used effectively in moving anatomies such as the liver, which is directly affected by B0 variations and tissue displacement. In addition, the B0 self-navigator depicts the respiratory motion in the Look-Locker acquisition despite the strong and rapid contrast variations.

Conclusion

A B0 self-navigation approach was proposed which enables the correction of temporal B0 variations and the estimation of respiratory motion in the presence of strong contrast variations.

Acknowledgments

The authors would like to thank Dr. Yu Ueda and Dr. Masami Yoneyama for their support with the implementation of the Look-Locker acquisition.

References

1. Wang N, Cao T, Han F, et al. Free-breathing multitasking multi-echo MRI for whole-liver water-specific T1, proton density fat fraction, and R2* quantification. Magn Reson Med. 2021
2. Feng L, Liu F, Soultanidis G, et al. Magnetization-prepared GRASP MRI for rapid 3 T1 mapping and fat/water-separated T1 mapping. Magn Reson Med. 2021;86(1):97–114.
3. Stelter JK, Wu M, Raspe J, et al. Dixon-Based B0-Navigation to Correct B0 Drift and B0 Fluctuations in Radial Stack-Of-Stars Multi-Echo Gradient Echo Imaging. Proc Intl Soc Mag Reson Med 31. 2023:1154
4. Stelter JK, Boehm C, Ruschke S, et al. Hierarchical Multi-Resolution Graph-Cuts for Water-Fat-Silicone Separation in Breast MRI. IEEE Trans Med Imag. 2022;41(11):3253–3265.
5. Wang X, Rosenzweig S, Roeloffs V, et al. Free-breathing myocardial T1 mapping using inversion-recovery radial FLASH and motion-resolved model-based reconstruction. Magn Reson Med. 2022;89(4):1368–1384

From 4D Flow MRI to MPI: A study of the flow dynamics in an aneurysm phantom

T. Reichl[1*], P. Winter[2], A. el Ahmar[2], M.A. Rückert[1], J. Günther[1], T. Kampf[1,3], T.A. Bley[4], V.C. Behr[1], S. Herz[4], S. Schnell[2], P. Vogel[1,5]

[1] Department of Experimental Physics 5 (Biophysics), Julius-Maximilians University, Würzburg, Germany.
[2] Department of MR, Physics, University of Greifswald, Germany.
[3] Department of Diagnostic and Interventional Neuroradiology, University Hospital, Würzburg, Germany.
[4] Department of Diagnostic and Interventional Radiology, University Hospital Würzburg, Germany.
[5] Pure Devices GmbH, Rimpar, Germany.

* Teresa.Reichl@physik.uni-wuerzburg.de

Synopsis: Flow dynamics in a realistic aneurysm phantom were measured and visualized using 4D flow MRI, MPI and OT. The measured flow dynamics are in good qualitative agreement. Furthermore, the aneurysm geometry was investigated as a parameter influencing the flow dynamics in an aneurysm phantom.

Introduction

An aneurysm is a pathological enlargement of a vessel. Both, risk of rupture of an aneurysm as well as treatment complications can lead to life-threatening bleeding. Since the flow dynamics may play an important role in understanding aneurysm formation and rupture, new methods to access the risk of rupture at an early stage are mandatory.

Only a few imaging techniques are capable of measuring fluid dynamics. In this study, 4D flow Magnetic Resonance Imaging (MRI), Magnetic Particle Imaging (MPI) and Optical Transmission (OT) were chosen. 4D flow MRI, provides multiple parameters with good precision such as wall shear stress but with the drawback of long acquisition times. OT allows to measure fluid dynamics directly, but transparency of the sample is required. MPI is a tracer-based radiation-free imaging technique providing rapid and direct imaging which can overcome mentioned issues of 4D flow MRI and OT. The aim of this study is to visualize the flow dynamics in an aneurysm phantom and investigate the influence of the aneurysm geometry on flow dynamics.

Methods

Phantom: The aneurysm phantom was manufactured following a step-by-step guide visualized in Fig. 1 [1,2]. In addition, connectors are added to obtain a waterproof plug-in system. The final 3D model is 3D printed using an SLA printer (Form3, Formlabs, USA) and flexible resin (Elastic50A, Formlabs, USA) emulating the flexibility and elasticity of human blood vessels.

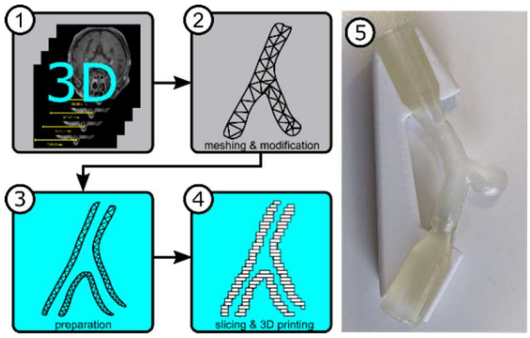

Fig. 1: Manufacturing process for aneurysm phantoms: **(1)** 3D data of desired region acquired with CT or MRI are used for extraction of the vessel structure. The extracted 3D model can be modified for different medical conditions **(2)**. The 3D model is prepared for 3D printing **(3)** and finally printed using an SLA printer with flexible resin **(4)**. The resulting 3D printed aneurysm phantom in a mount allowing correct anatomic geometry and positioning **(5)**.

The flow dynamics in the aneurysm phantom were determined and visualized using 4D flow MRI, MPI and OT.

4D flow MRI: A kt-GRAPPA (R=5) accelerated cartesian sequence [3], which combines 3D spatial encoding with 3D velocity encoding, was used for the measurements of pulsatile flow with femoral waveform (Compuflow 1000 MR, Shelley Medical Imaging Technologies, Canada) with a peak flow of 25ml/s in a 3T Magnetom Vida (Siemens Healthineers, Germany).

MPI: A bolus of 200µl Perimag® (Micromod, Germany) was directly visualized using a rapid

3D sequence within a TWMPI scanner with FFL encoding scheme [4,5].

OT: The optical transmission measurements were performed by filming a 2ml food color bolus in slow-motion mode (100FPS) under pulsatile flow (Ismatec MCP-Z, Cole-Parmer GmbH, Germany): 1251ml/min; 0.6s no flow, 0.2s flow.

Results

To investigate the influence of the aneurysm geometry on the flow dynamics with 4D flow MRI, multiple anatomical inflow angles were measured and visualized (see Fig. 2).

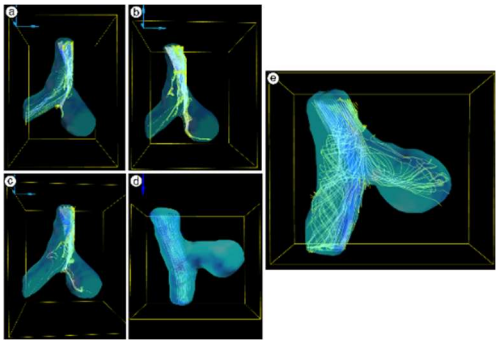

Fig. 2: Streamline visualization of flow dynamics in aneurysm phantom for different anatomical inflow angles: **(a)** smallest angle, **(b)** a bit smaller than original angle, **(c)** a bit larger than original angle, **(d)** straight aneurysm and **(e)** anatomical geometry. An example time frame is shown here for each time series.

Fig. 3 shows a complete measured time series of flow dynamics visualized with streamlines as an example.

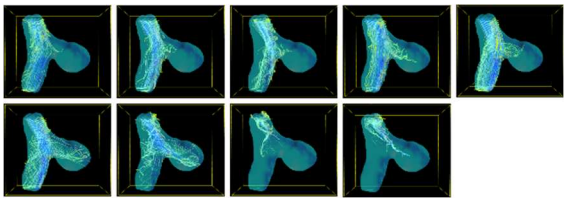

Fig. 3: Streamline visualization of 4D flow measurement at 25ml/s peak flow in aneurysm phantom with anatomical geometry.

The measured flow dynamics with MPI are displayed in Fig. 4.

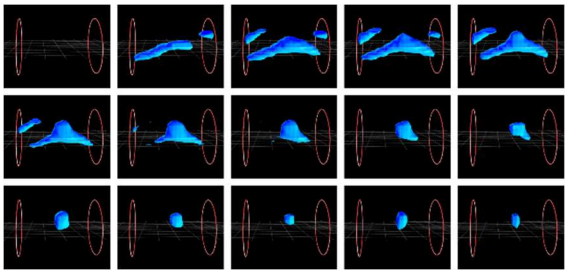

Fig. 4: Time series of a bolus flowing through an aneurysm phantom with anatomical geometry, which was measured with MPI. The red circles indicate the limits of the field of view (FOV).

For comparison, OT measurements were performed, which are displayed in Fig. 5.

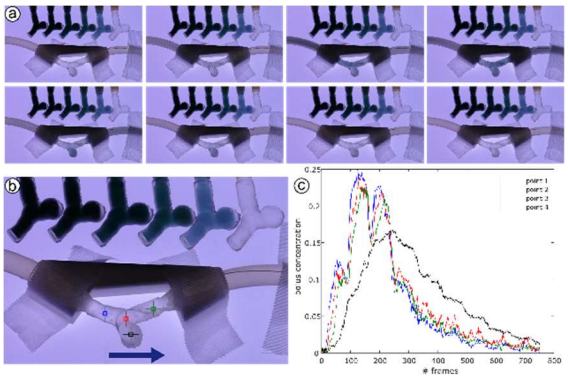

Fig. 5: **(a)** Time series of CCD camera images (100FPS) of food color bolus flowing through aneurysm phantom with pulsatile flow (1251ml/min; 0.6s no flow, 0.2s flow). **(b)** Intensity plot in dependency of time at four different positions as indicated in subfigure **(c)**.

Discussion

A qualitative comparison of measured flow dynamics with MRI, MPI and OT shows good agreement. It could be visualized that the fluid initially passes the aneurysm, partially swirls into the aneurysm and remains there for a longer period. The investigation of the influence of the aneurysm inflow angle on the flow dynamics using 4D flow MRI showed the closer the geometry of the aneurysm phantom matches the anatomical geometry the more flow is detected in the aneurysm. Since geometry was found to be a parameter influencing flow dynamics, further characterization of aneurysm geometry has to be performed.

Conclusion

To conclude it was possible to measure the flow dynamics in an aneurysm phantom with three different imaging modalities: 4D flow MRI, MPI and OT. Furthermore, the aneurysm inflow angle was found to be strongly influencing the flow dynamics. Further investigations are required to examine the influence of additional parameters on the flow dynamics.

References

1. Reichl, T. et al., Int J Mag Part Imag, 9(1), 2023

2. Guggenberger, K. & Krafft, A.J. et al., MRI. 83: 114-24, 2021.

3. Schnell. S. et al., JMRI 46(1):102-114, 2017.

4. Gleich B. & Weizenecker J., Nature. 435(7046): 1217-1217, 2005.

5. Vogel P. et al., Sci Rep, 13: 10472, 2023.

Towards UHF Spinal Cord MRI: Overcoming B_0 & B_1^+ Challenges

Christoph S. Aigner[1,2*], Manuel F. Sánchez Alarcon[1,3], Alexandre D'Astous[4,7], Eva Alonso-Ortiz[4,7], Julien Cohen-Adad[4,5,6,7], Sebastian Schmitter[1,8,9]

[1]Physikalisch-Technische Bundesanstalt (PTB), Braunschweig and Berlin, Germany
[2]Max Planck Institute for Human Development, Berlin, Germany
[3]Working Group on Cardiovascular Magnetic Resonance, Experimental and Clinical Research Center, a joint cooperation between the Charité Medical Faculty and the Max-Delbrück Center for Molecular Medicine, Berlin, Germany
[4]NeuroPoly Lab, Institute of Biomedical Engineering, Polytechnique Montréal, Quebec, Canada.
[5]Functional Neuroimaging Unit, CRIUGM, Université de Montréal, Quebec, Canada.
[6]Mila-Quebec AI Institute, Montréal, Quebec, Canada.
[7]Centre de recherche du CHU Sainte-Justine, Université de Montréal, Montréal, Quebec, Canada.
[8]Medical Physics in Radiology, German Cancer Research Center (DKFZ), Heidelberg, Germany
[9]Center for Magnetic Resonance Research, University of Minnesota, Minneapolis, MN, United States

* Contact communicating author

Synopsis: This work investigates the impact of respiration on the B_0 field, and the B_1^+ variations within the spinal cord (SC) at 7 Tesla. We found that tailored B_0 shims significantly reduce B_0 fluctuations, achieving a standard deviation of around 50Hz in the thoracolumbar SC. Respiration itself caused field offsets of up to 40Hz. Additionally, we explored the use of universal parallel transmission (pTx) RF shims to compensate for spatial variations in the B_1^+ field in the cervical and thoracolumbar SC. This calibration-free approach holds promise for streamlining SC imaging by eliminating lengthy pTx calibration procedures. This could make UHF SC MRI more accessible to researchers who are not experts in pTx techniques.

Introduction

Ultra-high field (UHF) MRI offers significant advantages for spinal cord (SC) imaging compared to lower field strengths, including higher in-plane resolutions to image small SC structures (1). However, UHF SC MRI can be hampered by two key challenges: spatial variations in the static magnetic field (B_0) and inhomogeneity and inefficiency of the B_1^+ transmit field (2). This study investigates these challenges using two approaches. First, we employed a 3D non-Cartesian multi-echo GRE sequence to acquire respiration-resolved B_0 field maps. This allowed us to assess the impact of respiration on B_0 field variations and the effectiveness of tailored B_0 shims. Secondly, we explored the use of pre-computed, universal pTx RF shims as an alternative to time-consuming, subject-specific calibrations for addressing B_1^+ inhomogeneity and inefficiency.

Methods

MRI scans were conducted on a 7T scanner (Magnetom 7T, Siemens, Germany) using two certified RF coils (MRI.Tools GmbH, Germany): an 8Tx/8Rx neck coil and an 8Tx/32Rx body array. 3D non-Cartesian thoracic multi-echo GRE datasets with radial phase encoding were acquired for B_0 mapping with a tailored pTx RF shim during free breathing (isotropic voxel size of 1.4mm). Two echo times (1.51/2.79ms) were used for B_0 field map computation, providing a range of ±390Hz. Subject-tailored B_0 shim solutions up to the 2nd order were optimized using a Shimming Toolbox (3). Relative B_1^+ maps to compute universal shims (US) were acquired differently for the cervical (C-Spine) and thoracolumbar spine (T/L-Spine). For the C-Spine, 2D B_1^+ maps were acquired using a free-breathing Cartesian GRE (voxel size of 2x2x4mm^3). In the T/L-Spine, 3D B_1^+ maps were collected for each volunteer using a radial phase-encoded GRE (isotropic voxel size of 2mm). US were individually optimized for the C- and T/L-Spine using a training library of 6/9 subjects, respectively (4). 3D high-resolution Cartesian multi-echo GRE were obtained for C-Spine under free breathing (isotropic voxel size of 1mm) and during breath-hold in 2D for T/L-Spine (voxel size of 1x1x2mm^3).

Results and Discussion

The acquired B_0 maps revealed consistent variations across subjects, with high-frequency fluctuations of approximately 50Hz next to the vertebrae and 250Hz in the lumbar SC region. Notably, respiration caused additional B_0 shifts of up to 40Hz. This study explored subject-tailored B_0 shims, achieving a substantial

reduction in B_0 variations across the T/L-SC. These results are shown in Figure 1, were the optimized shims and subsequent frequency adjustment led to a decrease in the root-mean-squared error (RMSE) by approximately 90% and a reduction in the standard deviation of B_0 by up to 31% in six subjects.

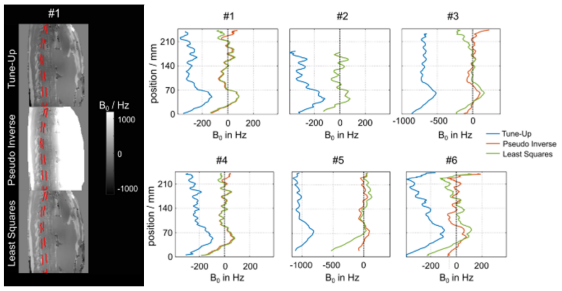

Fig. 1: Field maps before (Tune-Up) and after B_0 shimming (Pseudo Inverse and Least-Squares) in the first subject (left) and the median B_0 along the T/L-Spine (right) in all six subjects.

Figure 2 shows the impact of using correct and incorrect shims on exhale and inhale field maps which caused an additional B_0 variation of up to 40Hz and increased interquartile range.

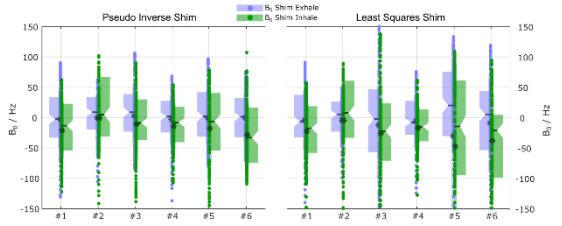

Fig. 2: Impact of applying 2nd order subject-tailored B_0 exhale shims on exhale/inhale B_0 field maps.

Two USs were designed (one for each of the two RF coils) and manually selected SC target regions in a library of B_1^+ maps (6/9 subjects for C- and T/L-Spine). The USs were then tested in three new volunteers. The proposed universal RF shims achieved an average two-fold improvement in B_1^+ efficiency and a 20% boost in B_1^+ field homogeneity compared to the default RF shim mode (see Figures 3 and 4). Notably, the USs delivered performance comparable to subject-specific pTx calibrations, but eliminated the need for lengthy calibration procedures, saving approximately 10 minutes per scan.

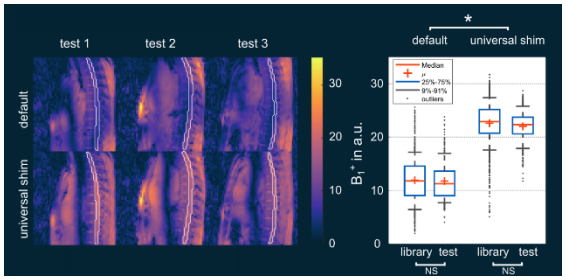

Fig. 3: B_1^+ prediction in the T/L-Spine.

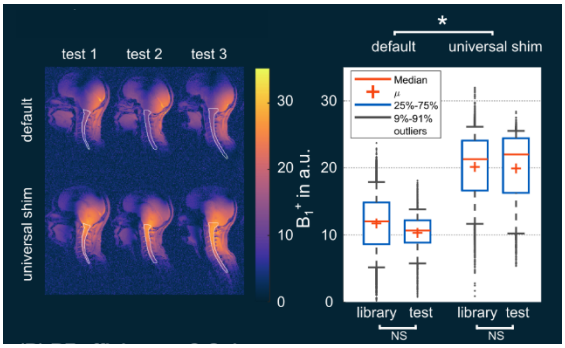

Fig. 4: B_1^+ prediction in the C-Spine.

Figure 5 shows 3D GRE data in the C-Spine that is imaged at 7T during free breathing with a 1mm isotropic resolution, while the GRE data in the T/L-Spine is acquired in 2D during a breath-hold (voxel size of 1x1x2mm^3). Qualitatively, good image quality is evident, confirming the feasibility of USs across the entire SC at UHF.

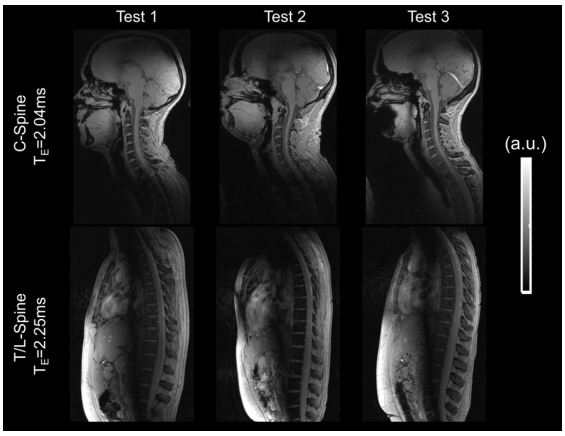

Fig. 5: 3D/2D GRE data using calibration-free pTx.

Conclusion

Universal pTx simplifies UHF SC MRI, while offering similar image quality to time-consuming subject-tailored pTx. Additionally, the study's findings show that slice- and respiration-specific B_0 shimming may be required for sequences that are sensitive to field variations.

References

1. Barry RL et al., Spinal cord MRI at 7T. Neuroimage, 2018; 168: 437–451.

2. Padormo F et al., Parallel transmission for ultrahigh-field imaging. NMR Biomed., 2006; 29: 1145– 1161

3. D'Astous A et al., Shimming toolbox: An open-source software toolbox for B0 and B1 shimming in MRI. MRM. 2022; 1-17

4. Aigner CS et al., Calibration-free parallel transmission of the cervical, thoracic, and lumbar spinal cord at 7T. MRM. 2024; 1-15

Quantitative Comparison of pTx Coils at 9.4T

Tim Haigis[1*], Georgiy Solomakha[1], Nikolai Avdievich[1], Klaus Scheffler[1,2] and Dario Bosch[1,2]

[1]High-Field MR Center, Max Planck Institute for Biological Cybernetics, Tübingen, Germany.
[2]Department of Biomedical Magnetic Resonance, University of Tübingen, Tübingen, Germany.

* tim.haigis@tuebingen.mpg.de

Synopsis: Parallel transmit performance of three transceiver array coils is systematically compared based on simulated slice selective pulses. Subject tailored 2-spoke excitation massively improves B1+ homogenity while reducing max local SAR and closes the gap between 8 and 16 channel systems.

Introduction

Parallel transmit (pTx) technology is a relevant topic in ultra high field research as it poses an effective solution to the inherent transmit (B_1^+) inhomogenity. While many pTx-capable RF coils were presented in the past, little work has been done on systematically comparing their designs and respective pTx performance. In this work, we explore three different transceiver arrays and evaluate them with respect to flip angle (FA) distribution and specific absorption rate (SAR) efficiency on subject tailored slice selective pulses.

Methods

Three transceiver RF array coils are investiged: An 8-channel single-row coaxial dipole array (1), a 16-channel dual-row dipole array (2), and a 16-channel dual-row loop array (3). Virtual observation points (4) are used for local SAR_{10g} monitoring. The Duke voxel model (5) serves as source for the numerical simulation of magnetization and field maps. Channel-wise B1+ maps for all coils were exported from electromagnetic simulation in CST and B_0 phase offsets were calculated (6). Circular Polarized (CP) mode is emulated by setting phase shifts according physical arrangement of transmit elements. Magnitude is optimized to produce mean target FA for each slab. Magnitude and phase of RF shims are optimized channel-wise. Our design of 2-spoke pulses is based on the spatial domain method with small tip angle approximation (7) solving the magnitude least squares problem (8). The algorithm is run for 10,000 spoke combinations, with the first spoke position being uniformly sampled in $-15\ m^{-1} \leq k_{xy} \leq 15\ m^{-1}$. The second spoke is placed at the center of *k*-space. Pulse energy is varied by repeating the experiment with 30 Tikhonov regularization factors $\lambda = \{10^n \mid n \in [-5, 1]\}$ and pulses exceeding the peak SAR_{10g} (pSAR) limit are discarded. The best pulse is selected according to minimum normalized root mean squared error (nRMSE). All sub-pulses are 400 µs in length, resulting in 1 ms total length for 2 spokes including gradient ramps.

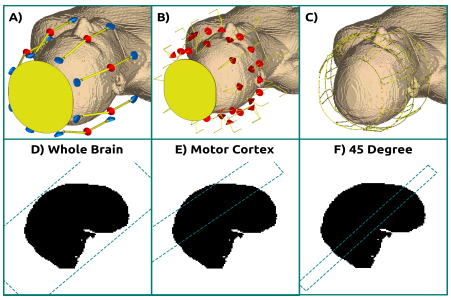

Fig. 1: A-C) CAD models of the three different coils with the Duke voxel model. A) 8 Dipoles. B) 16 Dipoles C) 16 Loops. D-F) Slabs used for optimization. D) Whole brain slab emulating global excitation. E) Motor cortex slab with additional coverage in occipital cortex and thickness of 5cm. F) 45 Degree slab with 2cm thickness.

To evaluate peak specific energy depositions (pSED) efficiency, optimization is run for a set of very conservative pSED limits from 4 to 80 mJ/kg with 15° FA. The resulting L-curves are displayed in figure 2. Additionally we simulate performance on a gradient echo (GRE) sequence with virtually no SAR restriction (5° target FA, 11 ms repetition time (TR), 9.5 W/kg pSAR limit). The resulting FA distribution is presented in figure 3 along with an overview of all results in table 1.

Results

The CP modes of the 16 Dipoles have lower error than those of 8 Dipoles at comparable peak energy in all slab positions (figure 2). The performance of 16 Loops heavily depends on slab position, as the array has low transmit sensitivity in dorsal parts of the brain in CP mode. Comparing the RF shims, 16 Dipoles drastically outperform 8 Dipoles in terms of error on most slabs and perform similar at very low energy limits. 2-Spoke pulses, 16 Dipoles perform best by a small margin in all settings.

Noteworthy is the significantly worse performance of 8 Dipoles in whole brain excitation due to global variations in B_1^+. In the motor cortex 16 Loops are worse than 8 Dipoles at low energies due to reduced sensitivity, but otherwise comparable to 16 Dipoles.

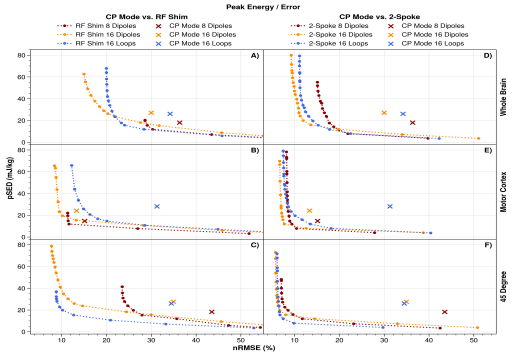

Fig. 2: Optimization results of three coils at different pSED limits. A-C) Comparison of RF shim performance and CP mode of three coils. D-F) Optimized 2-Spoke pulses compared to CP mode.

Figure 3 shows deviations from the target FA of 5° using 2-spokes are mostly within 20% for all three coils. 8 Dipoles and 16 Loops produce larger deviations in the perimeter than 16 Dipoles, but after averaging over slice *z* direction none of them stand out negatively.

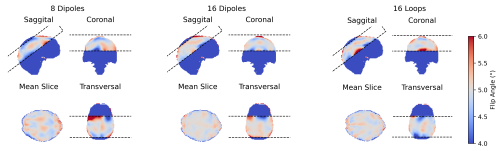

Fig. 3: Global excitation of 2-spokes in the motor cortex and mean flip angle distribution in slab-relative *z* direction for all coils.

These results are reflected in the motor cortex and 45 degree slabs of table 1. In whole brain excitation the difference is larger and 16 Loops outperform 8 Dipoles, while the 16 Dipoles have the overall lowest errors. None of the pulses were limited by pSAR.

Discussion & Conclusions

Generally 2-spoke pulses provide drastic improvements over both CP mode and RF shim while resulting in low peak energies compared to a sequence with 2.5 W/kg pSAR limit that would allow pulses with a pSED of 138 mJ/kg at 15° and 20 ms TR. Independent of pulse design, 16 Dipoles are the most versatile with best performance in many cases. 8 Dipoles are better suited for extremely low SAR budgets while16 Loops require higher budgets to achieve homogenity in dorsal regions. Issues with 8 Dipoles occur when the targeted slab is rotated about *x* or *y*. Two rows of transmit elements improve performance in these cases, having the required degrees of freedom to compose a homogeneous region of B_1^+ aligned with the ROI. 2-Spoke pulses massively improve signal homogenity in all settings. They result in very similar performance for 8 and 16 channel systems, making slices with bad excitation in CP mode accessible to all researchers. Subject safety is improved by means of lowering pSED. Follow up studies need to verify these simulated results *in vivo*. To do so, optimization of spokes pulses must be improved to the point where it becomes feasible to run it online during experiments.

	nRMSE (%)			pSAR (W/kg)		
	8 Dipoles	16 Dipoles	16 Loops	8 Dipoles	16 Dipoles	16 Loops
Whole Brain	14.94	8.84	10.64	0.56	4.61	2.36
Motor Cortex	7.96	6.26	6.32	2.00	2.29	7.56
45 Degree	7.55	5.88	6.28	0.44	1.55	2.50

Tab. 1: Full results of 2-spokes optimization for the GRE sequence.

References

1. Solomakha GA, et al. Evaluation of coaxial dipole antennas as transceiver elements of human head array for ultra-high field MRI at 9.4T. *Magn Reson Med*. 2024; 91: 1268-1280.
2. Nikulin AV, et al. Double-row 16-element folded-end dipole transceiver array for 3D RF shimming of the whole human brain at 9.4 T. *NMR in Biomedicine*. 2023; 36(10):e4981.
3. Avdievich NI, et al. Decoupling of a double-row 16-element tight-fit transceiver phased array for human whole-brain imaging at 9.4 T. *NMR Biomed*. 2018 Sep;31(9):e3964.
4. Eichfelder G, Gebhardt M. Local specific absorption rate control for parallel transmission by virtual observation points. *Magn. Reson. Med.*, 66: 1468-1476.
5. Christ A, et al. The Virtual Family--development of surface-based anatomical models of two adults and two children for dosimetric simulations. *Phys Med Biol.* 2010 Jan 21;55(2):N23-38.
6. Marques JP, Bowtell R. Application of a Fourier-based method for rapid calculation of field inhomogeneity due to spatial variation of magnetic susceptibility. *Concepts Magn. Reson.*, 25B: 65-78.
7. Grissom W, et al. Spatial domain method for the design of RF pulses in multicoil parallel excitation. *Magn Reson Med*. 2006; 56(3):620-629.
8. Setsompop K, et al. Magnitude least squares optimization for parallel radio frequency excitation design demonstrated at 7 Tesla with eight channels. *Magn Reson Med*. 2008 Apr;59(4):908-15.

A Low-Cost Magnetic Measurement System for Low-Field MRI Magnets based on a Motion Tracked Flexible-Joint Robot with 5 Degrees of Freedom

Pavel Povolni[1]*, Robin Bendfeld[2], Sergej Maltsev[1], Kai Buckenmaier[1] and Klaus Scheffler[1,3]

[1] High Field Magnetic Resonance, Max Planck Institute for Biological Cybernetics, Tübingen, Germany
[2] Institute for Nonlinear Mechanics, University of Stuttgart, Stuttgart, Germany
[3] Department of Biomedical Magnetic Resonance, University of Tübingen, Tübingen, Germany

* Contact communicating author: pavel.povolni@tuebingen.mpg.de

Synopsis: The number of low-field MRI scanners is on the rise, mostly due to the low costs and open-source design. Typically, the magnets are based on permanent magnets in Halbach configuration, which show strong manufacturing tolerances. Passive shimming is therefore required. Here, we present a compact and cheap measurement system based on a simple robot arm with 5 degrees of freedom and a self-developed Hall sensor. The functionality of the system is demonstrated by mapping a Halbach magnet with a magnetic field strength of 45mT (length magnet 300mm, diameter of the inner bore 160mm).

Introduction

Magnetic Resonance Imaging (MRI), nowadays a fundamental instrument in diagnostic imaging in Western industrialized countries, causes enormous costs for clinical devices. This significantly limits access in low- and middle-income counties (LMICs)[1]. As an alternative, open source MRI devices using permanent NdFeB magnets in a Halbach-Array have been developed and already used successfully in LMICs.

Halbach-Magnets show high inhomogeneities in the FOV due to manufacturing errors. Shimming becomes necessary. Typical mapping robots are expensive due to mechanics (bearings, etc.) and commercial field probes[2].

We present a new approach by using an inexpensive flexible joint robot in combination with a self-developed Hall-Sensor.

Methods

A robot arm with 5 Degrees of Freedom is used, whereby the joint angles can be set via Servo Motors. Motion tracking based on ArUco markers[3], a standard camera and the OpenCV-Python-library[4] was implemented to increase the accuracy of the system (see Fig. 1). A self-developed magnetic field sensor based on commercial Hall-Sensors (see Fig 2 and Fig 3) is mounted on the robot and is moved inside the magnetic field of a 45mT-Halbach-Magnet (13 disks with 2 circular Halbach-Arrays each, 536 NdFeB magnets) with a length of 300mm and an aperture of 160mm.

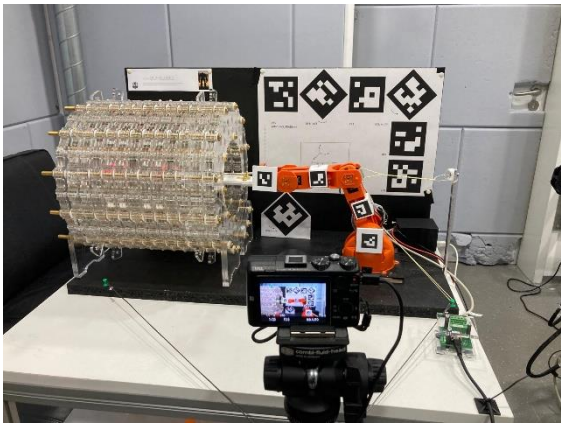

Fig. 1: Photograph of the presented system with the Halbach magnet, the robot arm, the reference board (backside) and the camera (Sony HX60).

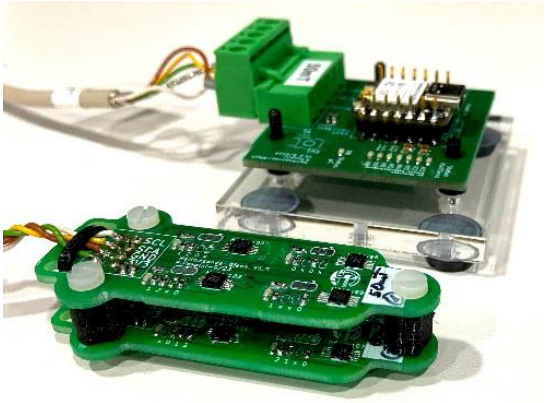

Fig. 2: Photograph of the assembled Hall sensor head (in front) and the central CPU (in background).

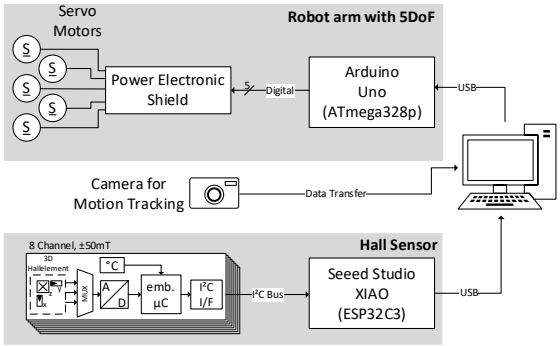

Fig. 3: Schematic of the control and measurement concept. Divided into separate electronics for the robot (based on ATmega 328p) and for the Hall sensor (based on ESP3C3 CPU).

Results

The mapping of the magnetic field in a cubic 75x75x75mm³ FOV with a step size of 5mm (4096 points) was performed in 2.8 hours. Due to the motion tracking a position accuracy <0.1mm was achieved in the xy-plane, which is comparable to standard mapping systems.

A mapping of a FOV with the size 75x75x75 mm³ was conducted with a step size of 5 mm, resulting in 4096 points over 512 movements. The mapping process was completed in less than 2.8 hours. To account for mechanical play in the joints, the measured maps were interpolated to a precise 5 mm grid, increasing the overall point count 6800 (See Fig. 4). Analysis of the interpolated magnetic field data yielded a mean magnetic field strength $\overline{B_0} = 45.26mT$, with a range $44.62mT < B_0 < 45.80\,mT$ and a homogeneity of $\Delta B_0 = 26069\,ppm$.

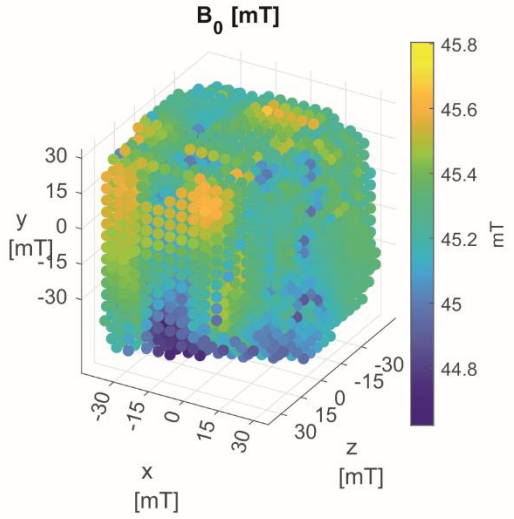

Fig. 4: 3D plot of the mapped magnetic field (interpolated to a perfect 5mm grid) with the presented system.

The accuracy of position determination was highly precise, with deviations along the x and y axes of $\Delta x, y \leq 0.1mm$ and for the z-axis $\Delta z \leq 11.6mm$ (assuming the sensor positioned at the center of the FOV)

Conclusion

The system's effectiveness was demonstrated using a prototype Halbach magnet. The positioning accuracy of the motion-tracked robot showed promising results. In the xy-plane (camera image plane, CIP), the accuracy was quite good and smaller than the measurement volume of the Hall sensor. However, in the yz-plane (perpendicular to CIP), there is a need for improvement to achieve efficient shimming. The Hall sensor demonstrated reliable performance during a measurement campaign that spanned several hours, ensuring both high speed and accuracy throughout the duration. The total cost of the system is less than €100, rendering it an optimal choice for cost-sensitive measurements, particularly in the context of training courses.

References

1. Anazodo UC, Ng JJ, Ehiogu B, Obungoloch J, Fatade A. A framework for advancing sustainable magnetic resonance imaging access in Africa. doi:https://doi.org/10.1002/nbm.4846

2. Han H, Moritz R, Oberacker E, Waiczies H, Niendorf T, Winter L. Open Source 3D Multipurpose Measurement System with Submillimetre Fidelity and First Application in Magnetic Resonance. *Sci Rep*. 2017;7(1):13452. doi:10.1038/s41598-017-13824-z

3. Garrido-Jurado S, Muñoz-Salinas R, Madrid-Cuevas FJ, Marín-Jiménez MJ. Automatic generation and detection of highly reliable fiducial markers under occlusion. *Pattern Recognition*. 2014;47(6):2280-2292. doi:10.1016/j.patcog.2014.01.005

4. Bradski G. The OpenCV Library. *Dr Dobb's Journal of Software Tools*. 2000.

Automated Gas Delivery System for Parahydrogen-Induced Polarisation at up to 10 bar

Harriet Wulff[1,2*], Andrey N. Pravdivstev[1], Frowin Ellerman[1], Martin Sandbrink[1], Philip Saul[1], Jan-Bernd Hövener[1]

[1] University Medical Center Schleswig-Holstein, Kiel University, Department of Radiology and Neuroradiology, Section Biomedical Imaging, Molecular Imaging North Competence Center (MOIN CC), Am Botanischen Garten 14, 24118 Kiel.
[2] Department of Physics, University College Cork (UCC), T12 YN60 Cork, Ireland.

* 121394676@umail.ucc.ie

Synopsis: This project aims to create an automated gas control system suitable for use in parahydrogen-induced polarisation experiments. The system is designed to function at pressures up to 10 bar and supply two gases (hydrogen and nitrogen). Valves and regulators allow for control of pressure and flow rate of gas.

Introduction

Magnetic resonance (MR) is a diagnostic tool commonly used in medical and chemical analysis. However, the low signal-to-noise-ratio (SNR) limits its effectiveness for in-vivo spectroscopy and imaging of nuclei other than 1H [1].

Hyperpolarization of nuclear spins boosts the signal of selected molecules by orders of magnitude, increasing the SNR[1]. One such hyperpolarization method is PHIP where spin order is transferred from parahydrogen (pH_2) to the target molecule and nucleus.

Parahydrogen is introduced to the solution by means of bubbling.

A previous study from our research group already presented the system for PHIP experiments that can tolerate pressures up to 34 bar[2]

Here, our aim was to simplify the system and make it compatible with the most commonly used pressures of about 10 bar. This greatly reduced the costs of the system and made it smaller. The system operates with two gases (e.g. hydrogen and nitrogen) at pressures up to 10 bar. A digital pressure gauge and flowmeter allow for gas pressure and flow to be set and monitored.

Methods

The design for this system was adapted from a previous portable polarizer built by our group[2].

The system consists of 7 solenoid gas valves, 3 needle valves, a flowmeter, digital pressure readout display, 10 bar pressure gauge, a pressure regulator, 2 quick connector intake valves (allowing for two different gas bottles to be simultaneously connected), 7 flip switches (allowing for manual operation), 3 PCBs and an exhaust valve. Each solenoid gas valve was attached to a circuit board with a red LED. The LED would turn on to indicate that the valve was open and turned off when the valve was closed.

The primary PCB was taken from the previous design of this system[2]. By interfacing with a National Instruments NI-USB-6251 card we were able to use pre-existing code to automate the operation.

The system was mounted on a laser-cut PMMA sheet (8 mm Plexiglas XT, Röhm GmbH; Speedy 310, Trotec Laser GmbH) with a handle cut allowing for easy transport and support legs either side for stability. Custom 3D-printed brackets and supports were used to hold all componets in place (Tough PLA filament, S5 3D printer, Ultimaker).

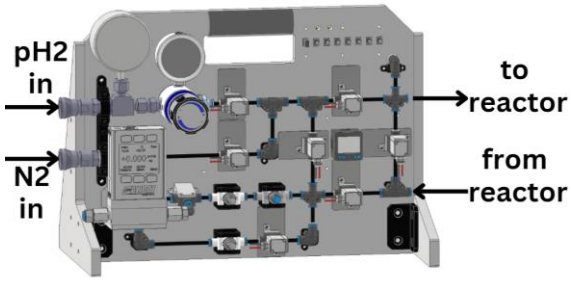

Fig. 1: Autodesk Inventor schematic of the system

Results

The designed (**Fig.** 1) and constructed gas control system (**Fig. 2, 3**) can bubble gas manually by using the flip switches and automatically using software written to the primary PCB board.

The sequence of valve opening and closing for bubbling was created and programmed into our in-house software (MatLab) which was interfaced to a National Instruments digital and analogue output card. This enabled the full bubbling process to be run at the push of a button including venting and accounting for backpressure in the tube. Alternatively, the system can be controlled by TTL commands from the Bruker NMR system.

The needle valves were used to manually fine tune the bubble size. Once the bubbles were set no further adjustment was needed during the course of the experiments.

To test the system we carried out SLIC-SABRE[1] experiments using [1-^{13}C]pyruvate as a substrate. The system was run continuously for a duration of three to five hours over multiple days and maintained consistent output and input pressure of 8 bar. All system components have a specified pressure tolerance of at least 10 bar.

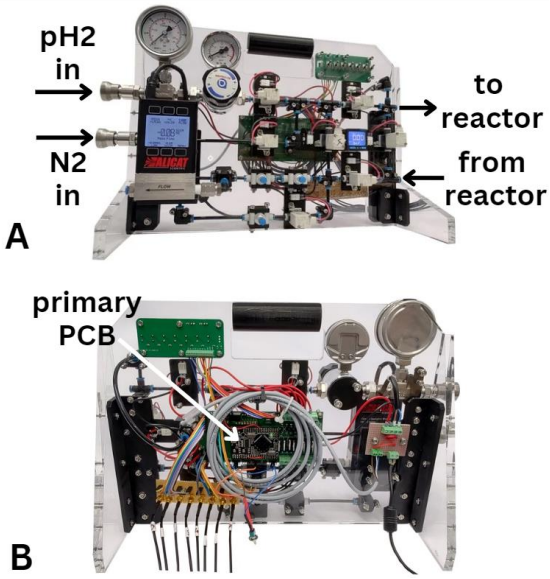

Fig. 2: Gas control setup: front view (A) and back view (B).

Discussion

The system was reliable in outputting parahydrogen gas at consistent pressure over multiple bubbling experiments.

At lower pressures it is possible to use standard 5mm NMR tubes with this device- as they are rated for 10 bar- however, for safety we used high pressure 5mm NMR tubes (rated for 20 bar)

Commercial bubbling systems are available, one example being the Xeus Technologies automated parahydrogen bubbling system. This system operates at pressure of 0-6 bar and costs €7,950 (excluding VAT) and has little opportunity for customization.

Our system has several advantages. It is more cost-effective, costing about €1700. The use of 3D-printed parts allows for easy alteration of the system layout to better fit the lab space. Our system also has a larger operating range of 0-10 bar. The code will soon be published open-source, enabling it to be replicated with off the shelf components.

Our design allows for the pressurization of the reaction solution so that gas is introduced from both sides of the liquid system without causing any splashes. When needed, opening a valve to a backpressure initiates steady bubbling.

Conclusion

The system built provides a reliable, portable, low-cost alternative to commercially available bubbling units for PHIP. The system has been proved to work at 8 bar, with the capacity to operate as high as 10 bar. By interfacing with MatLab code and the National Instruments card the bubbling process can be automated.

Future work will focus on running testing the system at higher pressure as well as automating the system further by adding the capacity to shuttle the sample from the bubbling tube to a benchtop NMR for measurement. We will also consolidate the three PCBs into one board.

Acknowledgments

We acknowledge funding from the German Federal Ministry of Education and Research (BMBF) within the framework of the e:Med research and funding concept (01ZX1915C), DFG (PR 1868/3-1, PR 1868/5-1, HO-4602/2-2, HO-4602/3, EXC2167, FOR5042, TRR287). MOIN CC was founded by a grant from the European Regional Development Fund (ERDF) and the Zukunftsprogramm Wirtschaft of Schleswig-Holstein (Project no. 122-09-053).

References

1. Ellerman F, Pravdivtsev A, Hövener JB. Open-source, partially 3D-printed, high-pressure (50-bar) liquid-nitrogen-cooled parahydrogen generator. *Magn. Reson*. 2021;2(1):49-62. doi:10.5194/mr-2-49-2021

2. Ellermann F, Sirbu A, Brahms A, et al. Spying on parahydrogen-induced polarization transfer using a half-tesla benchtop MRI and hyperpolarized imaging enabled by automation. *Nat Commun*. 2023;14(1):4774. doi:10.1038/s41467-023-40539-9

Easy Rebuildable Cubic 3-Axis Positioning Robot Based on Open-Source Hardware: Validated via Camera-Based Motion Tracking and Initial Application in Magnetic Low Field Mapping

Judith Samlow[1], Sergej Maltsev[1], Kai Buckenmaier[1], Klaus Scheffler[1,2] and Pavel Povolni[1]

[1]High Field Magnetic Resonance, Max Planck Institute for Biological Cybernetics, Tübingen, Germany.
[2]Department of Biomedical Magnetic Resonance, University of Tübingen, Tübingen, Germany

* Contact communicating author: judith.samlow@tuebingen.mpg.de

Synopsis: Homogeneity is a key factor in the development of low-field MRI scanners, especially for scanners based on a Halbach configuration. To enable shimming a precise mapping system is needed, that is cost-effective and easy to build. Here we present a measurement robot designed to evaluate the homogeneity of magnetic fields. By using a decentralized control an easier replication compared to existing systems is achieved. The positioning accuracy is proven with camera-based motion tracking. The system has been validated by mapping the magnetic field of a Halbach magnet.

Introduction

The field of MRI-Scanners is witnessing a growing interest in low-field devices, where the main magnetic field is generated by strong permanent magnets, for example in a Halbach configuration[1]. Apart from the advantages, the poor homogeneity is a significant issue that must be addressed through an additional shimming step. This necessitates the development of precise measurement systems.

Especially the system developed by Han et al.[2] is notable for being cost-effective, open source, precise and customizable due to exchangeable sensors. Based on this open source design, we present an improved design, with special attention paid to a wider range of applications and a simplified electrical system (see Fig 1).

Furthermore, the positioning accuracy of the developed system was validated by camera-based motion tracking, thereby enabling the identification and subsequent correction of any positioning errors made by the robot.

Fig. 1: Image of the robot with coordinate axes and mounted ArUco markers for precision measurement. The coordinate system utilized is a left-handed coordinate system.

Methods

The cubic frame was designed with item aluminum profiles. The robotic arm is moved by stepper motors through ball screw spindles. The motors can be controlled manually by a remote control or via a computer interface. To ensure that the system is as easy as possible to replicate and expand, the system has been decentralized (see Fig 2):

The hardware control is based on a central microcontroller using the Arduino Mega 2560, which facilitates the integration of further use cases though the open source hardware approach. The position is controlled via a Python script on the computer, thereby enabling the planning of complex trajectories with minimal effort. Furthermore, this script is capable of reading the current value of the Hall sensor. The accuracy was evaluated through motion tracking, using a standard camera.

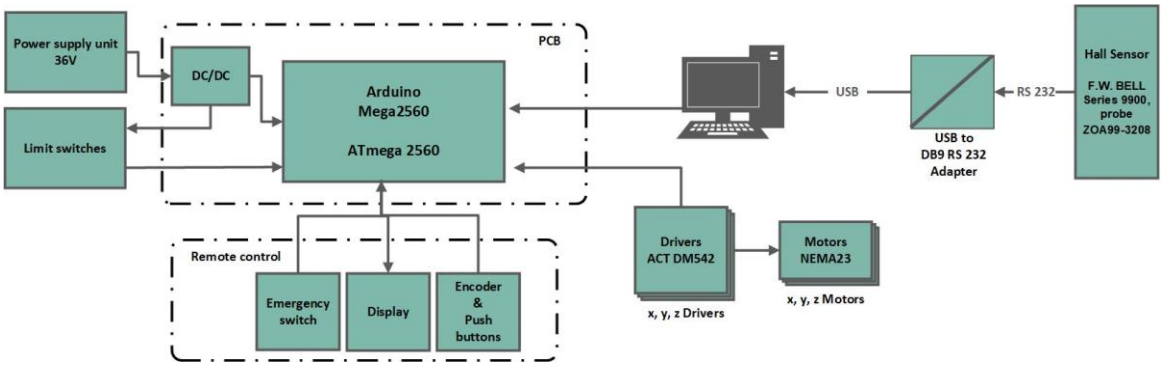

Fig. 2: Schematic structure of the electronic subsystem with the central microcontroller as the main component

The python library OpenCV[3] was used in combination with ArUco Markers[4] attached to the robot, whereby this type of markers proved to be reliable and easy to generate.

The system was validated by mapping a Halbach magnet (536 NdFeB magnets, $B_0 = 45mT$, length $300mm$, inner diameter $160mm$) using a 3axis Hall sensor (F.W. BELL Series 9900, probe ZOA99-3208, accuracy $\pm 0.57\%$).

Results

The Halbach magnet was mapped with a step size of $5mm$ in a cubic volume of $100 \times 100 \times 100mm$. The analysis of the motion tracked sensor showed a deviation of $\Delta x = 1.5\,mm,\ \Delta y = 1.9\,mm,\ \Delta z = 0.3mm$ (resp. Euler angles of $\alpha_x = 0.64°, \alpha_y = 0.45°,$ $\alpha_z = -0.42°$).

The mapped field of overall 9261 points is shown in Fig 3, whereby the measurement took in total 38 hours. The long duration can be attributed to the used Hall sensor due to a slow update rate and averaging for improved accuracy. Furthermore, the used USB/serial adapter introduced a disruption of the connection, necessitating a restart of the Hall sensor at some points. Due to an automatic offset compensation during the restart, a jump of the measured values can be observed.

The average magnetic field was $B_0 = 43.75\,\mathrm{mT}$ with a homogeneity of 5.5 %.

Conclusion

The functionality of the system was validated by tracking the sensor's position and by mapping it to the magnetic field of a Halbach magnet. Improvements can be expected through a more reliable communication.

The error through the positioning accuracy of the robot is lower than the measuring volume of the sensor, so that it is sufficiently accurate. In order to approach the entire measuring range, the calculated Euler angles can be stored as a calibration. Therefore, the remaining error will be only influenced by the mechanical play of the drive. The decentralized control system has demonstrated its efficacy, rendering it readily scalable and adaptable to new tasks. A detailed documentation of the system will be released as open source.

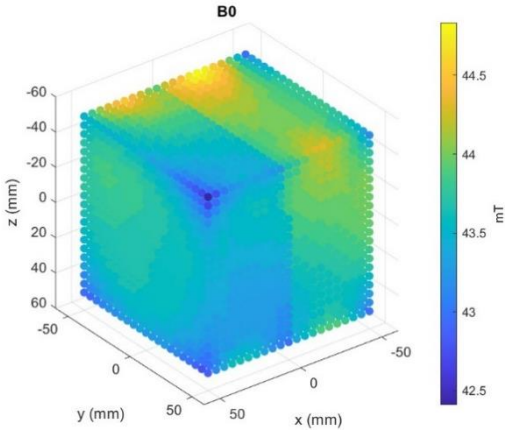

Fig. 3: Magnetic field of a Halbach magnet, whereby an average magnetic field of $B_0 = 43.75\,mT$, an overall homogeneity $\Delta B = 5{,}5\%$ were measured. The jump at $\Delta x = 5mm$ is due to a restart of the sensor.

References

1. Raich H, Blümler P. Design and construction of a dipolar Halbach array with a homogeneous field from identical bar magnets: NMR Mandhalas. Concepts in Magnetic Resonance Part B (Magnetic Resonance Engineering) 2004;23B(1):16-25. DOI: 10.1002/cmr.b.20018.

2. Han H, et al. Open source 3D multipurpose measurement system with submillimeter fidelity and first application in magnetic resonance. Scientific Report 2017;7(1):13452.

3. Bradski G. The OpenCV Library. Dr Dobb's Journal of Software Tools. 2000.

4. Garrido-Jurado S, Muñoz-Salinas R, Madrid-Cuevas FJ, Marín-Jiménez MJ. Automatic generation and detection of highly reliable fiducial markers under occlusion. *Pattern Recognition*.2014;47(6):2280-2292. doi:10.1016/j.patcog.2014.01.005

Inductively coupled coils for 1.5 T, 3 T and 7 T MRI

Moritz T. Sander[1] and Prof. Jan-Bernd Hövener[1,*]

[1] Section Biomedical Imaging, Molecular Imaging North Competence Center (MOIN CC), Department of Radiology and Neuroradiology, University Medical Center Schleswig-Holstein (UKSH), Kiel University, Kiel, Germany
* Jan.Hoevener@rad.uni-kiel.de

Synopsis: This work reproduces and characterizes inductively coupled coils previously used in dental MRI for use in other body parts and small animals. The coils were successfully constructed and characterized, but further testing using an MRI is needed.

Introduction

To improve image quality for small volume elements, inductively coupled coils (ICC) have successfully been used for dental MRI[1–3]. However, such coils are not widely available yet. The aim of this work was to reproduce and study these coils so that the concept maybe applied to other parts of the human body, other nuclei or small animals (e.g. finger joints, ^{13}C or mice, respectively).

Methods

ICCs were composed of two connected, circular loops with diameter *d* and distance *a*, wound on a 3D printed winding aid with 1,25 mm diameter insulated copper wire. A crossed diode and one or multiple (trimmable) capacitors were added in parallel to the coil (Farnell BAV99 DIODE, Johanson Cera-Trim Capacitor JK-023, Johanson Technology High Q/Los ESR Non-magnetic ceramic capacitor). The ICCs were coated with pattern resin (GC America pattern resin LS).

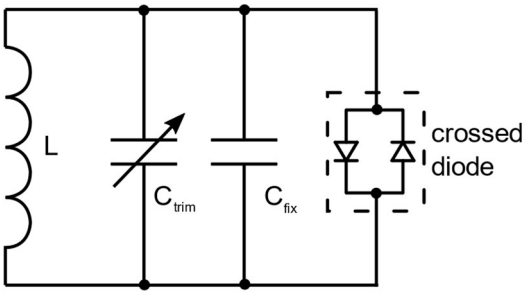

Fig. 1: Circuit diagram of an ICC consisting of a coil L, a fixed capacitor C_{fix}, a variable capacitor C_{trim} and a crossed diode.

A pick-up coil was built by bending a 2 mm diameter insulated copper wire into a circle of 8 cm and connecting each end to the inner and outer wire of a cut open coaxial cable.

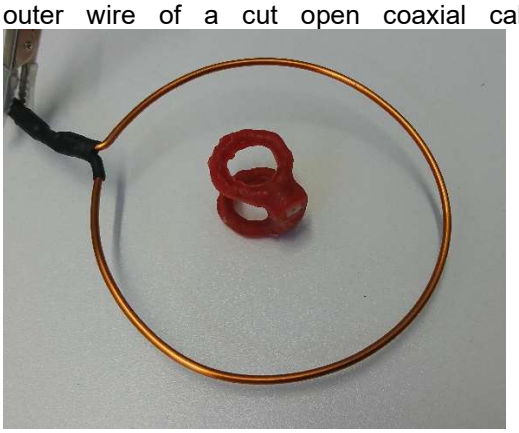

Fig. 1: Picture of ICC No. 5 inside a pick-up coil. The pick-up coil was elevated to the center of the ICC and connected to the network analyzer.

The ICCs were analyzed using a network analyzer in S_{11} mode and a pick-up coil (Rohde & Schwarz ZNL3 Vector NA 5 kHz-35 GHz). The resonance frequency of the coil was identified by an increased absorption of the S_{11} measurement, and the frequency span of the ICC was investigated by variation of the trim capacitor.

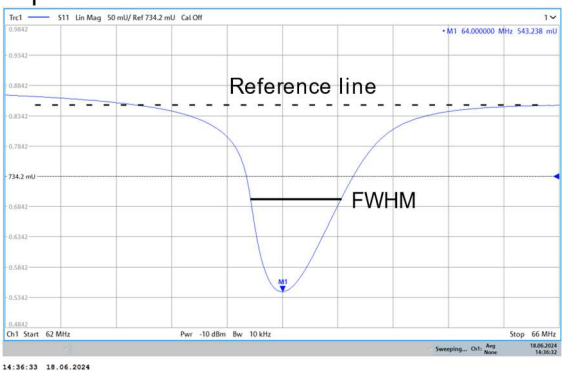

Fig. 2: Screenshot of the S_{11} measurement on the network analyzer, showing the absorption (ordinate, arbitrary units) as a function of frequency (abscissa, MHz). Here, the dip in the absorption at 64 MHz indicates the resonance of the coil (ICC 5), and the width (FWHM) was used to calculate the quality factor *Q*.

To determine the quality factor *Q*, the resonance frequency was divided by the full width at half minimum of the dip.

The inductivity of the coil was measured by using an LCR bridge (Rohde & Schwarz HM8118 LCR Bridge, 20 kHz) or calculated by using the nominal capacitance of the parts at highest and lowest trim and their corresponding resonance frequency (average).

The effect of the crossed diodes (decoupling) was investigated by observing changes in shape and position of the absorption peak as a function of transmission power.

To determine the impact of loading, a finger was moved in and out of the ICC (without touching it) and calculating the quality factor.

Results

A total of six ICCs with different sizes and capacitors were constructed, where the first few served mainly practicing purposes. ICC 5 and 6 were coated for further study in a 1,5 T and 3 T MRI.

ICC no.	4	5	6
***a* (cm)**	1,5	1,5	2
***d* (cm)**	1,5	1,5	2
C_{fix} (pF)	-	68	15
C_{trim} (pF)	6,5-25	6,5-25	1-5
$f_{r,min}$(MHz)	104	59,2	110,3
$f_{r,max}$ (MHz)	271	68,7	123,5
***L* (nH)**	-	75	104
Q	82,1	95,6	68,6

Tab. 1: Specifications of ICC 4 to 6. The values for ICC 5 and 6 correspond to their coated state.

ICC 6 showed a different frequency span after coating, changing from 111,5-125,4 MHz to 110,3-123,5 MHz, while ICC 5 was much less affected, only shifting downwards by 0,2 MHz.

ICC 4, which has no fixed capacitor, was used to investigate loading. The quality factor changed from 82,1 without load to 81,9 with load.

ICC 5 (coated) was used to investigate decoupling. At -10 dBm power setting, the resonance frequency is 64,2 MHz with a quality factor of 91,7. At 0 dBm the resonance frequency was shifted to 63,7 MHz with a quality factor of 35,4.

An ICC designed for use in a 7 T small animal MRI is under construction. Reaching the high frequencies needed appears not to be straight forward with the capacitors at hand.

Discussion

The ICCs were successfully reproduced as described in Ref. 1-3, although a test with MRI has yet to be performed.

The shifting of the resonance frequency for ICC 6 may become problematic, since the upper limit reaches close to the needed frequency of 123,24 MHz. Why this shifting after coating occurred in one ICC, but not the other, could not be explained.

Compared to previously constructed ICCs, a significant decrease of the quality factor should be expected when the ICC is loaded[1]. Unexpectedly, this did not occur with ICC 4.

Increasing the transmit power to bridge the diodes showed the expected result, where the resonance frequency was shifted and Q drastically reduced. Stronger shifts are expected for stronger transmission. Temperature and MRI measurements inside the MRI may help to ensure no unwanted effect on the temperature.

Determining the inductance of the coils with the LCR bridge used here appears to be unreliable, as it is measured at 20 kHz and does not match the inductance calculated by known capacity and corresponding resonance frequency and is also varying strongly. The differences in the calculated inductance ($L_{C,trim}$=104 nH and $L_{C,fix}$=95 nH) were likely caused by tolerances of the parts. For creating ICCs of similar sizes at different resonance frequencies, a good estimation of *L* is crucial for estimating the needed capacity.

Conclusion

The ICCs were successfully constructed and characterized with the network analyzer. Experimental verification of decoupling and MRI still have to be performed.

References

1. Ludwig, U. *et al.* Dental MRI using wireless intraoral coils. *Sci Rep* **6**, 23301 (2016).
2. Tesfai, A. S. *et al.* Inductively Coupled Intraoral Flexible Coil for Increased Visibility of Dental Root Canals in Magnetic Resonance Imaging. *Invest Radiol* **57**, 163–170 (2022).
3. Amrein, P. Inductively coupled intraoral receiving coils for dental MRI, Master Theis, U. Freiburg 2017.

SQUID based Method of Evaluating Noise Characteristics of High Temperature Superconductors used in Novel Low Field MRI Scanner Designs

Sergej Maltsev[1]*, Pavel Povolni[1], Marcel Schneider[1], Klaus Scheffler[1,2] and Kai Buckenmaier[1]

[1] High Field Magnetic Resonance, Max Planck Institute for Biological Cybernetics, Tübingen, Germany
[2] Department of Biomedical Magnetic Resonance, University of Tübingen, Tübingen, Germany

* Contact communicating author: Sergej.maltsev@tuebingen.mpg.de

Synopsis: Typical modern MRI devices are based on first-type superconductors, which need to be cooled by liquid helium. To enhance cost efficiency, the feasibility of utilizing high-temperature superconductors (2nd generation) cooled by liquid nitrogen is currently under investigation. However, it is essential to note that these modern superconductors exhibit a considerably higher noise level, which must be considered when designing the magnet of low-field MRI scanners. Here, we present a method for evaluating the intrinsic noise of high-temperature superconductors for low-field MRI applications.

Introduction

One of the most crucial methods for clinical diagnosis is Magnetic Resonance Imaging (MRI), which is employed particular in neuroscience and in the examination of soft tissue. Typical commercial MRI Scanners generate the main magnetic field with electric coils build from first-type superconductors cooled by liquid helium. This setup requires complex cryostats and results in high operational costs, thereby limiting access to this technology even in industrialized countries.[1]

To reduce the overall cost of MRI, new designs are being developed, such as low-field MRI utilizing high-temperature superconductors (HTS). By incorporating a suitable design, cooling with liquid nitrogen can be sufficient, leading to reduced operating costs. However, HTS generally intrinsically produce higher levels of noise. We present a method for investigating the noise characteristics of HTS at different operating points using a SQUID (superconducting quantum interference device)-based setup. The method was validated by evaluating the noise level of an HTS based on Gadolinium/Barium/Cuprate (GdBaCO).

Theory

Due to the complex crystal structure of HTS, crystal defects in the crystal layers are unavoidable. Sources of magnetic $1/f$ noise are the fluctuating magnetic moments of magnetic impurities or dangling bonds found in superconducting inductances, surface oxides, insulating oxide layers, and adsorbates. To capture magnetic flux inside the HTS, the external field needs to be applied during the cooling process, due to the so-called Meissner effect. Because of the relatively high operating temperature of $77.2\,K$ (boiling point of liquid nitrogen), the remaining thermal energy leads to strong excitation of the flux vortices, resulting in increased $1/f$ noise for the captured magnetic flux[2].

Methods

The HTS is cooled with liquid nitrogen. Accordingly, a holder was designed with a sufficiently large reservoir for the cooling medium, capable of withstanding the cryogenic temperature of liquid nitrogen (see Fig. 1). To capture magnetic flux inside the HTS, a permanent magnet with a central magnetic flux density of $45\,mT$ (Halbach Magnet, consisting of 536 NdFeB magnets) was used. To adjust the magnetic strength, the cooling process was carried out slightly further away from the center of the Halbach aperture at $B = 20.3\,mT$. The

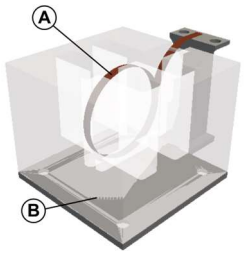

Fig. 1: Holder of the superconductor. (A) Superconductor GdBCO wound into a circular coil. (B) holder with a reservoir.

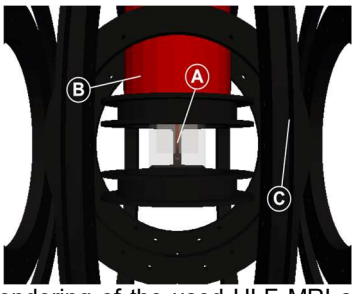

Fig. 2: Rendering of the used ULF MRI setup. (A) Holder of the HTS. (B) Position of the SQUID and (C) ULF MRI.

HTS wire is wound into a circular coil with a diameter of $40\ mm$.

To evaluate the magnetic field, the holder with the HTS was placed inside an Ultra-Low-Field (ULF) MRI system based on a SQUID (see Fig. 2). In order to obtain an accurate assessment of the noise observed in the HTS, it is essential to consider the background noise present in every measurement as a reference. The ULF-MRI is encased in a magnetic cancelation chamber, which ensures that only a residual magnetic flux density of less than $15\ nT$ is remaining. RF background noise is effectively shielded by the chamber. The noise signal was processed by capturing the generated noise inside the second-order gradiometer of the ULF system, which transforms it on to the SQUID (see Fig. 3). The resulting voltage was digitized with an Analog-to-Digital Converter (National Instruments PXI-6723, sample rate $\mathrm{f_{samp}} = 600\ kS/s$, $ENOB = 13\ bit$) and evaluated on a computer [3].

Results

The HTS GdBaCO has a length of 3.2 meters, resulting in 25 turns. The measured spectrum of this HTS is shown for two experiments (superconducting transition in magnetic field and transition without magnetic field) in Fig. 4. To reduce the influence of white noise and quantization noise from the ADC on the evaluation, ten measurement points were averaged.

A $1/f$ behavior is clearly discernible in both measurements, with a transition to white noise at higher frequencies. In the case of the trapped flux measurement, this transition occurs at

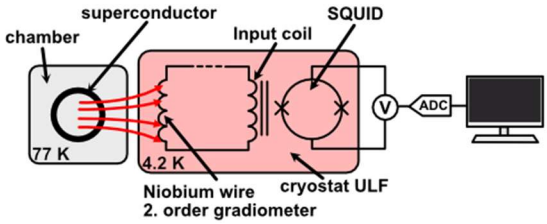

Fig. 3: Schematic representation of signal processing

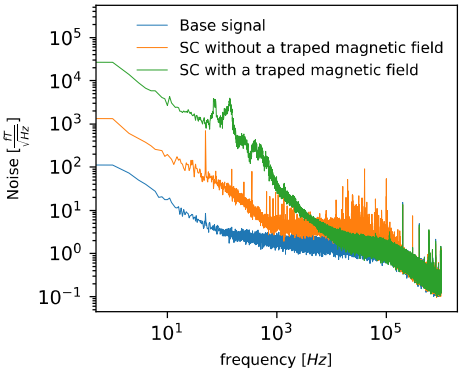

Fig. 4: Noise spectrum of the 2 experiments. In addition, the background noise was measured without the holder in the scanner.

approx. $10\ kHz$. Consequently, the influence of noise for this amount of HTS would no longer be noticeable in a proton-based NMR/MRI experiment for a $B0 > 240\mu T$. However, it needs to be noted that in a real build MRI scanner the overall quantity of HTS is significantly larger, which consequently results in elevated noise power.

Conclusion

The presented method for investigating the noise characteristics of HTS cooled with liquid nitrogen at 77.2K has been demonstrated to be functional. The measured HTS GdBaCO has been shown to be unsuitable for ultra-low-field MRI applications. However, at higher fields this should not be a problem, although the overall noise power is expected to increase due to the significantly higher amount of needed HTS.

For further investigation, simulations based on the aforementioned results can be designed, and therefore obtain a more detailed correlation and in-depth insights of the HTS itself.

This allows in the end the development of a low-noise low-field MRI magnet based on HTS with field strengths that can be designed to work at the lowest possible field strengths, thereby expanding the range of potential applications for superconductor-based MRI technology.

References

1. Hricak H, Abdel-Wahab M, Atun R et al Medical imaging and nuclear medicine: a Lancet Oncology Commission. Lancet Oncol. 2021 Apr;22(4):e136-e172. doi: 10.1016/S1470-2045(20)30751-8..
2. Herbst, M., Fleischmann, A., Hengstler, D. et al (2023). Measuring Magnetic 1/f Noise in Superconducting Microstructures and the Fluctuation-Dissipation Theorem - Data [Dataset]. In Zenodo (CERN European Organization for Nuclear Research). https://doi.org/10.5281/zenodo.7774388
3. Buckenmaier, K., Rudolph, M., Fehling, P. et al (2018b). Mutual benefit achieved by combining ultralow-field magnetic resonance and hyperpolarizing techniques. Review of Scientific Instruments Online/Review of Scientific Instruments, 89(12). https://doi.org/10.1063/1.50433

Scientific Session 3

MRI Sequence Development and Optimization

Oral presentations

301	Andreas Holl	*Open SPEN and Non-linear Gradient Implementation using Pulseq*
302	Simon Weinmüller	*MR-zero meets FLASH – Controlling the transient signal decay in gradient- and rf-spoiled gradient echo sequences using Phase Distribution Graphs*
303	Martin Freudensprung	*Reproducible pTx sequence development using Pulseq*
304	Ariel Hannum	*PNS-Constrained Arbitrary Gradient Waveform Design for DWI on Ultra-High-Performance MRI Systems*
305	Fabian Gutjahr	*Addressing the Ejection Fraction Dependence of FAIR-ASL Perfusion*
306	Jacopo Frignani	*3D Filter-Exchange Imaging Using Slab-Selective Excitation*
307	Niklas Himburg	*Errors in Actual Flip Angle Imaging (AFI) of polyvinylpyrrolidone (PVP) solutions at 3T and 7T*
308	Yannik Ott	*Training deep learning reconstruction models for radial real-time cardiac cine MRI using synthetic golden-angle data*

Posters

P301	Chris Lippe	*CEST MRI multi-pool quantification through simplified model-based analysis*
P302	Jonathan Endres	*Direct Encoded Signal Control with Phase Distribution Graphs for readout-tailored multipulse pTx optimization*
P303	Franziska Lohrengel	*Implementing whole brain spectroscopy on a vendor agnostic pulse programming platform*
P304	Caroline Scheufler	*Optimization of multi-VENC compressed sensing 4D flow MRI for high-resolution neurovascular applications*
P305	Clemens Mey	*SNR requirements for quantitative frequency-modulated bSSFP*
P306	Clemens Mey	*T2 mapping based on frequency-modulated bSSFP*
P307	Fabian Müller	*The impact of fat-navigator resolution on motion parameter estimation accuracy*
P308	Jakob Schattenfroh	*Ultra-Low Frequency MR Elastography*

Open SPEN and Non-linear Gradient Implementation using Pulseq

AndreasHoll[1*], Frank Zijlstra[2], Maxim Zaitsev[1] and Sebastian Littin[1]

[1] Department of Radiology, Medical Physics, University Freiburg, Faculty of Medicin, Freiburg, Germany.
[2] Department of Radiology and Nuclear Medicine, St. Olav's University Hospital, Trondheim, Norway.

* andreas.holl@uniklinik-freiburg.de

Synopsis: We implemented spatiotemporal encoding in Pulseq to increase the accessibility. We also showed that additional gradient hardware can be used for spatiotemporal encoding.

Introduction

SPatiotemporal-ENcoding (SPEN) represents an alternative encoding method in Magnetic Resonance Imaging (MRI). A quadratic phase profile is utilized for encoding with the objective to establish a direct correlation between the acquisition time and the spin's position. Recent research has demonstrated that SPEN has the potential to mitigate geometric distortions due to magnetic field inhomogeneities and to circumvent chemical shift artifacts [1,2]. A linearly frequency-swept Radio Frequency (chirp RF) pulse is usually employed to generate the quadratic phase profile. It has been demonstrated that the quadratic phase profile can also be induced by utilizing the built-in active shimming coils [2]. However, temporal control of active shim coils is usually not possible, and they are not magnetically screened. Therefore, this approach renders a clinical application impractical [2].

Despite the aforementioned limitations, SPEN methods remain inaccessible due to their experimental status. The implementation on different MRI systems from different vendors is a significant challenge that is hindering further research on this topic.

In this work, we present the implementation of SPEN in the open-source framework Pulseq for vendor-independent pulse sequence development. Our objective is to remove the barriers to accessibility and reproducibility of SPEN by making the implementation openly available.

In addition, the SPEN implementation allows to control additional gradient hardware to induce a quadratic phase profile without the need of a lengthy and SAR intensive chirp RF pulse. We demonstrate that non-linear gradients can be employed to perform SPEN, taking advantage of the spatial encoding without being constrained by the drawbacks associated with the use of a chirp RF pulse or active shimming coils for the generation of a quadratic phase profile.

Methods

Pulseq implementation: We implemented a wideband, uniform rate, smooth truncation (WURST) adiabatic pulse function for Pulseq in MATLAB (R2023b, The Mathworks, Inc., Natick, Massachusetts) along with appropriate gradient calculations, fulfilling the SPEN condition [1,2]. Moreover, we implemented the possibility to include a gradient waveform for external gradient hardware control into the developed Pulseq sequence [3].

To show the advantages of SPEN, we implemented a SPEN-Spin-Echo (SPEN-SE) and a SPEN-SE-Echo-Planar Imaging (SPEN-SE-EPI) sequence utilizing the developed chirp pulse function and the additional gradient hardware for the quadratic phase profile generation.

We used an 84-channel non-linear matrix gradient coil [3] and the same EPI K-space trajectory for both methods. For reconstruction, we used a convolution method, which is capable of suppressing aliasing artifacts. The SPEN images were acquired on a 3T Siemens Trio (Siemens Healthineers, Erlangen, Germany) equipped with a custom built 31-channel head coil. A spherical phantom which contains rods with different diameters was imaged.

Results & Discussion

The developed chirp RF pulse function in Pulseq enables to define the desired flip angle, the sweeping bandwidth and amplitude modulation of the RF pulse. The chirp RF function in combination with the appropriate SPEN excitation gradient and acquisition gradient allow to excite the spins in a desired slice and simultaneous induce a quadratic

phase profile. The phase parabola can then be used for encoding combined with different acquisition methods like EPI. As can be seen in the characteristic shape of the hybrid K-space data in Fig.1, the SPEN implementation using the chirp RF method works and it is possible to achieve artifact-free images, also shown in Fig.1.

Compared to the hybrid K-space data in Fig.2 acquired by using the external non-linear matrix gradient coil to induce the quadratic phase profile, it is visible that gradient imperfections have a greater impact on the chirp RF method than on the additional gradient hardware method. Although there are no visible differences in the reconstructed images in Fig.1 and Fig.2 due to the aliasing and ghosting suppression of the used reconstruction method. In the hybrid K-space data of the chirp RF method in Fig.1 is also a greater signal attenuation visible, compared to the external gradient method. Because a longer RF duration is necessary to keep the sweeping-bandwidth lower to stay within the Specific Absorption Rate (SAR) limitations, the at the beginning excited spins are losing more signal during the acquisition. The signal loss and SAR limitation problems are mitigated by using the external gradient method since a normal EPI excitation and read-out is used with an application of the quadratic gradient in between. By choosing the duration of the external gradient to be the same as the delay to achieve the desired repetition time, the SPEN external gradient method does not require additional time compared to a normal SE-EPI sequence.

Conclusion

SPEN was successfully implemented in Pulseq. This will increase the accessibility to SPEN methods significantly. Without additional effort and with little compromises it is possible to combine SPEN with other acquisition methods to counteract field inhomogeneities and chemical shift artifacts by using the uploaded chirp RF pulse and external gradient method implementation and example Pulseq sequences [4]. As visible in Fig.3, we also showed that it is possible to generate the necessary quadratic phase profile by using additional gradient hardware to fully exploit the advantages of SPEN without suffering from SAR limitation and long RF pulses arising from the chirp RF pulse method.

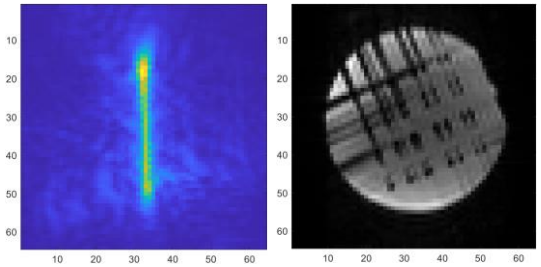

Fig. 1: Hybrid k-space data (left) and reconstructed SPEN-SE-EPI image (right) acquired by using the chirp RF method.

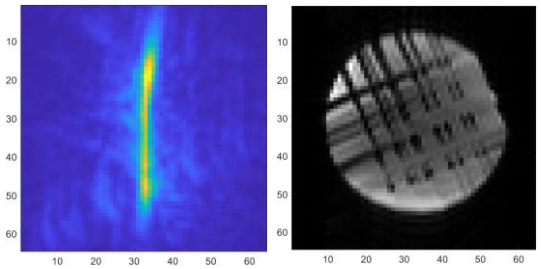

Fig. 2: Hybrid k-space data (left) and reconstructed SPEN-SE-EPI image (right) acquired by using the external gradient hardware to generate the quadratic phase profile for encoding.

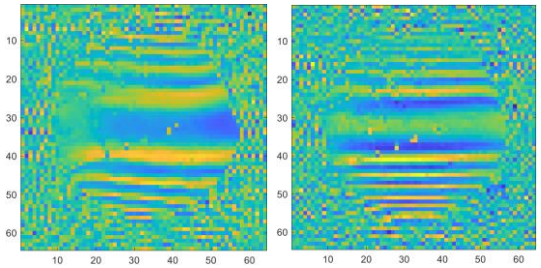

Fig. 3: Quadratic phase profile of the reconstructed images using the external gradient hardware for the generation of the quadratic phase profile (left) and using the chirp RF pulse method (right).

References

1. Pipe J G. Spatial Encoding and Reconstruction in MRI with Quadratic Phase Profiles, Magnetic Resonance in Medicine. 1995; **33**(1), 24--33.

2. Marhabaie S, Bodenhausen G and Pelupessy P. Spatio-temporal encoding by quadratic gradients in magnetic resonance imaging. Journal of Magnetic Resonance Open. 2020; Volumes 4–5, 2020, 100008.

3. Littin S, Jia F, Layton K J, Kroboth S, Yu H, Hennig J and Zaitsev M. Development and implementation of an 84-channel matrix gradient coil. Magnetic Resonance in Medicine. 2017; **79**(2), 1181--1191.

4. Open SPEN implementation using Pulseq: https://github.com/andih98/Open-SPEN

MR-zero meets FLASH – Controlling the transient signal decay in gradient- and rf-spoiled gradient echo sequences using Phase Distribution Graphs

Simon Weinmüller*,[1] Jonathan Endres,[1] Nam Dang,[1] Rudolf Stollberger,[2] Moritz Zaiss[1,3]

[1] Institute of Neuroradiology, Universitätsklinikum Erlangen, Friedrich-Alexander-Universität Erlangen-Nürnberg, Erlangen, Germany
[2] Insitute of Biomedical Imaging, Graz University of Technology, Graz, Austria
[3] Department Artificial Intelligence in Biomedical Engineering, Friedrich-Alexander-Universität Erlangen-Nürnberg, Erlangen, Germany

* simon.weinmueller@uk-erlangen.de

Synopsis:

We propose a flexible method for improving the transient signal behavior of gradient- and rf-spoiled gradient echo sequences / FLASH-sequences, which was validated in vitro and in vivo. The proposed flip angle train and phase cycling can improve small artifacts in magnitude and phase images

Introduction

A common problem in transient Fast Low-Angle Shot (FLASH) sequences is the decay of the magnetization which still affects quality of the image, as the decay in k-space acquisition leads to ringing or blurring artifacts. This decay can be described by the Look-Locker decay rate[1]:

$$S_{LL}(n \cdot TR) = (S_i - S_{SS}) \cdot \exp\left(-\frac{n \cdot TR}{T_{1,LL}}\right) + S_{SS}. \quad (1)$$

Interestingly, this mono-exponential reflects an idealized description in the case of ideal spoiling. In real measurements the signal decay follows only coarsely this exponential function, but has complex substructure that depends, among other factors, on the rf-spoiling[2]. Herein, these deviations are reproduced and reduced using the end-to end optimization MR-zero[3].

Methods

Unencoded measurement (Phantom)

To visualize the substructures, FLASH sequence parameters as described by Epstein et al.[2] are employed for both, unencoded simulation and measurement: α = 10°, TR = 10 ms, TE = 5 ms, bandwidth = 217 Hz/pixel, FOV = 200 mm, slice thickness = 10 mm, matrix = 128 x 128, rf spoiling with a quadratic increment of Ψ = 117° and gradient spoiler, saturation preparation with recovery time TREC = 970 ms. Parameters of a tube phantom (T1 ≈ 1.0 s, T2 ≈ 0.17 s, D ≈ $1.6 \cdot 10^{-3}$mm²/s) were set in a single voxel phantom for unencoded simulations and optimization.

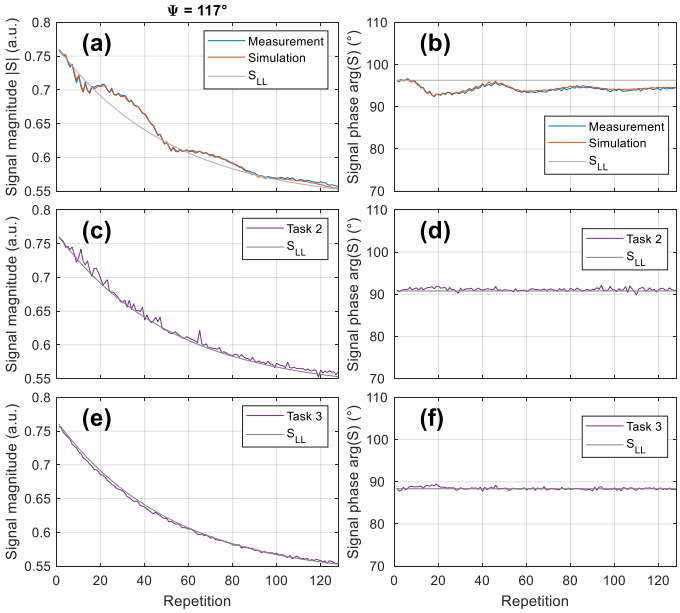

Fig. 1: Unencoded FLASH signal magnitude and phase for Ψ = 117° (a,b), task 2 (c,d) and task 3 (e,f).

Encoded measurement (Subject)

To make the existing signal fluctuations stronger visible in an image, we decreased TE and increase the flip angle. To achieve shorter TE and TR of TE = 3.2 ms and TR = 6 ms, the bandwidth was increased to 500 Hz/pixel. The excitation flip angle α = 19.5° was increased and no preparation was used. We doubled the resolution using a 2-shot sequence with the same rf trains for each shot. For optimization task, again just one representative voxel was used with parameters matching the median of the brain phantom (T1≈1.5s, T2≈0.11s, D≈0.84·10^{-3}mm²/s). All other parameters where chosen equally to the unencoded experiment. A centric reordering for acquisition was used.

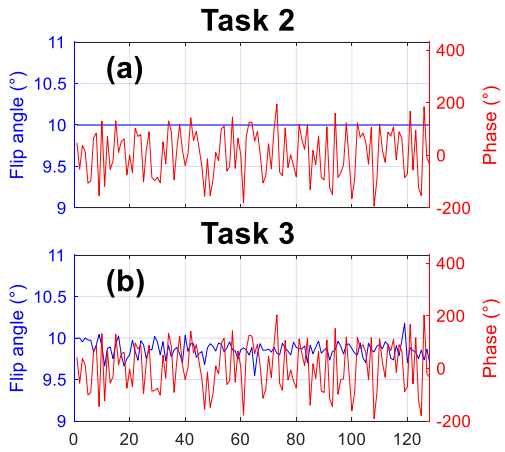

Fig. 2: Flip angle und phase of rf trains of task 2 (a) and 3 (b).

For simulation and optimization the differentiable end-to-end optimization framework MR-zero[3] employing the with Phase Distribution Graph simulation[4] written in PyTorch is used to optimize rf trains of the FLASH sequence using the ADAM optimizer. We focus herein on minimizing deviations from the ideally spoiled signal S_{LL} by using a mono-exponential Look-Locker target.

We first obtain the transient FLASH signal decay substructure, and then minimize the deviation to the Look-Locker decay by optimizing the individual (task 1) flip angles ($\vec{\alpha}$), task 2) rf phases ($\vec{\varphi}$) and (task 3) flip angles and rf phases ($\vec{\alpha},\vec{\varphi}$). Comparison between measurement and simulation are performed using Pulseq[5] in 1D and 2D.

The measurements were performed at a 3T MAGNETOM PRISMA scanner (Siemens Healthcare, Erlangen) on healthy subjects after written informed consent and approved by the local ethics committee.

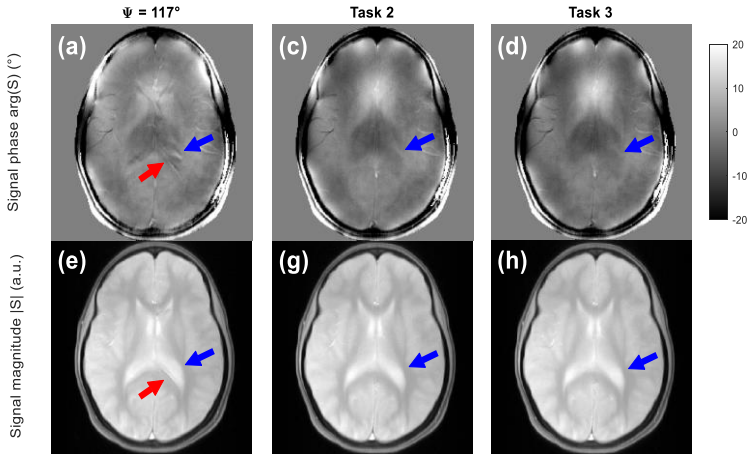

Fig. 3: FLASH magnitude and phase images for Ψ = 117° (a,e), task 2 (c,g) and task 3 (d,h).

Results

We focus here on task 2 and 3 and Ψ = 117°. In Fig. 1, we obtain the finding of Epstein et al.[2] and find an excellent agreement between measurement and simulation in the unencoded experiment (a,b). The overall result is that for task 2 and 3 we get closer to the target signal upon optimization. The individual flip angles and rf phases for the two optimization tasks are visible in Fig. 2.

The FLASH magnitude and phase images can be seen in Figure 3. The rf increment of 117° produce clear artefacts in the magnitude image, as well as in the phase image. This is reduced by task 2 and 3

Discussion and Conclusion

We revisited the problem of the transient FLASH signal decay using the end-to-end MR-zero framework. We showed that a general target-driven signal optimization is possible by optimization of each and every rf pulse angle and phase of the pulse sequence.

Interestingly, our rf phase cycling optimization challenges the often-used concept of quadratic phase cycling. Thus, we want to point out that a quadratic phase cycling Ψ, most famous Ψ=117°, is derived using a steady-state argumentation, by finding the signal that is most close to the dynamic FLASH equation or Look-locker equation[6]. Our solution has impact on model-based Look-Locker reconstruction, by improving T1 quantification (data not shown).

References

1. Look DC. Time Saving in Measurement of NMR and EPR Relaxation Times. Review of Scientific Instruments. 1970;41(2):250-251.
2. Epstein FH. Spoiling of transverse magnetization in gradient-echo (GRE) imaging during the approach to steady state. MRM. 1996;35(2):237-245.
3. Loktyushin A. MRzero - Automated discovery of MRI sequences using supervised learning. MRM;86(2):709-724.
4. Endres J. Phase distribution graphs for fast, differentiable, and spatially encoded Bloch simulations of arbitrary MRI sequences. MRM. 2024; 1-16.
5. Layton KJ. Pulseq: A rapid and hardware-independent pulse sequence prototyping framework: Rapid Hardware-Independent Pulse Sequence Prototyping. MRM;77(4):1544-1552.
6. Zur Y, Wood ML, Neuringer LJ. Spoiling of transverse magnetization in steady-state sequences. MRM. 1991;21(2):251-263.

Reproducible pTx sequence development using Pulseq

Martin Freudensprung,[1] Simon Weinmüller[1], Jonathan Endres[1], Armin Nagel[2,3] and Moritz Zaiss[1,3]

[1] Institute of Neuroradiology, Uniklinikum Erlangen, Friedrich-Alexander Universität Erlangen-Nürnberg, Erlangen, Germany.
[2] Institute of Radiology, Uniklinikum Erlangen, Friedrich-Alexander Universität Erlangen-Nürnberg, Erlangen, Germany
[3] Department Artificial Intelligence in Biomedical Engineering, Friedrich-Alexander-Universität Erlangen-Nürnberg, Erlangen, Germany

* martin.freudensprung@uk-erlangen.de

Synopsis: The new pTx extension for Pulseq enables the creation, simulation and measurement of new pTx related sequences. We show a DREAM sequence for B_1 mapping, the TIAMO approach and the first results of our k_t-points implementation

Introduction

MRI scanners, especially ultra-high-field (UHF) scanners with a static magnetic field (B0) >= 7T, create new opportunities for medical imaging, such as high SNR and spectral resolution, but also new challenges. One major challenge is the inhomogeneity of the radiofrequency field (B1+), leading to artifacts in the generated images. The usage of parallel transmission (pTx) can address these problems by superimposing the fields of multiple transit coils.

An essential factor for pTx development is the ability to test new ideas fast. The Pulseq[(1)] standard and framework recently enormously improved fast MRI sequence prototyping. To enable this functionality we introduce a pTx extension to the Pulseq standard [(2)]. To speed up prototyping the Pulseq pTx extension was integrated in the PDG simulation[(3)] of MR-zero. With this extension we can now implement and optimize several pTx approaches in Pulseq.

Methods

The pTx extension we introduced at ESMRMB 23[(5)] based on the possibility of RF shimming of every individual RF Event, defined in the Pulseq file. This is done by new shimming elements in the .seq file. The information is stored with two new IDs entries for RF events. These are refer to the exact magnitude and phase information stored in the shape section of the Pulseq file. This architecture allows the reusage of this information and a minimal change of the existing Pulseq environment for definition, simulation as well as interpretation at a pTx-enabled scanner. The new Pulseq Toolbox based on PyPulseq is available here (https://gitlab.cs.fau.de/mrzero/pypulseq_rfshim).

The generating python code if the following examples can be found here: https://gitlab.cs.fau.de/mrzero/pypulseq_rfshim/-/tree/main/pypulseq/seq_examples/scripts_rfshim

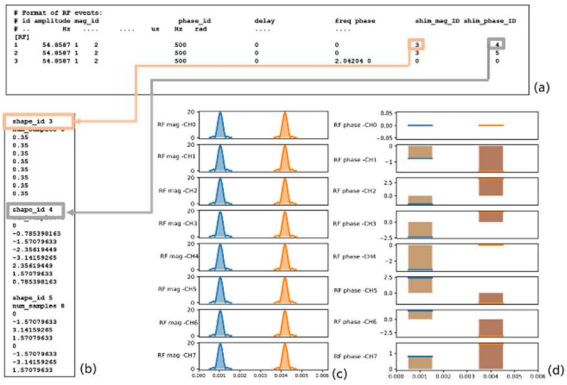

Fig. 1: The new shim IDs (a) extents the RF events definition, and refer to the information, stored in shape section(b). A new plot method enables the user to visualize the different pTx channels (c,d).

The PDG Simulation[(3)] introduced by Endres et. al. speed up the simulation of arbitrary Pulseq sequence. In this simulation we integrated the pTx Pulseq extension and published it. On the Playground MR0, a pTx simulation can be found. https://mrzero-core.readthedocs.io/en/latest/playground_mr0/pulseq_sim_pTx.html

Results

To get a full pTx Pulseq pipeline, the first method we need is a B_1 mapping method. For this problem we implement the DREAM[(6)] approach. In Fig 2 the resulting complex B_1 maps for each channel are shown. This mapping method can later be used for the PDG simulation.

In the TIAMO[(7)] approach every k-space line is measured twice, once with circulated once with elliptical polarization. In the reconstruction, the sum of both k-space lines is used.

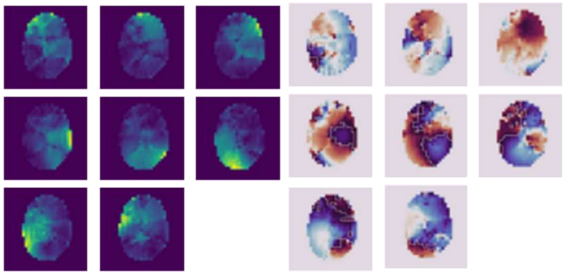

Fig. 1: The resulting B_1 maps from an 8 channel pTx scanner. On the left the magnitude and on the right the phase of the complex B_1 map are shown.

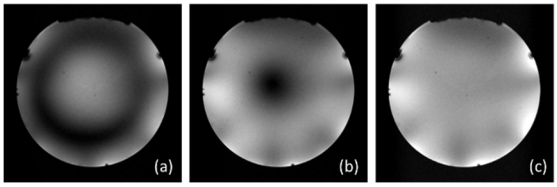

Fig. 3: A FLASH image in CP mode (a), in EP mode and combined TIAMO FLASH(c)

The next approach we are implementing is the k_t-point[8]. For this the RF event of an 3D FLASH sequence is replaced with a series of short tailored shimmed RF and gradients Events.

To tailor these kt-points the B_1 maps are integrated to the PDG simulation and the optimized with a target with homogenous B_1 map. A Google Colab implementation can be found here: https://colab.research.google.com/drive/1RY6Fc8mF6QUnQYsnai9CU62ZCu470Mqg?usp=sharing

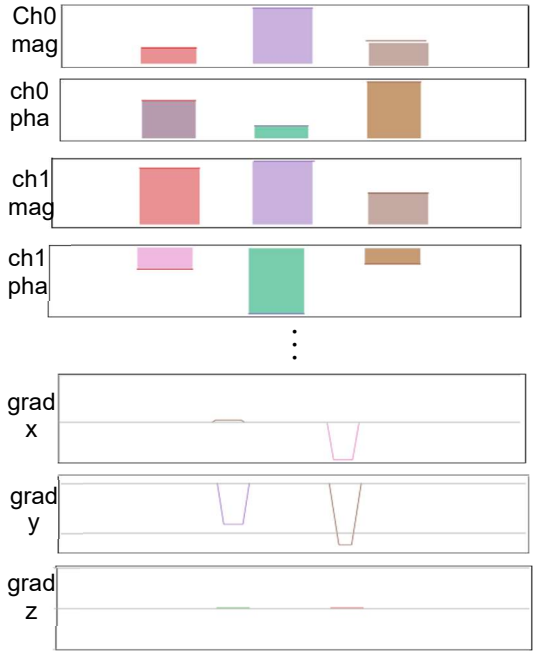

Fig. 4: This Figure shows a three k_t-point approach. Every block pulse RF event is shimmed individually and separated with a 3D gradient event in between.

Discussion

The pTx extension enables the Pulseq community to deal with the pTx channels. More advanced sequences like k_t-points are possible without the usage of additional toolboxes at the scanner. To get good results for these advanced sequences it is necessary to measure the B_1 map individually for every measurement and use it for optimization. This integration of the B_1 map into the digital phantom is quite challenging. We are optimistic that we will be able to accurately reproduce the already functioning simulation in the measurement by the time of the presentation.

Conclusion

The approach enables the user to develop pTx approaches with Pulseq and get rid of vendor specific toolboxes for pTx specific adaption of RF pulses.

References

1. Layton et.al „Pulseq: A Rapid and Hardware-Independent Pulse Sequence Prototyping Framework: Rapid Hardware-Independent Pulse Sequence Prototyping“. *Magnetic Resonance in Medicine* 77, Nr. 4 (April 2017): 1544–52. https://doi.org/10.1002/mrm.26235.

2. Ravi et.al. „PyPulseq: A Python Package for MRI Pulse Sequence Design“. *Journal of Open Source Software* 4, Nr. 42 (12. Oktober 2019): 1725. https://doi.org/10.21105/joss.01725.

3. Endres, et.al. „Phase Distribution Graphs for Fast, Differentiable, and Spatially Encoded Bloch Simulations of Arbitrary MRI Sequences“. *MRM*, 4. April 2024, mrm.30055. https://doi.org/10.1002/mrm.30055.

4. Loktyushin, et.al . „MRzero - Automated Discovery of MRI Sequences Using Supervised Learning“. *Magnetic Resonance in Medicine* 86, Nr. 2 (August 2021): 709–24. https://doi.org/10.1002/mrm.28727.

5. Freudensprung, Martin, et.al „A simple pTx Pulseq extension for pulse-specific B1 shimming (LT53)“. In *In Proc. ESMRMB 2023*. Basel, 2023. https://doi.org/10.1007/s10334-023-01108-9.

6. Nehrke, et. al. „DREAM—a Novel Approach for Robust, Ultrafast, Multislice B_1 Mapping“. *MRM* 68, Nr. 5 (November 2012): 1517–26. https://doi.org/10.1002/mrm.24158.

7. Orzada, et. al „RF Excitation Using Time Interleaved Acquisition of Modes (TIAMO) to Address B_1 Inhomogeneity in High-field MRI“. *MRM* 64, Nr. 2 (August 2010): 327–33. https://doi.org/10.1002/mrm.22527.

8. Cloos, et. al.„K_T -points: Short Three-dimensional Tailored RF Pulses for Flip-angle Homogenization over an Extended Volume“. *MRM* 67, Nr. 1 (Januar 2012): 72–80. https://doi.org/10.1002/mrm.22978.

PNS-Constrained Arbitrary Gradient Waveform Design for DWI on Ultra-High-Performance MRI Systems

Ariel J. Hannum,[1,2,3*] Michael Loecher,[2,3] Qingping Chen,[1] Sebastian Littin,[1] Kawin Sestompop[2], Daniel B. Ennis[2,3] and Maxim Zaitsev[1]

[1] Division of Medical Physics, Department of Diagnostic and Interventional Radiology, University Medical Center Freiburg, Faculty of Medicine, University of Freiburg, Freiburg, Germany
[2] Department of Radiology, Stanford University, Stanford, CA, USA
[3] Division of Radiology, Veterans Administration Health Care System, Palo Alto, CA, USA

* ahannum@stanford.edu/ ariel.hannum@uniklinik-freiburg.de

Synopsis: Peripheral nerve stimulation (PNS) needs to be managed on ultra-high-performance gradient systems, particularly for diffusion encoding. The aim of this work was to utilize PNS-constrained arbitrary gradient waveform design in a vendor-neutral sequence on an ultra-high-performance gradient system. We integrated optimized diffusion-encoding waveforms into a vendor-neutral single-shot EPI sequence. One phantom and one volunteer were imaged on Cima.X, demonstrating the feasibility of utilizing open-source, optimized gradient waveform design to minimize TE while mitigating PNS for diffusion-weighted imaging.

Introduction

Diffusion-weighted imaging (DWI) is a non-invasive imaging technique to probe tissue microstructure with demonstrated clinical utility throughout the body.[1] However, patient, bowel, respiratory, and cardiac motion can lead to signal losses and artifacts in DWI. Gradient moment nulling is an essential tool to compensate for these motions but at the cost of an extended echo-time (TE). Ultra-high-performance MRI systems (G_{max} = 200 mT/m, S_{max} = 200 T/m/ms) are therefore an excellent opportunity as they can substantially shorten TEs and regain SNR. However, systems lack specialized strategies to manage peripheral nerve stimulation (PNS). Conventional gradient waveform design cannot balance competing needs for moment nulling, avoiding PNS, and minimizing TE.

Numerical gradient optimization algorithms, such as the Gradient Optimization Toolbox[2] (GrOpt) enable time-optimal arbitrarily shaped gradient waveform design subject to constraints. We previously demonstrated that GrOpt minimized TEs while avoiding PNS in simulation and proof-of-concept on commodity systems (G_{max} = 45 mT/m, S_{max} = 200 T/m/ms).[3] However, this toolbox has not been utilized on ultra-high-performance MRI systems.

The purpose of this work was to evaluate the ability of GrOpt to minimize TE and avoid PNS on an ultra-high-performance MRI system.

Methods

We designed a spin-echo single-shot diffusion EPI sequence[4] (ramp-sampling) using the PyPulseq[5] toolbox with the following parameters: FOV = 220x220mm^2, resolution = 2.5x2.5x2.5mm^3, 1 slice, b-value = [0, 1000] s/mm^2, Partial Fourier = 0.75, time to TE = 14.3ms, TR=3s. One non-DWI and three DWIs along the three orthogonal axes were acquired.

GrOpt diffusion waveforms (Pulseq-GrOpt) were then added. The model for the GrOpt PNS-constraint was based on the International Engineering Standard (IEC 60601-2-33) with coefficients: $\alpha = 0.333m$, $r = 23.4\,T/s$, $S_{min} = 60\,T/ms$, $c = 334\,\mu s$ and designed below a PNS threshold of 90%. We designed GrOpt waveforms with no motion-compensation (GrOpt-M_0) and with velocity-compensation (GrOpt-M_1). For comparison, conventional Stejskal-Tanner trapezoidal (TRAP) waveforms were designed with identical parameters and moment nulling (TRAP- M_0 and TRAP-M_1).

Proof-of-concept data was acquired at ultra-high-performance 3T MRI (Cima.X, Siemens). This protocol was first evaluated in a diffusion phantom that contained vials with different ADC values using an 18-channel body coil and 12-channel table coil. One healthy volunteer (M, 40 years old) was then IRB consented, approved and imaged. Images were processed using Pulseq EPI reconstruction Matlab scripts.[4]

Results

GrOpt utilized dynamic slewing to maximize hardware capabilities while avoiding PNS. GrOpt-M_1 reduced the TE by over 16.3ms compared to TRAP (Fig. 1). There was a TE reduction of 3.0ms for GrOpt-M_0 (TE=46.6ms) compared to TRAP-M_0 (TE=43.6ms).

All waveforms ran successfully on the MRI system. Preliminary Pulseq-GrOpt images demonstrate non-diffusion and diffusion-weighting (Fig. 2).

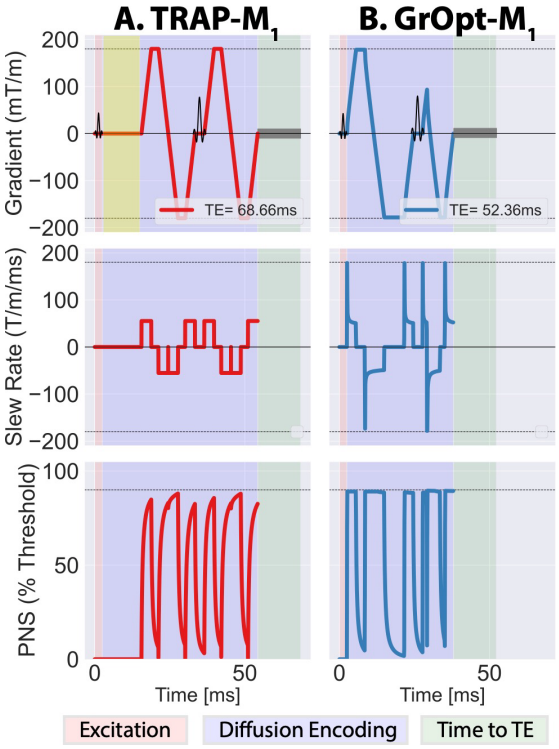

Fig. 1: (A) TRAP-M_1 vs. (B) GrOpt-M_1 waveform. TRAP waveforms have unused time (yellow) to allow for moment nulling while GrOpt utilizes the full slew-rate, avoids PNS and fulfills other constraints.

Discussion

We demonstrated that GrOpt successfully encoded diffusion-weighting on an ultra-high-performance system. Dynamic slewing aided in generating waveforms that yielded large TE reductions during moment nulling, whereas typical diffusion has dead time to allow for moment nulling. Preliminary data demonstrates promising results for a Pulseq-GrOpt sequence that can be utilized for DWI throughout the body.

Future work will improve the efficiency of the Pulseq implementation of the DWI sequence EPI trajectory. We will continue to evaluate eddy currents and Maxwell fields, which can be additional constraints. We will also thoroughly evaluate GrOpt vs. conventional TRAP waveforms. Furthermore, we also plan to test this sequence in Body DWI, where motions occur on a much larger scale and gradient moment nulling is a necessity.

Conclusion

This work demonstrates the first instance of utilizing PNS-constrained arbitrary gradient waveform design using the GrOpt toolbox to encode diffusion on an ultra-high-performance system. Proof-of-concept images demonstrate the feasibility of vendor-neutral and PNS-constrained arbitrary gradient waveform design.

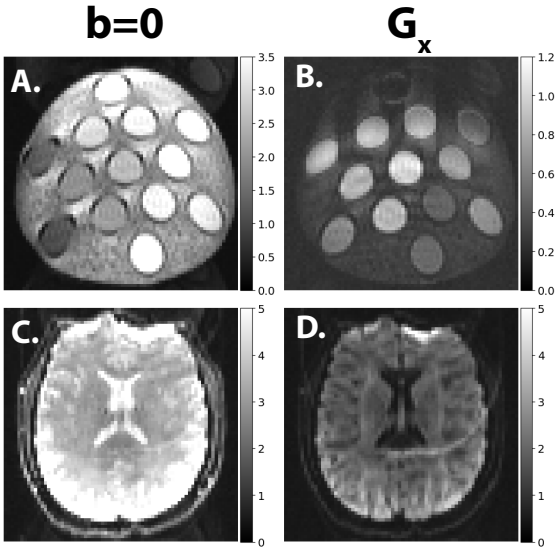

Fig. 2: Example images from M_1-nulled Pulseq-GrOpt. Phantom (A) b=0 and (B) DWI with sensitivity along Gx. Images from a volunteer for (C) b=0 and (D) diffusion encoding along the x-axis. Small ghosting and distortion were observed.

Acknowledgements

Funding Sources: AHA.23PRE1018442 to AJH, Smart Health-NSF 2205103 to DBE and the ISMRM Research Exchange Program.

References

1. Le Bihan D, Breton E. Imagerie de diffusion in-vivo par resonance magnetique nucleaire. *CR Acad Sci.*.1985;301(15):1109–1112.

2. Loecher M, Middione MJ, Ennis DB. A gradient optimization toolbox for general purpose time-optimal MRI gradient waveform design. *Magn Reson Med*. 2020;84(6):3234-3245.

3. Hannum AJ, Loecher M, Setsompop K, Ennis DB. Mitigation of Peripheral-Nerve Stimulation with Arbitrary Gradient Waveform Design for Diffusion-Weighted MRI. Proc. 32nd Annual Meeting ISMRM 2024;2441.

4. Layton KJ, Kroboth S, Jia F, et al. Pulseq: A rapid and hardware-independent pulse sequence prototyping framework. *Magn Reson Med*. 2017;77(4):1544-1552.

5. Ravi, Keerthi, Sairam Geethanath, and John Vaughan. "PyPulseq: A Python Package for MRI Pulse Sequence Design." Journal of Open Source Software 4.42 (2019): 1725.

Addressing the Ejection Fraction Dependence of FAIR-ASL Perfusion

Gutjahr FT[1*], Kampf T[1,2], Christa M[3], Bauer WR[3], Jakob PM[1]

[1] Experimental Physics V, University of Würzburg, Germany

[2] Institute of Diagnostic and Interventional Neuroradiology, University Hospital Würzburg, Germany
[3] Cardiac MRI, Department of Internal Medicine I, University Hospital Würzburg, Germany.

* Fabian.Gutjahr@uni-wuerzburg.de

Synopsis: After the proposal of FAIR-ASL it was quickly adapted for myocardial perfusion quantification in small animals and has since been used in several studies. FAIR ASL is based on the signal difference between an experiment after a slice selective and a global inversion. Ideally, after the slice selective inversion, relaxed blood will be perfused into the imaging slice, only. However, this cannot be achieved leading to underestimation of perfusion. The amount of underestimation is dependent on the heart rate.

In this work we propose an adapted approach to reduce the underestimation and dependence on the heart rate.

Introduction

In the Flow Sensitive Alternating Inversion Recovery (FAIR)-Arterial Spin Labeling technique, perfusion is encoded in the difference between of the signal after a global (labeling) or a slice selective inversion (reference) using a fast Snapshot FLASH readout of the magnetization evolution. This method has become the de facto standard for myocardial perfusion imaging in mice [1]. Nonetheless, a fundamental assumption of FAIR-ASL is the non-alteration of inflowing blood during the reference experiment. This premise, however, cannot be fulfilled in experiments, as the slice selective inversion pulse inadvertently labels blood within the ventricles in the reference experiment [2]. In Fig. 1 a typical position and size of both the measurement slice (A) and the inversion slice thickness (B) are shown. (B) typically exceeds (A) by a factor of three to ensure an even degree of inversion throughout the whole imaging slice. This leads to the inadvertent labeling of a large portion of the blood in the left ventricle which consecutively will flow into the imaging slice. This will reduce the difference between the labeling and the reference experiment.

Consequently, such inadvertent labeling leads to a systematic underestimation of perfusion. The degree of underestimation can be expected to be dependent on the heart rate and ejection fraction. To mitigate this issue, we suggest replacing the slice selective inversion experiment and measure the magnetization-transient from the initial equilibrium state (M_0) to steady state (M_∞).

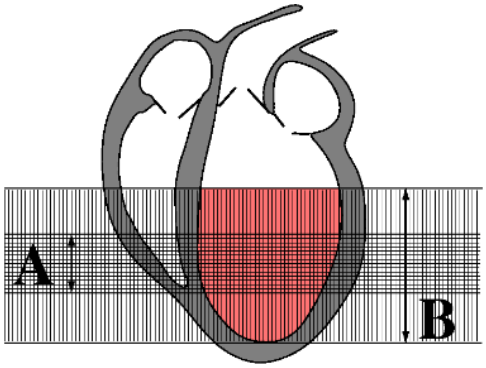

Fig. 1: Schematic overview of a typical position of measurement (A) and selective inversion slice (B) with the inadvertently labeled blood in the left ventricle (red).

By removing the slice selective magnetization preparation, the blood in the left ventricle will only experience the much weaker readout pulses within the measurement slice in the reference experiment.

As a drawback however, the dynamic range of the experiment is reduced, leading to a lower SNR. To counterbalance this effect a higher measurement time is required.

Methods

Experiments were conducted on a 7T small animal system (Pharma Scan, Bruker Ettlingen, Germany). The vendor's FISP sequence was adapted to allow segmented Inversion Recovery Snapshot FLASH (IRSF) measurements with either global or slice selective magnetization preparation. The

magnetization preparation is triggered to the cardiac phase, consecutive readouts are untriggered. The exact timing of all RF-Pulses is recorded alongside the ECG data to enable retrospective triggering for a model based reconstruction as described in [3].

C57BL/6 mice underwent either Sham or Myocardial Infarction (MI) surgery and were measured via MRI eight weeks post MI. This ensured a wide range of different ejection fractions.

All animals were measured using a) a global inversion preparation, b) a slice selective inversion preparation and c) no preparation pulse. Perfusion maps were calculated from measurements a)+b) for FAIR-ASL and a)+c) for the novel method.

Sequence parameters: Matrix 128x88, FOV 30x20 mm^2, imaging/inversion slice-thickness 1.5 mm/4.5 mm, TE/TR 1.22 ms/3.6 ms, 2794 readouts per inversion, 1760 readouts for the transient. K-Space was segmented 8-fold. Inversion experiments were repeated four times, transient experiments repeated 12 times. With a relaxation delay of 10 s this results in measurement time of 10 min for each inversion and 16 min for the transient experiment.

The cardiac ejection fraction was quantified using a stack of short axis cines covering the whole heart.

Results

In Fig. 2 an exemplary myocardial perfusion map of an animal using the FAIR ASL approach (left) as well as the novel approach (right) is shown. As expected, quantified perfusion values for the novel approach are higher than for FAIR ASL.

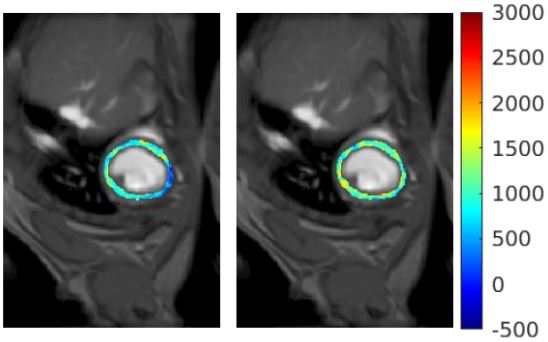

Fig. 2: Perfusion in ml/mg/min calculated using the FAIR ASL (left) and the novel approach (right).

In Fig. 3, a plot showing the growth of the median perfusion calculated from FAIR ASL to the perfusion values calculated from the novel approach for all animals are shown in dependence on their respective ejection fraction.

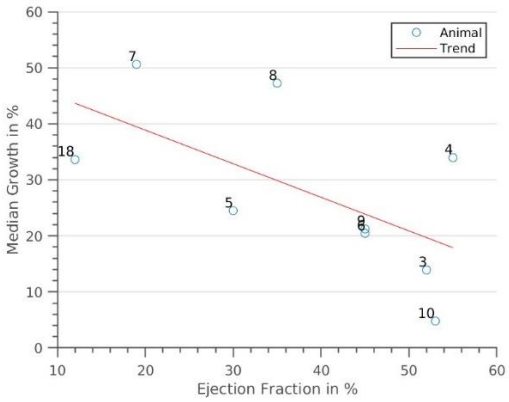

Fig. 3: Growth of median perfusion over the whole myocardium calculated for each animal in dependence on the ejection fraction.

Discussion

Initial results show that the novel method both reduces the underestimation of perfusion in comparison to the FAIR ASL approach, as well as reduces the ejection fraction dependence of this effect. However, this comes at the cost of a higher measurement time. Further developments should focus on optimizing the acquisition efficiency to increase the applicability of the novel approach.

Conclusion

A modified FAIR ASL approach to reduce the dependence of perfusion quantification on the ejection fraction could be demonstrated.

References

1. Naresh NK. Repeatability and Variability of Myocardial Perfusion Imaging Techniques in Mice: Comparison of Arterial Spin Labeling and First-Pass Contrast-Enhanced MRI. Magn Reson Med, 2015: 75:6:2394-2405

2. Kampf T, Myocardial perfusion quantification using the T1-based FAIR-ASL method: The influence of heart anatomy, cardiopulmonary blood flow and look–locker readout. Magn Reson Med. 2013: 71:5:1784-1797

3. Gutjahr FT, Quantification of perfusion in murine myocardium: A retrospectively triggered T1-based ASL method using model-based reconstruction. Magn Reson Med. 2014: 74:6:1705-1715

3D Filter-Exchange Imaging Using Slab-Selective Excitation

Jacopo Frignani[1], Athanasia Kaika[1], Ben Danzer[1], Sandra Sühnel[1], Luca Nagel[1], Geoffrey Topping[1], Franz Schilling[1]

1 Department of Nuclear Medicine, TUM School of Medicine and Health, Klinikum rechts der Isar, Technical University of Munich, Munich, Germany

Synopsis: Filter Exchange Imaging (FEXI) can be used to characterize the transmembrane water permeability through the AXR (apparent exchange rate) and is a promising non-invasive biomarker for several pathologies. Due to the acquisition of numerous diffusion-weightings, mixing times and averages, FEXI is time-consuming, particularly if also sequentially measuring multiple slices. This abstract presents a novel 3D slab-FEXI sequence that speeds up AXR measurements. A comparison of slab-FEXI and multi-slice FEXI in glioblastoma multiforme (GBM) bearing mice that underwent radiotherapy shows similar AXR values.

Introduction

Filter Exchange Imaging (FEXI) (1) is a non-invasive imaging technique that is sensitive to water molecule transmembrane exchange between the intra- and extracellular compartments. The method consists of 3 modules: the diffusion filter, the exchange period, and the detection module. First, a reference ADC (apparent coefficient diffusion) is measured at equilibrium without the diffusion filter. Then, the filter, which suppresses signal from fast-diffusing water molecules, is applied and leads to a decrease in the ADC (Fig. 1a). With increasing t_m (mixing time) between the diffusion filter and the detection module, the transmembrane water exchange leads to an ADC relaxation back to equilibrium, which is described by the AXR (apparent exchange rate) (2). This process is repeated for several t_ms. The signal is acquired with an EPI readout.

The necessity to acquire multiple ADCs, along with the requirement for numerous averages due to low SNR, makes FEXI a time-consuming method. Repeating the single-slice FEXI sequence on different slices ("multi-slice FEXI") to obtain a volume thus takes an impractical amount of time.

In this work, we implemented a new 3D FEXI method ("3D slab FEXI"), which speeds up FEXI acquisition substantially.

Methods

Scanner

All measurements were conducted on a 7 T preclinical scanner (Agilent MR901 with Bruker Avance III electronics) using a $^{13}C/^{1}H$ volume resonator for signal transmission and a mouse brain surface coil ^{1}H 300 MHz for signal reception (Rapid Biomedical).

3D FEXI sequence

The sequence is based on a single-slice FEXI sequence (3). Rather than separately and consecutively applying the diffusion filter for each slice, the filter is applied to slabs volumes consisting of grouped adjacent slices. The volume-selective filter is followed by a series of slice-selective excitations and detection modules, timed to allow each slice in the volume to experience one of the desired exchange times (Fig. 1b). During the exchange time of one slice, other slices' exchange times and detection modules simultaneously occur (Fig. 1b). Furthermore, during the repetition time (TR) of one volume, the same three modules are applied to the other volumes (Fig. 1c). This process is repeated several times so that each slice is acquired for all mixing times.

Mice experiment

3D slab FEXI was tested on 4 mice as part of a study of the response of glioblastoma multiforme (GBM) brain tumors to radiotherapy (RT) in mice. For every mouse, a common slice was acquired with single-slice and 3D slab FEXI, with the 3D method acquiring a total of 6 or 8 slices, and 3 or 4 mixing times, and 2 b-values.
AXRs were calculated in three different regions: healthy brain, untreated tumor, and treated tumor (Fig. 2a, 2b).
Hypothesis:
The newly implemented 3D slab-FEXI method and conventional single-slice FEXI method measure similar AXR values in the common slice of the murine GBM tumors.

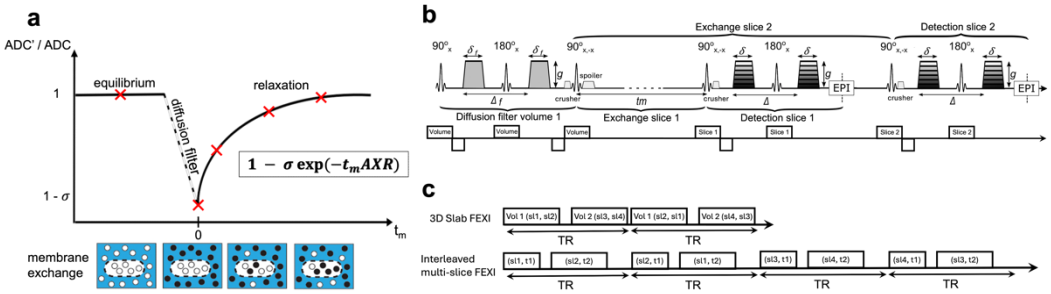

Fig. 1: Theoretical principles for 3D FEXI using slab-selective excitations. a Representation of the principle of FEXI. **b** 3D FEXI using slab-selective excitation pulse diagram. The diagram shows just one volume block of the sequence. **c** Comparison between the 3D slab FEXI and the interleaved multi-slice FEXI approaches to acquire 2 slices at 2 different t_m. In Vol 1 (sl1, sl2) the diffusion filter is applied to the first volume, subsequently acquiring slice 1 with $t_{m,1}$ and slice 2 with $t_{m,2}$. In (sl1, t1) the first slice is acquired with $t_{m,1}$.

Results

The time saving of 3D slab FEXI compared to conventional 2D multi-slice FEXI depends on the sequence parameters. Using the 8-slice in vivo protocol described in methods, interleaved multi-slice FEXI can acquire a maximum of 5 slices in 9 min, while 3D slab FEXI can acquire 20 slices in the same amount of time.

Mice experiment

The correlation plot (Fig. 2c) reveals a strong correlation ρ between the two methods (ρ = 0.82). A paired t-test between the ROI values does not indicate a statistically significant difference between the results of the 3D slab and single-slice FEXI methods (two tailed p = 0.056).

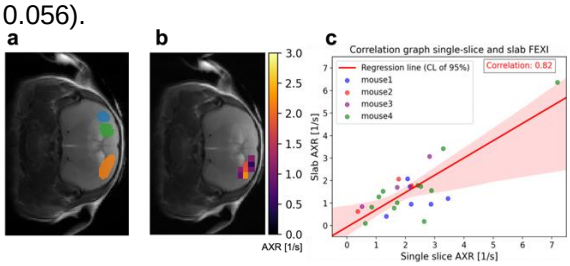

Fig. 2: Region of interest selection for AXR and results. a Segmentation of mouse brain in the 3 regions of interest: healthy brain (orange), treated tumor (blue), and untreated tumor (green). **b** Example of Slab AXR map for healthy brain region. **c** Correlation plot, with regression line, in the common slice between single-slice and 3D slab FEXI in vivo. The AXRs are acquired in 4 mice over different days

Discussion

Time-earning computation

The simulation shows that 3D slab FEXI is faster than the interleaved repetition of the single-slice FEXI, enabling the acquisition of more slices in the same amount of time. This feature can be used to increase the number of slices or increase SNR by acquiring more averages.

Mice experiment

The two methods show a strong correlation, suggesting that the two methods measure the same physical quantity.

Furthermore, the extremely high treated tumor AXR value compared to others in mouse 4 (Fig. 2c) demonstrates that also 3D slab FEXI can be used as a biomarker for early treatment response to radiotherapy (2).

Conclusion

In summary, we developed a new multi-slice FEXI method using a volume-selective diffusion filter and slab-selective excitations for the exchange and detection modules. The newly developed 3D slab FEXI sequence measures similar AXR values compared to a single-slice sequence and can acquire more slices than a conventional multi-slice FEXI protocol in the same amount of time.

References

1. Lasič S, Nilsson M, Lätt J, Ståhlberg F, Topgaard D. Apparent exchange rate mapping with diffusion MRI. *Magnetic Resonance in Medicine*. 2011;66(2):356-365. doi:10.1002/mrm.22782

2. Schillmaier M, Kaika A, Schilling F. Chapter 6. Disentangling Intercompartment Exchange from Restricted Diffusion. In: *New Developments in NMR*. ; 2020:154-185. doi:10.1039/9781788019910-00154

3. Schillmaier M, Kaika A, Topping GJ, Braren R, Schilling F. Repeatability and reproducibility of apparent exchange rate measurements in yeast cell phantoms using filter-exchange imaging. *Magma*. 2023;36(6):957-974. doi:10.1007/s10334-023-01107-w

Errors in Actual Flip Angle Imaging (AFI) of polyvinylpyrrolidone (PVP) solutions at 3T and 7T

Niklas Himburg,[1*] Max Lutz,[1] Lorenz Mitschang,[1] Jan Gregor Frintz,[1] Sebastian Schmitter[1,2,3]

[1] Physikalisch-Technische Bundesanstalt, Braunschweig and Berlin, Germany
[2] Medical Physics in Radiology, German Cancer research Center (DKFZ), Heidelberg, Germany
[3] University of Minnesota, Center for Magnetic Resonance Research, Minneapolis, MN, United States

* niklas.himburg@ptb.de

Synopsis: Actual flip angle imaging (AFI) is a widely used flip angle (FA) measurement technique that is highly suitable for validating electromagnetic simulations in phantoms. Practical phantom fillings are polyvinylpyrrolidone (PVP) solutions. This work aims to explain the incorrect FAs measured with AFI under certain conditions in PVP solutions. FAs in a PVP solution are measured at 3T and 7T for different RF-spoiling phase increments (Φ_0). NMR spectra verify the existence of off-resonant PVP signals and integrating two compartments with different frequencies into a simulation of the resulting AFI acquisition qualitatively confirms the deviations from expected FA values.

Introduction

Magnetic resonance imaging (MRI) at ultra-high magnetic fields (UHF) can yield heterogeneous flip angle (FA) distributions that lead to signal voids and image contrast alterations[1]. Actual flip angle imaging[2] (AFI) is used frequently to map FA distributions in dedicated phantoms to validate B_1^+ fields of UHF transmit arrays[3,4]. PVP solutions are highly suitable phantom fillings due to their human-tissue-equivalent dielectric properties[5].

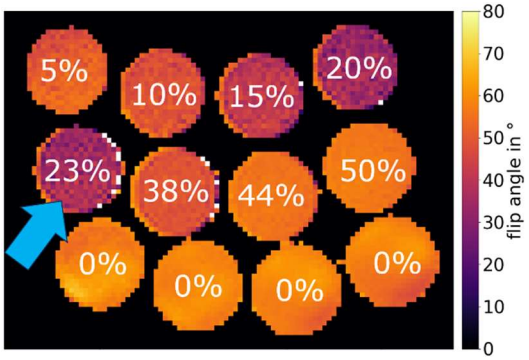

Fig. 1: Transversal AFI-FA map of tubes with different PVP ratios (value denoted in weight % in each tube) acquired at 3T (Φ_0=40°). The FA is underestimated in some tubes with the strongest effect (44% underestimation) for 23wt.% PVP.

Under certain (including recommended) RF-spoiling conditions, we found substantial deviations from the expected FA when using AFI in combination with certain PVP solutions (Fig. 1). We investigate this effect for different RF-spoiling phase increments (Φ_0) at 3T and 7T. NMR spectroscopy and extended phase graph[6] (EPG) simulations are used to explain the effect and the resulting FA errors.

Methods

All FA maps were acquired in a PVP phantom with a non-selective 3D cartesian AFI (field-of-view=256x192x160mm; resolution=2x2x5mm; TE/TR1/TR2=1.90/25/125ms; nominal FA=60°; spoiler-gradient-areas: A_{G1}/A_{G2}=117.5/587.5 mT·ms/m) using a 32-channel head coil. Measurements were performed at 3T (Cima.X, Siemens) and 7T (Magnetom, Siemens) with Φ_0 ranging from 0°-180° in 20°-steps. The phantom consists of water and 23 weight (wt.) % PVP (ADC=0.99·10^{-3} mm^2/s, T1/T2=1210/680ms at 3T; T1/T2=1400/604ms at 7T), i.e. we selected the tube showing the strongest effect in Fig.1.

FA reference values were acquired with the same setup but substantially increased gradient spoiling moments (A_{G1}/A_{G2}=900/4500 mT·ms/m at 3T, A_{G1}/A_{G2}=352.6/1763 mT·ms/m at 7T) and Φ_0=140°.

^{1}H-NMR spectra of a PVP/D2O sample (20wt.%PVP, T=298K) were acquired at a 1.88T spectrometer (Fourier80, Bruker). Inversion recovery (TI=0-200ms, 20 timesteps) was used to measure T1-times of the PVP resonances.

1-dimensional-EPG simulations, including diffusion, were performed to simulate the FA dependency on Φ_0. In a first approach, only a single precession frequency was used together with the parameters T1/T2/ADC.

In a second approach, two precession frequencies with difference $\Delta\nu$ (320Hz at 3T,

740Hz at 7T) were used and their signals combined by:

$$S_{1/2} = S_{1/2,a} + w \cdot S_{1/2,b} \cdot e^{-i(2\pi \cdot \Delta\nu \cdot TE + \varphi)}$$

Simulation of signal $S_{1/2,a}$ was performed as in the first approach and $S_{1/2,b}$ with $T1_b/T2_b$=100/6ms to resemble a PVP resonance from the ^{1}H-NMR spectrum. An additional weighting factor w and a phase term with an optional fitting phase φ were added.

Results and Discussion

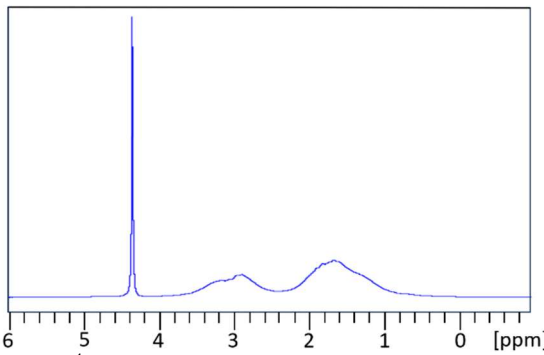

Fig. 2: ^{1}H-NMR spectrum of a PVP/D2O sample with 20wt.% PVP ratio. PVP resonances are visible at 1.6ppm and 3.0ppm besides the residual water peak.

Fig. 2 shows the ^{1}H-NMR spectrum of the PVP/D2O sample. Besides the residual water peak at 4.2ppm, two PVP resonances are visible in the spectrum at 3.0ppm and 1.6ppm with FWHM/T2*=0.7ppm/5.7ms. The measured T1-value is T1=100ms. In combination with the high nominal FAs in AFI, these resonances might impact the resulting FAs.

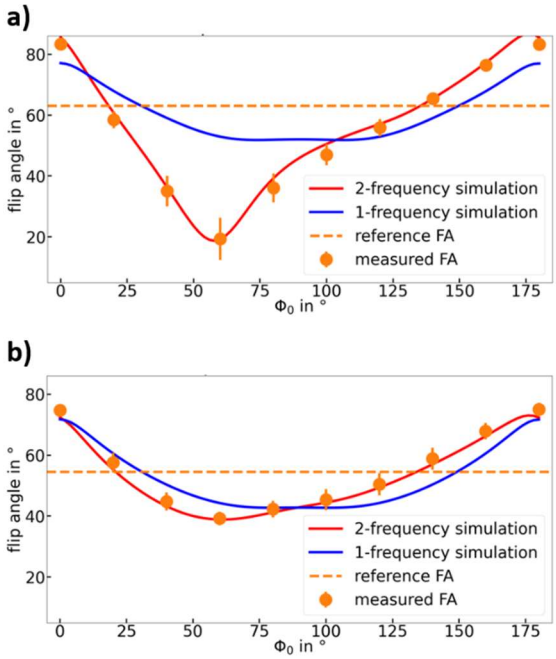

Fig. 3: RF Spoil increment dependency of the AFI in a 23wt.% PVP solution at a) 3T and b) 7T. Results of EPG simulations performed with one or two precession frequencies are indicated by solid lines.

Fig. 3 displays the impact of different Φ_0 values on the FA at a) 3T and b) 7T. In both cases the spoiling curves appear asymmetric and show a minimum at Φ_0=60° with an underestimation of the reference flip angle of a) -70% and b) -28%. The simulated curves resulting from only one precession frequency do not agree with the measurement results. However, they agree with the results for a water phantom as presented in ref.[7,8].

Results from two-frequency simulations with a) w=0.12, φ=-0.18π and b) w=0.07, φ=0.1π match measured results at 3T as well as 7T. Therefore, taking the influence of the PVP resonances into account by combining the signals of two EPG simulations with different precession frequencies allows to reproduce the measured Φ_0 dependency. A change in B_0 can be included by adjusting the phase factor and weighting between the two signals.

The interference between these signals can be effectively reduced by increasing the echo time TE due to the small T2* values of the PVP resonances. Additionally, increasing the gradient spoiler moments will reduce known spoiling-related errors.

Conclusion

Signals resulting from PVP resonances must be considered for accurate AFI-based quantification of B_1^+ fields in PVP solutions under certain spoiling conditions. This is important particularly for coil validation or reproducibility studies, where PVP phantoms are being used. To reduce the interference-based errors on B_1^+, one can i) increase the PVP/water ratio, ii) substantially increase the spoiling moment or iii) take advantage of the small T2* times of the PVP resonances by increasing the echo time. If such measures are considered/included, the known recommendations[7] for choosing Φ_0 should be applicable.

References

1. Ladd ME et al. Prog Nucl Magn Reson Spectrosc. 2018 Dec;109:1-50 . doi: 10.1016/j.pnmrs.2018.06.001.
2. Yarnykh VL. Magn Reson Med. 2007 Jan;57(1):192-200. doi: 10.1002/mrm.21120.
3. Woo MK et al. Sensors. 2021 Oct;21(21):7250. doi: 10.3390/s21217250.
4. Schmidt S et al. Magn Reson Med. 2024 Feb;91(2):513-529. doi: 10.1002/mrm.29866.
5. Ianniello C, et al. Magn Reson Med. 2018 Jul;80(1):413-419. doi: 10.1002/mrm.27005.
6. Weigel M. J Magn Reson Imaging. 2015 Feb;41(2):266-95. doi: 10.1002/jmri.24619.
7. Yarnykh VL. Magn Reson Med. 2010 Jun;63(6):1610–26. doi: 10.1002/mrm.22394.
8. Nehrke K. Magn Reson Med. 2009 Jan;61(1):84-92. doi: 10.1002/mrm.21592.

Training deep learning reconstruction models for radial real-time cardiac cine MRI using synthetic golden-angle data

Yannik Ott,[1,2*] Marc Vornehm,[1,2] Jens Wetzl,[2] Daniel Giese,[2,3] and Florian Knoll[1]

[1] Computational Imaging Lab, Friedrich-Alexander-Universität Erlangen-Nürnberg, Erlangen, Germany.
[2] Magnetic Resonance, Siemens Healthineers AG, Erlangen, Germany.
[3] University Hospital Erlangen, Friedrich-Alexander-Universität Erlangen-Nürnberg, Erlangen, Germany.

* yannik.ott@fau.de

Synopsis: We propose a set of augmentations that allow to train golden-angle real-time cardiac cine reconstruction networks on synthetically generated radial data. The effect of our approach is investigated for image-based and k-space-based network architectures.

Introduction

Cardiac cine imaging is the gold-standard method for evaluating cardiac function. Due to long scan times, conventional approaches are not feasible in patients with limited breath-hold capabilities and/or arrhythmias. Real-time cine MRI acquires data during one single heartbeat thus resulting in highly undersampled data. Advanced reconstruction methods are required to compensate the aliasing artifacts. Deep learning (DL) approaches have been demonstrated to be promising methods for real-time cine reconstruction (1). Instead of conventional Cartesian sampling, radial golden-angle sampling offers the benefits of less susceptibility to motion, self-gating opportunities, and flexible temporal resolution. However, golden-angle sampling suffers from gradient delay effects (2) that need to be accounted for. Because of this effect, it is difficult to obtain artifact-free fully-sampled data. This work proposes a set of augmentations that enable the use of cartesian data to train golden-angle reconstruction networks.

Methods

We trained DL models by generating synthetic golden-angle data from the open-source OCMR data set (3) that contains cartesian cardiac cine MRI raw data. We generated retrospectively undersampled data by Fourier transformation of complex valued images and degridding the Cartesian k-space data onto a radial golden-angle trajectory. During network training, each radial trajectory was randomly augmented by tilting the individual spoke angles by $\pm 1^\circ$ and applying a gradient delay shift, which can be described by an ellipse $\mathbf{S}$ as in (4). Figure 1 depicts the influence of different ellipse values on the radial trajectory. Furthermore, a random bias field was applied to the images. During training, 216 cine acquisitions were undersampled with three different trajectories with 11, 13, and 15 radial spokes per image frame. The training and validation data set contained 519 and 129 samples, respectively. Additionally, 38 samples were undersampled with 13 spokes and served as retrospective test data.

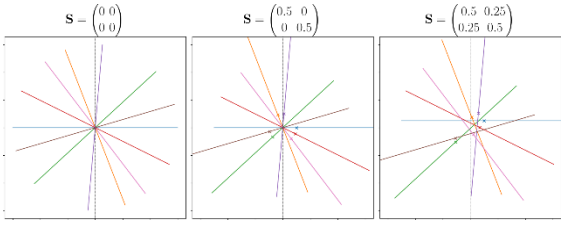

Fig. 1: Radial trajectory with different simulated gradient delays.

The DL architectures that were compared consisted of a U-Net (5) that utilized 2D spatial and 1D temporal convolutions and the Variational Network (VN) (6). The VN applies a data-consistency step and a U-Net as regularization network for nine cascades. Both models consisted of approximately 400,000 learnable parameters. The Adam algorithm was used to minimize the Structural similarity index measure (SSIM) loss during training.

For quantitative evaluation, we computed the SSIM between ground truth and predicted images on the retrospective test data. In addition, the mean SSIM of multiple

spatiotemporal profiles through the center of the heart was calculated, which is referred to as $SSIM_{ST}$. Both DL architectures were compared with and without the proposed data augmentations. In addition, an expert reader study was used to compare temporal total variation compressed sensing (CS) and the two DL architectures trained with the proposed data augmentations. The reader study was performed on 48 prospectively acquired real-time radial golden-angle cine acquisitions from eight healthy volunteers. Two cardiac MRI experts rated the reconstructed images in the categories "temporal fidelity and image sharpness" and "residual artifacts", where higher scores indicate better reconstructions in both categories.

Results

Figure 2 illustrates the achieved $SSIM$ and $SSIM_{ST}$ values of the implemented network architectures with and without augmentations. Both networks reached higher metric values with the additional augmentations. The highest values were achieved by the VN with augmentations, while the VN without augmentations performed worst. For all methods $SSIM_{ST}$ results were significantly lower than $SSIM$ results.

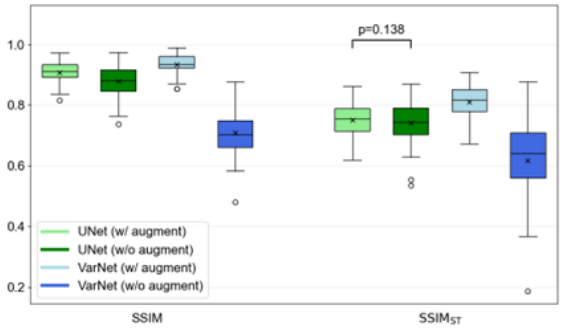

Fig. 2: $SSIM$ and $SSIM_{ST}$ values of the compared methods on retrospective test data.

Figure 3 illustrates the expert rating results. The DL approaches performed on par, while CS was outperformed. All methods achieved higher rating scores in terms of "temporal fidelity and image sharpness".

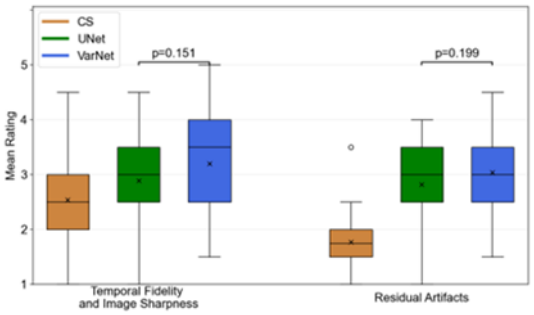

Fig. 3: Results of the expert reader study on prospective volunteer data

Discussion

The difference in performance when models were trained with and without augmentations indicates that the DL models require the gradient delay effect in the training data to be able to compensate it during inference.

The higher offset between the VN versions is likely caused by the fact that the architecture receives k-space and trajectory information in contrast to the U-Net.

The results of the expert rating suggest that training DL models on synthetically augmented cartesian data to reconstruct golden-angle acquisitions is feasible.

Furthermore, although the VN performed better with respect to quantitative metrics, both approaches performed on par in the reader study.

Conclusion

We successfully trained two different DL model architectures on synthetically augmented cartesian data and applied it to golden-angle acquisitions. Both DL approaches outperformed CS in reconstructing real-time cine acquisitions.

Future work may include an ablation study to investigate the effect of the individual data augmentations. In addition, testing different parameter configurations would allow more insights about how both DL architectures compare.

References

1. Vornehm M et al. Variational Network Meets Conjugate Gradient: Inline Reconstruction and Strain Analysis of Accelerated Cardiac Cine MRI. ISMRM 2024.

2. Feng L. Golden-angle radial MRI: basics, advances, and applications. JMRI 2022, pp. 45-62.

3. Chen C et al. OCMR Dataset from www.ocmr.info. 2020.

4. Rosenzweig S et al. Simple auto-calibrated gradient delay estimation from few spokes using Radial Intersections (RING). MRM 2019, pp. 1898-1906.

5. Ronneberger O et al. U-Net: Convolutional networks for biomedical image segmentation. MICCAI 2015, pp. 234-241.

6. Hammernik K et al. Learning a variational network for reconstruction of accelerated MRI data. MRM 2018, pp. 3055-3071.

CEST MRI multi-pool quantification through simplified model-based analysis

Chris Lippe,[1*] Verena Hoerr[1,2]

[1] Clinic of Radiology, University of Münster, Münster, Germany.
[2] Heart Center Bonn, Department of Internal Medicine II, University Hospital Bonn, Bonn, Germany.

* chris.lippe@uni-muenster.de

Synopsis: We developed a simplified model for Chemical Exchange Saturation Transfer (CEST) MRI multi-pool quantification, reducing the number of free parameters from 21 to 14 while maintaining noise-level accuracy. Using simulated 7-pool Z-spectra data, we demonstrated the model's superior performance and reliability compared to traditional MTR_{asym} and model-based analysis. This approach enhances the robustness and efficiency of CEST analysis, offering a valuable tool for accurate metabolite concentration quantification in preclinical research.

Introduction

Chemical Exchange Saturation Transfer (CEST) MRI has emerged as a promising spectroscopic imaging technique, but accurate quantification remains a challenge due to its low selectivity [1].

Model-based analysis is an appealing approach to overcome this issue, particularly for the case of continuous wave (cw)-irradiation applicable in preclinical research. Within this frame, accurate models for CEST and MT effects have already been derived from Bloch-McConnell (BM) equations [2]. However, for an inverse problem formulation, these models often lead to effective overparameterization.

Here, we show that the number of free parameters can be substantially reduced while retaining noise-level accuracy of the full model. We demonstrate the effectiveness and reliability of the simplified model in CEST MRI multi-pool quantification, and its superior performance compared to conventional analysis using MTR_{asym}.

Methods

For validation, we utilized simulated data of 7-pool Z-spectra, including pools for water, magnetization transfer (MT), nuclear Overhauser effect (NOE), hydroxyl, amine, guanidine, and amide. The simulations were performed using Pulseq-CEST [3], and Rician noise was added to mimic realistic conditions. We examined 10 different B_1 values ranging from 0.2 to 2.0 µT and 10 concentrations for each pool, from 10 to 100 mM (five-fold for NOE).

Initially, the numerical solution comprised 26 parameters, and the original analytical solution included 21 parameters [2]. For our simplified model approach, this was reduced to 14 parameters by neglecting R_2 relaxation effects for all CEST pools and combining the amine and hydroxyl pools into a single composite pool. We quantified linearity between fitted proton fractions and simulated concentrations using goodness-of-fit R^2 for both, the full analytical and our simplified model. We then compared these to the respective values obtained using MTR_{asym} (averaged over a range of ± 0.5 ppm around chemical shift frequency).

Results

Figure 1 illustrates the simulated data and fit of our simplified model for identical concentrations of all pools (five-fold for NOE), highlighting the precision and effectiveness of our model.

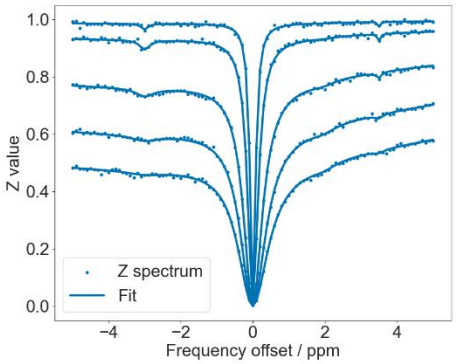

Fig. 1: Simulated data and analytical fit for identical concentrations (50 mM) of all pools except NOE (250 mM). Remaining parameters were provided as in [4] except MT, which was assumed to have a Lorentzian line-shape with an offset of -3 ppm.

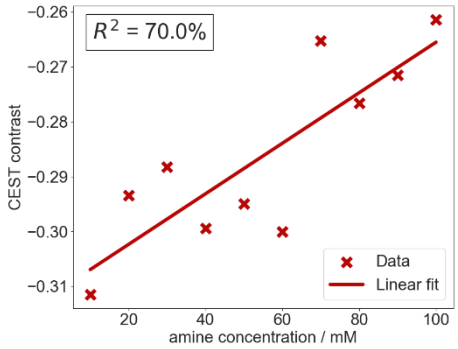

Fig. 2: Exemplary linearity analysis of the calculated CEST contrast (averaged MTR_{asym}) and metabolite concentration (amine).

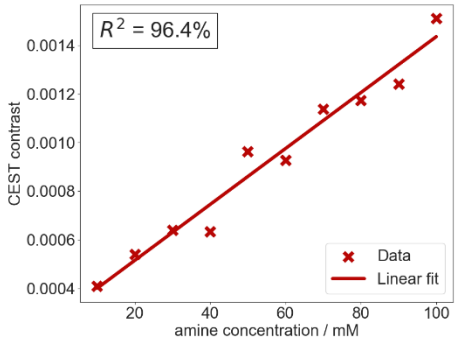

Fig. 3: Exemplary linearity analysis of the calculated CEST contrast (proton fraction, simplified model) and metabolite concentration (amine).

CEST Pool	Highest R^2 (%) MTR_{asym}	R^2 (%) full analytical model	R^2 (%) simplified model
NOE	97.0	93.0	95.0
OH	62.0	56.8	70.5
Guanidine	95.4	95.8	98.3
Amine	70.0	50.8	96.4
Amide	83.9	88.6	97.8

Tab. 1: Summary of R^2 values, measuring linearity of CEST contrast obtained with MTR_{asym} and model-based analysis. For MTR_{asym}, only the highest R^2 for all simulated B_1 were considered.

Figures 2 and 3 provide exemplary linearity analyses of the calculated CEST contrast (mean MTR_{asym} and proton fraction of our simplified model, respectively) and metabolite concentration for the amine pool. These figures show how our model improves upon conventional methods in terms of accuracy and consistency.

Table 1 summarizes the R^2 values, reinforcing the quantitative improvements our model provides over the MTR_{asym} method. The obtained R^2 values indicate that the simplified model, while reducing the number of free parameters, retains a high level of accuracy. This method consistently delivered higher or comparable R^2 values across different pools. Particularly fast exchanging pools (amine, hydroxyl) benefit from the combined pool model.

Discussion

The results underscore that our simplified model efficiently quantifies metabolite concentrations in CEST MRI by maintaining the noise-level accuracy of the full model with fewer parameters. Utilizing a combined pool for amine and hydroxyl group did not measurably impact the model's accuracy. The superior linearity of fitted proton fractions compared to MTR_{asym} highlights the robustness of our approach. The higher R^2 values across various pools demonstrate the model's reliability and its potential as a valuable tool in preclinical research, offering a more accurate and efficient method for analyzing CEST and MT effects. Further, model-based analysis can distinguish changes in CEST contrast induced by either concentration or exchange rate, as well as multiple pools simultaneously.

Conclusion

Our study demonstrates that the simplified model approach for CEST MRI multi-pool quantification not only enhances the robustness and reliability of CEST analysis but also outperforms traditional methods such as MTR_{asym} in terms of linearity and precision. The ability to efficiently distinguish changes in CEST contrast due to concentration or exchange rate, as well as analyze multiple pools simultaneously, underscores the potential of this model as a powerful tool in preclinical research.

Acknowledgements

This work was supported by the Deutsche Forschungsgemeinschaft (German Research Foundation, Project-ID 431460824).

References

1. Ward KM et al. A new class of contrast agents for MRI based on proton chemical exchange dependent saturation transfer (CEST). J Magn Reson, Volume 143; 2000.

2. Zaiss M, Bachert P. Chemical exchange saturation transfer (CEST) and MR Z-spectroscopy in vivo: a review of theoretical approaches and methods. Phys Med Biol, Volume 58; 2013.

3. K Herz K et al. Pulseq-CEST https://pulseq-cest.github.io/; 2023.

4. van Zijl PCM et al. Magnetization Transfer Contrast and Chemical Exchange Saturation Transfer MRI. NeuroImage, Volume 168; 2018.

Direct Encoded Signal Control with Phase Distribution Graphs for readout-tailored multipulse pTx optimization

Jonathan Endres*,[1] Simon Weinmüller,[1] Martin Freudensprung,[1] Peter Dawood,[1,2] Felix Glang,[3] Armin M. Nagel,[4] Moritz Zaiss[1,5]

[1] Institute of Neuroradiology, Universitätsklinikum Erlangen, Friedrich-Alexander-Universität Erlangen-Nürnberg, Erlangen, Germany
[2] Experimental Physics 5, University of Würzburg, Würzburg, Germany
[3] Magnetic Resonance Center, Max Planck Institute for Biological Cybernetics, Tübingen
[4] Institute of Radiology, Universitätsklinikum Erlangen, Friedrich-Alexander-Universität Erlangen-Nürnberg, Erlangen, Germany
[5] Department Artificial Intelligence in Biomedical Engineering, Friedrich-Alexander-Universität Erlangen-Nürnberg, Erlangen, Germany

* Jonathan.Endres@uk-erlangen.de

Synopsis:

DESC optimizes the statically shim of each individual pulse considering readout, reordered encoding, and reconstruction leading to less inhomogeneities in the final image using Phase Distribution Graph as simulation in the MR-zero framework.

Introduction

RF shimming using parallel transmission is a widely used technique to increase the homogeneity of the transmit (B1+) field, especially at high field strengths. This approach already has been successfully extended by optimizing static shimming for each pulse of a multipulse sequence individually. This means that an individual pulse does not need to be as homogeneous as possible, only the resulting magnetization over the course of the sequence. This technique was introduced before, titled Direct Signal Control[1] using spatially resolved Extended Phase Graphs[2,3]. By using Phase Distribution Graphs[4] for accurate signal simulations, we extend this approach even further by optimizing the reconstructed image instead of the unencoded signal. This gives the optimization even more freedom, as the magnetization does not need to be homogeneously excited anymore, as long as the inhomogeneities are not visible in the final image.

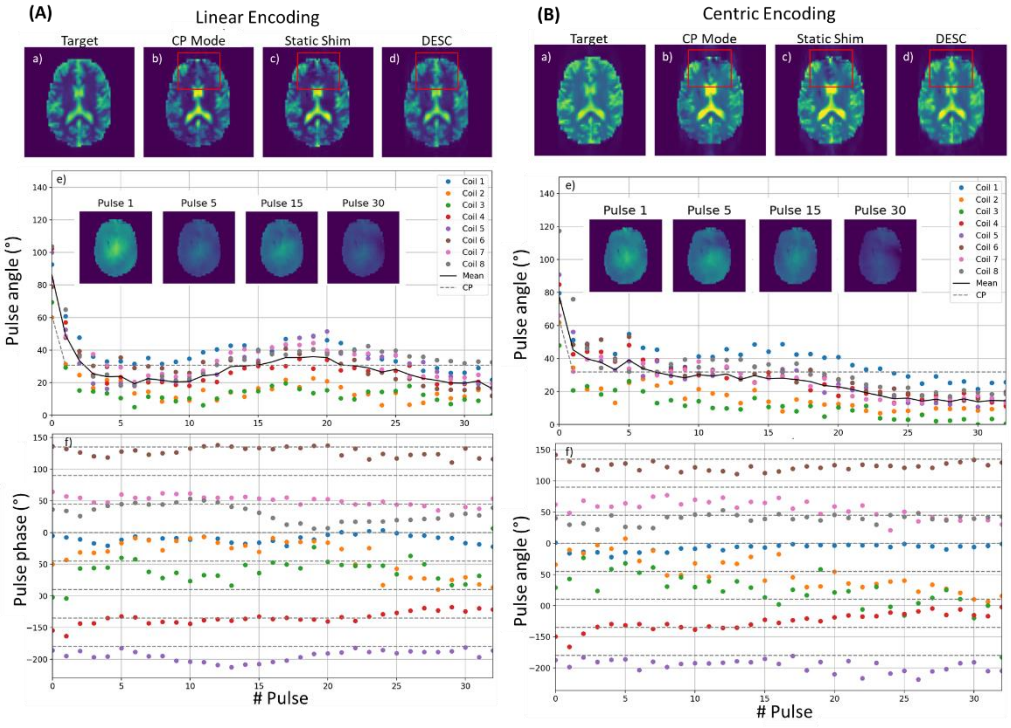

Fig. 1: Simulation result of the optimization process for linear (A) and centric (B) encoding. Target (a) is compared to standard CP Mode (b), static shim (c) and DESC result (d). The resulting flip angles of each pulse is shown in (e). Red box points out the main improvements. The image inlays in e) show varying B1+ fields of selected RF pulses.

Methods

In this work, PDG and the MR-zero[5] framework were extended to include multiple transmit coil sensitivities. With this, calculating the

reconstructed image for per-pulse statically shimmed sequences is possible.

The whole simulation and reconstruction pipeline are implemented PyTorch, which enables sequence optimization with gradient descent. The optimized transient-state TSE sequence uses 90° excitation, one first 180° refocusing pulse dummy pulse, followed by subsequent 90° refocusing pulses. For optimization a resolution of 64x64 with GRAPPA 2 is used. Except from the excitation flip angle (CP mode), all other shim modes were optimized individually. The chosen loss function is the RMS of the magnitude difference between the reconstruction and an ideal target image, which is simulated with constant, mean relative B1+ value of the CP mode. The phantom chosen for the simulation is a combination of BrainWeb[6] data and B0 and multi-channel B1+ maps measured at 7T with the DREAM sequences[7]. The resulting shim modes were exported using the pTx extension of the Pulseq standard[8,9]. To double the resolution, a two-shot sequence is used with equal pulse trains. The measurements were performed at a 7T MAGNETOM Terra.X scanner (Siemens Healthcare, Erlangen) on a healthy subject after written informed consent and approved by the local ethics committee.

Results

The optimization took on average 3 minutes for 100 iterations and results in different flip angles and pulse-specific shimming patterns for both reorderings (Fig. 1 e-f). The resulting homogeneity is better than for the shown static shimming method (Fig. 1 a-d). The applied pulse-specific B1 fields can be seen in Fig. 1.

For the centric reordering, a homogeneous B1+ field is achieved early on in the sequence, which is not as important for linear readouts. Fig. 2 displays the measured images which confirm the simulation results.

Discussion and Conclusion

Full ‘sequence shimming’ or ‘direct encoded signal control’ in reasonable time is possible with PDG. As it simulates the whole acquisition and reconstruction pipeline, it produces improved tailored optimizations compared to solutions that ignore readout, reordered encoding, and reconstruction. Inhomogeneities in the magnetization are acceptable, as long as they do not influence the currently measured k-space samples. Additionally, central k-space lines have a larger impact on the reconstructed image and are more susceptible to inhomogeneities than outer k-space lines. The end-to-end optimization utilized here takes this automatically into account by comparing the resulting reconstruction, eliminating the need of hand-tuning loss functions. We can match intensity and phase of the transmit k-space k_T and the receive k-space k_R.

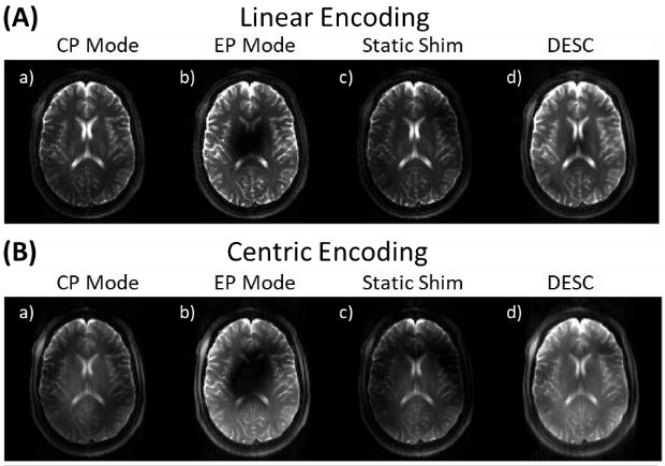

Fig. 2: In vivo measurement of the CP mode (a), EP mode (b), the static shim mode (c) and DESC (d) for linear (A) and centric (B) encoding.

References

1. Malik SJ. Direct signal control of the steady-state response of 3D-FSE sequences. MRM; 73: 951-963.
2. Weigel M. Extended phase graphs: Dephasing, RF pulses, and echoes - pure and simple. JMRI;41(2):266-295.
3. Malik SJ. Spatially resolved extended phase graphs: Modeling and design of multipulse sequences with parallel transmission. MRM;68(5):1481-1494.
4. Endres J. Phase distribution graphs for fast, differentiable, and spatially encoded Bloch simulations of arbitrary MRI sequences. MRM. 2024; 1-16.
5. Loktyushin A. MRzero - Automated discovery of MRI sequences using supervised learning. MRM;86(2):709-724.
6. BrainWeb: Online Interface to a 3D MRI Simulated Brain Database. http://www.bic.mni.mcgill.ca/users/crisco/HBM97_abs/HBM97_abs.html. Accessed July 12, 2022.
7. Nehrke K. DREAM-a novel approach for robust, ultrafast, multislice *B*1 mapping: DREAM *B1* Mapping. MRM;68(5):1517-1526.
8. Layton KJ. Pulseq: A rapid and hardware-independent pulse sequence prototyping framework: Rapid Hardware-Independent Pulse Sequence Prototyping. MRM;77(4):1544-1552.
9. Freudensprung M. A simple pTx Pulseq extension for pulse-specific B1 shimming (LT53). *In Proc. ESMRMB 2023*. Basel; 2023.

Implementing whole brain spectroscopy on a vendor agnostic pulse programming platform

Franziska Lohrengel[1], Oded Gonen[2] and Jan-Bernd Hövener[1]
[1] Section Biomedical Imaging, Molecular Imaging North Competence Center (MOIN CC), Department of Radiology and Neuroradiology, University Medical Center Schleswig - Holstein, Kiel University, Kiel, Germany.
[2] Center for Advanced Imaging Innovation and Research (CAI2R), Department of Radiology, New York University Grossman School of Medicine, New York, NY USA

Synopsis:
We explored implementing whole-brain magnetic resonance spectroscopy (wbMRS) using a vendor agnostic platform (pulseq). Data acquired on a spherical model solution containing brain metabolites, but no lipids, showed that a simple one-pulse sequence of the manufacturer yielded identical data as our implementation, but a more complex water suppression scheme showed differences. The full wbNAA sequence, combining inversion recovery, water suppression binominal excitation and subtraction, yielded well resolved metabolite spectra with 8.8 Hz full width at half maximum after manual shim. Future work will focus on resolving the differences and in vivo testing.

Introduction

Magnetic resonance spectroscopy (MRS) uniquely enables non-invasive, in vivo quantification of brain metabolites. While localized spectroscopy is effective for focal diseases, it falls short in non-focal brain conditions. Whole-brain spectroscopy (wb-MRS), particularly for N-Acetyl-l-Aspartate detection, addresses this limitation. Challenges include robust water signal suppression, skull lipid resonances, and brain-wide magnetic field homogeneity.

These challenges were successfully addressed by a whole-brain NAA (wbNAA) sequence were a multi-pulse WS (WET[1]) was combined with a binominal $1\bar{3}3\bar{1}$ excitation pulse for suppressing water and lipids. An adiabatic inversion pulse nullifies NAA signals while recovering lipid resonances, facilitating metabolite spectrum extraction by subtracting even and odd scans.[2]

While wb-NAA MRS was successfully demonstrated at several sites, implementations were limited to one vendor, and an open source, vendor agnostic version does not exist yet.

Thus, the goal of this work was to implement the latest generation of whole-brain MRS sequences[3] in an open-source format, facilitating the transfer across different scanners and software versions.

Methods

A whole body 3T MRI system with a 64 channel head/neck coil was used (Cima.x, Siemens) to record spectra of a spherical, 1.4 l model solution containing 50 mM potassium phosphate monobasic, 5 mM sodium hydroxide, 12.5 mM N-acetyl-L-aspartatic acid (NAA), 10 mM creatine hydrate, 3 mM choline chloride, 7.5 mM myo-inositol, 12.5 mM L-glutamic acid, 5 mM DL-lactic acid, 15mM sodium azide, and 1.8mM Magnavest.

The manufacturers' free induction decay (FID) sequence with and without WET[1] WS, a custom-written FID sequence and a combination of (custom-written) WET module, an adiabatic inversion pulse and a binominal $1\bar{3}3\bar{1}$-pulse were used. A wbMRS sequence was implemented by combing these components as described by Soher et al.[3] For shimming, the static tune-up shim and manual optimization were used. Raw data was imported and processed offline.

Results

The full width at half maximum (FWHM) of the signal acquired with the manufacturers FID yielded 24.6 Hz with the tune up shim, 7.4 Hz after manual optimization, and 811.8 Hz after deliberately worsening the shim (Fig. 1).

Comparing the manufacturers FID with our own sequence yielded very similar results (Fig. 1) The manufacturers implementation of WET, however, reduced the water signal by a factor of 23 (Fig. 2), while our implementation yielded a factor of 6 (Fig. 3). In both cases, the metabolite signals were identified on the slope of the residual water signal.

The wbNAA sequence yielded the strongest suppression of the water signal. The signal of NAA and other metabolites was clearly resolved (Fig. 4) with a FWHM of 8.8 Hz.

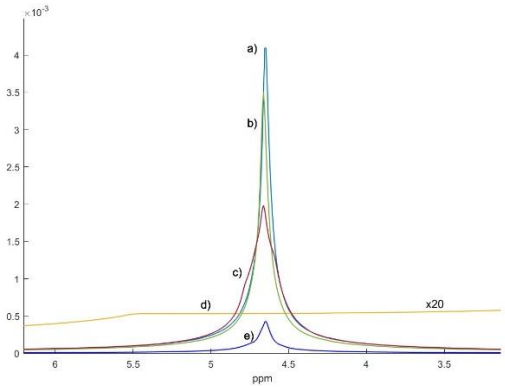

Fig. 1: Magnitude non-localized 1H-MR spectra of the spherical model solution: (a) our implementation,

(b-d) manufacturer's FID with different shims: (b) manually optimized (FWHM = 7.4 Hz), (c) poor manual (FWHM = 811.8 Hz), and (d) Siemens' Tune-Up (FWHM = 24.6 Hz). (e) shows the minimal discrepancy between (a) and (b), confirming very similar pulse sequences.

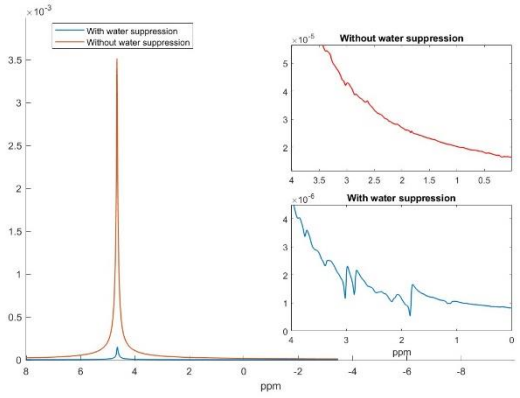

Fig. 2: Magnitude non-localized ^{1}H-MR spectra of the spherical model solution acquired with the manufacturers FID sequence with and without WS (WET), both with identical and optimized shimming. The water signal is notably reduced by a factor of 23, enhancing visibility of metabolite peaks.

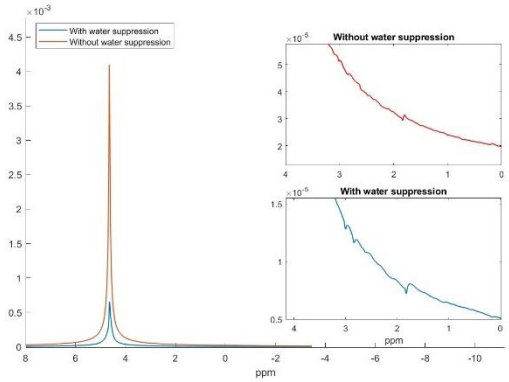

Fig. 3: Non-localized ^{1}H-MR spectra of the model solution acquired with our implementation of the FID sequence with and without WT WS, with identical and optimized shimming. The water signal was reduced by a factor of 6.

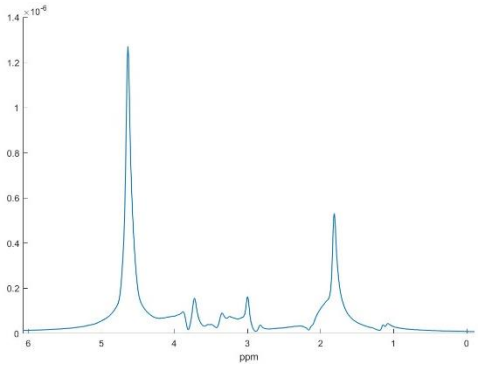

Fig. 4: Magnitude non-localized ^{1}H-MR spectrum of the model solution acquired with the wbNAA sequence and manually optimized shim. The water signal was reduced by a factor of 270, allowing the preparation of the metabolite peaks. The NAA-peak yielded a linewidth of 8.8 Hz.

Discussion

We successfully implemented the wbNAA sequence on a vendor-agnostic pulse programming platform, emphasizing the importance of water suppression (WS) and magnetic field homogeneity for MRS. Effective WS significantly improved metabolite detection by reducing the dominant water signal. Manually optimized shimming enhanced spectral peak sharpness and definition.

A comparison of the custom FID sequence with the manufacturer's FID yielded similar results, suggesting accurate replication of the sequence, despite some minor differences in WS-FID features. The wbNAA sequence reduced the water signal by a factor of about 270 and revealed clearer metabolite peaks. However, our model solution lacked lipids, a significant in vivo challenge. Future work should include the manufacturer's 3D shim and a direct comparison to a native wbNAA sequence to assess implementation effectiveness.

Conclusion

A first version of the wbNAA sequence was successfully implemented and yielded well resolved spectra of a spherical model solution without lipids. When comparing sequences implemented using the vendors' environment or a vendor-agnostic solution, a simple pulse sequences resulted identical spectra, but the effect of a more complex WS scheme was different. Future work will focus on resolving these matters, adding lipids and testing the sequence in vivo.

References

1. Ogg RJ, Kingsley RB, Taylor JS. WET, a T1- and B1-Insensitive Water-Suppression Method for in Vivo Localized 1H NMR Spectroscopy. *Journal of Magnetic Resonance, Series B*. 1994;104(1):1-10. doi:10.1006/jmrb.1994.1048

2. Gonen O, Viswanathan AK, Catalaa I, Babb J, Udupa J, Grossman RI. Total brain N-acetylaspartate concentration in normal, age-grouped females: Quantitation with non-echo proton NMR spectroscopy. *Magnetic resonance in medicine*. 1998;40(5):684-689.

3. Soher BJ, Wu WE, Tal A, et al. Automated whole-brain N-acetylaspartate proton MRS quantification. *NMR in Biomedicine*. 2014;27(11):1275-1284.

Optimization of multi-VENC compressed sensing 4D flow MRI for high-resolution neurovascular applications

Caroline Scheufler[1*], Ali El Ahmar[1], Patrick Winter[1], Stephan Koenig[1], Mark Höller[1], Daniel Giese[2], and Susanne Schnell[1]

[1] Department of Medical Physics, University of Greifswald, Greifswald, Deutschland.
[2] Magnetic Resonance, Siemens Healthineers AG, Erlangen, Germany

* Contact communicating author: caroline.scheufler@stud.uni-greifswald.de

Synopsis: This study aims to optimize a Multi-VENC Compressed Sensing (CS) 4D Flow MRI sequence for imaging brain blood vessels at a resolution of 1mm. Using a 3T MRI scanner, we evaluated 2 CS parameter sets (CSPs) on a silicon intracranial model with an aneurysm. The measurements showed that the CSP_1 provided higher vessel area and mean flow rate values. Streamline visualization highlighted significant differences in aneurysm depiction. Further validation will compare these results with GRAPPA-accelerated sequences and higher R-factor measurements.

Introduction

4D flow MRI is a technique used for the quantification and visualization of blood flow dynamics within a 3D volume throughout the cardiac cycle (1, 2).

Recently, a new Multi-VENC Compressed Sensing (CS) 4D flow sequence has been developed and validated for aortic flow with a resolution of 2.5mm (1, 3). Our study aims to optimize this sequence for imaging blood vessels in the brain at a resolution of 1mm. Given the undersampling inherent in CS methods, which reduce scanning time and allow for higher acceleration factors (R-factor), a specific set of Compressed Sensing Parameters (CSPs) is essential for solving the CS reconstruction challenge (1,8). The sequence incorporates the typical CS parameters: spatial regularization, and temporal regularization, and has an additional scaling factor for temporal regularization (1,8). Additionally, a variable setup for Corner Cutting and sampling density in the k-space center is given (1,3) to allow further acceleration.

Material & Methods

4D flow MRI measurements

All scans were performed on a 3T MRI scanner (MAGNETOM Vida, Siemens, Erlangen, Germany) with a Small Ultra Flex 18-channel coil using a compressed sensing accelerated 4D flow research sequence. Sequence parameters: voxel size=1mm isotropic, TE=3.95ms, TR=5.96ms, temp. res.=41.72ms, FA=7°, $VENC_1$=50cm/s, $VENC_2$=100cm/s. For two CSPs including the minimum and maximum for each parameter, dual-VENC measurements were acquired. (Tab.1)

Name of CSP	Compressed Sensing and additional parameter				
	Spatial regulation	Temporal regulation	Additional Scaling	Corner Cutting	Density k-space center
CSP_1	0.002	3	0	0.2	0.01
CSP_2	0.001	2	1	1	0.29

Table 1: used CSP for 4D flow CS dual-VENC measurements

Phantom set-up

A silicon intracranial model with an anterior cerebral artery aneurysm (“HN-S-A-010”) (ELASTRAT, Geneva, Switzerland) filled with a blood-mimicking fluid (composed of 60% water and 40% glycerol, doped with Gadovist at 0.1 mol/ml, approximately 0.2% by volume) was used. (5). A pulsatile flow of 25ml/s and 72BPM with a carotid physiological waveform was provided by a CompuFlow 1000-MR pump (Shelley Medical Imaging Technologies, London, Canada). The Circle of Willis (CoW) Phantom was surrounded by Gd-doped water-embedded beads to reduce the motion of the vessels and increase SNR (4).

Data analysis

We utilized an in-house MATLAB tool for preprocessing (2,7). Following this, volumetric flow quantification and vessel area was conducted using a semi-automatic in-house MATLAB tool (6) for four CoW vessels: RICA, LICA, RACA, and LACA. (Tab.2).

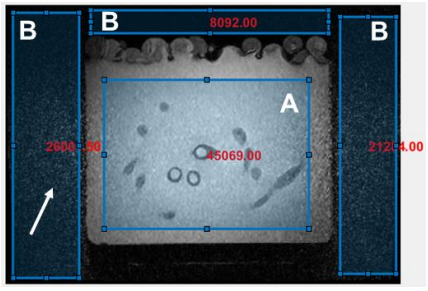

Fig. 1: example of SNR ROI: **(A)** signal mean area **(B)** noise std regions

Moreover, the signal-to-noise ratio (SNR) was assessed in the magnitude images by dividing

the mean signal (rectangle covering approx. 80% of the phantom) by the standard deviation of the noise (three rectangles placed outside the phantom) (see Fig. 1). This calculation was performed for all magnitude images in the series and was used to verify the first visual inspection.

Results

The visual inspection showed less sharpness and more noise for CSP_2, which used less spatial regularization. The CSP_1 had an SNR of 12.11±1.31 whereas CSP_2 had an SNR of 10.67±1.74 (Tab.2). Analysis of the Dual-VENC acquisitions revealed that the CSP_1 not only had larger mean vessel area (p = 0.044) but also showed higher mean flow across (p = 0.043) the four vessels compared to the CSP_2.

name	area [mm^2] (± std)		mean flowrate [ml/s] (± std)		mean velocity [m/s] (± std)	
	CSP_2	CSP_1	CSP_2	CSP_1	CSP_2	CSP_1
RICA	18.42 (2.17)	19.05 (2.67)	1.09 (0.07)	1.15 (0.06)	0.06 (0.007)	0.07 (0.008)
LICA	23.84 (3.22)	24.61 (3.36)	1.42 (0.09)	1,46 (0.09)	0.07 (0.01)	0.07 (0.01)
RACA	4.91 (0.47)	5.03 (0.66)	0.27 (0.03)	0.28 (0.02)	0.06 (0.005)	0.06 (0.007)
LACA	7.4 (0.72)	7.79 (0.83)	0.71 (0.08)	0.74 (0.07)	0.10 (0.006)	0.10 (0.004)

Table 2: Comparison of mean and standard derivation for area, mean flow rate, and mean velocity between best and worst CS parameter settings (CSP_1, CSP_2) for RICA, LICA, LACA, RACA.

In addition, streamline visualization revealed qualitative differences between the two CSPs, especially within the aneurysm. The CSP_1 showed a higher streamline density compared to the CSP_2. Moreover, noticeable differences in the shape of the aneurysm were observed. In the data using the CSP_2 a lack of flow was apparent (Fig. 2, marked with an arrow).

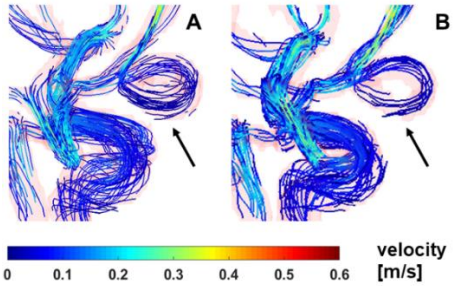

Fig. 1: **(A)** CSP_1 - Streamline visualization shows consistent helical circulating flow and higher streamline density in the aneurysm compared to **(B)** CSP_2

Discussion & Conclusion

Two CSP settings were applied for Dual-VENC 4D flow acquisitions of a CoW phantom. Lower spatial regularizion (in CSP_2) causes increased noise and the visual deterioration of the image. A detailed vessel-wise flow analysis was performed. The CSP_1 setting revealed higher values for mean vessel area, and flow rate. The streamlines clearly show that the CSP_1 represents the aneurysm better, with a well-defined helical flow. The flow data shows significantly higher values for the CSP_1.

Outlook

Further investigation will include systematic testing for each of the CS and acceleration parameters, to receive a CSP for an intracranial future workflow. Also, we will compare our results with flow data obtained from a GRAPPA-accelerated (R=2) dual-VENC 4D flow MRI sequence (2). Additionally, we plan to validate our findings by determining the velocity-to-noise ratio (VNR) (2). Once we determined suitable acceleration, we aim to explore using more than two VENCs (multi-VENC).

References

1. Ma LE, Markl M, Chow K, et al.: Aortic 4D flow MRI in 2 minutes using compressed sensing, respiratory controlled adaptive k-space reordering, and inline reconstruction. *Magn Reson Med* 2019.

2. Schnell S, Ansari SA, Wu C, et al.: Accelerated dual-venc 4D flow MRI for neurovascular applications. *Journal of Magnetic Resonance Imaging* 2017.

3. Ma LE, Chow K, Forman C, et al.: Highly acclerated 4D flow with compressed sensing for evaluation of aortic hemodynamics, abstract: 30th Annual Meeting of the Society for Magnetic Resonance Angiography, Glasgow, Scotland, 2018.

4. El Ahmar A, Winter P, König S, Duckert A, Kromrey M-L, Schnell Susanne: Using water beads as static tissue in a Circle of Willis flow phantom in 4D flow MRI, 2024, ISMRM

5. Lorenz R, Bock J, Snyder J, Korvink JG, Jung BA, Markl M: Influence of eddy current, Maxwell and gradient field corrections on 3D flow visualization of 3D CINE PC-MRI data. *Magn Reson Med* 2014.

6. Vali A, Aristova M, Vakil P, et al.: Semi-automated analysis of 4D flow MRI to assess the hemodynamic impact of intracranial atherosclerotic disease. *Magn Reson Med* 2019.

7. Bock J, KBW, HJ, & MM. *Optimized Pre-Processing of Time-Resolved 2 D and 3 D Phase Contrast MRI Data*, JB_velomaptool_ISMRM2007. 2007

8. Lustig M, Donoho D, Pauly JM. Sparse MRI: the application of compressed sensing for rapid MR imaging. Magn Reson Med.2007

SNR requirements for quantitative frequency-modulated bSSFP

Clemens Mey,[1] Walter A. Wohlgemuth[1] and Anne Slawig[1]

[1] University Clinic and Polyclinic for Radiology Halle (Saale), Germany

Synopsis: In-silico study evaluates SNR requirements for quantitative frequency-modulated bSSFP MRI. Simulations show considerable deterioration in accuracy of T1 and T2 with lower SNR. Frequency-modulated bSSFP offers fast qMRI, but SNR affects accuracy, requiring trade-offs in scan time for reliable results.

Introduction

BSSFP sequences provide the highest SNR per unit time of any known MRI sequence and short scan times (1). However, the signal's amplitude is greatly affected by off-resonance as well as sensitive to changes in T1, T2, flip angle and TR. This distinct off-resonance profile is already utilized for qMRI by phase-cycled bSSFP approaches (2). The signal can be described as an ellipse in the complex plane by:

$$\mathrm{I}(\theta) = \mathrm{M}\frac{1 - \mathrm{a}\exp(\mathrm{i}\theta)}{1 - \mathrm{b}\cos(\theta)}$$

For quantitative mapping, T1 and T2 can be determined as:

$$\mathrm{T1} = -\frac{\mathrm{TR}}{\ln\frac{\mathrm{a}(1+\cos\alpha-\mathrm{ab}\cos\alpha)-\mathrm{b}}{\mathrm{a}(1+\cos\alpha-\mathrm{ab})-\mathrm{b}\cos\alpha}}$$

$$\mathrm{T2} = -\frac{\mathrm{TR}}{\ln(\mathrm{a})}$$

Current approaches require at least four or six full phase-cycled acquisitions. Using a frequency-modulated (fm) method (3,4), the entire signal is acquired in a single measurement. While potentially resulting in a shorter total scan time, it comes at the cost of lower SNR than multiple phase-cycled acquisitions (5).

$$SNR = \frac{\sum_{n=1}^{N}|I_n(\theta)|}{N\,\sigma}$$

This simulation study was conducted, to determine suitable measurement parameters for a fm bSSFP measurement and to evaluate the SNR requirements for a reliable fit of the elliptical signal model to calculate relaxation parameters.

Methods

The behavior of the fm bSSFP signal has been simulated using Bloch equations. The signal trajectory is determined by the parameters TR, flip angle, relaxation times T1 and T2, and modulation rate. First, the modulation rate was adjusted from 0° to 1° per readout while keeping other parameters fixed (TR = 2TE = 10 ms, FA = 70°, T1 = 1000 ms, and T2 = 80 ms). Secondly, simulations were performed for the same settings, with a set modulation rate of 0.01°. White noise was added to the resulting signals with SNRs ranging from 20 to 450 in increments of 5. Typical values for bSSFP measurements range between 30 and 150 (5). The noisy simulated signals were fitted with the elliptical signal model, T1 and T2 were determined from the fit parameters. An exemplary signal is shown in Fig. 1.

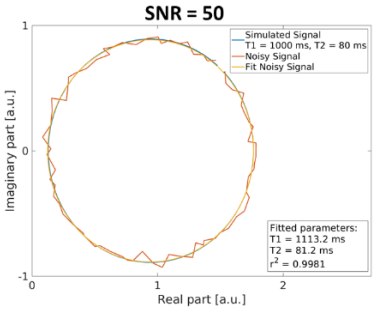

Fig. 1: Simulated signal (blue) for TR = 2TE = 10 ms, T1 = 1000 ms, T2 = 80 ms, FA = 70°, and a modulation rate of 0.01°. White noise is added (orange) with SNR of 50 and its fit (yellow).

The distributions of T1 and T2 values over 1,000 repetitions were analyzed by fitting the resulting histograms with a log-normal distribution. Based on this, the minimum SNR required to determine T1 or T2 with 95 % accuracy was computed for various tissue-typical relaxation time combinations.

Results

Simulated signals for various modulation rates are shown in Figure 2.

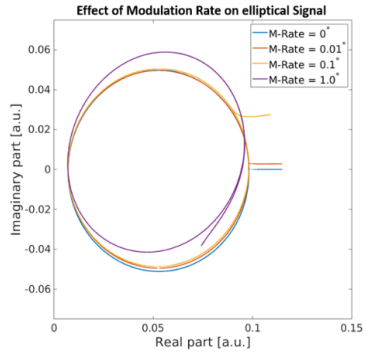

Fig. 2: Simulated signal for different modulation rates (0°, 0.01°, 0.1°, 1°). The parameters TR = 2TE = 10 ms, T1 = 1000 ms, T2 = 80 ms, and FA = 70° are kept constant. As the modulation rate decreases, the signal shape approaches the elliptical signal model

While the signal model is valid for small modulation rates, it does not fit the data at high modulation rates.

Figure 3 shows the minimum SNR required to fit T1 or T2 with 95% accuracy for various combinations of T1 and T2. As T1 or T2 increases, the SNR required for an accurate determination increases. The necessary SNR for accurate T2 fitting is much lower than that required for T1 fitting.

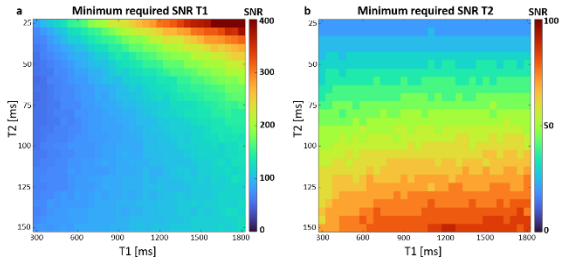

Fig.3: Minimum SNR to achieve 95% accuracy of T1 (a) and T2 (b). The initial parameter settings for the simulation are TR = 10 ms, FA = 70°, and the modulation rate is 0.01° at 1000 repetitions. Please note the different scaling of the color bars.

Discussion

The model is suitable for fm-bSSFP when the modulation rate is low, which is consistent with literature. The maximum modulation rate to maintain steady state is usually given as 1°-3° per readout (4).

Ellipse fitting is highly sensitive to small changes. T1 is affected by even the slightest corruption, despite appearing visually sound. On the other hand, T2 is more robust. Generally, the SNR achievable in a single in vivo bSSFP measurement will be just sufficient for a reasonable determination of T2, but not for T1.

The main difference to phase-cycled measurements is the repetition. Phase-cycled algorithms, like Planet (2), are based on multiple full acquisitions, which naturally results in higher SNR. Fm bSSFP could achieve higher SNR by acquiring the ellipse multiple times at the expense of the scan time advantage. Analyses of SNR requirements can help determine how much data, and therefore scan time, is needed for a robust fit.

Major Limitation of this work is that only white noise was added. In reality, many different sources can contribute to the corruption of the signal in each voxel. Examples include undersampling artifacts, motion, and eddy currents.

Conclusion

Frequency-modulated bSSFP offers the opportunity for faster qMRI than is possible with phase-cycled approaches. However, our simulations show that the accuracy depends strongly on the SNR, which in practice could be increased by averaging. A careful balance between accuracy and scan time is required.

References

1. Klaus Scheffler and Stefan Lehnhardt. “Principles and applications of balanced SSFP techniques.” In: European radiology 13.11 (2003), pp. 2409–2418.

2. Yulia Shcherbakova et al. “PLANET: an ellipse fitting approach for simultaneous T1 and T2 mapping using phase-cycled balanced steady-state free precession.” In: Magnetic resonance in medicine 79.2 (2018), pp. 711–722

3. Anne Slawig et al. “Multifrequency reconstruction for frequency-modulated b SSFP.” In: Magnetic resonance in medicine 78.6 (2017), pp. 2226–2235.

4. DL Foxall. “Frequency-modulated steady-state free precession imaging.” In: Magnetic Resonance in Medicine: An Official Journal of the International Society for Magnetic Resonance in Medicine 48.3 (2002), pp. 502–508.

5. Marcus Björk et al. “Parameter estimation approach to banding artifact reduction in balanced steady-state free precession.” In: Magnetic resonance in medicine 72.3 (2014), pp. 880–892. doi:10.1002/mrm.2498.

T2 mapping based on frequency-modulated bSSFP

Clemens Mey,[1] Walter A. Wohlgemuth[1] and Anne Slawig[1]

[1] University Clinic and Polyclinic for Radiology Halle (Saale), Germany.

Synopsis: This study investigates T2 mapping based on a fast frequency-modulated bSSFP MRI measurement. In vivo tests show promising results, correlating well with reference T2 maps. Challenges include SNR limitations and the sensitivity of the fit model.

Introduction

The signal of bSSFP is greatly affected by off-resonance as well as sensitive to changes in T1, T2, flip angle, and TR (1). This distinct signal profile is already utilized for qMRI by various phase-cycled bSSFP approaches (2,3). It can be described as an ellipse in the complex plane by:

$$\mathrm{I}(\theta) = \mathrm{M}\frac{1 - \mathrm{a}\exp(\mathrm{i}\theta)}{1 - \mathrm{b}\cos(\theta)}$$

Based on this model, T2 can be determined as:

$$\mathrm{T2} = -\frac{\mathrm{TR}}{\ln(\mathrm{a})}$$

In a frequency-modulated (fm) bSSFP experiment (4,5), the off-resonance is continually shifted from readout to readout. As a result, the entire off-resonance profile can be acquired in a single measurement. While potentially resulting in a shorter scan time, the frequency steps are limited to very small step widths. This means that a minimum number of steps is required to cover one period of the off-resonance profile.

This study was conducted to evaluate an in-vivo T2 map based on the elliptical signal model for a frequency-modulated bSSFP sequence.

Methods

In-vivo measurements of a single slice in the lower leg were conducted using an 18-channel body coil on a 3T Magnetom Vida MRI scanner (Siemens Healthineers).

For reference, a spin echo sequence was acquired with a total of 19 echoes (TR = 1500 ms, TEs between 18.8 and 188.0 ms, flip angle = 180°, image resolution = 1.2 mm, slice thickness = 10 mm, band width = 1149 Hz/Px). The total acquisition time was 7:17 min. Data was processed offline by fitting an exponential function to the signal intensity in the 19 consecutive echoes according to:

$$S = S0 * e^{-\frac{TE}{T2}} + y0$$

A reference T2 map was prepared from the fitting parameter.

Additionally, a tiny golden angle radial fm bSSFP experiment was performed (TR = 14 ms, TE = 7 ms, flip angle = 75°, base resolution = 256, modulation step width = 0.05°, spokes = 8192, image resolution= 1.2 mm, slice thickness = 10 mm, bandwidth = 1500 Hz/Px). The total acquisition time was 1:45 min.

In an offline postprocessing pipeline, the initial images were reconstructed by gridding 200 radial readout spokes into one k-space. A total of 36 images were thus derived using a sliding window approach. Due to the continuous shift in fm bSSFP, each of the images represents a different off-resonance case, similar to phase-cycled imaging. The subsequent reconstruction approach enforced the elliptical signal model and data consistency iteratively, similar to MAP proposed by Tran-Gia (6). A total of five iterations were performed. The T2 map was calculated based on the fitting parameter of the elliptical signal model.

Results

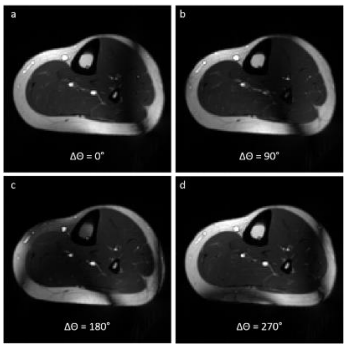

Fig. 1: Frequency-modulated bSSFP images of a lower leg with different off-resonances. Sliding window reconstruction is performed so that the resulting images are equivalent to four 90° phase-cycled images. As the off-resonance increases, the banding artifact shifts across the image.

Initially reconstructed images show strong undersampling artifacts, which are mitigated after the iteration reconstruction process. Four example images are shown in Figure 1. Good

anatomical detail is discernible and the banding artifact is shifted across the image, as in phase-cycled acquisitions.

Figure 2 displays data points and the respective fit of the elliptical signal model in two exemplary voxels, located in calf muscle and bone marrow. Both clearly differ in size and shape, according to the underlying tissue properties. Deviations are caused by noise and undersampling.

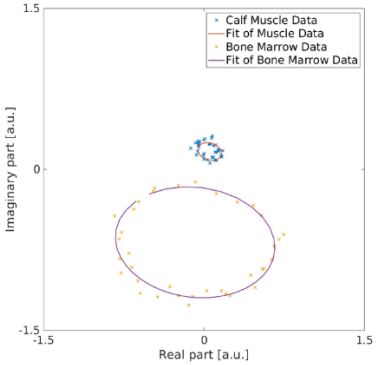

Fig. 2: Elliptical signals were observed in one pixel of the calf muscle (marked with a blue cross) and bone marrow (marked with a yellow cross), respectively, and their fits were determined based on the elliptical signal model.

The algorithm provides the quantitative T2 map, shown in Figure 3, which is similar to the reference map acquired by multi-echo spin echo. The bSSFP-derived T2 map retains some undersampling artifacts radiating from a high-intensity blood vessel.

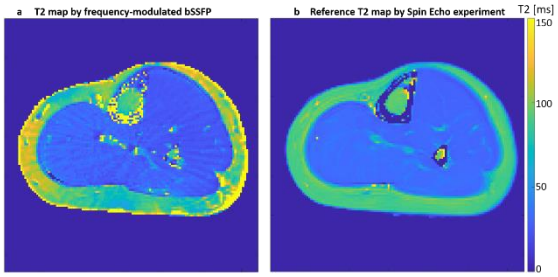

Fig.3: T2 maps of the lower leg were acquired using frequency-modulated bSSFP (a) and spin echo experiment (b) as a reference.

Discussion

T2 mapping based on fm bSSFP and the elliptical signal model is possible. The resulting maps are comparable to the gold standard.

Similar approaches currently require at least four or six fully phase-cycled acquisitions to obtain multiple measurement points along this ellipse (2,3), while here the entire signal behavior is covered in one fm scan. Nevertheless, the maximum modulation speed is limited in order to maintain the steady state and the suitability of the signal model, and is usually given as 1° to 3° per readout (5). While it is not reasonable to acquire so many lines for a single 2D slice, it is of interest for 3D or cardiac acquisitions.

Although the model contains T1 information, it was not possible to generate reasonable T1 maps in this study. The most likely cause is insufficient SNR, as the elliptical fitting model is very sensitive to even small perturbations.

A further limitation of this study is the stopping criteria for the iterative reconstruction, which was determined empirically and is highly dependent on the given setup.

Conclusion

Frequency-modulated bSSFP offers the possibility of faster qMRI than is possible with phase-cycled approaches. The T2 map calculated from the off-resonance behavior of the bSSFP measurements corresponds to the reference. Future work should extend the approach to 3D measurements or cardiac applications to fully exploit the potential for scan time reduction.

References

1. Klaus Scheffler and Stefan Lehnhardt. “Principles and applications of balanced SSFP techniques.” In: European radiology 13.11 (2003), pp. 2409–2418.

2. Yulia Shcherbakova et al. “PLANET: an ellipse fitting approach for simultaneous T1 and T2 mapping using phase-cycled balanced steady-state free precession.” In: Magnetic resonance in medicine 79.2 (2018), pp. 711–722

3. Kübra Keskin, Uğur Yılmaz, and Tolga Çukur. “Constrained ellipse fitting for efficient parameter mapping with phase-cycled bssfp mri.” In: IEEE Transactions on Medical Imaging 41.1 (2021), pp. 14–26. doi: 10.1109/TMI.2021.3102852.

4. Anne Slawig et al. “Multifrequency reconstruction for frequency-modulated b SSFP.” In: Magnetic resonance in medicine 78.6 (2017), pp. 2226–2235.

5. DL Foxall. “Frequency-modulated steady-state free precession imaging.” In: Magnetic Resonance in Medicine: An Official Journal of the International Society for Magnetic Resonance in Medicine 48.3 (2002), pp. 502–508.

6. Johannes Tran-Gia et al. “Model-based acceleration of parameter mapping (MAP) for saturationprepared radially acquired data.” In: Magnetic resonance in medicine 70.6 (2013), pp. 1524–1534.doi: 10.1002/mrm.24600.

The impact of fat-navigator resolution on motion parameter estimation accuracy

Fabian Müller [1*], Klaus Scheffler [1,2], and Dario Bosch [1,2]

[1] High-Field MR Center, Max Planck Institute for Biological Cybernetics, 72076 Tübingen, Germany.
[2] Department for Biomedical Magnetic Resonance, University of Tübingen, 72074 Tübingen, Germany.

* fabian.mueller@tuebingen.mpg.de

Synopsis: In this work, we investigate the impact of the resolution of the fat-navigator on the performance of retrospective motion estimation. For this, the extracted motion data is compared with the camera data. Furthermore, we evaluate wether two or three sub-pulse binomial pulses are better for fat-selective excitation at 9.4 T.

Introduction

High-resolution MR images are susceptible to the inevitable motion of the subject during the long acquisition time. Therefore, these images contain motion artifacts. To reduce the motion artifact in the image, the effects of the motion must be corrected. This can be achieved by motion correction based on navigator images[1,2]. In this work, we consider retrospective motion correction. The motion parameters are estimated by fat-navigators acquired after each partition, such that the relative position between the partitions is known. To avoid increasing the measurement time, low-resolution navigators would be beneficial. They also avoid additional energy deposition. Therefore, we investigate the impact of the resolution on the estimation accuracy of motion parameters estimation.

In order to obtain useful fat-navigators for motion correction, we first consider fat-selective binomial pulses[3] with two or three sub-pulses. The performance of these pulses in generating fat-navigator images is compared at 9.4 T. This is important since the three-sub-pulsed binomial pulse has a 50% longer duration than a two-sub-pulsed one, which can result in an increase in the total measurement time.

Based on this comparison we perform motion estimation on with the better binomial pulses for different fat-navigator resolutions. The obtained motion parameters are then compared with motion parameters measured by a commercial camera system.

Methods

The comparison of the fat-selective binomial pulses with two or three sub-pulses is conducted on an image with an isotropic voxel size of 2.3 mm and Grappa 4x4 acceleration. This is comparable to the later used fat-navigators. Both binomial pulses have a flip angle of 4° and a π-phase shift between the pulses.

Based on the observations from the binomial pulse comparison (see Fig. 1), a binomial pulse with three sub-pulses is utilized for the fat-navigator of all subsequent experiments. These navigators are Cartesian-sampled, accelerated by 4x4 Grappa with a separate fat-selective Grappa pre-scan, and have a flip angle of 4°. The full resolution of the navigator is 94 k-space points in each dimension, which corresponds to a voxel size of 2.4x2.4x1.9 mm. These fat-navigators are acquired after each partition of a MPRAGE. Based on these fat-navigators, the images are co-registered and the relative motion is estimated using SimpleITK[4]. To investigating different resolutions, the fat-navigator k-space is down-sampled to the desired size. Subsequently, the motion parameters are first calculated with the reduced

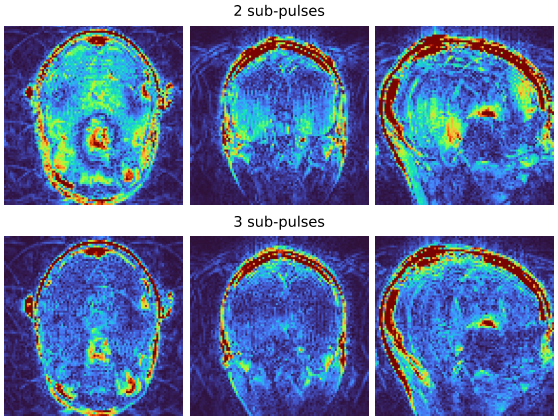

Fig. 1: Highly accelerated fat image (Grappa 4x4, voxel size: 2.3 mm) acquired with two and a three sub-pulsed binomial pulse, with a cut-off at 12.5% of the original maximum signal.

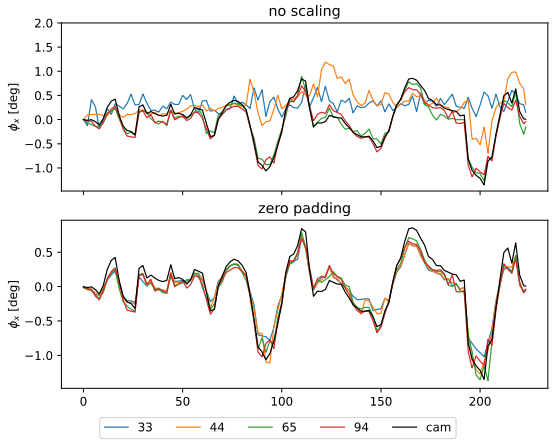

Fig. 2: Estimated rotation parameters for one axis compared to the rotation obtained by the camera for different k-space base resolutions 33, 44, 65 and 94. The correlation coefficient is about 97% for the best resolution.

navigator size. In a second run, the fat-navigators are up-scaled by zero-padding k-space to the original size. As the rotation angles are independent of the rotation center and translation, we use only the rotation angles to compare them with the camera system.

The MPRAGE is accelerated by a Grappa 2x1. Since the full k-space is reconstructed with a Grappa reconstruction the missing motion parameters are linearly interpolated.

Results

Fig. 1 shows the fat image obtained by binomial pulses with two or three sub-pulses. This demonstrates that both work, and artifacts due to signals from other tissues, except fat tissue, are reduced. However, the fat image obtained by three sub-pulses has approximately 20% less noise than the binomial pulse with two sub-pulses. The noise is defined as the mean value of all voxels with an intensity below 12.5% of the maximum value.

The comparison of different fat-navigator resolutions is shown in Fig. 2. This figure demonstrates that high resolutions support co-registration. As showed in Fig. 2, without scaling the high-resolutions are closer to the camera data than the low-resolution fat-navigators. However, this performance difference decreases with k-space zero-padding. It can be observed that the correlation coefficient for the 33 k-space point isotropic navigator increases from approximately 1.8% to 97% on the best axis, corresponding to the full resolution, when zero-padding is applied. The improvement on the worst axis is from approximately 0.5% to 68%.

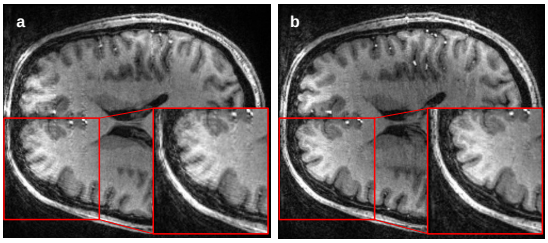

Fig. 3: Slice of image for comparison of direct and motion-corrected reconstruction. (a) Reconstructed image without motion correction. (b) Same image but with retrospective motion correction.

The estimated motion parameters are used in the image reconstruction with retrospective motion correction. Fig. 3 shows the original and improved MPRAGE image, in which motion artifacts have been reduced. This results in a higher image quality.

Discussion

As previously stated, the binomial pulse with three sub-pulses has less noise than the one with two sub-pulses. This is due to the fact that a three sub-pulsed binomial pulse is less sensitive to timing errors than the two sub-pulsed ones.

Fig. 3 shows that our workflow for retrospective motion correction based on fat navigators works. By applying zero-padding to fat-navigators with lower resolution, one can achieve estimation performance comparable to that of the full fat-navigator. The abstract is only based on two measurements. Further quantification of the performance increase due to up-scaling the resolution by zero-padding will require additional measurements.

Conclusion

The results indicate that binomial pulses with three sub-pulses are better than two for fat-selective excitation at a 9.4 T scanner. Additionally, the estimation precision of rotation angles for retrospective motion correction decreases with lower resolution. However, this can be improved by up-scaling the navigator image resolution by k-space zero-padding.

References

1. Gallichan D et al 2016.
   Magn Reson Med 75:1030–1039.
2. Federau C et al 2016.
   PLoS ONE 11(5): e0154974.
3. Thomasson D et al 1996.
   Magn Reson Med 35:563–568.
4. Yaniv Z et al 2018.
   J Digit Imaging 31(3): 290-303

Ultra-Low Frequency MR Elastography

Jakob Schattenfroh[1*], Rolf Reiter[1,2], Steffen Görner[1], Ingolf Sack[1]

[1] Department of Radiology, Charité - Universitätsmedizin Berlin, Germany.
[2] Berlin Institute of Health at Charité - Universitätsmedizin Berlin, Germany.

* Contact communicating author: jakob.schattenfroh@charite.de

Synopsis: This study successfully implements abdominal ultra-low frequency magnetic resonance elastography (MRE) (5 - 35 Hz) for detecting stiffness and fluid tissue behavior in vivo. It addresses technical challenges related to the inversion of low-frequency shear waves used to provide insights into the biophysical markers of abnormal tissue fluidity, potentially identifying pre-cancerous niches at risk for tumor dormancy and metastatic colonization.

Motivation

Alterations in soft tissues that favor the formation of solid tumors are frequently linked to abnormal viscosity and tissue fluidity. These abnormalities often result from inflammation, extracellular matrix accumulation, and vascular leakage. Soft biological tissues exhibit unique viscoelastic dispersion properties, behaving similarly to liquids at low mechanical vibration frequencies and to rigid solids at higher frequencies. The viscoelastic dispersion of soft tissues could be used as a biophysical marker of abnormal tissue fluidity to identify pre-cancerous niches[1], which are at risk for tumor dormancy and metastatic colonization.

Magnetic resonance elastography[2] (MRE) non-invasively probes tissue biomechanics by introducing shear waves into the tissue. Images are acquired at multiple time points during the wave propagation. The data requires an inversion algorithm to translate the observed wave patterns into quantitative maps of tissue stiffness and elasticity.

In this study, we successfully implement abdominal ultra-low frequency MRE (5 - 35 Hz) to detect fluid tissue behavior in vivo and solve technical challenges related to the inversion of low-frequency shear waves.

Methods

Our clinical MRE system uses compressed air to drive passive actors placed on the skin near the organ of interest. At standard MRE vibration frequencies (35 - 60 Hz), the actor deflection behaves sufficiently sinusoidal, introducing shear waves at the desired frequency.

Generating a sinusoidal excitation in the ultra-low frequency range (5 Hz), however, was technically challenging with the current design. Instead, we generated a 5 Hz square wave displacement, Fig. 1, which can be expressed in the frequency domain as alternating ON/OFF peaks with decreasing amplitude according to the power law x^{-1}.

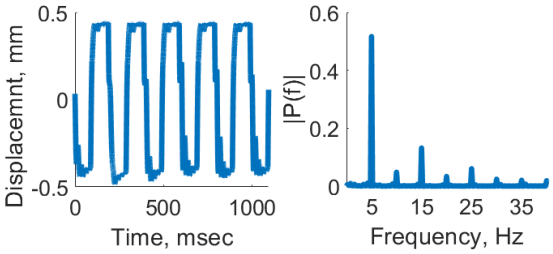

Figure 1: 5 Hz displacement wave and spectrum.

This results in a superposition of waves at different frequencies. The odd harmonic components were separated using a Fourier transform and subjected to viscoelastic inversion individually.

Lower vibrational frequencies are associated with longer wavelengths, which can exceed the length of the organ itself, often causing the inversion algorithm to underestimate wave speed. Consequently, the radial filter used to suppress compression waves during inversion was adjusted. These optimized filter settings were validated through both ex-vivo and in-vivo measurements.

To calculate the ground truth shear wave speed (SWS) of a viscoelasticity phantom[3], MRE measurements were performed between 5 and 10 Hz at 1 Hz intervals and between 15 and 40 Hz in 5 Hz intervals. A plane wave model with complex wave number $k^* = k' + ik''$ was fitted into the complex shear wave field. The real part represents the wave speed, and the imaginary part the frequency-dependent attenuation coefficient. The shear wave speed was derived for each measurement.

$$u^* = A\, e^{-i\,\vec{k}^*\cdot\vec{r}} = \underbrace{A\, e^{-\vec{k}''\cdot\vec{r}}}_{|u^*|} \cdot \underbrace{e^{-i\,\vec{k}'\cdot\vec{r}}}_{Phase}$$

$$\lambda = \left|\frac{2\cdot\pi}{k'}\right|, \qquad SWS = \frac{\omega}{k'} = \lambda\cdot f$$

Eq. 1: Plane shear wave model.

The radial filter was optimized such that the RMSE of the shear wave speed, calculated by wave fitting and derived by the kMDEV inversion algorithm, was minimal.

Ultra-low frequency MRE with a 5 Hz vibration frequency was performed on a cohort of 5 healthy volunteers as well as 4 patients with liver disease (2x LPAC, 2x NASH). The 5 Hz shear wave component and all odd higher harmonic components up to 35 Hz were extracted and subjected to kMDEV inversion with optimized radial filters for low frequency shear waves.

Results

The filter optimization based on phantom measurement resulted in a high-pass radial filter with a cut-off frequency linearly dependent on vibration frequency, $f_g = 0.5\ {}^{1}/_{\mathrm{Hz\ m}}$. The RMSE between the manual wave fitting and the optimized kMDEV was 0.108.

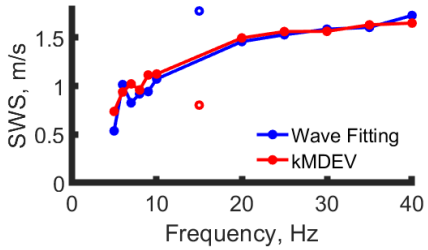

Fig. 1: Viscoelastic dispersion of the phantom based on wave fitting and kMDEV with optimized radial filter.

Representative SWS maps averaged over the odd harmonics up to 35 Hz for a healthy volunteer and a NASH patient, along with the viscoelastic dispersion curves over the frequency range, are shown in Figures 3 and 4, respectively.

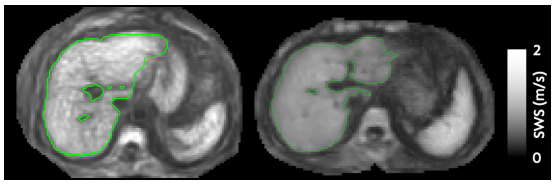

Fig. 3: NASH patient (left) and healthy (right)

The slope of the SWS-dispersion in the double logarithmic plot measures tissue fluidity across the frequency range. The curve for healthy volunteers shows a linear increase, indicating constant fluidity. The LPAC patients exhibits a similar linear trend with reduced steepness, representing constant but reduced fluidity. In contrast, both NASH patients can be observed with varying fluidity across the frequency range.

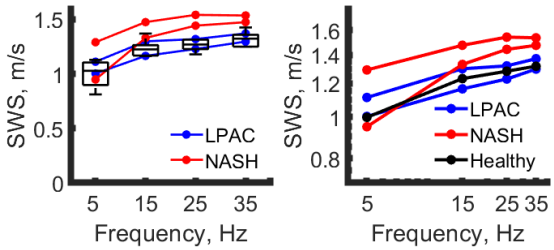

Fig. 4: Viscoelastic dispersion of healthy volunteers and patients in linear and double logarithmic scales.

Discussion and Conclusion

For the first time, ultra-low frequency MRE has enabled dispersion analysis across an extended frequency spectrum. Low vibration frequencies can now be combined with the classical frequency ranges in MRE for full wideband analysis.

Preliminary results indicate that NASH patients exhibit increased liver stiffness and inconsistent tissue fluidity across the frequency range. The degree of fluidity alteration in NASH may correlate with changed matrix-fluid mechanical interactions due to different disease stages. In future, ultra-low frequency MRE could provide valuable insights into tissue fluidity and may serve as a predictive marker for tumor formation and malignant transformation.

This project focused primarily on technical development, limiting the number of subjects. Future work may extend this approach to a larger cohort and other organs.

References

1. Reiter R. Influence of fibrosis progression on the viscous properties of in vivo liver tissue elucidated by shear wave dispersion in multifrequency MR elastography. JMBBM. 2021; 121:104645

2. Sack I. Magnetic resonance elastography from fundamental soft-tissue mechanics to diagnostic imaging. Nat Rev Phys. 2023; 5:24-42

3. Morr A. Liquid-Liver Phantom: Mimicking the Viscoelastic Dispersion of Human Liver for Ultrasound- and MRI-Based Elastography. Invest Radiol. 2022; 57(8): 502–509

Scientific Session 4

Clinical and Biological Applications

Oral presentations

401	Dennis C. Thomas	*Mapping of cerebral metabolite concentrations in brain tumors using 1H-MRSI and quantitative MRI*
402	Enrica Wilken	*bSSFP acquisition in time-lapse MRI: three-dimensional single-cell tracking with high temporal resolution*
403	Robert Alexander Vornhusen	*Light-switchable giant unilamellar vesicles: A model for cell size and transmembrane water exchange*
404	Vinod Kumar	*Mesoscopic functional mapping of the globus pallidus nuclei at 9.4T*
405	Rolf Otto Reiter	*Intervertebral disc degeneration assessed by in vivo multifrequency MR elastography*
406	Maik Rothe	*Multi-parametric characterization and clustering of fast relaxing knee tissues using 3D UTE*
407	Elizabeth Huaroc Moquillaza	*Free-breathing full pancreas water T1 mapping*
408	Christoph Birkl	*Performance of Quantitative Susceptibility Mapping in brain tissue with extreme iron content*

Posters

P401	Fiona Mankertz	*Association Between Arterial Hypertension and Spinal Degeneration: An MRI-Based Cross-Sectional Study*
P402	Sascha Santaniello	*Automatic evaluation of the properties of the glymphatic system using diffusion MRI data*
P403	Simon Mayr	*Cardiac CINE imaging at 0.55T – a comparison to 1.5T*
P404	Gisela Hagberg	*How similar is quantitative MRI in the human brain measured ex vivo and in vivo?*
P405	Ali Ajouz	*Impact of image registration and fibre orientation on the DTI-ALPS-index*
P406	Wolfgang Weber-Fahr	*Neurobiochemical correlates of long-term neuropsychiatric consequences of COVID-19 disease*
P407	Yan Ma	*Optogenetic fPET/fMRI Reveals Distinct Roles of the Substania Nigra in Motor and Cognitive Processes*
P408	Aayush Nepal	*Semi-Automated Segmentation Pipeline for Dynamic MRI Analysis of Knee Joint Kinematics*
P409	Aref Kalantari	*Tract masks for refined analysis of diffusion properties in motor tracts related to functional recovery after stroke in mice*
P410	Fatima Anum	*Unravelling yeast metabolism with real-time deuterium magnetic resonance spectroscopy*

Mapping of cerebral metabolite concentrations in brain tumors using ^{1}H-MRSI and quantitative MRI

Dennis C. Thomas*[1,2,3,4], Seyma Alcicek[1,2,3,4], Andrei Manzhurtsev[1,2,3,4], Elke Hattingen[1,2,3,4], Katharina J. Wenger[1,2,3,4], Ulrich Pilatus[1,2,3,4]

[1] Institute of Neuroradiology, University Hospital Frankfurt, Goethe University Frankfurt, Frankfurt am Main, Germany

[2] University Cancer Center Frankfurt (UCT), Frankfurt am Main, Germany

[3] LOEWE Center Frankfurt Cancer Institute (FCI), Frankfurt am Main, Germany

[4] German Cancer Research Center (DKFZ) Heidelberg and German Cancer Consortium (DKTK)

* Communicating author: Dennis C. Thomas, ChittisseryThomas@med.uni-frankfurt.de

Synopsis:

The value of 2D proton MRSI increases considerably if absolute concentrations of metabolites can be extracted. Using the tissue water as a reference signal has become common practice, but the required acquisition of the unsuppressed spectrum of the tissue water, that serves as a concentration reference, is time consuming. In addition, it suffers from the difficulty to measure the fully relaxed water signal accurately. This becomes problematic in brain pathologies, where relaxation times can vary significantly between individuals. The goal of this work was to combine MRS (single voxel STEAM) and the quantitative measurement of the water MR signal (multi-echo imaging sequence). The method is demonstrated and tested against a standard water referencing method in 5 volunteers. Its application is demonstrated in a brain tumor patient.

Introduction

In brain tumors, changes in relative and absolute concentrations of metabolites serve as a diagnostic marker[1–3]. The extraction of absolute concentrations if of high clinical value. Using the tissue water as a reference signal for their estimation has become common practice, but the required acquisition of the unsuppressed spectrum of the tissue water is time consuming. The inherent advantage that both water suppressed and unsuppressed spectra are acquired under the same condition also leads to a doubling of acquisition time, which is especially troubling for already lengthy 2D MRSI protocols. In addition, this technique suffers from the difficulty to measure the fully relaxed water signal accurately. This becomes problematic in brain pathologies, where relaxation times can vary significantly between individuals.

Here, we develop a ^{1}H MRSI quantification approach which uses proton density (PD) from multi-parametric quantitative MRI (mp-qMRI) as water reference. Calibration of the PD values was performed using the water signal intensity from a single-voxel STEAM acquisition. Our approach enables the accurate calculation of concentration of metabolites, both in mmol per Litre of water and mmol per Litre of voxel volume for the entire MRSI slice.

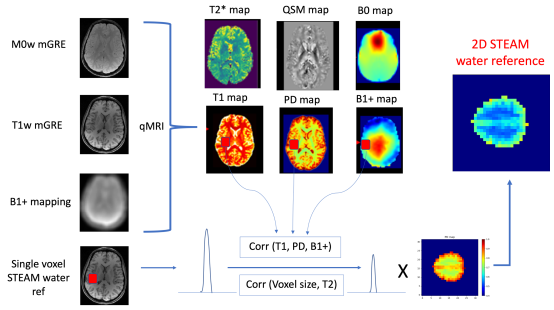

Figure 1: Overview of the proposed method for water referencing using single voxel STEAM and mp-qMRI. The water reference intensity measured using STEAM is corrected for B1+, PD and T1 with values from qMRI. Multiplying the PD map with the corrected STEAM water signal provides a water reference image with spectroscopic metrics, i.e., scaling refers to assumed water intensity at any voxel.

Methods

In vivo measurements were performed on 5 healthy volunteers and 1 brain tumor patient on a whole-body 3T MR Scanner (MAGNETOM Prisma (VE11C), Siemens Healthineers, Erlangen, Germany). The protocol included a 2D MRSI semi-LASER (s-LASER) acquisition. For the reference water calibration method, the spectroscopic water reference was acquired with the same parameters as the 2D sLASER, but without water suppression. LCModel was used for spectroscopic data analysis and calibration of metabolite data by the water reference. For the proposed water calibration method, a STEAM spectrum was acquired with the voxel placed in WM (on the contra-lateral side for the brain tumor patient). The signal intensity from the STEAM spectrum was used to calibrate PD from qMRI as outlined in **Fig 1**. The qMRI measurements included measuring 2 multi-Echo Gradient-Echo (mGRE) images (M0w and T1w) in order to map PD, T1, T2*, QSM (**Fig 1**). An additional sequence was acquired for B1+ mapping as described in [5]. The total measurement time required for the qMRI protocol including B1+ mapping was 8 minutes. By reslicing the calibrated PD map to the sLASER slice and adjusting to the MRSI resolution, we generated a water reference image with MRS metrics. To calculate the quantitative metabolite maps, the metabolite intensities obtained from LCModel without water referencing were divided voxel-wise by the

calibrated PD map. Three different approaches of quantification were assessed. First, the reference method with the water relaxation effects corrected using the T1 and T2 values from literature and the GM, WM and CSF masks ('Ref method'). Second, the reference method with the water relaxation effects corrected for using the T1 and T2 relaxation values obtained from the qMRI scans ('Ref-method-with-qMRI'). Third, the proposed method using STEAM and the H_2O map ('Proposed-method').

Results

Fig 2 shows the bar plots for average ROI total NAA ('t-NAA'), total creatine ('tCr') and total choline ('tCho') in the 5 healthy subjects. The four ROIs, were defined in the MNI space as shown in **Fig 2a**. The 'Ref-method' values are significantly higher than the values obtained using the 'Ref-method-with-qMRI' for almost all of the ROIs and metabolites. The values obtained using the proposed method are in very good agreement with the 'Ref-method-with-qMRI'.

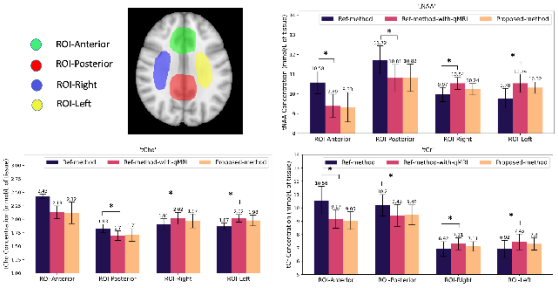

Fig. 1: a) Definition of the ROIs on the MNI-atlas T1w image in the MNI space. b,c,d) Bar plots of the mean value of different metabolites across 5 volunteers in the 4 ROIs.

Fig 3 shows the obtained metabolite maps in a brain tumor patient (IDH-mutant diffuse astrocytoma). The maps obtained using the 'proposed-method' are compared with those obtained using the 'Ref-method'. Analyzing the difference maps shown in **Fig 3** reveals an overestimation of the metabolite concentrations in the healthy tissue and an underestimation of the metabolite values in the tumor tissue with the 'Ref-method'.

Discussion

Here we propose a method for absolute quantification in ^{1}H MRSI data. The method replaces the time-consuming acquisition of an unsuppressed water dataset by a fast qMRI protocol and a single voxel measurement. While no additional measurement time is required, the new method provides a relaxation corrected water reference image, maps for B1+/- corrections and 4 additional qMRI maps, which also can be used for tissue segmentation. Our results demonstrate the importance of relaxation corrections for the studies of brain tumors patients. The method, which relies on the ability to transform a PD map into a water reference image by a calibration with single voxel spectroscopy, has been confirmed in a study on 5 healthy subjects and on a brain tumor patient.

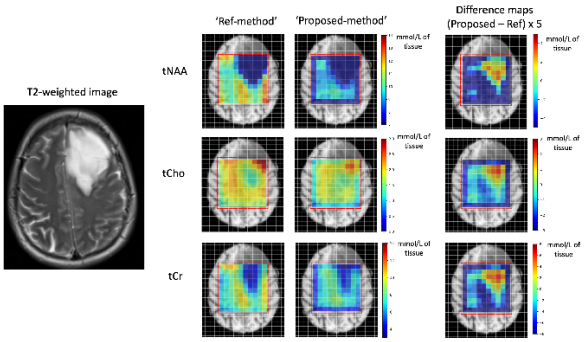

Fig 3: Metabolite maps obtained in a brain tumor patient with the 'Ref-method' and the 'Proposed-method'.

Conclusion

To conclude, an 8-minute protocol for accurate water calibration of qMRSI has been developed and validated here.

References

1. Weinberg BD, Kuruva M, Shim H, Mullins ME. Clinical applications of magnetic resonance spectroscopy (MRS) in of brain tumors: from diagnosis to treatment. *Radiol Clin North Am*. 2021;59(3):349-362. doi:10.1016/j.rcl.2021.01.004

2. Horská A, Barker PB. Imaging of Brain Tumors: MR Spectroscopy and Metabolic Imaging. *Neuroimaging Clin N Am*. 2010;20(3):293-310. doi:10.1016/j.nic.2010.04.003

3. Padelli F, Mazzi F, Erbetta A, et al. In vivo brain MR spectroscopy in gliomas: clinical and pre-clinical chances. *Clin Transl Imaging*. 2022;10(5):495-515. doi:10.1007/s40336-022-00502-y

4. Short echo time 1H-MRSI of the human brain at 3T with minimal chemical shift displacement errors using adiabatic refocusing pulses - Scheenen - 2008 - Magnetic Resonance in Medicine - Wiley Online Library. https://onlinelibrary.wiley.com/doi/10.1002/mrm.21302. Accessed November 7, 2023.

5. Volz S, Nöth U, Rotarska-Jagiela A, Deichmann R. A fast B1-mapping method for the correction and normalization of magnetization transfer ratio maps at 3 T. *Neuroimage*. 2010;49(4):3015-3026. doi:10.1016/j.neuroimage.2009.11.054

bSSFP acquisition in time-lapse MRI: three-dimensional single-cell tracking with high temporal resolution

Enrica Wilken[1*], Asli Havlas[1], Clemens Diwoky[2], Max Masthoff[1] and Cornelius Faber[1]

[1] Clinic of Radiology, University of Münster, Münster, Germany.
[2] Institute of Molecular Biosciences, University of Graz, Graz, Austria.

* wilkene@uni-muenster.de

Synopsis: We showed that bSSFP imaging improves tracking of single iron-labeled cells using time-lapse MRI. Phantom and in vivo experiments were performed employing 2D Cartesian and 3D radial sampling. 2D Cartesian single-slice bSSFP enables dynamic cell tracking at high temporal resolution resulting in reduced blurring compared to conventional gradient echo imaging. 3D radial sampling facilitates whole-brain, three-dimensional cell tracking at isotropic spatial resolution. Both sequences achieve a higher velocity detection limit in vitro compared to the established gradient echo sequence. Higher temporal resolution in time-lapse MRI is a major step to resolve faster monocytes giving insights into inflammation by single-cell tracking.

Introduction

By repetitive T2*-weighted imaging, time-lapse MRI allows non-invasive tracking of single iron-labeled immune cells deep within tissues. Extended acquisition times at required high spatial resolutions result in temporal blurring, constraining the detection limit to 60 µm/min [1,2]. To study fast immune cells, e.g. engaged in inflammatory processes, accelerated acquisition is required.

Here, we first employed a fully balanced steady-state (bSSFP) acquisition with 2D Cartesian sampling and compared it to the established gradient echo (GE) sequence[1,2] in phantom experiments. To validate our approach, we conducted in vivo experiments. Furthermore, the method was extended using a 3D radial sampling scheme with bSSFP imaging in phantoms and in vivo.

Methods

Time-lapse MRI was performed at 9.4 T with cryogenic probe. The scan parameters for 2D Cartesian bSSFP imaging were: TE/TR: 6/12 ms, 32 averages, 59x59 µm^2 in-plane resolution, 1 slice of 300 µm, 1:42 min per timeframe. 3D radial sampling used: TE/TR: 0.9/4 ms, 120188 spokes, 77x77x77 µm^3 spatial resolution, 8:01 min per timeframe.

To mimic cell movement, agar phantoms containing micron-sized iron particles were scanned using a rotating phantom system, both static and rotating with resulting particle speeds of up to 1.6 mm/min. Signal loss of single particles was calculated in the static and rotating phantom. Subsequently, a velocity detection limit was obtained as previously described[3].

In vivo experiments imaging the mouse brain used cells labeled in vivo by i.v. injection of iron-based contrast agent 24 h prior to scanning. Cells were manually identified as hypointense spots.

Results & Discussion

Both phantom and in vivo experiments showed successful imaging and tracking of single iron-labeled cells using bSSFP acquisition (Fig.1A,2,4). The detected hypointensities resembled those observed using GE (Fig.1,2).

In the rotating phantom, temporal blurring of single iron particles was observed as decreased contrast (i.e. reduced signal loss) and elongated shapes (Fig.1A,B, 2A,B). Due to the high temporal resolution of the 2D Cartesian sequence, this effect was weaker using bSSFP than GE (Fig. 1B). Particle visibility was affected by velocity and contrast in the static case. For the investigated signal losses, a velocity detection limit of 0.6-0.8 mm/min for 2D Cartesian bSSFP and of 0.2-0.4 mm/min for 3D radial bSSFP was derived, which was in both cases higher compared to the established GE sequence (0.1-0.2 mm/min) (Fig.3).

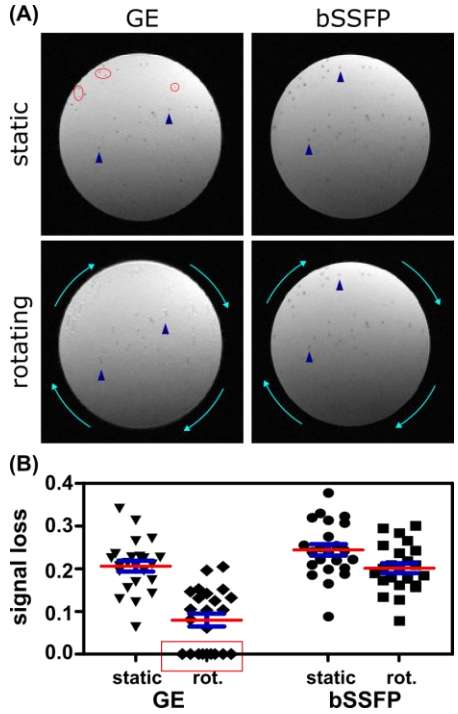

Fig. 1: Phantom measurements using 2D Cartesian bSSFP in time-lapse MRI. (A) When rotating, particles are blurred (blue arrowhead) or fade (red circles). (B) In GE images, some particles disappear (red box) and signal loss of iron particles decreases, while in bSSFP there is only a slight reduction when rotating (here: $4.4*10^{-3}$ rpm). Data points indicate individual hypointensities, mean in red, SEM in blue.

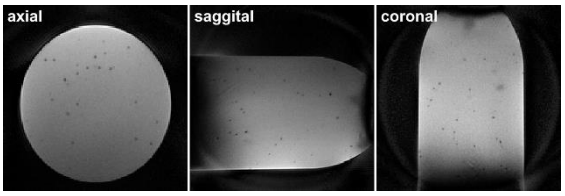

Fig. 2: Phantom measurements using 3D radial bSSFP in time-lapse MRI. Single iron particles can be detected in all three orientations.

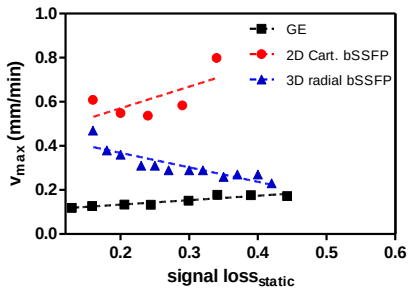

Fig. 3: Velocity detection limit of time-lapse MRI in vitro.

In vivo (Fig.4), banding artifacts occurred. Yet, dynamic tracking of single iron-labeled cells moving across several voxels in consecutive timeframes was possible. For 2D Cartesian sampling, N = 38 cells detected in at least 2 timeframes with distinct motion had a mean velocity of 19 ± 2 µm/min. 2D Cartesian sampling allowed tracking at a high temporal resolution, however was limited to a single-slice. In contrast, 3D radial sampling enabled the three-dimensional tracking of single cells imaging the whole brain at high isotropic spatial resolution.

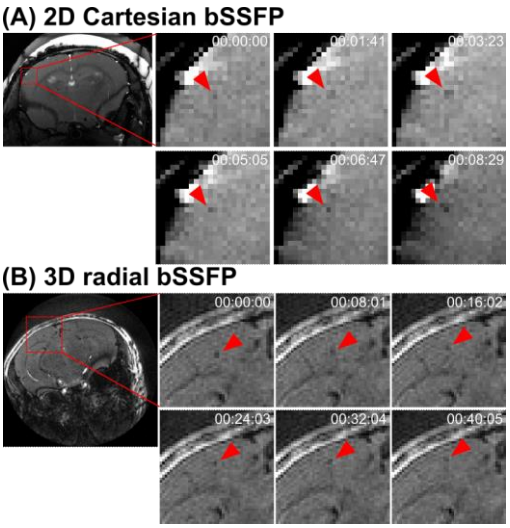

Fig. 4: In vivo (A) 2D Cartesian and (B) 3D radial bSSFP time-lapse MRI of a mouse brain: Image details (red rectangle) show single iron-labeled cells (red arrows) moving across several voxels in consecutive timeframes.

Conclusion

bSSFP time-lapse MRI improves single-cell tracking by enhancing temporal resolution and consequently reducing blurring effects. In vitro, the velocity detection limit was increased up to 8-fold when using 2D Cartesian sampling. Additionally, 3D radial sampling facilitated the three-dimensional tracking of individual cells, offering whole-brain coverage and isotropic spatial resolution.

Future research goals include minimizing banding artifacts, exploiting undersampling and compressed sensing to further accelerate the acquisition, and enhancing the signal contrast of labeled cells to more efficiently capture fast-moving monocytes in vivo, which may enable early detection of inflammation.

References

1. Masthoff M, Gran S, Zhang X, et al. Temporal window for detection of inflammatory disease using dynamic cell tracking with time-lapse MRI. *Sci Rep*. 2018;8(1):9563.
2. Masthoff M, Freppon FN, Zondler L, et al. Resolving immune cells with patrolling behaviour by magnetic resonance time-lapse single cell tracking. *EBioMedicine*. 2021;73:103670.
3. Wilken E, Havlas A, Masthoff M, Moussavi A, Boretius S, Faber C. Radial compressed sensing imaging improves the velocity detection limit of single cell tracking time-lapse MRI. *Magn Reson Med*. 2024;91(4):1449-1463.

Light-switchable giant unilamellar vesicles: A model for cell size and transmembrane water exchange

Robert Vornhusen,[1*] Bastian Maus,[1] Daniele Di Iorio,[2] Seraphine Wegner[2] and Cornelius Faber[1]

[1] Experimental Magnetic Resonance, Clinic of Radiology, Faculty of Medicine, University of Münster, Münster, Germany.
[2] Light Controlled Systems, Physiological Chemistry and Pathobiochemistry, Faculty of Medicine, University of Münster, Münster, Germany.

* r.vornhusen@uni-muenster.de

Synopsis: Using two different diffusion-weighted MRI models we were able to observe differences in transmembrane water exchange in light-switchable giant unilamellar vesicles prepared with the synthetic phosphatidylcholine AzoPC.

Introduction

In medical diagnostics, the microstructure and the membrane water permeability of tissue are key markers for tracing tumor progression, neuronal damage and other diseases [1, 2]. Cell size but also the transmembrane water exchange (TMWE), both have an impact on the temporal displacement of water, which can be probed via diffusion-weighted MRI (dMRI). While cell size determination can easily be studied *in situ* via MRI on cell phantoms, the ability to specifically modulate TMWE in one sample is missing. The synthetic phosphatidylcholine variant 1-stearoyl-2-(4-(n-butyl)phenylazo-4'-phenylbutyroyl) phosphocholine (AzoPC) contains the photoisomerizable moiety azobenzene. When incorporated into a vesicle membrane, AzoPC in *trans* configuration acts as a saturated fatty acid, in *cis* conformation however it enables TMWE [3]. We tested giant unilamellar vesicles (GUVs) with different dMRI techniques to assess their suitability as phantoms for cell size and TMWE determination.

Methods

GUVs were prepared via the hydration method. For light switchable GUVs, membranes were composed of 10 mg/mL phosphocholine with 20 mol% AzoPC and 2 mol% biotin. As controls, non-light-switchable GUVs were prepared without AzoPC. All GUV samples were condensed into a visible patch by adding 5-10 µg/mL streptavidin to the suspension and brief centrifugation. The patch in suspension was imaged in a Bruker BioSpec 94/20 MR scanner using a cryoprobe. Samples in the scanner were illuminated with blue light ($\lambda = 460$ nm, *trans*) or UV light ($\lambda = 370$ nm, *cis*) to control the TMWE. Light was provided by LEDs, connected to the sample via a glass fiber (Fig. 1). GUV radii and TMWE under both light regimes were determined using two different models, the IMPULSED (Imaging Microstructural Parameters Using Limited Spectrally Edited Diffusion) and the joint model [4].

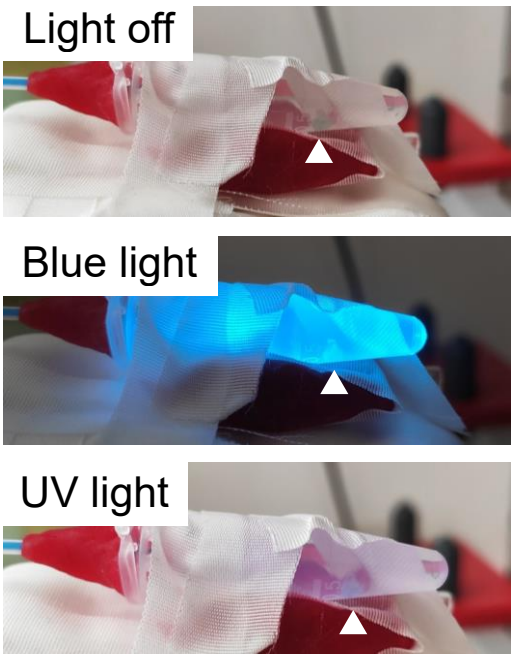

Fig. 1: GUVs (arrow head) in 1.5 mL suspension in an Eppendorf tube. Light is delivered to the sample via a glass fiber fit through a hole in the tube cap and sealed with wax. Pictures were taken at constant ambient light.

Results and Discussion

Aggregated GUV patches were visible in dMRI as hyperintense areas with low ADC compared to the surrounding medium (Fig.2A). IMPULSED-derived GUV radii (Fig. 2B) were in the range of 5-17 µm across samples.

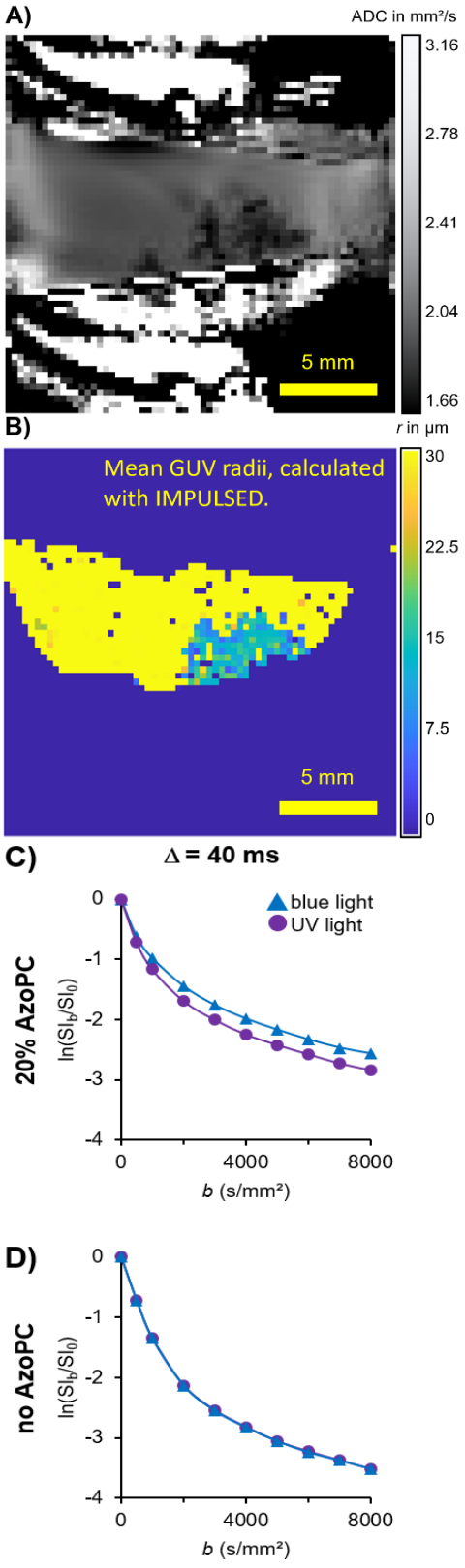

Fig. 2: A) ADC map of GUVs in Eppendorf tube and (B) pixelwise fit of IMPULSED radii. Signal changes within the GUV patch relative to b_0 under UV light (purple) and blue light (blue) ($\delta = 7$ ms) for GUVs with (C) and without AzoPC (D).

When observing diffusion in the GUV patch at long diffusion times, a stronger relative drop in signal at high b-vales was found for AzoPC-containing GUVs under UV light, compared to blue light (Fig. 2C). This light-dependent difference in signal attenuation was not found in samples without AzoPC (Fig. 2D). In *cis* configuration AzoPC enables water to cross membranes more easily, therefore it may diffuse over longer distances. This leads to stronger b-dependent signal attenuation compared to *trans*-AzoPC membranes and membranes without AzoPC. The IMPULSED and joint model delivered GUV radii comparable to radii determined by light microscopy.

Conclusion and Outlook

Our results show, that TMWE was reliably detectable only when AzoPC-containing samples were exposed to UV light. In the future, TWME should be quantified using further dMRI models like the standard model with exchange (SMEX[5]), time-dependent diffusion kurtosis (DKI(*t*)[6]) and filter exchange imaging (FEXI[7]).

References

1. Ruggiero MR, Baroni S, Pezzana S, *et al*. Evidence for the Role of Intracellular Water Lifetime as a Tumour Biomarker Obtained by In Vivo Field-Cycling Relaxometry: Angew Chem Int Ed. 2018;57:7468–7472.

2. Williamson NH, Ravin R, Cai TX, *et al*. Water exchange rates measure active transport and homeostasis in neural tissue. PNAS Nexus. 2023; 2:pgad056.

3. Simon J, Schwalm M, Morstein J, *et al*. Mapping light distribution in tissue by using MRI-detectable photosensitive liposomes. Nat Biomed Eng. 2022.

4. Jiang X, Devan SP, Xie J, *et al*. Improving MR cell size imaging by inclusion of transcytolemmal water exchange. NMR in Biomed. 2022.

5. Olesen JL, Østergaard L, Shemesh N, *et al*. Diffusion time dependence, power-law scaling, and exchange in gray matter. NeuroImage. 2022; 251:118976.

6. Li C, Fieremans E, Novikov DS, *et al*. Measuring water exchange on a preclinical MRI system using filter exchange and diffusion time dependent kurtosis imaging. Magn Reson in Med. 2023; 89:1441–1455.

7. Schillmaier M, Kaika A, Topping GJ, *et al*. Repeatability and reproducibility of apparent exchange rate measurements in yeast cell phantoms using filter-exchange imaging. Magn Reson Mater Phy. 2023; 36:957–974.

Mesoscopic functional mapping of the globus pallidus nuclei at 9.4T

Vinod Kumar[1*], Jonas Bause[1], Christian F. Beckmann[2], Klaus Scheffler[1,3] & Wolfgang Grodd[1]

[1]Max Planck Institute for Biological Cybernetics, Tübingen, Germany.

[2]Donders Institute for Brain, Cognition, and Behaviour, Nijmegen, The Netherlands

[3]Department of Biomedical Magnetic Resonance, University Clinic Tübingen, Tübingen, Germany

* vinod.kumar@tuebingen.mpg.de

Synopsis: The pallidal nuclei are implicated in several brain functions, as well as neurological disorders, including motor disorders such as Parkinson's disease. Despite of its importance, our understanding of the communication between the cortex and pallidum in the human brain is limited. Therefore, this study investigates the depth-specific functional connectivity of the cortex with the pallidal nuclei. We found depth specificity with different cortical areas, suggesting feedback and feedforward functional interactions during spontaneous rest.

Introduction

The globus pallidus/pallidum (GP) receives cortical feedback from deeper layer V via the striatum and connects with the thalamus and other subcortical nuclei (1-2). The GP connected thalamus further engages in feedforward input to the medial layer 4 of the cortex (3). With such a connectivity scheme within the cortico-basal ganglia-thalamo-cortical loop, GP engages in a broad array of brain functions, including motor control and cognitive functions. However, the GP's functional connectivity concerning cortical laminar organization has not been investigated in the human brain. To address this gap, our study employed high-resolution fMRI to map the functional connectivity of the GP with respect to the cortical depth in the human brain.

Methods

Subjects: 16 healthy subjects (Age 23-39 Y, Mean age: 27 Y, 9 F, 7 M) participated in the study with written informed consent before participation. The local research ethics committee approved the study.

Data acquisition: MRI was performed at 9.4 Tesla (Magnetom, Siemens) using a custom-built 16 transmit and 31 receive channel head coil. We acquired structural MP2RAGE (0.6 mm isotropic) and rsfMRI data (SMS EPI, FLEET pre-scan, MB 3, 1mm isotropic, TR 2200 ms, TE 27 ms, 117 slices, 300-360 scans, 10 scans with reversed phase encoding) (4).

Data Analysis:

i). Laminar Delineation:

The MP2RAGE was reconstructed using raw data with in-house Matlab code The uniform contrast was analyzed using presurfer (5). The layer delineation in 11 equidistance bins was performed after the freesurfer segmentation and manual quality control using LAYNII (6).

ii). rs-fMRI analysis:

The thermal noise correction of the fMRI data was performed using the NORDIC Matlab toolbox (7). The fMRI preprocessing was performed in native subject space using AFNI with despiking, slice time correction, distortion correction, coregistration, motion correction, anaticor (noise correction), and without smoothing (9). The correlations between the GP and cortex were computed using AFNI. Subsequently, smoothing within layers (0.7 FWHM was performed using LAYNII (Figure 1). The computed correlation maps (z) were then corrected for multiple comparisons (FDR p 0.05) with AFNI.

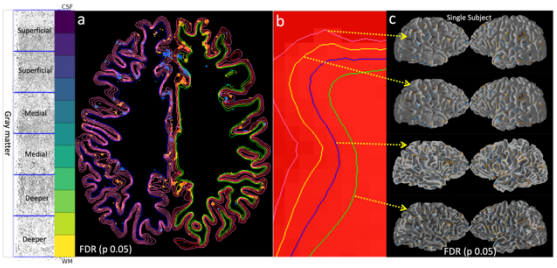

Figure 1: Left Pallidum Functional Connectivity with cortical depth: a) An axial slice depicts the pallidum's multiple comparison corrected (FDR p 0.05) correlations with the cortex. b-c) The cortical gray matter ribbon is divided into four layers for visualization, and corresponding correlations of the left pallidum in a single subject from superficial to deeper cortical depth are visualized for the right and left-brain hemisphere.

iii). Group Profile Tracking Analysis: The depth profile of the functional connectivity of the GP with each cortical area was determined using non-linear modeling (9). In the next step, the predicted similar depth profiles with the peak connectivity in the medial and deeper cortical depth were segregated and visualized (Figure 2).

Results

The majority of cortical areas show association with GP in the medial and deeper cortical depth (Figure 2). The GP connectivity with medial depth in cortical regions covers mainly the default mode, visual, fronto-parietal, and salience networks, suggesting the GP is more involved in the feedforward flow of information to these cortical networks during rest (Figure 2). In contrast, deeper depth-specific highly correlated cortical regions cover mainly somatosensory, visual, cingulate, temporal, and frontal areas, suggesting the GP is more involved in the feedback flow of information from these cortical areas during rest. The left and right pallidum show similar depth preferences with cortical areas, with slight laterality differences.

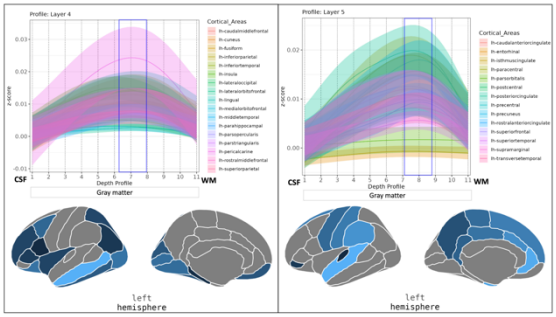

Figure 2: Left Pallidum Functional Connectivity - Profile Tracking Analysis with cortical depth: Left: Plot displays cortical areas with peak connectivity in the medial Depth. The left Pallidum shows high correlations with the Medial depth in mainly areas of the default-mode-network, hippocampal, visual, insula, and lower temporal cortices, suggesting that the pallidum is more involved in the feedforward flow of information to these cortical areas during rest. **Right**: Plot displays correlated cortical areas with peak connectivity in the deeper Depth. Left Pallidum shows high correlations with the deeper Layer in mainly somatosensory areas, cingulate, frontal, and temporal cortices, suggesting the GP is more involved in the feedback flow of information from these cortical areas during rest.

Discussion

The depth-specificity with different cortical regions hints a feedforward and feedback communication at rest. The study allows a coarser interpretation concerning cortical laminar profiles, as individual layers may vary with size and density in different cortical areas. GRE BOLD fMRI has limitations to the spatial specificity of the signal and can be biased by cortical orientation; therefore, depth-specificity may be enhanced with other imaging functional contrasts, i.e., VASO and bSSFP.

Conclusion

The whole brain cortical layer-specific connectivity analysis reveals a depth-specific spatial precision of the functional connectivity between cortical areas and pallidum.

Acknowledgements:

This work was supported by the German Research Council (DFG) Grant GZ: GR 833/11-1 and DFG SCHE 658/17. We thank Sriranga Kasyap and Gang Chen for the helpful discussions.

References

1. Lanciego JL, Luquin N, Obeso JA. Functional Neuroanatomy of the Basal Ganglia. *Cold Spring Harb Perspect Med*. 2012;2(12). doi:10.1101/cshperspect.a009621

2. Moberg S, Takahashi N. Neocortical layer 5 subclasses: From cellular properties to roles in behavior. *Front Synaptic Neurosci*. 2022;14. https://www.frontiersin.org/articles/10.3389/fnsyn.2022.1006773. Accessed November 28, 2023.

3. Hua Y, Loomba S, Pawlak V, et al. Connectomic analysis of thalamus-driven disinhibition in cortical layer 4. *Cell Rep*. 2022;41(2):111476. doi:10.1016/j.celrep.2022.111476

4. Polimeni JR, Bhat H, Witzel T, et al. Reducing sensitivity losses due to respiration and motion in accelerated Echo Planar Imaging by reordering the auto-calibration data acquisition. *Magn Reson Med*. 2016;75(2):665-679. doi:10.1002/mrm.25628

5. Kashyap S, Ivanov D, Havlicek M, Poser BA, Uludağ K. Impact of acquisition and analysis strategies on cortical depth-dependent fMRI. *NeuroImage*. 2018;168:332-344. doi:10.1016/j.neuroimage.2017.05.022

6. Huber L (Renzo), Poser BA, Bandettini PA, et al. LayNii: A software suite for layer-fMRI. *NeuroImage*. 2021;237:118091. doi:10.1016/j.neuroimage.2021.118091

7. Moeller S, Pisharady PK, Ramanna S, et al. NOise reduction with DIstribution Corrected (NORDIC) PCA in dMRI with complex-valued parameter-free locally low-rank processing. *NeuroImage*. 2021;226:117539. doi:10.1016/j.neuroimage.2020.117539

8. Cox RW. AFNI: software for analysis and visualization of functional magnetic resonance neuroimages. *Comput Biomed Res Int J*. 1996;29(3):162-173. doi:10.1006/cbmr.1996.0014

9. Chen G, Nash TA, Cole KM, et al. Beyond linearity in neuroimaging: Capturing nonlinear relationships with application to longitudinal studies. *NeuroImage*. 2021;233:117891. doi:10.1016/j.neuroimage.2021.117891

Intervertebral disc degeneration assessed by in vivo multifrequency MR elastography

Rolf Reiter[1,2,*], Pinkas Mürdel[3], Florian N. Loch[4], Mehrgan Shahryari[1], Rebecca Strehle[1], Christian Bayerl[1], Bernd Hamm[1], Jürgen Braun[1], Ingolf Sack[1], Patrick Asbach[1], David Kaufmann[5]

[1]Radiology, Charité – Universitätsmedizin Berlin, Berlin, Germany

[2]Berlin Institute of Health at Charité – Universitätsmedizin Berlin, BIH Charité Digital Clinician Scientist Program, Berlin, Germany

[3]Orthopedic surgery, Waldfriede Hospital, Berlin, Germany

[4] Surgery, Charité – Universitätsmedizin Berlin, Berlin, Germany

[5]Radiology, University of Augsburg, Augsburg, Germany

*rolf.reiter@charite.de

Synopsis: Despite the success in detecting intervertebral disc degeneration with high-resolution T2 sequences, conventional MRI is limited by large inter-reader variability as well as lacking stratification of clinical trials and their assessment of treatment responses. Several studies have shown the technical feasibility of MR elastography for the study of the intervertebral disc, but its clinical relevance remains unclear. This study shows an excellent diagnostic performance of high-resolution multifrequency MR elastography in the evaluation of lumbar spine intervertebral disc degeneration.

Introduction

Intervertebral disc (IVD) degeneration is one of the most common causes of low back pain and has been associated with several pathological conditions such as disc herniation or spinal stenosis (1). The causes of IVD degeneration include many factors such as mechanical stress, biochemical influences, age, smoking and genetics (2). Despite the success in detecting IVD degeneration with high-resolution T2 sequences, conventional MRI is limited by large inter-reader variability as well as lacking stratification of clinical trials and their assessment of treatment responses (3, 4). Several studies have shown the technical feasibility of MR elastography (MRE) for the study of the IVD, but its clinical relevance remains unclear (5-10). Therefore, we aimed at investigating the diagnostic performance of MRE for the assessment of lumbar spine IVD degeneration.

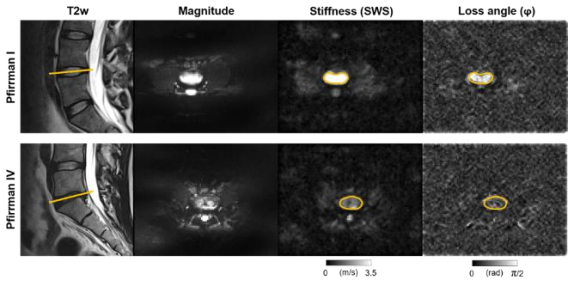

Fig. 1: Upper row: Healthy 31-year-old man without disc degeneration (Pfirrman I) and shear wave speed (SWS) of 3.72 ± 0.90 m/s and loss angle (φ) of 1.02 ± 0.29 rad. Lower row: 30-year-old man with low back pain and advanced disc degeneration (Pfirrman IV) and SWS of 1.63 ± 0.33 m/s and φ of 0.67 ± 0.19 rad. Regions of interest are shown by orange circles and their location within the lumbar spine by orange lines.

Methods

In this prospective study, 60 subjects (41±17 years, BMI 23.9±3.7 kg/m^2, 25 women) were investigated using tomoelastography by multifrequency MRE from 40 to 70 Hz. Maps of shear wave speed (SWS in m/s) and loss angle (φ in rad), representing stiffness and viscous properties, respectively, were generated using tomoelastography data processing. The Pfirrmann score was used as reference standard to assess lumbar IVD degeneration on sagittal T2 images. Diagnostic performance was assessed using the mean value of 3 readers. Interreader agreement of 3 readers was assessed using the intraclass correlation coefficient (ICC).

Results

Figure 1 shows a case of a patient with IVD degeneration and a healthy volunteer. Figure 2 shows boxplots of MRE parameters according to Pfirrman scores. Area under the curve (AUC) analysis showed an excellent diagnostic performance for detecting IVD degeneration (Pfirrman score ≥II/III/IV/V; 95% confidence intervals in parentheses): for SWS: ≥II, 0.825 (0.716-0.914); ≥III, 0.919 (0.858-0.968); ≥IV, 0.962 (0.919-0.991); V, 0.942 (0.873-0.991); and for φ: ≥II, 0.873(0.767-0.964); ≥III, 0.938 (0.885-0.980); ≥IV, 0.981 (0.954-0.999); V, 0.931 (0.871, 0.982). A good interreader agreement was found for SWS with an ICC of 0.87, and an excellent agreement was found for φ with an ICC of 0.92.

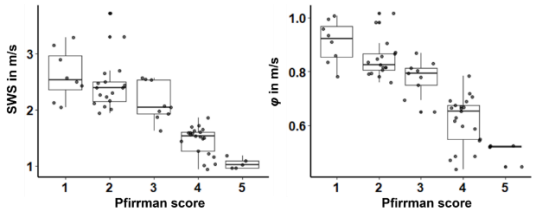

Fig. 2: Box plots of shear wave speed (SWS) and loss angle (φ) according to Pfirrman scores.

Discussion

MRE for the assessment of lumbar IVD degeneration has shown an excellent diagnostic performance with a good to excellent interreader agreement.

Conclusion

The characterization of viscoelastic properties may inform early treatment decisions for the mechanical regeneration of the intervertebral disc.

References

1. Hughes SP, Freemont AJ, Hukins DW, McGregor AH, Roberts S. The pathogenesis of degeneration of the intervertebral disc and emerging therapies in the management of back pain. J Bone Joint Surg Br. 2012;94(10):1298-304.

2. Patel AA, Spiker WR, Daubs M, Brodke D, Cannon-Albright LA. Evidence for an Inherited Predisposition to Lumbar Disc Disease. Journal of Bone and Joint Surgery. 2011;93(3):225-9.

3. Pfirrmann CWM, A; Zanetti, M; Hodler, J; Boos, N. Magnetic resonance classification of lumbar intervertebral disc degeneration. Spine. 2001;26(17):1873-8.

4. James F Griffith Y-XJW, Gregory E Antonio, Kai Chow Choi, Alfred Yu, Anil T Ahuja, Ping Chung Leung. Modified Pfirrmann Grading System for Lumbar Intervertebral Disc Degeneration. Spine. 2007;32(24):E708-E12.

5. Co M, Dong H, Boulter DJ, Nguyen XV, Khan SN, Raterman B, et al. Magnetic Resonance Elastography of Intervertebral Discs: Spin-Echo Echo-Planar Imaging Sequence Validation. J Magn Reson Imaging. 2022.

6. Beauchemin PF, Bayly PV, Garbow JR, Schmidt JLS, Okamoto RJ, Cheriet F, et al. Frequency-dependent shear properties of annulus fibrosus and nucleus pulposus by magnetic resonance elastography. NMR Biomed. 2018;31(10):e3918.

7. Walter BA, Mageswaran P, Mo X, Boulter DJ, Mashaly H, Nguyen XV, et al. MR Elastography-derived Stiffness: A Biomarker for Intervertebral Disc Degeneration. Radiology. 2017;285(1):167-75.

8. Ben-Abraham EI, Chen J, Felmlee JP, Rossman P, Manduca A, An KN, et al. Feasibility of MR elastography of the intervertebral disc. Magn Reson Imaging. 2017;39:132-7.

9. Streitberger KJ, Diederichs G, Guo J, Fehlner A, Hamm B, Braun J, et al. In vivo multifrequency magnetic resonance elastography of the human intervertebral disk. Magn Reson Med. 2015;74(5):1380-7.

10. Cortes DH, Magland JF, Wright AC, Elliott DM. The shear modulus of the nucleus pulposus measured using magnetic resonance elastography: a potential biomarker for intervertebral disc degeneration. Magn Reson Med. 2014;72(1):211-9.

Multi-parametric characterization and clustering of fast relaxing knee tissues using 3D UTE

Maik Rothe[*,1, 2], Selina Riedel[1, 2], Walter A. Wohlgemuth[1, 2], Alexander Gussew[1, 2]

1 Medical Physics Group, University Clinic and Outpatient Clinic for Radiology, University Hospital Halle (Saale), Halle (Saale), Germany.
2 Halle MR Imaging Core Facility, Medical Faculty, Martin-Luther-University Halle-Wittenberg, Halle (Saale), Germany

* maik.rothe@uk-halle.de

Synopsis:

This study presents an approach to segment the knee joints of 20 healthy volunteers using only quantitative parameters. From four UTE images, 3D T_1, T_2^* and water fraction maps were calculated and merged into a 3D histogram. The K-means clustering algorithm was then applied on this data and separated three distinct regions in the knee joints. Skeletal muscle and lipid-rich tissue could be distinguished from other joint tissues. Further parameters can be added in the future to improve the segmentation results.

Introduction

Many important structures in musculoskeletal imaging show very fast apparent transverse relaxation times (T_2*). Therefore, they generate nearly no MR-signal in conventional imaging and their quantitative imaging requires alternative approaches like ultra-short echo times (UTE) MRI(1). Quantitative parameters, such as T_2^* and T_1 can be determined from UTE data, and were previously shown to provide an enhanced characterization of structural changes in tendinopathies(2) or in affected ligaments, for example after injuries or reconstructions(3). However, the distribution of T_2^* and T_1 largely overlaps in most knee tissues. A third parameter that could further improve tissue characterization and separation is water fraction (WF). In this study, we used three parameters (T_2^*, T_1 and WF) to characterize eight different tissues in knee joints and used the results for automatic clustering and segmentation.

Methods

In this study the knees of 20 healthy volunteers (14/6 female/male, 26.6±6.2 years) where examined. All measurements were performed on a 3T MR-scanner (MAGNETOM Vida, Siemens Healthineers, Erlangen, Germany) using an 18-channel transmit/receive knee coil and a 3D spoiled gradient echo UTE research application sequence with stack of spirals readout(4). The T_1- and T_2^*-mapping approach has been previously presented and validated(5, 6). To perform a three-point Dixon approach to measure the voxel-based water fraction, a fourth measurement was added with an off-phase echo time of 1.23ms in the same orientation and resolution (0.8mm isotropic) as the three measurements for T_1- and T_2^*-mapping.

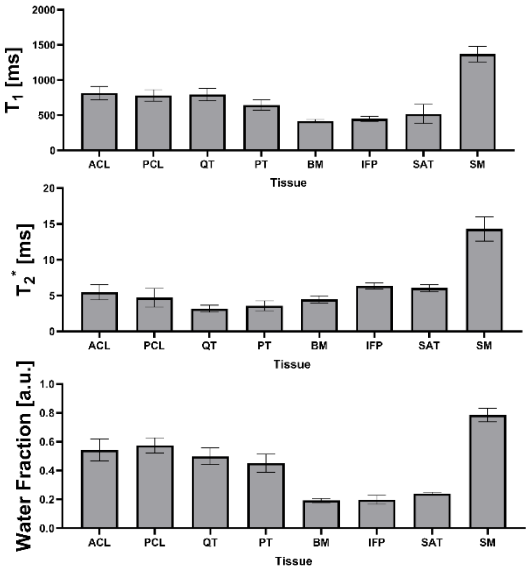

Fig. 1: Results of the three parameters for 20 healthy volunteers in the anterior cruciate ligament (ACL), posterior cruciate ligament (PCL), quadriceps tendon (QT), patellar tendon (PT), bone marrow (BM), infrapatellar fat pad (IFP), subcutaneous adipose tissue (SAT) and skeletal muscle (SM).

The eight different tissue volumes (Fig. 1) were manually drawn in UTE subtraction images using 3D Slicer (https://www.slicer.org(7)). The individual VOIs were then applied to the calculated maps and the mean WF, T_2^* and T_1 values were determined for each tissue. For each individual

dataset, a K-means clustering algorithm was applied based on a 3D histogram (Fig. 2).

Results

The results of the quantitative values are shown in Figure 1, an example of the clustering results is shown in Figure 2.

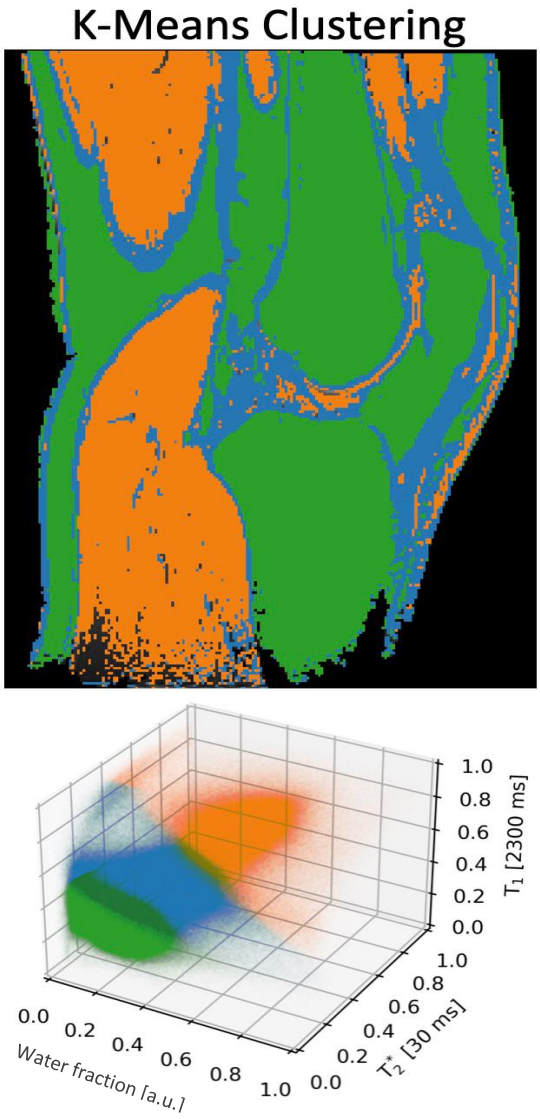

Fig. 2: Visualization of a participant's K-means results as a knee image (top) and as a 3D histogram (bottom).

Discussion

While T_2^* is not able to clearly differentiate between the four tendon/ligament tissues (ACL, PCL, QT, PT) and the three adipose tissues (BM, IFP, SAT), T_1 and WF show clearer differences. Skeletal muscle shows elevated values for all parameters. Based on these manual segmentation results, three starting positions were selected for the K-means algorithm, which then classified all 12 million measured voxels of an individual knee joint into these three categories. Additional parameters can be used in the future to further improve segmentation results and potentially distinguish even more tissues.

Conclusion

In this study, UTE imaging was used to characterize three tissue clusters of the knee joint using only quantitative parameters; no morphological information was used.

Acknowledgement

The authors thank Siemens Healthineers and Thomas Benkert (MR Application Predevelopment, Siemens Healthineers GmbH, Erlangen, Germany). This study was founded by the German Research Foundation (DFG, INST 271/ 406-1 FUGG).

References

1. Wehrli FW: Magnetic resonance of calcified tissues. *J Magn Reson* 2013; 229:35–48.

2. Grosse U, Syha R, Hein T, et al.: Diagnostic value of T1 and T2∗ relaxation times and off-resonance saturation effects in the evaluation of achilles tendinopathy by MRI at 3T. *J Magn Reson Imaging* 2015; 41:964–973.

3. Chu CR, Williams AA: Quantitative MRI UTE-T2* and T2* Show Progressive and Continued Graft Maturation Over 2 Years in Human Patients After Anterior Cruciate Ligament Reconstruction. *Orthop J Sport Med* 2019; 7:1–10.

4. Qian Y, Boada FE: Acquisition-weighted stack of spirals for fast high-resolution three-dimensional ultra-short echo time MR imaging. *Magn Reson Med* 2008; 60:135–145.

5. Rothe M, Deistung A, Brill R, Wohlgemuth WA, Gussew A: Validation of fast in vivo T1 and T2* mapping of tissues in the knee using 3D UTE. In *Jt Annu Meet ISMRM-ESMRMB*. London; 2022:1342.

6. Rothe M, Riedel S, Deistung A, Brill R, Wohlgemuth WA, Gussew A: In vivo T1 and T2* relaxation times of fast relaxing tissues of the healthy knee. In *ISMRM ISMRT Annu Meet Exhib*. Toronto; 2023:1623.

7. Fedorov A, Beichel R, Kalpathy-Cramer J, et al.: 3D Slicer as an Image Computing Platform for the Quantitative Imaging Network. *Magn Reson Imaging* 2012; 30:1323–1341.

Free-breathing full pancreas water T_1 mapping

Elizabeth Huaroc Moquillaza[1*], Camila Bustos[1], Kilian Weiss[2] and Dimitrios C. Karampinos[1]

[1] Department of Diagnostic and Interventional Radiology, School of Medicine, Technical University of Munich, Munich, Germany
[2] Philips GmbH Market DACH, Hamburg, Germany

* elizabeth.huaroc@tum.de

Synopsis: T_1 mapping provides valuable insights for the assessment of pancreatic diseases. However, a high-resolution, fast and water-specific T_1 mapping method remains a challenge. This work proposes a fast free-breathing multi-slice single-shot water T_1 mapping technique combining respiratory-triggering, non-slice-selective adiabatic inversion pulses and slice-specific dictionaries.

Introduction

High-resolution, fast T_1 mapping of the entire pancreas is a challenge due to the complexity of this anatomy and the long acquisition time of current T_1 mapping methods. For example, the MOLLI (1) method and magnetic resonance fingerprinting (2) have been used for pancreas T_1 mapping acquiring one slice in a 10 s breath hold and in free breathing in 9 s, respectively. Moreover, given that T_1 is biased in the presence of fat (3), frequently seen in lipomatous and atrophic pancreas, a technique for water T_1 (wT_1) mapping would be of advantage.

To overcome these drawbacks, the work in (4) proposed a high-resolution, rapid, continuous inversion-recovery Look-Locker method combining a spiral read out with Dixon and a dictionary-based processing for wT_1 mapping. To scan the entire pancreas, three breath holds were needed which might be not possible for patients unable to hold their breath.

The present work proposes a free-breathing technique using a non-slice-selective inversion (NSS) and slice-specific dictionaries for the T_1 estimation. The entire pancreas is scanned using a respiratory-triggered acquisition at a rate of 1.5 s per slice.

Methods

Pulse sequence design: The single-shot sequence presented in (4) has been modified for the present work as shown in Fig. 1. An adiabatic NSS inversion pulse followed by 100 5° RF pulses every TR = 15 ms is used to encode T_1. After every 5° pulse, a spiral readout of 9.2 ms is acquired at TE_1/TE_2 = 2.3/3.3 ms and is rotated for varying spatial encoding. The respiratory-triggered acquisition of one slice lasts 1.5 s.

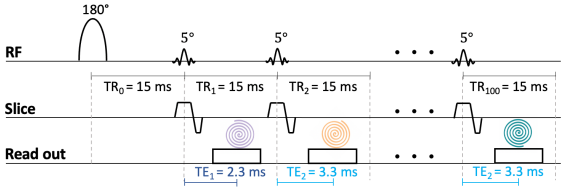

Fig. 1: Proposed pulse sequence.

Multi-slice acquisition: Multiple slices are acquired in an interleaved manner using a 3 T Ingenia Elition X scanner (Philips Healthcare). The acquisition of each slice is triggered at the beginning of expiration determined by the vendor's respiratory motion tracking system.

Slice-specific dictionary: As shown in Fig. 2, a dictionary per slice is calculated considering the effect of prior NSS pulses on the acquired slice. Before the pulse sequence, the dictionary considers all previous NSS pulses and the time in between which is equivalent to the time between triggered acquisitions. The tissue parameters considered for the dictionary calculations are T_1 = [100:5:3000] ms, T_2 = [50] ms and B_1 = [1] since the sequence is robust to B_1 inhomogeneities.

Quantification methodology: Fig. 2 presents also the proposed quantification methodology for one slice. The pre-scan B_0 map is used for deblurring and for water-fat separation together with a 7-peak fat model (5). To obtain the wT_1 map, the water signals are matched to a slice-specific dictionary.

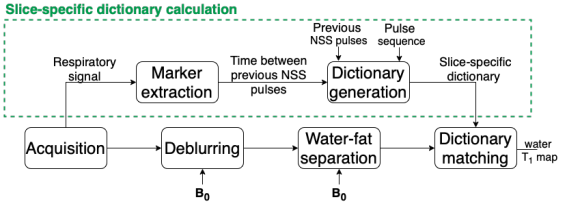

Fig. 2: Slice-specific dictionary calculation and quantification methodology.

In vivo measurements: The proposed method was evaluated in four volunteers. 20 slices were acquired to cover the entire pancreas using FOV = 450 mm, resolution = 2 x 2 x 5 mm^3, slice gap = 1 mm and under-sampling factor = 14. For all volunteers, an optimized interleaved slice ordering is employed as shown in Fig. 3.

To calculate the pancreas wT_1 mean value, the entire pancreas was segmented (6) in the obtained wT_1 maps.

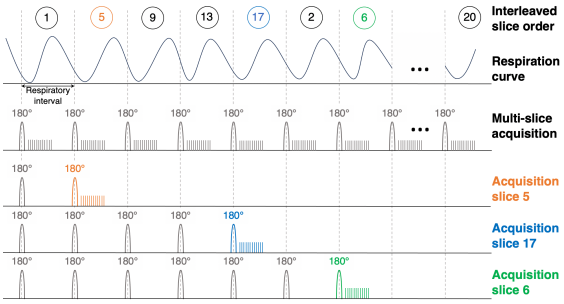

Fig. 3: The respiratory interval defines the time between two consecutive acquisitions. The acquisition is interleaved and triggered at expiration. For example, slice 5 is actually the second slice to be acquired; therefore, the magnetization within slice 5 is affected by one previous NSS pulse.

Results

The proposed method covers the entire pancreas and captures its complex anatomy. The volunteers' respiratory signals provided the expected information to calculate the slice-specific dictionaries considering also the previous NSS pulses. For all volunteers, Fig. 4 shows one wT_1 map and the whole pancreas segmentation, possible due to the entire pancreas coverage.

Discussion

The use of NSS pulses, respiratory-triggered acquisitions and the short duration of the single-shot sequence help to overcome the through-plane respiratory motion effects. Moreover, the use of slice-specific dictionaries increases the robustness of the wT_1 to different respiratory intervals, potentially enabling free breathing pancreas wT_1 mapping in patients with irregular respiratory motion and poor compliance.

Conclusion

This work proposes a novel free-breathing technique for wT_1 mapping of the entire pancreas combining slice-specific dictionaries based on NSS pulses, the monitoring of the respiratory motion signal and a single-shot sequence. The acquisition of one slice is triggered by the exhalation phase and lasts 1.5 s.

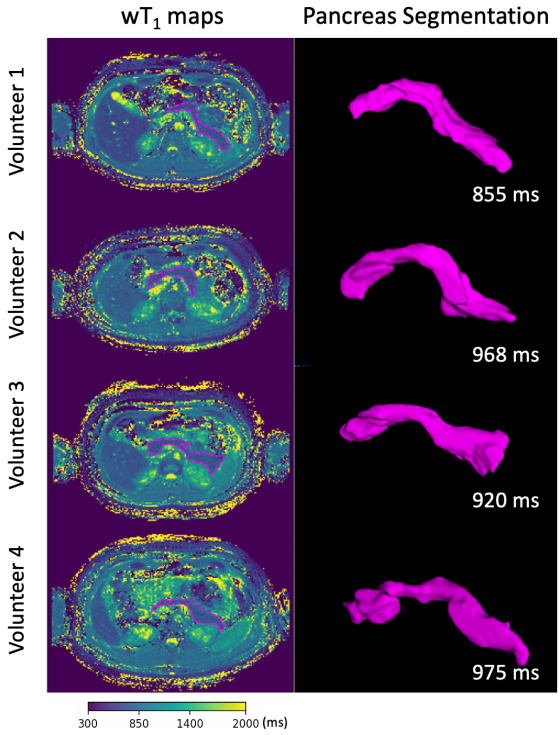

Fig. 4: One slice was selected to show the variation of the pancreas shape between volunteers. The wT_1 mean value of the pancreas is shown in the right bottom corner of each segmentation.

References

1. Wang M, Gao F, Wang X, Liu Y, Ji R, Cang L, Shi Y. Magnetic resonance elastography and T(1) mapping for early diagnosis and classification of chronic pancreatitis. J Magn Reson Imaging 2018.
2. Serrao EM, Kessler DA, Carmo B, Beer L, Brindle KM, Buonincontri G, Gallagher FA, Gilbert FJ, Godfrey E, Graves MJ, McLean MA, Sala E, Schulte RF, Kaggie JD. Magnetic resonance fingerprinting of the pancreas at 1.5 T and 3.0 T. Sci Rep 2020;10(1):17563.
3. Higashi M, Tanabe M, Okada M, Furukawa M, Iida E, Ito K. Influence of fat deposition on T1 mapping of the pancreas: evaluation by dual-flip-angle MR imaging with and without fat suppression. Radiol Med 2020;125(1):1-6.
4. Huaroc Moquillaza E, Steinhelfer L, Weiss K, Lee YJ, Stelter J, Amthor T, Koken P, Makowski MR, Braren R, Doneva M, Karampinos DC. High-resolution full pancreas water T1 mapping. 2024; Singapore.
5. Ren J, Dimitrov I, Sherry AD, Malloy CR. Composition of adipose tissue and marrow fat in humans by 1H NMR at 7 Tesla. J Lipid Res 2008;49(9):2055-2062.
6. Yushkevich PA, Piven J, Hazlett HC, Smith RG, Ho S, Gee JC, Gerig G. User-guided 3D active contour segmentation of anatomical structures: significantly improved efficiency and reliability. Neuroimage 2006;31(3):1116-1128.

Performance of Quantitative Susceptibility Mapping in brain tissue with extreme iron content

Christoph Birkl,[1*] Marlene Panzer,[2] Christian Kames,[3] Alexander Rauscher,[3] Bernhard Glodny,[1] Elke R. Gizewski,[1] and Heinz Zoller,[2]

[1] Department of Radiology, Medical University of Innsbruck, Innsbruck, Austria.
[2] Department of Medicine I, Medical University of Innsbruck, Innsbruck, Austria.
[3] Department of Physics and Astronomy, University of British Columbia, Vancouver, Canada

* Christoph.birkl@i-med.ac.at

Synopsis The majority of Quantitative Susceptibility Mapping (QSM) algorithms fail in brain regions with extreme iron overload. QSM with multi-echo combination during dipole inversion provides reliable susceptibility values in brain regions with extreme iron content. Conversely, QSM algorithms employing multi-echo combination prior to background field removal and dipole inversion tend to underestimate the magnetic susceptibility in such brain regions.

Introduction

Aceruloplasminemia (ACP) is a rare autosomal recessive disorder characterized by progressive iron deposition in various organs, notably the pancreas, liver and brain. Diagnosis typically involves detecting iron overload using MRI. [1] Quantitative Susceptibility Mapping (QSM) is regarded as a novel and robust MRI technique for assessing iron content in the brain. However, challenges such as susceptibility artifacts and the need for standardization persist with QSM. This study aimed to evaluate the efficacy of various QSM algorithms in assessing brain iron levels in patients with extreme iron overload compared to healthy controls.

Methods

We acquired images using a 3D multi-echo gradient echo sequence for QSM in three patients with ACP and three healthy subjects. Following six algorithms for QSM were compared: (I) fast nonlinear susceptibility inversion (FANSI)[2], (II) improved sparse linear equation and least-squares (iLSQR) [3], (III) morphology enabled dipole inversion (MEDI) [4], (IV) streaking artifact reduction (star) QSM [5] with rapid opensource minimum spanning tree algorithm (ROMEO) phase unwrapping [6], (V) star QSM with Laplacian phase unwrapping and (VI) multi-echo rapid two step (merts) [7] QSM. Regional QSM values were assessed in the caudate nucleus, putamen, globus pallidus and thalamus.

Results

Different QSM algorithms lead to slightly different maps of the same subject, for both controls and patients. This is most notable by the different degree of regularization, and occurrence of dipole artifacts (Fig. 1). Regional QSM analysis showed that the selected algorithm had a significant effect on the susceptibility values in the caudate nucleus, globus pallidus, putamen and thalamus of the healthy controls. These differences in magnetic susceptibility, become even more pronounced in patients with ACP. Especially in deep gray matter structures, where the highest iron content is observed, some algorithms fail to properly estimate the magnetic susceptibility. This is reflected in unrealistically low susceptibility values or signal dropouts (Fig. 1). Furthermore, regional susceptibility analysis showed a significant dependency of the susceptibility values on the used algorithm of the patients (Fig. 2). In the globus pallidus, only merts QSM measured higher susceptibility values in patients compared to controls, all other algorithms yielded similar or even lower susceptibility values in patients compared to controls.

Discussion and Conclusion

One major finding of our study was, that in the globus pallidus only one algorithm (merts QSM) measured higher susceptibility values in patients compared to controls. All other QSM algorithms measured similar or even lower susceptibility values than in controls. A previous post mortem study found much higher susceptibility and absolute iron levels in the globus pallidus of patients with ACP compared to controls. [1]

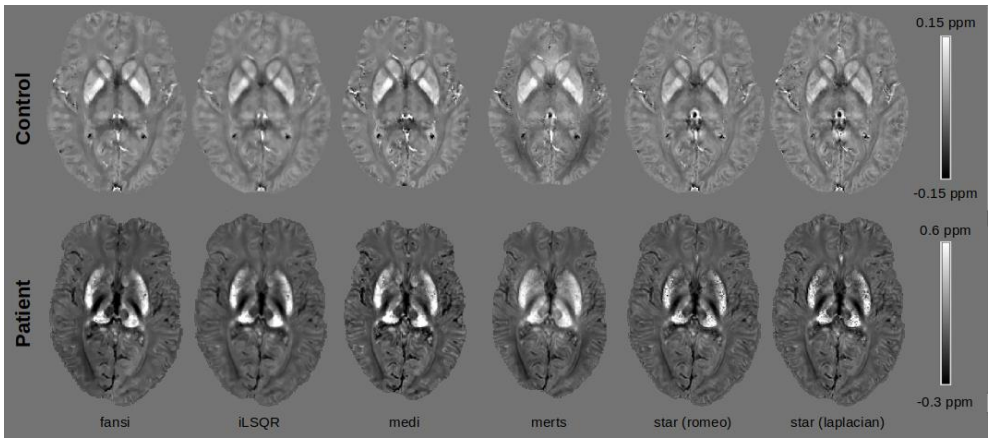

Fig. 1: Comparison of susceptibility maps computed using six different QSM algorithms of a 50 year old healthy woman and a 50 year old woman with aceruloplasminemia.

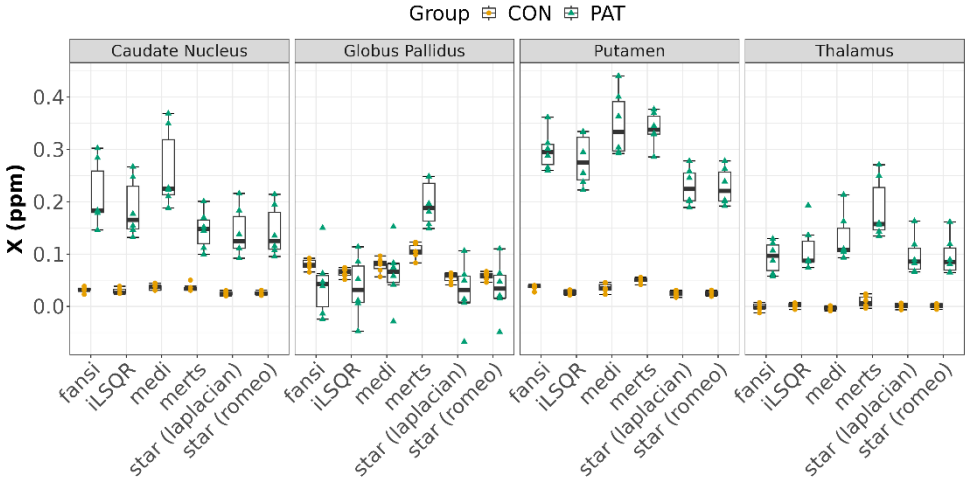

Fig. 2: Regional analysis of magnetic susceptibility values of three healthy subjects (yellow dots) and three patients with aceruloplasminemia (green triangles), across different QSM algorithms.

This supports our conclusion that only merts QSM does properly estimate the susceptibility values caused by the high iron content in the globus pallidus.

Our findings suggest that only a few QSM algorithms provide maps that are in agreement with extreme iron overload in brain tissue. Furthermore, we conclude that an echo combination prior to phase unwrapping and background field removal is more likely to produce artifacts and signal dropouts leading to overall unrealistically low susceptibility values.

References

1. Vroegindeweij LHP, Wielopolski PA, Boon AJW, et al. MR imaging for the quantitative assessment of brain iron in aceruloplasminemia: A postmortem validation study. NIMG. 2021;245(July):118752.

2. Milovic C, Bilgic B, Zhao B, Acosta-Cabronero J, Tejos C. Fast nonlinear susceptibility inversion with variational regularization. Magn Reson Med. 2018;80(2):814-821.

3. Li W, Wu B, Liu C. Quantitative susceptibility mapping of human brain reflects spatial variation in tissue composition. NIMG. 2011;55(4):1645-1656.

4. Liu T, Liu J, de Rochefort L, et al. Morphology enabled dipole inversion (MEDI) from a single-angle acquisition: comparison with COSMOS in human brain imaging. Magn Reson Med. 2011;66(3):777-783.

5. Wei H, Dibb R, Zhou Y, et al. Streaking artifact reduction for quantitative susceptibility mapping of sources with large dynamic range. NMR Biomed. 2015;28(10):1294-1303.

6. Dymerska B, Eckstein K, Bachrata B, et al. Phase unwrapping with a rapid opensource minimum spanning tree algorithm (ROMEO). Magn Reson Med. 2021;85(4):2294-2308.

7. Kames C, Doucette J, Rauscher A. Multi-echo dipole inversion for magnetic susceptibility mapping. Magn Reson Med. 2023;89(6):2391-2401.

Association Between Arterial Hypertension and Spinal Degeneration: An MRI-Based Cross-Sectional Study.

Fiona Mankertz,[1*] Kim Lisa Westphal,[1] Lukas Rasche[2], Robin Bülow[1], Norbert Hosten[1] and Carolin Malsch[2]

[1] Institute for Diagnostic Radiology and Neuroradiology, University Medicine Greifswald, Greifswald, Germany
[2] Institute for Mathematics and Computer Science, University of Greifswald, Greifswald, Germany

* fiona.mankertz@uni-greifswald.de

Synopsis: The aim of this study was to evaluate the association between the presence of arterial hypertension and spinal degeneration through MRI-based assessment. Two independent readers measured thoracic spondylophyte area in mm^2 in the area of T8-T11 in a population cohort of 857 study participants using axial T2-weighted fat sat Flash 3D MRI sequence and analysed the relationship between arterial hypertension and spondylophyte area using logistic and linear regression. We found a borderline significant association between hypertension and an increased likelihood of thoracic spondylophytes (OR 1.83, p = 0.06). The study highlights the potential link between hypertension and spinal health.

Introduction

Back pain is a prevalent health issue, affecting over two thirds of the German population annually and resulting in significant healthcare costs and societal burden. (1) Degenerative spinal conditions are major contributors to back pain, especially in older adults. A lesser researched contributor of back pain is the presence of spondylophytes. Spondylophytes are exostotic vertebral bone formations that form as a result of a compensatory process where additional bone mass at the edge of the affected vertebrae is formed, resulting in improved and more even pressure distribution on the vertebrae. (2) The aortic pulse has additionally been linked to the inhibition of spondylophyte development on the left thoracic side in the paraaortic area of T8-T12. (3) While known risk factors for spondylophytes include age, obesity, and physical activity, the role of arterial hypertension remains unclear. The role of higher arterial pressure and a subsequent higher aortic pulse in the formation of thoracic spondylophyte development has to this point not been fully explored. (4) This study aims to explore the association between arterial hypertension and thoracic spondylophytes.

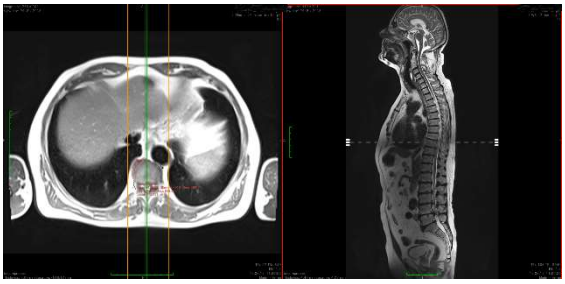

Fig. 1: MRI images from the Study of Health in Pomerania's START cohort. The left image shows an axial view of the thoracic spine. The red outline indicates the measured area of a right-sided thoracic spondylophyte in mm^2. Right: Sagittal view of the entire spine. The dashed line marks the axial level corresponding to the image on the left for anatomical orientation.

Methods

This cross-sectional study utilised data acquired voluntarily from the Study of Health in Pomerania's START cohort using a two-stage stratified and cluster sampling scheme. The area of thoracic spondylophytes of adult volunteers between 45-64 years were assessed using magnetic resonance imaging (MRI) of vertebral segments T8-T11. The determination of thoracic spondylophyte area was performed using an axial T2-weighted Flash 3D MRI sequence with fat saturation in the thoracic spine region, with the following parameters: Repetition time = 3230 ms, Echo time = 34 ms, Flip angle = 180, Voxel size = 1.6 x 1.6 x 3.0 mm, Duration = 2.43 min, Resolution = 512 x 512 pixels, Pixel bandwidth = 170 Hz/pixel, carried out by two independent readers. Spondylophytes were first classified as present or absent based on MRI findings, and then independently measured in square millimetres (mm^2). Hypertension was defined according to standard clinical guidelines, including systolic and diastolic blood pressure measurements. (5)

Directed Acyclic Graphs (DAGs) were used to identify and adjust for potential confounders. Statistical analyses included logistic regression to examine the presence of spondylophytes and linear regression to assess the extent of spondylophyte formation, controlling for age, body mass index (BMI), and other relevant variables.

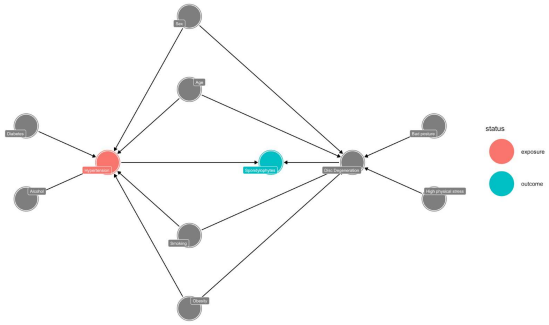

Fig. 2: Directed Acyclic Graph (DAG) illustrating possible relationships between hypertension and the presence of spondylophytes, with potential confounding variables. Hypertension (exposure) is highlighted in red, and spondylophytes (outcome) in blue. Other variables like age, sex, BMI, smoking, alcohol consumption, diabetes, obesity, high physical stress, bad posture, and disc degeneration, are represented in gray. Arrows indicate the direction of the relationship.

Results

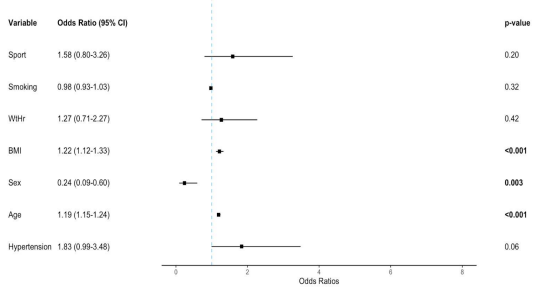

Fig. 3: Forest plot showing the Odds Ratios (OR) with 95% Confidence Intervals (CI) for various variables associated with the presence of thoracic spondylophytes. Variables include physical activity (Sport), smoking status, waist-to-hip ratio (WtHr), body mass index (BMI), sex, age, and hypertension. The dashed vertical line represents an OR of 1, indicating no effect.

The study included 857 participants with complete data on hypertension status and MRI findings. The prevalence of thoracic spondylophytes in the study population was 88%. Logistic regression analysis revealed that hypertension was associated with an increased likelihood of having thoracic spondylophytes (Odds Ratio [OR] 1.83, 95% Confidence Interval [CI] 0.99 – 3.48), which was borderline significant (p = 0.06). Additionally, logistic ridge regression analysis indicated that hypertension significantly predicted the extent of spondylophyte formation at specific thoracic levels (positive predictive value = 0.77, p < 0.01).

Discussion

This study aimed to explore the association between arterial hypertension and thoracic spondylophytes. The findings of this study demonstrate an association between arterial hypertension and thoracic spondylophytes. Several mechanisms may underlie this relationship. Shared risk factors could contribute to both conditions. (6) Additionally, hypertension may exert direct vascular effects on spinal structures, promoting degenerative changes. The results align with previous studies that have linked hypertension to other degenerative musculoskeletal conditions. (7) However, the cross-sectional design of this study limits the ability to draw causal conclusions. Longitudinal research is needed to evaluate these findings in a prospective setting. Moreover, the study population, which is predominantly Caucasian middle-aged adults from a specific region, may limit the generalisability of the findings.

Conclusion

The aim of this study was to evaluate the association of arterial hypertension and spinal degeneration using the example of thoracic spondylophytes. In a population study of 857 participants we found that there was a slightly increased positive association between arterial hypertension and thoracic degeneration in the area of T8-T11. Thus, effective management of blood pressure may also translate to benefits for musculoskeletal health. These findings underscore the importance of integrated approaches to managing hypertension and spinal health. Subsequent research might lead to further understanding the relationship between vascular disease and spinal degeneration.

References

1. v.d. Lippe *et al*. J Health Monit. 2021:2-14.
2. Farshad *et al*. Spine J. 2022:1903-1912.
3. Tan *et al*. Ann Rheum Dis. 2019:922-928.
4. Zukowski *et al*. J Anat. 2012:57-66.
5. Mancia *et al*. J Hypertens. 2024:194.
6. Pérez-Martínez *et al*. Nutr Rev. 2017:307-26.
7. Lo *et al*. J Orthop Translat. 2021:12-20.

Automatic evaluation of the properties of the glymphatic system using diffusion MRI data

Sascha D. Santaniello[1*], Markus Janko[1], Gabriel Gonzalez-Escamilla[2], Sergiu Groppa[2], Marc A. Brockmann[1], Ahmed Othman[1], Andrea Kronfeld[1]

[1] Department of Neuroradiology, University Medical Center of the Johannes Gutenberg University Mainz, Germany.
[2] Department of Neurology, University Medical Center of the Johannes Gutenberg University Mainz, Germany.

*santanis@uni-mainz.de

Synopsis: The properties of the glymphatic system were evaluated using diffusion-MRI of multiple sclerosis patients and healthy controls. The aim of this work was to automatically calculate the DTI-ALPS index in order to estimate the characteristics of glymphatic systems of MS patients and healthy controls.

Introduction

The glymphatic system (GS) is a network of perivascular canals that is involved in the removal of metabolic waste in the brain. It is suspected to be disturbed or altered in various neurodegenerative diseases such as multiple sclerosis (MS), Alzheimer's or Parkinson's disease [1]. The DTI-ALPS index is a method that makes it possible to evaluate the properties of the microstructure of the brain and thus the GS on the basis of diffusion-weighted images [2]. An index value of 1.0 indicates a minimal diffusion along the perivascular space, while higher values indicate a correspondingly greater diffusivity.

Methods

This study includes 171 MS patients (112 female; 17-59 years; mean age 33.7 years) and 57 healthy subjects (31 female; 19-56 years; mean age 30.2 years). The subjects' diffusion data is preprocessed (denoising, ringing removal, FSL's eddy+topup) and then transformed linearly and non-linearly into standard space using the MNI152-template. Then, the diffusivity in x-, y- and z-direction in the projection and association fibers along the perivascular space is determined for these subjects by using the 4 ROIs shown in Fig. 1.

An index value for the diffusivity along the perivascular space is determined from their ratio (ALPS index) using the following formula, where $D_{x,y,z}$ stands for the diffusivity in the corresponding direction as well as D_{assoc} and D_{proj} indicate association and projection fibres respectively:

$$ALPS\ index = \frac{mean(D_{xproj}, D_{xassoc})}{mean(D_{yproj}, D_{zassoc})}$$

This value is then correlated with clinical parameters such as age, sex, lesion volume, type of MS and disease duration, where the last three variables were set to zero for healthy controls.

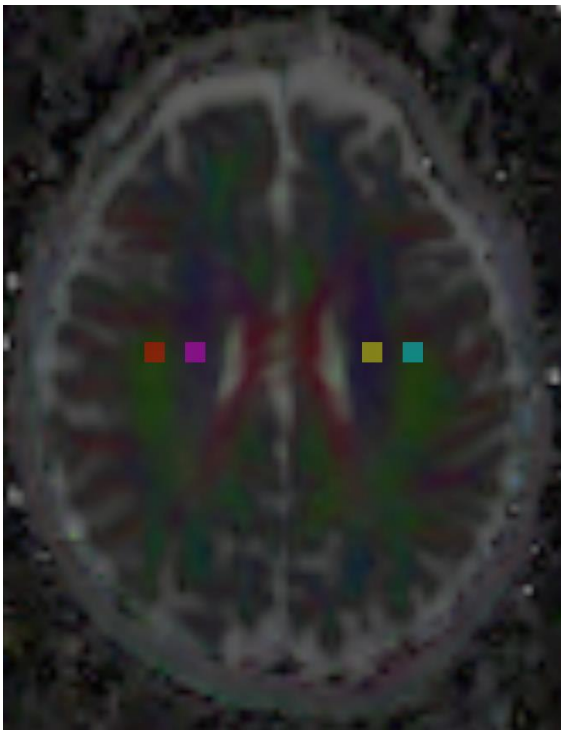

Fig. 1: Color-coded diffusivity map with ROIs for the projection (red: left, blue: right) and association fibres (purple: left, yellow: right).

Results

The calculated ALPS index is on average higher in the healthy control group than in MS patients. For the MS patients the mean ALPS index was 1.525 ± 0.223, while for the healthy controls the mean ALPS index was 1.640 ± 0.203 as shown in Fig. 2.

The Pearson correlation (α=0.01) shows significant correlations between the ALPS index and all of the clinical parameter as illustrated in Fig. 3: Age (r=-0.214), sex (r=0.270), lesion volume (r=-0.475), type of MS (r=-0.234), and disease duration (r=-0.283).

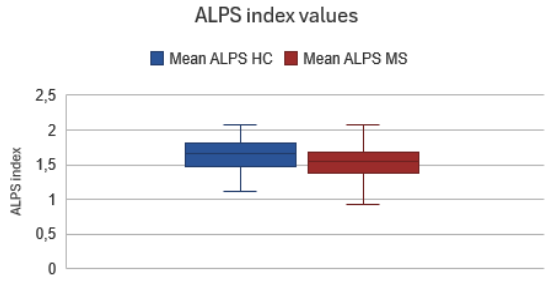

Fig. 2: ALPS index values of MS patients and healthy control groups.

Fig. 3: Pearson correlation of ALPS index values and clinical parameters.

Discussion

The ALPS index is suitable for showing changes in the GS. By using our fully automated approach, consistent and reproducible ALPS index values can be obtained. However, since these values are calculated using the diffusivity in the perivascular area near the lateral ventricle only, statements about the overall activity of the GS are difficult to make. Furthermore, it is not yet possible to predict if a subject is healthy or not by using only the ALPS index. It should also be investigated in future work whether the ALPS index can be used to make statements about the progression of MS over several points in time.

Conclusion

The properties of the glymphatic system were evaluated using the automatically calculated ALPS index. Our results show a correlation between changes in GS and MS.

References

1 Iliff JJ, Wang M, Liao Y, Plogg BA, Peng W, Gundersen GA, Benveniste H, Vates GE, Deane R, Goldman SA, Nagelhus EA, Nedergaard M. A paravascular pathway facilitates CSF flow through the brain parenchyma and the clearance of interstitial solutes, including amy-loid β. Sci Transl Med. 2012 Aug 15;4(147):147ra111.

2 Taoka T, Masutani Y, Kawai H, Nakane T, Matsuoka K, Yasuno F, Kishimoto T, Naganawa S. Evaluation of glymphatic system activity with the diffusion MR technique: diffusion tensor image analysis along the perivascular space (DTI-ALPS) in Alzheimer's disease cases. Jpn J Radiol. 2017 Apr;35(4):172-178.

Cardiac CINE imaging at 0.55T – a comparison to 1.5T

Simon Mayr,[1,*] and Matthias S May[1]

[1] Radiologisches Institut, Universitätsklinikum Erlangen, Friedrich-Alexander-Universität Erlangen-Nürnberg, Germany. [2] Imaging Science Institute, Universitätsklinikum Erlangen, Germany.

* simon.mayr@fau.de

Synopsis: We acquired cardiac CINE images at 0.55 T and at 1.5 T and compared functional parameters. The measurements extracted from the 0.55 T sequences provide a good assessment of the cardiac function. However, the 0.55 T measurements generally produced significantly lower volumetric measurements than the 1.5T CMR, suggesting a systematic error within the scan protocol.

Introduction

Low-field magnetic resonance imaging (MRI) might improve individual and global accessibility of MRI. Leveraging compressed sensing-based image acquisition techniques, cardiovascular magnetic resonance (CMR) at low-field MRI has become more feasible than ever (1).

We compared cardiac function acquired at 0.55 T and at 1.5 T, by quantifying left ventricular volumes and geometrical measurements, in patients referred for a clinical CMR.

Methods

Nineteen patients were recruited for an additional cardiac exam on a commercial 0.55 T system (MAGNETOM Free.Max, Siemens Healthineers AG, Erlangen, Germany), 1 hour prior to their clinically scheduled CMR at 1.5 T(MAGNETOM Sola, MAGNETOM Aera Siemens Healthineers AG, Erlangen, Germany).

Research cine-sequences of the short and the long axis using bSSFP with compressed sensing acceleration were acquired. Using Simpson's method, all data was semi-automatically analyzed, for their volumetric parameters.

Cine acquisition parameters at 0.55 T and 1.5 T

long axis			short axis	
Scanner	0.55T	1.5 T	0.55T	1.5 T
Flip angle (°)	90	80	90	80
TE (ms)	1.58	1.16	1.53	1.11
TR (ms)	31.60	35.5	26.46	42.4
Slice thickness (mm)	8	6	8	8mm
Acceleration mode	CS	GRAPPA	CS	GRAPPA
Acceleration Factor	3.2	2	3.3	2
Bandwidth (Hz/Px)	930	930	930	930
Voxel Size (mm³)	1.8×1.8×8.0	1.8×1.8×6.0	2.1×2.1×8.0	1.8×1.8×8.0

Table 1: Cine acquisition parameters at 0.55 T and 1.5 T

These included left ventricular (LV) parameters: end-diastolic volume (EDV), end-systolic volume (ESV), ejection fraction (EF), left-ventricular stroke volume (SV), LV end-diastolic mass (ED-Mass), as well as geometric measurements of the LV end-diastolic diameter (LV-EDD), interventricular septum thickness (IVS), left atrial size(LAS) and right atrial size (RAS).

To compare the volumetric and geometrical values, two-sided t-tests for dependent variables were used for data exhibiting standard distribution, determined by the Shapiro-Wilk normality test. For data not matching this criteria the Wilcox-Test for two dependent variables was applied.

Regarding visual assessment, one radiologist with 15 years of diagnostic experience, was tasked with inspecting both datasets for wall-motion abnormalities and visible valve pathologies and scoring the diagnostic confidence of the images.

Results

The EF showed good agreement with 1.5 T. There were no significant differences in EF between the two scanners (e.g., EF: $t(18) = 1.6284$, $p = 0.12$, mean difference = - 1.53 %).

All of the volumetric parameters showed significant differences, with the 1.5 T CMR always producing higher mean values (e.g.

EDV: p = 3.815e-06, mean difference = - 29.3 ml; ESV: p = 0.005329, mean difference = - 12.3 ml; SV: t(18) = - 4.735, p = 0.0001653, mean difference = - 16.27 ml; ED-Mass: t(18) = 2.6804, p = 0.01528, mean difference = - 7.3 g).

Excluding the IVS, the mean geometric values at 1.5 T were also significantly bigger, compared to 0.55 T (e.g. LV-EDD: p = 0.0003683; IVS: t(18) = 2.2372, p = 0.03816, mean difference = 0.83 mm; LAS: t(18) = - 3.1587, p = 0.005433, mean difference = - 2.908947 mm; RAS: t(18) = - 3.495, p = 0.002586, mean difference = - 4.095789 mm).
The data of EDV, ESV, and LV-EDD did not exhibit the standard distribution, thus the Wilcox test was utilized.

Discussion

The assessment of the data showed significant differences between the methods, except for the EF, which displayed no significant difference. With the EF being the most important clinical parameter for assessing heart function, CMR at 0.55 T shows great potential for future clinical application.

There seems to be a systematic mistake, within the sequence protocol, which led to the absolute cardiac volumes being consistently measured lower at 0.55 T compared to 1.5 T. With some further adjustments of the sequence protocol, an accurate assessment of heart function at 0.55 T is achievable.

Conclusion

A commercial 0.55 T MRI is able to deliver a functional CMR that allows a good approximation of the cardiac function in patients, comparable to a 1.5 T CMR.

References

1. Varghese J, Jin N, Giese D, Chen C, Liu Y, Pan Y, Nair N, Shalaan MT, Khan M, Tong MS, Ahmad R, Han Y, Simonetti OP. Building a comprehensive cardiovascular magnetic resonance exam on a commercial 0.55 T system: A pictorial essay on potential applications. Front Cardiovasc Med 2023;10:1120982.

How similar is quantitative MRI in the human brain measured ex vivo and in vivo?

Gisela E Hagberg[1,2*] Thomas Shiozawa[3], Bernhard Hirt[3] and Klaus Scheffler[1,2]

[1] Biomedical Magnetic Resonance, University Hospital Tübingen, Tübingen, Germany.
[2] Highfield Magnetic Resonance, Max-Planck-Institute for Biological Cybernetics, Tübingen, Germany
[3] Institute for Clinical Anatomy and Cellanalytics, University Hospital Tübingen, Tübingen, Germany

* gisela.hagberg@tuebingen.mpg.de

Synopsis: Despite increased R_1 and R_2* ex vivo, automatic segmentation was successful, indicating ca 15% tissue shrinkage. Cortical QSM values were comparable ex/in vivo, and sensitive to age-based estimates of iron concentrations.

Introduction

Ultra-high spatial resolutions can be obtained ex vivo with long image acquisition times[1]. For validation purposes, ex vivo MRI can be useful when used in combination with histology[2,3] and µCT[4] . But how relevant are ex vivo quantitative MRI (qMRI) measurements for clinical in vivo studies? Besides the post-mortem-interval (PMI)[5], substitution of CSF with a fixative agent alters the dielectric[6] and relaxation properties (qMRI)[7] can modify the magnetic properties of the tissue leading to different results than in vivo. Here we measured ex vivo whole brain samples from healthy donors with short PMI, during immersion fixation and compared qMRI results in automatically segmented regions-of-interest with results obtained in vivo with young and elderly healthy volunteers.

Methods

Ex vivo whole brains (N=4, 80±1y 2F, PMI≤12h) were immersion fixed in formalin (Roti®-Histofix 4, Carl Roth GmbH+Co. KG) with added NaCl (140mM) and KCl (2.7mM) with known dielectric properties[6] which yielded a more homogeneous distribution of the flip angles and improved MRI quality compared to the standard fixative (Fig.1). MRI was performed multiple times between 30-194days of fixation. Five elderly (69±4, 2F) and five young (31±8y, 2F) healthy subjects volunteered to participate. The study was approved by the Ethics committee, University of Tübingen.

The MRI-protocol at 9.4T (Siemens Erlangen, Germany) consisted of B_1-mapping with AFI[8–10]; MP2RAGE; (TI_1/TI_2=900/3500ms; TR=6ms; TE=2.3ms; volume TR=9s; FA=4/6°; voxel: 0.8×0.8 ×0.8mm^3) and 3DGRE (TR=34ms; TE= 6.03, 12, 18, 24, 30ms; FA =15°; voxel size=0.4×0.4 ×0.4mm^3). T_1-weighed (CNT) and qMRI (R_1, R_2* and QSM) images were obtained as described previously [11,12].

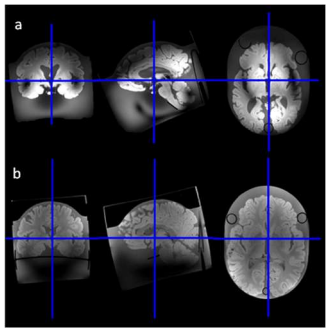

Fig.1 Ex vivo, proton density weighted MRI in CP mode transmission at 9.4T with a) standard fixative b) phosphate buffered saline 4% formalin

Tissue segmentations was obtained from skull-stripped[13] CNT and R_1 images using CAT12 (version 12.9, in Matlab R2018b) and LN2_RIM_POLISH[14] after reslicing into 3DGRE space using trilinear interpolation. Inverse spatial deformation fields were used to obtain brain parcellations in native space using CAT. qMRI data were extracted from cortical and subcortical regions, and the molar susceptibility and relaxivity values were determined based on age-based estimates of the tissue iron concentrations in nine brain regions[12,15].

Results

The image quality rating in CAT12[16] was excellent (A-) using CNT for the in vivo and R_1 for ex vivo data. The average cortical thickness was stable during 30-192 days of immersion fixation but was ca 15% smaller than in elderly subjects measured in vivo (Table 1). In cortical areas where fixation is faster than in deeper regions, QSM values remained stable and were similar to in vivo values while R_2* and R_1 varied with immersion time and were higher than in vivo (Fig.2). Including both cortical and subcortical regions, the estimated iron-dependent change in qMRI was similar to in vivo data for QSM after 30 days of immersion

fixation, and 2-3 times higher for R_2* and R_1, also reflected by the r_1-r_2* relaxivity (Table 1).

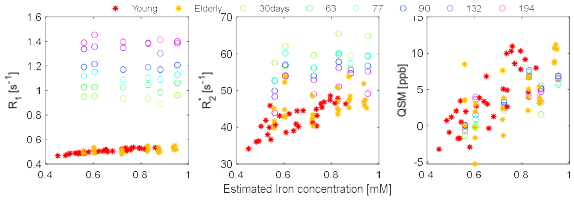

Fig. 2: Dependence of qMRI on age-based estimates of the iron concentration in 6 cortical areas for young and elderly subjects in vivo, and for an ex vivo whole brain sample measured at different timepoints of immersion fixation.

Table 1 Cortical thickness (CT) and change in qMRI parameters with age-based estimations of region-specific iron-concentrations in cortical and sub-cortical regions

	CT [mm]	susceptibility ppb/mM	r_2* [s^{-1}/mM]	r_1 [s^{-1}/mM]	r_1-r_2* [$\cdot 10^3$]
Young	2.25± 0.05	25.9± 2.3	19.4± 2.3	0.075± 0.010	3.86± 0.55
Elderly	1.92± 0.07	22.8± 6.3	15.7± 5.2	0.059± 0.006	3.92± 1.05
Ex vivo	1.61± 0.16*	23.4± 6.7	32.3± 10.5	0.200± 0.037	6.20± 1.04

Discussion and Conclusion

Tissue segmentation is usually based on T_1-weighted MRI, which is the qMRI parameter that undergoes the largest changes during immersion fixation. Despite this, ex vivo R_1 maps had sufficient image contrast to allow segmentation using CAT12 with no significant variation in the estimated average CT across different immersion times. The CT diminished by 15% from young to elderly, and by another 15% from the elderly to ex vivo.

qMRI showed higher R_1 and R_2* values and increased relaxivity after fixation, while QSM in cortical grey matter areas and the molar susceptibility was similar to in vivo.

During formalin fixation diffusion is slowed down, leakage of biometals[17] into free water pools and changes in iron redox state can occur. All these factors can influence qMRI ex vivo. Further studies are required to establish the exact causes behind the differences and similarities observed ex vivo compared to in vivo at 9.4T.

References

1. Edlow, B. L. *et al.* 7 Tesla MRI of the ex vivo human brain at 100 micron resolution. *Sci. Data* **6**, 1–10 (2019).
2. Bagnato, F. *et al.* Tracking iron in multiple sclerosis: a combined imaging and histopathological study at 7 Tesla. *Brain* **134**, 3602–3615 (2011).
3. Hametner, S. *et al.* The influence of brain iron and myelin on magnetic susceptibility and effective transverse relaxation - A biochemical and histological validation study. *Neuroimage* **179**, 117–133 (2018).
4. Lee, J. Y. *et al.* Distribution of corpora amylacea in the human midbrain: using synchrotron radiation phase-contrast microtomography, high-field magnetic resonance imaging, and histology. *Front. Neurosci.* **17**, (2023).
5. Shepherd, T. M. *et al.* Postmortem interval alters the water relaxation and diffusion properties of rat nervous tissue — Implications for MRI studies of human autopsy samples. *Neuroimage* **44**, 820–826 (2009).
6. Nazemorroaya, A. *et al.* Developing formalin-based fixative agents for post mortem brain MRI at 9.4 T. *Magn. Reson. Med.* **87**, 2481–2494 (2022).
7. Dusek, P. *et al.* The choice of embedding media affects image quality, tissue R 2 * , and susceptibility behaviors in post-mortem brain MR microscopy at 7.0T. *Magn. Reson. Med.* **81**, 2688–2701 (2019).
8. Yarnykh, V. Effect of the phase increment on the accuracy of T1 measurements by the variable flip angle method using a fast RF spoiled. *Control* **15**, 2007 (2007).
9. Yarnykh, V. L. Optimal radiofrequency and gradient spoiling for improved accuracy of T1 and B1 measurements using fast steady-state techniques. *Magn. Reson. Med.* (2010) doi:10.1002/mrm.22394.
10. Pohmann, R. & Scheffler, K. A theoretical and experimental comparison of different techniques for B1 mapping at very high fields. *NMR Biomed.* **26**, 265–275 (2013).
11. Hagberg, G. E. *et al.* Whole brain MP2RAGE-based mapping of the longitudinal relaxation time at 9.4T. *Neuroimage* **144**, 203–216 (2017).
12. Hagberg, G. E. *et al.* Phase-based masking for quantitative susceptibility mapping of the human brain at 9. <scp>4T</scp>. *Magn. Reson. Med.* **88**, 2267–2276 (2022).
13. Hoopes, A., Mora, J. S., Dalca, A. V., Fischl, B. & Hoffmann, M. SynthStrip: skull-stripping for any brain image. *Neuroimage* **260**, 119474 (2022).
14. Huber, L. (Renzo) *et al.* LayNii: A software suite for layer-fMRI. *Neuroimage* **237**, 118091 (2021).
15. Hallgren, B. & Sourander, P. The effect of age on the non-haemin iron in the human brain. *J. Neurochem.* **3**, 41–51 (1958).
16. Gaser, C. *et al.* CAT – A Computational Anatomy Toolbox for the Analysis of Structural MRI Data. *bioRxiv* 2022.06.11.495736 (2023) doi:10.1101/2022.06.11.495736.
17. Schrag, M. *et al.* The effect of formalin fixation on the levels of brain transition metals in archived samples. *BioMetals* **23**, 1123–1127 (2010).

Impact of image registration and fibre orientation on the DTI-ALPS-index

Ali Ajouz,[1,2,3*] Olav Jansen,[1] Lynn Johann Frohwein,[3] and Jan-Bernd Hövener[1,2*]

[1] Department of Radiology and Neuroradiology, UKSH, CAU Kiel, Kiel, Germany.
[2] Department of Radiology and Neuroradiology, SBMI, CAU Kiel, Kiel, Germany.
[3] Siemens Healthineers AG, Forchheim, Germany.

* ali.ajouz@ rad.uni-kiel.de
jan.hoevener@rad.uni-kiel.de

Synopsis: This work aims to increase the robustness of the ALPS-index computation by considering the principal axis system of the diffusion tensors. As the calculation is done along the axon orientation and not along a fixed direction, the impact of the patient's position inside the scanner and non-uniformly oriented axons is supposed to be reduced.

Introduction

The along the perivascular space (ALPS) -index computation enables collecting information about the glymphatic system[1]. However, the robustness of the method is yet to be approved[1,2].

Recently, a method was published[2], in which the orientation of the human head inside the scanner can be neglected due to a registration of the calculated diffusion tensor (DT) to an oriented Fractional anisotropy (FA) -map in the Montreal Neurological Institute (MNI) space. However, registration to the FA-map[2] results in loss of information.

This work aims to investigate if an ALPS-index computation in the principal axis system (PAS)[3] eliminates the orientation dependence of the imaged volume without registration to the FA-MNI template as well as the fixed orientation.

Methods

All images were acquired with a MAGNETOM Cima.X scanner (Siemens Healthineers AG, Forchheim) with a maximal gradient amplitude of 200 mT/m, a maximum slew rate of 200 T/m/s and 2 Tx and 64 Rx head neck coil. Using a 2D EPI sequence, 72 diffusion volumes were acquired with 30 gradient directions (b-value of 1000 s/mm², average of 2) and 6 b0 images (plus 6 images in the opposite phase encoding direction). FOV=220 x 220 x 120 mm³, isotropic resolution=2mm, TE=48 ms, TR=6600 ms, bandwidth=1698 Hz/Px, flip angle=90°. GRAPPA (factor 2, 30 reference lines), effective echo spacing=0.3 ms. In addition, a T1w image with the MP-RAGE sequence (FOV= 256x256x192 mm³, isotropic resolution=1 mm, TE=2.45 ms, TR=1900 ms) was acquired.

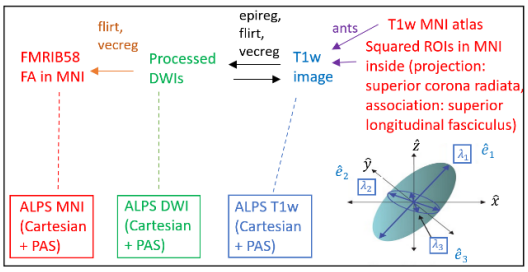

Fig. 1: The arrows illustrate registrations (including tools), and the dashed lines symbolize the space, in which the ALPS-index is calculated. The ALPS computation was done in the Cartesian system ($\hat{x}$, $\hat{y}$, $\hat{z}$) and in the PAS ($\hat{e}_1$, $\hat{e}_2$, $\hat{e}_3$).

The diffusion weighted imaging (DWI) preprocessing pipeline included denoising, unringing (Mrtrix), distortion and eddy current corrections (FSL). The DT metrics were calculated (Dipy). The T1w image was corrected for bias field correction, denoised and a brain mask was calculated (Ants).

Fig. 1 illustrates the pipeline of the index computation, which was done in T1w (blue), DWI (green) and MNI (red) spaces by registration.

For the ALPS-index computation in T1w space, the MNI-T1w_1mm template and two MNI JHU-ICBM atlases[4] for the ALPS regions of interests (ROIs) (4x4x4 mm³) were transformed onto the acquired T1w image (Ants). A mean b0 image was registered to the acquired T1w image (epireg, FSL) and the transformation matrix was applied onto the diffusion metrics (flirt, vecreg, FSL). Applying the ROIs allowed for the computation of the ALPS-index, described in reference [1].

For the ALPS computation in DWI space, the ROIs in the acquired T1w space were registered to DWI space by inverting the transformation from epireg. This enabled the direct calculation of the ALPS-index without further transformation of the DT metrics.

For the ALPS-index computation in MNI space, the calculated FA in DWI space was registered onto the MNI FMRIB58 FA template (flirt, FSL) and the registration matrix transformed the other diffusion metrics to MNI space (flirt, vecreg, FSL)[5], allowing for ALPS-index computation in MNI space.

In this work, an additional calculation method was performed using the DT in its PAS, see Figure 1. The modified ALPS-index equation is:

$$\text{ALPS-index-PAS} = \frac{\overline{\lambda_{x,proj}, \lambda_{x,assoc}}}{\overline{\lambda_{y,proj}, \lambda_{z,assoc}}}$$

, where λ_x refers to the eigenvalue (excluding the largest eigenvalue), whose eigenvector contains the larger x-component and λ_y and λ_z belong to the remaining eigenvalue, depending on the investigated ALPS region ($proj$ = projection, $assoc$ = association).

To test the robustness of the different ALPS-index computations, two healthy subjects (subject 1: female, 24 years; subject 2: male, 30 years) were scanned with the protocol described above. The computation pipeline (Fig. 1) including the Cartesian and PAS calculation for each of the three spaces was run 5 times for each subject to compare the ALPS-index variations in a statistical boxplot analysis.

To visualize the mean DT orientation, a mean tensor in the projection area was computed.

Results

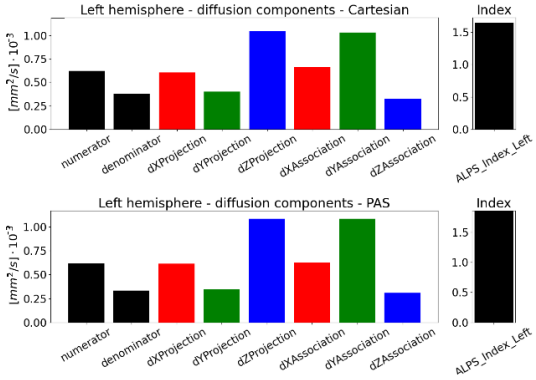

Fig. 2: The DT components and the ALPS-index in DWI space, calculated in the (top) Cartesian and in the (bottom) PAS system, obtained from subject 1.

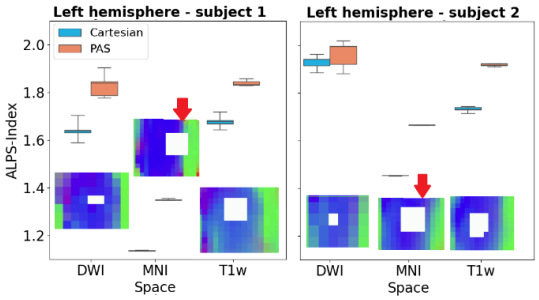

Fig. 3: The 5 repetitions of ALPS-index computation in the three different spaces of the two subjects. For each space, the projection area in the left hemisphere is shown on top of the first eigenvector.

Fig. 2 and Fig. 3 show a higher ALPS-index in the PAS compared to the Cartesian system.

Fig. 3 illustrates a lower deviation in the MNI space and in general lower indexes compared to other spaces, which contain similar indexes, also regarding the two healthy subjects. The ROIs align well with the metrics in DWI and T1w spaces, but not in MNI space, especially for subject 1 (red arrows).

Fig. 4 shows the misalignment of the PAS compared to the Cartesian system.

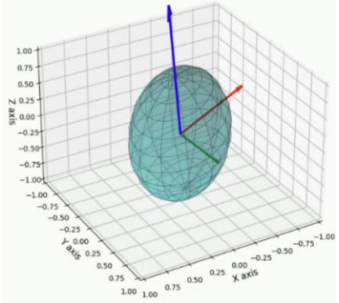

Fig. 4: The mean DT in the projection area in the left hemisphere, described in the Cartesian system in MNI space of subject 2.

Discussion

The higher index in the PAS results from the not perfectly oriented axons, demonstrated by the mean DT even in MNI space.

The lower index in MNI space resulted from poor registration, especially for subject 1, whereas DWI and T1w space contain indexes, which are typical for healthy, young subjects[1]. As the lowest deviation in MNI space is due to more area voxels included in the computation, increasing the limit for binarization after registration should decrease the deviations for DWI and T1w space.

Conclusion

The calculation in the PAS and not in the Cartesian system enabled the calculation of the ALPS-index independent of the orientation of the head in the scanner as well as of the orientation of the axons in the ROIs.

References

1. Taoka T, Masutani Y, Kawai H, et al. Evaluation of glymphatic system activity with the diffusion MR technique: diffusion tensor image analysis along the perivascular space (DTI-ALPS) in Alzheimer's disease cases. *Jpn J Radiol*. 2017;35(4):172-178. doi:10.1007/s11604-017-0617-z
2. Tatekawa H, Matsushita S, Ueda D, et al. Improved reproducibility of diffusion tensor image analysis along the perivascular space (DTI-ALPS) index: an analysis of reorientation technique of the OASIS-3 dataset. *Jpn J Radiol*. 2023;41(4):393-400. doi:10.1007/s11604-022-01370-2
3. Basser PJ, Mattiello J, LeBihan D. MR diffusion tensor spectroscopy and imaging. *Biophysical Journal*. 1994;66(1):259-267. doi:10.1016/S0006-3495(94)80775-1
4. Schartz D, Finkelstein A, Hoang N, Bender MT, Schifitto G, Zhong J. Diffusion-Weighted Imaging Reveals Impaired Glymphatic Clearance in Idiopathic Intracranial Hypertension. *AJNR Am J Neuroradiol*. 2024;45(2):149-154. doi:10.3174/ajnr.A8088

Neurobiochemical correlates of long-term neuropsychiatric consequences of COVID-19 disease

Wolfgang Weber-Fahr*[1],Markus Sack[1], Sandra Dommke[1], Nabil Alzein[1], Robert Becker[1], Claudia Schiling[2] and Gabriele Ende[1]

[1] Neuroimaging, Central Institute of Mental Health, Mannheim, Germany.
[2] Neuropsychiatric Sleep Disorders, Clinic Psychiatry and Psychotherapy, Central Institute of Mental Health, Mannheim, Germany.
* w.weber-fahr@zi-mannheim.de

Synopsis: 31P MRSI at 3T shows deficits in the brain's energy metabolism in patients with neuropsychiatric consequences of COVID-19 disease. Changes in ATP seem to be correlated with cognitive test scores.

Introduction

Post-COVID syndrome: recovered, but not healthy. Symptom complex with typical symptoms such as fatigue, shortness of breath and cognitive disorders, which occurs within three months of infection, lasts for at least two months, for which there is no explanatory alternative diagnosis,may fluctuate and can occur after a free interval. Brain and cerebrospinal fluid examinations indicate that an inflammatory reaction of the brain tissue[1] and a disturbance of the neuronal energy metabolism[2] play a role.

Hypotheses for 31P- MR Spectroscopy in NP-Long-COVID-Patients: Alterations in the cellular energy metabolism in the brain. These findings correlate with the neuropsychological findings.

Metabolite Images

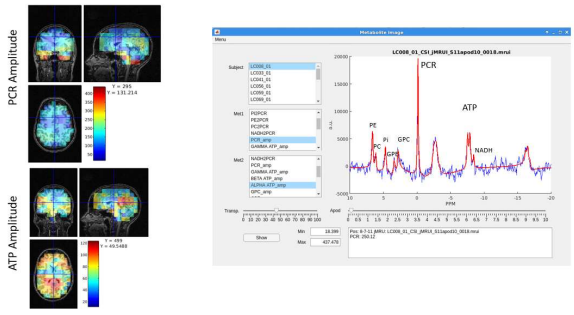

Fig. 1: Exemplary 31P MR spectrum and metabolite maps for PCr and ATP. ATP: Adenosintriphosphate; PC: Phosphocholine; GPC: Glycerophosphocholine; PCr Phosphocreatine; PE: Phosphoethanolamine; GPE: Glycerophosphoethanolamine; NADH: Nicotinamide adenine dinucleotide oxidized.

Methods

In total 30 subjects (18 long Covid patients and 11 controls) were measured at a 3T PRISMA Fit (Siemens) using a double-tuned send-receive coil. Measurements included an anatomical MPRage as well as an 31P 3D-CSI FID (FOV: 200x240x240mm³; Matrix 8x10x10 interpolated to 16x16x16; TR=2s; 15 weighted averages; 204ms Waltz 4 decoupling) over 25:32 minutes. Additionally, a phantom containing 50mL of concentrated hexamethyl-phosporous triamide solution (HMPT) was fixed at a predefined position inside the coil and FID data were acquired with each subject. The MR signal of HMPT is about 5800 Hz upfield from the PCr signal, and thus outside of the in-vivo bandwidth, was used for absolute quantification.

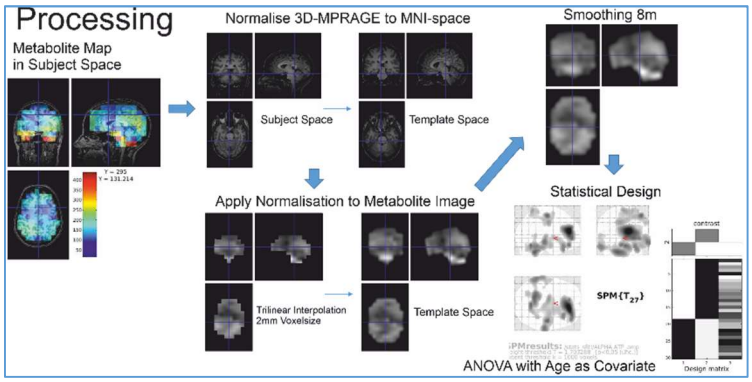

Fig. 2: Metabolite processing pipeline

Quantification of each CSI dataset was done with AMARES (jMRUI[3]), referenced to HMPT and a 3D metabolite image was created for each subject/metabolite in subject space (nii-format).

SPM12 was used for spatial normalization and statistics were . All metabolite images were brought into standard space by first normalizing each anatomical MPRage to the MNI Template and successively applying the non-linear transformation to each metabolite image using trilinear interpolation and a resolution of 2x2x2mm³. Finally, the normalized metabolite maps were smoothed (8mm) and statistically tested in a second level ANOVA with age as co-variate (Fig. 1+2).

Results

We see reduced GPC/HMPT and reduced ATP/HMPT in the patient group compared to the control group, mostly in the ACC but also in

the brain-stem (Fig. 3+4). Additionally Phosphate (PI/PCR) was reduced in the ACC ($p_{FDRClus}$=0.018) and the Cuneus (trend $p_{FDRClus}$=0.074; data not shown)

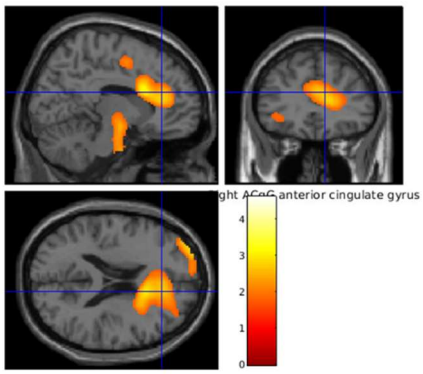

Fig. 3: Long Covid patients show reduced GPC mainly in the ACC and brainn stem (ACC cluster: pFDRClus=0.053 threshold p<0.01).

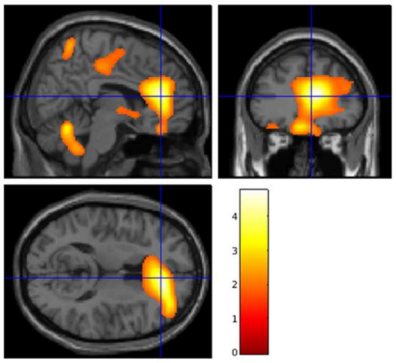

Fig. 4: Reduced ATP is observed in several brain regions most significantly in the ACC ((ACC cluster: pFDRClus=0.016 threshold p<0.01).

Post hoc tests over the mean spectra of 4 MRS-voxel located in the ACC region further revealed a correlation of ATP/PCr with cognitive test. i.e. the Moca and the trail making test (TMT, Fig. 5).

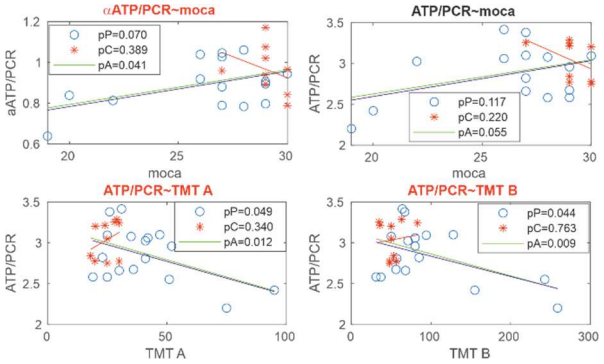

Fig. 5: Significant correlations of ATP/PCR with behavioral tests were observed in the ACC. Correlation significance pP within patient Group, pC within controls, pA overall.

Discussion

The transformation and spatial normalization of 3D metabolite maps as well as its statistical evaluation with SPM second level models seems to be robust so far and shows reproducible results that are in line with manual regional voxel selection. We see first indications that ATP and GPC are decreased in NP-long-COVID patients.

Conclusion

There seem to be deficits in the brain's energy metabolism in NP patients that can be detected with 31P MRSI.

References

1. Busatto G. F. et al., Post-acute sequelae of SARS-CoV-2 infection: relationship of central nervous system manifestations with physical disability and systemic inflammationPsychol Med. May 6 2022: 1–12.

2. Paul, Lemle, Komaroff, & Snyder, Redox imbalance links COVID-19 and myalgic encephalomyelitis/chronic fatigue syndrome Proc Natl Acad Sci U S A., 2021; 118(34): e2024358118.

3. Vanhamme L, Van Huffel S, Van Hecke P, van Ormondt D. Timedomain quantification of series of biomedical magnetic resonance spectroscopy signals. J Magn Reson 1999;140:120–130.

Optogenetic fPET/fMRI Reveals Distinct Roles of the Substania Nigra in Motor and Cognitive Processes

Yan Ma, [1, 2] * Fernando Bravo,[1] Sabrina Haas,[1] Tudor M. Ionescu,[1] Kristina Herfert[1]

[1] Department of Preclinical Imaging and Radiopharmacy, Werner Siemens Imaging Center, Eberhard Karls University Tübingen, Germany
[2] Department High-field Magnetic Resonance, Max Planck Institute for Biological Cybernetics, Tübingen, Germany

* Yan.Ma@med.uni-tuebingen.de

Synopsis: In this study we used data from simultaneous [^{18}F]FDG-PET/BOLD-fMRI experiments to investigate how optogenetic stimulation of the substantia nigra pars compacta (SNc) in rats affects brain functional (FC) and metabolic connectivity (MC). Our data show an isolation of the striatum during stimulation and negative correlations of the SNc with cortical and cerebellar regions, supporting evidence of a Cb-SNc connection.

Introduction

In Parkinson's disease (PD), nigrostriatal degeneration and subsequent cerebellar dysfunction are well-characterized pathological hallmarks. Advancements in neuroimaging, particularly PET and fMRI, have become instrumental in unraveling the intricate interplay between these brain regions. Our study employs a novel multimodal approach, combining bolus plus infusion [^{18}F]FDG-fPET and BOLD-fMRI during optogenetic stimulation of the substantia nigra pars compacta (SNc) in rats. This approach aims to comprehensively assess both metabolic and functional connectivity of the nigrostriatal pathway.

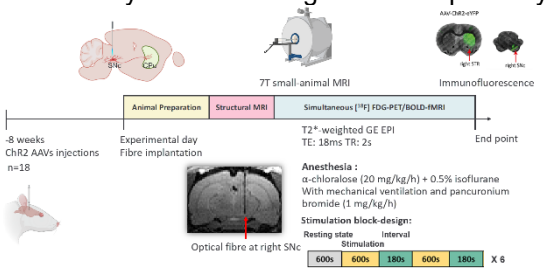

Fig. 1: Schematic representation of simultaneous PET/fMRI with block-design optogenetic stimulation.

Methods

Eighteen ChR2-overexpressing rats underwent simultaneous dynamic [^{18}F]FDG-PET/fMRI scans while receiving optogenetic stimulation in the rSNc (1). The stimulation protocol consisted of six 10-minute blocks alternating with five 3-minute intervals. Each stimulation block comprised eight cycles of 60 seconds light-on followed by 15 seconds light-off. FC and MC were investigated using canonical ROI-to-ROI connectivity (2). This analysis involved contrasting brain activity during stimulation blocks compared to intervals, and intervals compared to resting state.

Results

Optogenetic stimulation of the SNc in rats revealed positive funmetabolic connectivity within the nigrostriatal circuit as measured by [^{18}F]FDG-fPET, but not by BOLD-fMRI. Hemodynamic connectivity analysis showed positive connectivity with ipsilateral areas like the nucleus accumbens and amygdala, while negative connectivity with the contralateral CPu when comparing the stimulation > interval. Conversely, MC analysis revealed positive connectivity within the stimulated nigrostriatal circuit under both contrasts but negative connectivity with the cerebellum for the contrast Interval > Resting state. Furthermore, MC segregated cortical and subcortical regions into distinct clusters, with cortical regions exhibiting negative connectivity with the CPu and subcortical regions displaying positive connectivity with the CPu for the contrast of stimulation > interval. These findings suggest a dissociation between metabolic activity and functional connectivity in the nigrostriatal pathway upon SNc stimulation.

Discussion

Our study underscores differences in MC and FC as measured by [^{18}F]FDG-fPET and BOLD-fMRI, respectively, in elucidating the interplay between the nigrostriatal pathway and other brain regions. MC analysis revealed additional brain regions not captured by FC, suggesting complementary insights provided by each modality. Positive MC within the stimulated nigrostriatal circuit in both stimulation and

interval comparisons indicates that increased glucose metabolism reflects neuronal activity and projection pathways. The negative connectivity observed between cortical regions and the CPu in MC during the stimulation-interval contrast may imply differential energy allocation. Additionally, the anti-correlation between the cerebellum and the nigrostriatal pathway during the interval-rest contrast suggests functional specialization between the nigral-striatal and cerebellar-nigral pathways in motor function. FC analysis using BOLD-fMRI showed increased CPu connectivity with dopamine-related regions, suggesting enhanced dopamine release during stimulation. This might be due to the complex interplay between neurovascular coupling and dopamine signaling, requiring further investigation.

Conclusion

This *in vivo* study combining dynamic [^{18}F]FDG-fPET and BOLD-fMRI reveals distinct roles of the substantia nigra in motor and cognitive processes. Metabolic connectivity highlights positive nigrostriatal circuit connectivity and cerebellar involvement, while functional connectivity emphasizes dopamine-related regions. Our findings are in line with a previous study showing cerebellar nuclei provide monosynaptic inputs to midbrain dopaminergic neurons in the substantia nigra (3). The observed metabolic negative connectivity likely reflects adaptations within the brain network. These findings contribute to understanding brain function and lay the groundwork for future research exploring the nuanced interactions within the nigrostriatal pathway.

References

1. Haas S, Bravo F, Ionescu TM, Gonzalez-Menendez I, Quintanilla-Martinez L, Dunkel G, et al. Active Suppression of the Nigrostriatal Pathway during Optogenetic Stimulation Revealed by Simultaneous fPET/fMRI. 2023:2023.10.19.556049.
2. Whitfield-Gabrieli S, Nieto-Castanon A. Conn: a functional connectivity toolbox for correlated and anticorrelated brain networks. Brain Connect. 2012;2(3):125-41.
3. Washburn S, Onate M, Yoshida J, Vera J, Bhuvanasundaram R, Khatami L, et al. The cerebellum directly modulates the substantia nigra dopaminergic activity. Nature neuroscience. 2024;27(3):497-513.

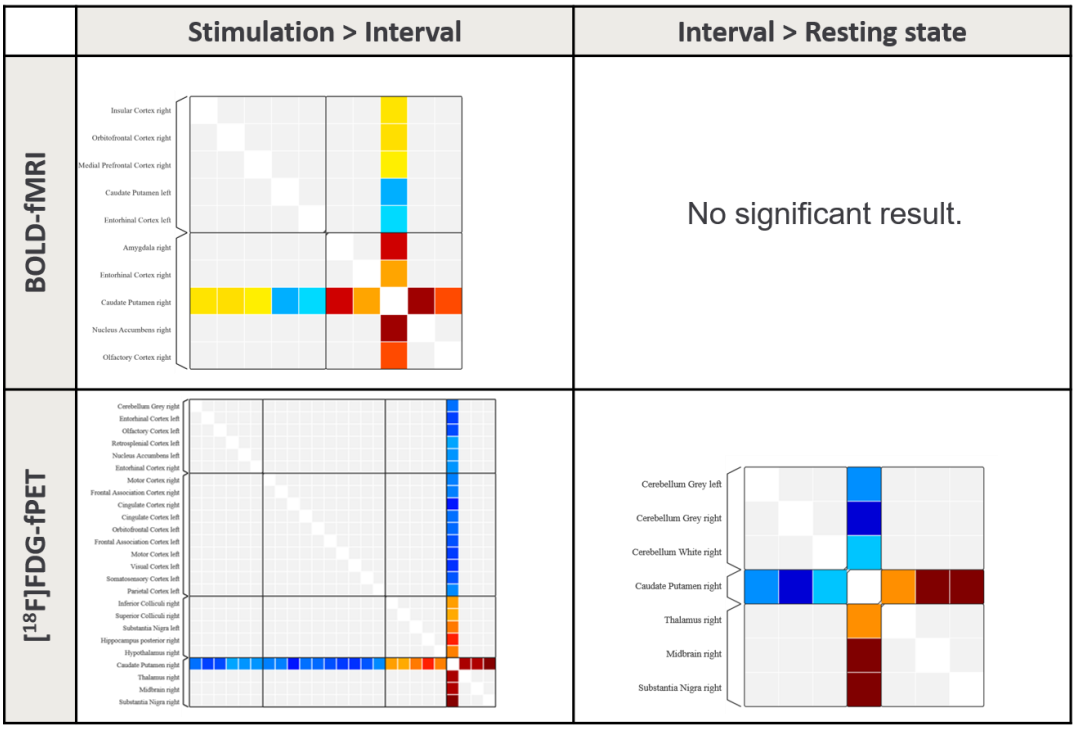

Fig. 2: rCPu Seeded ROI-to-ROI Hemodynamic and Metabolic Connectivity. (Note: Cluster thresholded at p < 0.05, cluster-level p-FDR corrected (MVPA omnibus test); connections thresholded at p-uncorrected < 0.05)

Semi-Automated Segmentation Pipeline for Dynamic MRI Analysis of Knee Joint Kinematics

Aayush Nepal[1*], Nicholas M. Brisson[2,3], Georg N. Duda[2,3], Jürgen R. Reichenbach[1] and Martin Krämer[1]

[1]Medical Physics Group, Institute of Diagnostic and Interventional Radiology, Jena University Hospital, Friedrich Schiller University Jena, Germany

[2]Julius Wolff Institute, Berlin Institute of Health at Charité – Universitätsmedizin Berlin, Germany

[3]Berlin Movement Diagnostics (BeMoveD), Center for Musculoskeletal Surgery, Charité – Universitätsmedizin Berlin, Germany

* aayush.nepal@uni-jena.de

Synopsis: Accurate segmentation of the tibia and femur from dynamic MRI scans during knee flexion-extension can provide detailed insights into joint kinematics. Developing a semi-automated segmentation pipeline enables a streamlined approach to tibiofemoral kinematic analysis, offering potential advancements in clinical and research applications.

Introduction

The study of tibiofemoral kinematics often employs three-dimensional MRI datasets to accurately capture the complex motion patterns of the knee joint [1]. Typically, these studies require a combination of static and dynamic scans, alongside sophisticated modelling techniques and algorithms to extract kinematic parameters [2]. While this approach is comprehensive, it is time intensive; other alternatives may simplify and hasten the acquisition and analysis.

This study introduces a semi-automated pipeline designed to segment the tibia and femur during knee flexion-extension cycles from single slice CINE images in the sagittal view, and to track kinematic parameters from these segments. By bypassing the need for high-resolution static scans and complex computational approaches like machine learning, this streamlined process offers a practical, less resource-intensive alternative for conducting kinematic assessments.

Methods

Dynamic MRI scans were acquired for five healthy volunteers (28-39 years old) using a Siemens 3T Prisma scanner. Volunteers underwent scans of the left leg as they actively completed repetitive, open chain knee flexion-extension cycles to the beat of a metronome (6 cycles/min), under both loaded (12 kg added weight) and unloaded conditions using a special MRI safe device for guided knee motion [3].

MRI was captured using a 2D radial golden-angle gradient echo FLASH sequence with echo time of 2.51 ms, flip angle of 8° and repetition time of 5.8 ms. The acquisition matrix size was 176 x 176 x 1. Each scan lasted 160 s, with a total of 100 k-space repetitions acquired. Cine images were reconstructed, with each frame representing a 2° interval of knee motion using iterative and non-Cartesian reconstruction techniques.

The semi-automated segmentation process was executed in five main steps: (1) Canny edge detection was used to identify edges in the image for the tibia and femur; (2) connected-component labeling technique was used to pick out edges of the interior boundary of the cortical bone; (3) key reference points were established on the binary edge outputs, facilitating frame-to-frame transformations using greedy nearest neighbor sorting and cubic spline interpolation; (4) transformation matrices that map the position of the bone edge from one frame to the next were determined through optimization of a cost function. This function quantified the alignment error between subsequent frames by calculating the minimal distances between transformed and target coordinates. Optimization of this function was conducted by using the nonlinear least squares approach to obtain the optimal set of translation and rotation parameters; and (5) these matrices were applied to the boundaries of the tibia and femur segments in the first frame, automating segmentation across the remaining frames in the motion cycle.

After segmentation, the angle between the long axes of the tibia and femur was derived using principal component analysis, and the Euclidean distance between anatomical landmarks at the distal and proximal points of these bones was measured.

Results

The segmentation algorithm consistently achieved a point-to-point alignment error of less than 0.40 ± 0.02 mm in tracking bone edges. Fig. 1 illustrates the semi-automatic segmentation of the tibia and femur (green) achieved for one of the datasets across the knee flexion-extension movement cycle. As shown in Fig. 2 and Fig. 3, the angle between the bones were similar between loaded and unloaded conditions, whereas the distance between anatomical landmarks showed some deviations during the initial stages of flexion.

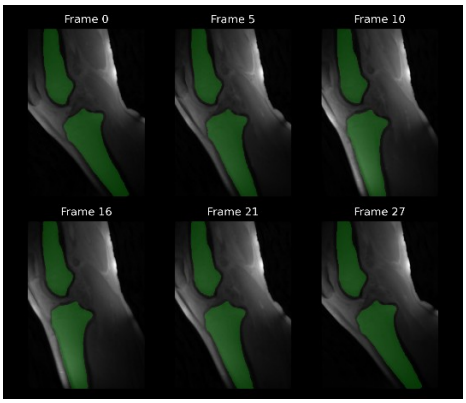

Fig. 1: Example segmentation: the tibia and femur (green) were segmented from one dataset at different points during the knee motion cycle.

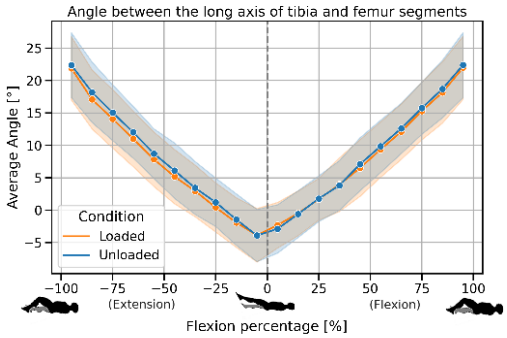

Fig. 2: Average angle between the long axes of the tibia and femur throughout the motion cycle under loaded (12 kg) and unloaded conditions. The shaded regions represent one standard deviation of uncertainty across all datasets.

Discussion

This study presents a semi-automated approach to tibiofemoral kinematic analysis, demonstrating that kinematic assessments can be effectively conducted by solely using dynamic 2D CINE images. Central to this approach is the automated segmentation of the tibia and femur across all frames, which significantly reduces the manual labor and time involved in the analysis process.

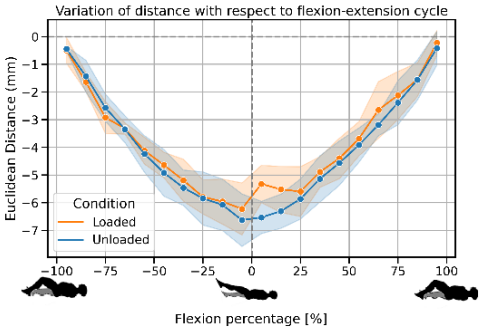

Fig. 3: Plot showing the variation of the Euclidean distance between anatomical landmarks on the tibia and femur with respect to time in the motion cycle. The shaded region represents one standard deviation of uncertainty across all datasets.

Notably, this method was able to capture differences in kinematic parameters such as the distance between anatomical landmarks, under different knee loading conditions, highlighting its practical application.

A study limitation was the occasional difficulty of restricting leg movement to a single plane, which may have affected the precision of the kinematic data. Future research could address this challenge by refining the mechanical setup. Furthermore, the application of this segmentation technique to other joints could be of interest, for instance, to analyze patellofemoral kinematics.

Conclusion

Through the development and application of a novel semi-automated algorithm, our proposed technique not only facilitates kinematic analysis using 2D dynamic MRI but also supports the potential for resource-efficient kinematic studies in clinical and research environments.

References

1. Hull ML. Coordinate system requirements to determine motions of the tibiofemoral joint free from kinematic crosstalk errors. Journal of Biomechanics. 2020.

2. d'Entremont AG et al. Do dynamic-based MR knee kinematics methods produce the same results as static methods? Magnetic Resonance in Medicine 69.6: 1634–1644. 2013.

3. Brisson NM et al. A novel multipurpose device for guided knee motion and loading during dynamic magnetic resonance imaging. Zeitschrift für Medizinische Physik 32:4 2022.

Tract masks for refined analysis of diffusion properties in motor tracts related to functional recovery after stroke in mice

A. Kalantari[1]*, L. Ruthe[1], V. M. Wiemer[1 2], T. Paul[1 2], L. J. Volz[1], G. R. Fink[1 2], **M. Aswendt**[1]

[1] University Hospital Cologne, Department of Neurology, Köln, North Rhine-Westphalia, Germany

[2] Research Centre Juelich, Institute of Neuroscience and Medicine (INM-3), Jülich, North Rhine-Westphalia, Germany

* akalant1@smail.uni-koeln.de

Synopsis: The study examines the integrity of the corticospinal tract (CST) and its relation to motor deficits and recovery post-stroke in mice. Utilizing diffusion tensor imaging (DTI) and the Allen Mouse Brain Atlas, tract masks were created to detect anisotropy changes in sensorimotor tracts. Quantitative validation showed significant coverage by viral tracing data. Longitudinal DTI analysis revealed a significant decrease in fractional anisotropy (FA) in stroke-affected tracts, correlating with motor impairment. The results align with human studies, indicating axonal degeneration as a primary factor in anisotropy changes. Ongoing research aims to correlate these findings with motor recovery and histological analysis.

Introduction

The integrity of the corticospinal tract (CST) is linked to motor deficits and outcome in stroke patients [1]. Wallerian degeneration causes structural disintegration and reduced anisotropy. Clinical studies show mixed results [2], and animal studies with diffusion analysis and histological validation do not provide conclusive insights into white matter changes related to motor behavior. Using DTI processing with the Allen Mouse Brain Atlas [3-4], small and elongated regions like the CST are affected by spatial shifts, possibly explaining the difficulty in quantifying reliable anisotropy changes.

Methods

We used a method of tract templates to detect anisotropy changes, previously developed for MRI in stroke patients [2]. Tract masks (Figure 1A) were created from a GQI mouse diffusion MRI atlas for various sensorimotor tracts by modifying fiber tracking parameters, seed region size, and manually delineating regions of avoidance. The masks were quantitatively validated by spatial registration with viral tracing data from the Allen Mouse Brain Connectivity Atlas (Figure 1B). Masks were included in the postprocessing using AIDAmri [5] for a dataset of 61 stroke and 16 sham C57BL/6J mice, with homogeneous cortical stroke lesions, longitudinal in vivo DTI, and motor tests.

Results

The visual overlay showed consistency in the three-dimensional projection of the mask and viral tracing. Quantitative analysis revealed 51.58% to 99.61% coverage by viral tracing fluorescence data. Statistical comparison between time points (Figure 1C) showed a significant early decrease in FA in all fiber tracts of the stroke group, with no significant difference from baseline in the optic tract at later time points. No significant changes were found in the sham group. A strong decrease in FA was detected at later time points in interhemispheric tracts (CC: baseline and day 29, $p<0.001$) and corticospinal tract (baseline and day 21, $p<0.001$). Quantitative analysis of AD, MD, and RD showed similar but less pronounced changes.

Discussion and Conclusion

Results with the tract mask approach confirm results in human stroke patients. MD in the corpus callosum and corticospinal tract increased, while AD and FA decreased, indicating axonal degeneration as the main cause of anisotropy changes. Detailed correlations to motor recovery and histological analysis are ongoing.

References

[1] Boyd LA, Hayward KS, Ward NS, Stinear CM, Rosso C, Fisher RJ, et al. Biomarkers of stroke recovery: Consensus-based core recommendations from the Stroke Recovery and Rehabilitation Roundtable. Int J Stroke.

2017;12: 480–493. doi:10.1177/1747493017714176

[2] Paul T, Cieslak M, Hensel L, Wiemer VM, Grefkes C, Grafton ST, et al. The role of corticospinal and extrapyramidal pathways in motor impairment after stroke. Brain Commun. 2022;5: fcac301. doi:10.1093/braincomms/fcac301

[3] Aswendt M, Pallast N, Wieters F, Baues M, Hoehn M, Fink GR. Lesion Size- and Location-Dependent Recruitment of Contralesional Thalamus and Motor Cortex Facilitates Recovery after Stroke in Mice. Transl Stroke Res. 2021;12: 87–97. doi:10.1007/s12975-020-00802-3

[4] Pallast N, Wieters F, Nill M, Fink GR, Aswendt M. Graph theoretical quantification of white matter reorganization after cortical stroke in mice. Neuroimage. 2020;217: 116873. doi:10.1016/j.neuroimage.2020.116873

[5] Pallast N, Diedenhofen M, Blaschke S, Wieters F, Wiedermann D, Hoehn M, et al. Processing Pipeline for Atlas-Based Imaging Data Analysis of Structural and Functional Mouse Brain MRI (AIDAmri). Front Neuroinform. 2019;13: 42. doi:10.3389/fninf.2019.00042

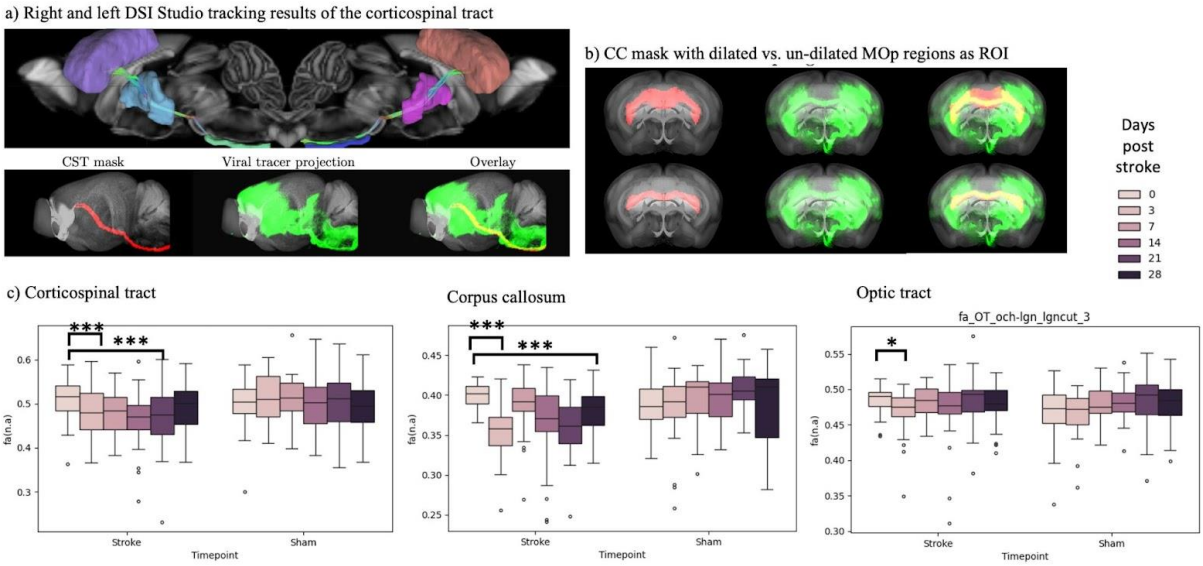

Figure 1: Representative examples for diffusion atlas-based tract mask and FA results a) Fiber tracking result for the corticospinal tract and qualitative validation with viral tracer projection (experiment ID 100141780). b) Qualitative validation of a dilated vs. non-dilated corpus callosum mask with each individual viral tracer projection (experiment ID 100141780). Overlay of Allen Mouse Brain atlas template (grey), CC masks (red) and viral tracing (green). c) FA results for corticospinal tract, corpus callosum and optic tract masks in stroke and sham mice. Repeated measures ANOVA between day 0 (baseline before stroke) and subsequent days 3, 7, 14, 21, and 28 post stroke.

Unravelling yeast metabolism with real-time deuterium magnetic resonance spectroscopy

Fatima Anum[1*], Charbel Assaf[1], Farhad Haj Mohamad[1], Maria Anikeeva[1], Jyotirmoy Dey[2], Simon Kaltenberger[2], Eric Beitz[3], Lina Welz[4], Victoria Annis[5], Manuel van Gemmeren[2], Simon Duckett[5], Jan-Bernd Hövener[1] and Andrey N. Pravdivtsev[*]

[1]University Medical Center Schleswig-Holstein, Kiel University, Department of Radiology and Neuroradiology, Section Biomedical Imaging, Molecular Imaging North Competence Center (MOIN CC), Am Botanischen Garten 14, 24118 Kiel.
[2]Otto Diels Institute for Organic Chemistry, Kiel University, Otto- Hahn Platz 4, 24118 Kiel, Germany.
[3]Pharmaceutical Institute, CAU Kiel, Gutenbergstr. 76, 24118 Kiel.
[4]Institute of Clinical Molecular Biology, CAU Kiel & Physician at Department of Internal Medicine I, UKSH Rosalind-Franklin-Straße 12 24105 Kiel, Germany.
[5]Centre for Hperpolarization in Magentic Resonance, University of York, Heslington, York, YO10 5DD, UK

* fatima.anum@rad.uni-kiel.de

Synopsis: Implementing deuterium NMR (D-NMR) of yeasts allowed us to measured T_1, T_2 and chemical shifts for 25 deuterium labeled substrates with a sensitivity of SNR = 3 per mM deuterium in case of fumarate-d_2 (**Figure 1**) at 9.4 T. We observed and quantified real-time metabolism of a) pyruvate-d_3 to ethanol-d_3 and acetate-d_3, b) fumarate-d_2 to malate-d_2, c) nicotinamide-d_4 to nicotinic acid-d_4, and d) glucose-d_2 to ethanol-d_2 and acetate-d_2, e) acetone-d_6 to propan-2-ol-d_6. Thus, yeast, deuterated substrates and deuterium NMR at 9.4 T are well-suited for studying metabolism on a timescale of seconds to hundreds of minutes.

Introduction

Analyzing the metabolism of an organism is crucial for understanding and monitoring diseases and treatments. Nulcear magnetic resonance (NMR) is the only technique allowing to measure the metabolism non invasively, in vivo and in vitro, statically and dynamically. However, the effectivieness of this technique is limited by a relatively low sensitivity.

This issue is addressed by ever improving hardware and the hyperpolarization of nuclear spins. The latter boosts the NMR signal by several order of magnitude, but requires specialized equipment and allows only a short observation window of one or two minutes.

Recently, deuterium labelled MR was rediscovered and used for metabolic imaging in humans[1]. The only equipment needed is a deuterium-capable system. Still, many important parameters of potential DMI tracers remain unreported, and a simple, robust system for metabolic in vitro D-NMR is yet to be developed.

Our study addresses these challenges using baker's yeast (*Saccharomyces cerevisiae*) as a model system for metabolic D-NMR and various deuterium labeled substrates. Yeast solutions can be a standard test phantom for D-NMR due to their availability and metabolic simplicity.

Methods

1 g of food-grade baker's yeast was suspended in 7 mL deionized water, incubated at 32°C for 10 min, and shaken every 3 min to release CO_2. 248 µL of this suspension were transferred to a preheated NMR tube with glass beads at the bottom and placed in a 400 MHz NMR at 310 K (WB 400, Avacne Neo, Bruker). Deuterated substrate solutions [10-30 mM in 100 mM phosphate buffered saline (PBS)] were injected via 1/32"x0.25 mm capillary tubing. ^{2}H, 90° spectra were acquired by averaging 8 scans over 1.53 min with 11.5 sec repetition time (TR). pH was measured after each experiment. Some experiments included adding pyruvate at variable concentration and incubating for 10 min before adding glucose-d_2 or nicotinamide-d_4.

T_1, T_2 and chemical shifts for 25 tracer molecules were calculated using protic aqueous solution of 100 mM pH 7.4 PBS at 310 K with a concentration of 10-30 mM (**Table 1**), glucose-d_2 (gluc-d_2), pyruvate-d_3 (pyr-d_2), acetate-d_3 (acet-d_2), formate-d (form-d_2), lactate-d_3 (lact-d_2), serine-d_3 (ser-d_2) from euristop; methanol-d_4 (meth-d_2), ethanol-d_5 (eth-d_5), fumarate-d_2 (fum-d_2), acetone-d_6 (ace-d_2), glucose-d_7 (gluc-d_7), and succinate-d_4 (suc-d_2) from sigma aldrich; nicotinamide-d_4 (nam-d_4) and tryptophan-d_5 (tryp-d_5) synthesized in-house.

Signals were zero filled and analyzed using MNova (14.2.2, Mestrelab Research S.L.) Integrals were used to model first-order kinetics with mono-exponential decay fitting.

Results

T_1, T_2 and chemical shifts were successfully measured for 25 substrates (**Table 1**). Using these parameters, optimal repetition time was set to 11.5 s ensuring relaxation of all products.

Adding the deuterated tracers to the yeast solutions allowed us to observe several different metabolic fluxes and to fit the kinetic model: pyr-d_3 to eth-d_3 and acet-d_3 via pyruvate decarboxylase (PDC), alcohol dehydrogenase (ADH) and aldehyde dehydrogenase (ALD); fum-d_2 to mal-d_2 (**Figure 1**) via fumarase (FDH). The transfer and metabolism of Fum was shown to relatively slow in healthy cells and fast in necrotic ones. Here, the deionized water is likely to have created osmotic stress, lysis, FDH release and enhanced malate production; nam-d_4 to na-d_4 via nicotinamide amidohydrolase; gluc-d_2 to eth-d_2 and acet-d_2 mainly via hexokinase, PDC, ADH and ALD.

When the cells were prefed with pyruvate, the conversion rates changed, indicating a deviation of normal fermentation.

***Table 1**: T_1, T_2 and chemical shifts of biomolecules (30-10 mM) in PBS (100 mM) at pH 7.4, 310 K and 9.4 T. Chemical shifts were calibrated to the residual water resonance at 4.70 ppm. Exemplary data for 5 biomolecules out of the25 measured are given.*

Tracers	Chemical shift (ppm)	T_1, (ms)	T_2, (ms)
Water-*d*	4.70	630±20	610±50
D-Gluc-d_2	3.8 (unresolved)	93±5 (avg)	80±3 (avg)
Pyr-d_3	2.47	2010±30	1950±1120
Fum-d_2	6.65	247±2	246±18
NAM-d_4	9.09, 8.88, 8.42, 7.77	182±12 (avg)	165±59 (avg)

Discussion

Yeast proved effective for studying metabolism with deuterated substrates, being easy to prepare and cost-effective. However, using deionized water can lead to unstable osmotic pressure and cell lysis, promoting fumarase release for fumarate to malate conversion. Using a buffer has already been reported to stabilize the cell environment, but it slows fumarase release.

Our sensitivity (SNR per deuterium label) for fum-d_2 was approximately 1 / mM with a single, 90° acquisition and 3 Hz exponential filter. Higher magnetic fields will increase signal and reduce T_1, allowing faster repetitions. The TR of 11.5 s used here aimed to balance relaxation and temporal resolution, ensuring thermal equilibrium and quantitative data.

In some cases, the products had longer T_1 than the substrates. For instance, the observed T_1 of gluc-d_2 was (93 ± 5) ms, while T_1(eth-d_2)= (1100 ± 5) ms and T_1(acet-d_2) = (3140 ± 4) ms. Therefore, choosing appropriate repetition times is crucial for accurate quantification.

The method was sensitive enough to detect differences in metabolism of cells prefed with pyruvate, forcing them to produce lesser ethanol and higher acetoin or 2,3-butanediol. Conversion rates will be presented at the conference.

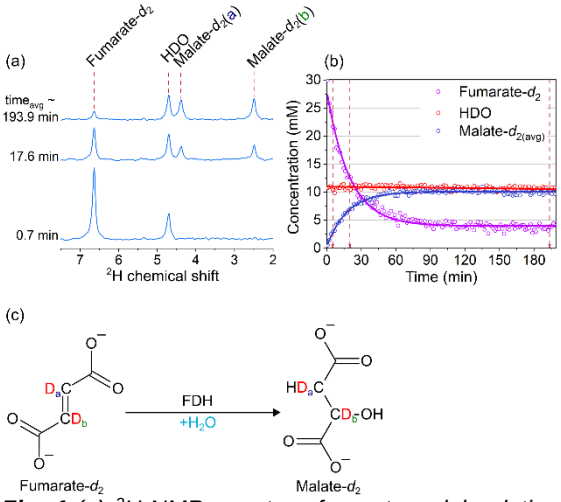

***Fig. 1:**(a) ^{2}H-NMR spectra of yeast model solution acquired 0.7 min, 17.6 min and 193.9 min after supply of fum-d_2. Metaboic converstion to mal-d_2 was found and used to fit a kinetc model (b) of the reaction depicted in (c). Note the increasing malate signal with time, indicating the subsequent release of FDH into the solution under osmotic stress. Each spectrum is the average of 8 (90°) scans acquired in 1.53 min.*

Conclusion

Yeast, deuterated substrates and deuterium NMR at 9.4 T are well-suited for studying metabolism on a timescale of seconds to hundreds of minutes. The sensitivity of D-NMR enables the monitoring of some, but not all, metabolic steps. As hyperpolairzed MRI probes processes on a different time frame, the combination of both techniques promises to provide a more complete picture of metabolism, the foundation of all life.

Acknowledgements

We acknowledge our funding from German Federal Ministry of Education and Research (BMBF) with framework of e:Med research funding concept (01ZX1915C), BMBF hyperquant consortium (BlueHealthTeach, 03WIR6208A9), DFG (PR1868/3-1, PR 1868/5-1, HO-4602/3, EXC2167, FOR5042, TRR2879), MOINCC was funded by the grant from the European Regional Development Fund (ERDF) and the Zukunftsprogramm Wirtschaft of Schleswig-Holstein (Project no. 122-09-053).

References

1. De Feyter, H. M. *et al. Sci.Adv* **4**, eaat7314 (2018)